SECONDARY INSTABILITIES OF BOUNDARY LAYERS

by

Jamal Ahmad Masad

Dissertation submitted to the Faculty of the

Virginia Polytechnic Institute and State University

in partial fulfillment of the requirements for the degree of

Doctor of Philosophy

in

Engineering Mechanics

APPROVED:

Ali H. Nayfeh, Chairman

Saad A. Ragab

Dean T. Mook

Demetri P. Telionis

Eugene M. Cliff

September, 1990

Blacksburg, Virginia

SECONDARY INSTABILITIES OF BOUNDARY LAYERS

by

Jamal Ahmad Masad

Ali H. Nayfeh, Chairman

Engineering Mechanics

(ABSTRACT)

Several aspects of the subharmonic instability of boundary layers are studied. First, the subharmonic instability of incompressible flows over a flat plate is investigated using the resonant triad model and the Floquet model. The primary wave is taken in the form of a two-dimensional (2-D) Tollmien-Schlichting (T-S) wave. The subharmonic wave is taken in the form of a three-dimensional (3-D) wave. Results from both models are presented and compared with the experimental data and numerical simulation. It is found that the results of the Floquet model are in good agreement with the experimental data and numerical simulation, whereas the results of the resonant triad model agree only qualitatively with the experimental data.

Second, the subharmonic instability of incompressible flows over a 2-D hump is studied using the Floquet model. The mean flow over the hump is calculated by using interacting boundary layers, thereby accounting for viscid/inviscid interactions. The results show that increasing the hump height results in an increase in the amplification factors of the primary and subharmonic waves. When the hump causes separation, the growth rates of both the primary and subharmonic waves are considerably larger than those obtained in the case of no separation.

Third, the subharmonic instability of compressible boundary layers over a flat plate is studied using the Floquet model. Results are presented for adiabatic wall boundary conditions and subsonic, transonic, and supersonic flows. For supersonic flows results are presented for first- and second-mode primary waves. The effect of

Mach number, spanwise wavenumber, primary-wave amplitude, Reynolds number, and frequency are studied.

Fourth, results for the effect of heat transfer on the subharmonic instability of a two-dimensional compressible boundary layer over a flat plate are presented for different Mach numbers. For supersonic flows results are presented for first- and second-mode waves. The effect of different levels of heat transfer on changing the features of the subharmonic compressible instability is evaluated.

Fifth, results for the effect of suction on the subharmonic instability of a two-dimensional compressible boundary layer over a flat plate are presented. It is found that when the primary wave is a first-mode merging with a second-mode, the subharmonic wave is strongly destabilized by suction.

Sixth, the effect of a bulge on the subharmonic instability of compressible boundary layers is studied. It is found that the effect of compressibility on reducing the growth rate of the disturbances weakens as the hump height increases.

Acknowledgements

At the top of the list of gratitude is Dr. Ali H. Nayfeh. Without his supervision this work would not have materialized. Thanks are given to Dr. S. A. Ragab for many useful discussions and suggestions. Thanks are also given to Drs. D. T. Mook, D. P. Telionis, and E. M. Cliff for their contribution as committee members.

I would like to thank my wife Candy for her patience and understanding. Thanks are given to Sally Shrader for her excellent work of typing this thesis. This work was supported by the Office of Naval Research under Grant No. N00014-85-K-0011.

To my parents Ahmad and Roshdieh and my wife Candy

Acknowledgements

Table of Contents

1. INTRODUCTION

1.1. Routes to Transition

Experimental studies on the transition from a laminar 2-D boundary layer to a turbulent boundary layer of incompressible flows over flat plates using hot wire anemometers and flow visualization have revealed that transition takes place in several stages. First 2-D T-S waves appear and propagate downstream, these waves are selectively amplified by the boundary layer, then the higher harmonics of the T-S waves are generated, and the mean flow is distorted. In the next stage of transition a spanwise variation in the disturbance field starts to show up, this variation increases and eventually sets in strong three-dimensionality in both the disturbance field and the mean flow. Following this, two types of transition can take place. In the first type, this inflectional instantaneous velocity profiles with embedded high-shear layers at the peak positions develop. Then small-scale high frequency oscillations (spikes) are formed in the neighborhood of the shear layers thus setting in irregular motion and leading to breakdown of the laminar flow. The second type of transition

is characterized by a low-frequency breakdown of a laminar flow (without formation of turbulent spots) through excitation of a subharmonic wave and incommensurable low frequency fluctuations and by the filling of the spectrum as a result of a nonlinear interaction of high- and low-frequency disturbances.

1.2. Subharmonic Instability in Incompressible Boundary Layers Over a Flat Plate

The experiments of Klebanoff et al. (1962) showed the spontaneous growth of oblique waves having a frequency that is near that of the primary T-S wave, but they did not provide any evidence of the generation of subharmonic oblique waves. Kachanov, Kozlov and Levchenko (1977) were the first to provide an evidence for the excitation of subharmonic waves. In their experiment they specified a fairly large amplitude of the wave, from the very onset, and studied mainly the spectral composition of the disturbance field. They noted from the spectrum of the disturbance that after the appearance of the primary wave and its harmonics there comes a region which is characterized by the appearance and growth of certain low-frequency disturbances which should be attenuated according to linear theory. At the end of this region the entire low-frequency part of the spectrum begins to grow with a distinguishable harmonic having a frequency that is equal to one-half the frequency of the primary wave; that is, a subharmonic wave. The excitation of the subharmonic wave was considered afterwards in the experiments of Kachanov and Levchenko (1984), Saric and Thomas (1984) and Corke and Mangano (1989). Saric and co-worker used a smoke-wire technique for flow visualization and obtained

pictures such as those in Figure 1.1 for the onset and development of three-dimensionality. At low T-S amplitudes, one observes the arrangement in Figure 1.1a. The Λ –shaped vortex loops are staggered, repeating every $2\lambda_x$, where λ_x is the wavelength of the T-S waves, indicating a subharmonic of the T-S waves. The hot-wire measurements record a frequency that is one-half that of the T-S wave (i.e., subharmonic). In some observations $\lambda_z > \lambda_x$ and in others $\lambda_z < \lambda_x$, where λ_z is the spanwise wavelength of the staggered vortices. At higher T-S amplitudes, one observes the arrangement in Figure 1.1b. The Λ –shaped vortex loops are such that the peaks and valleys are aligned, repeating every λ_x. The fixed hot-wire measurements record a frequency that is equal to that of the T-S wave (i.e., fundamental). Typically, $\lambda_z < \lambda_x$.

Using hot-wire anemometer probes, Kachanov and Levchenko (1984) recorded the development of wave disturbances and the structure of the mean flow in a boundary layer on a flat plate. The experiments were conducted in a low-turbulence wind-tunnel (test section: 1 m high, 1 m wide, 4 m long) at a freestream speed of 9.18 m/s and a turbulence level less than 0.02%. The flat plate used in the experiments is 1.5 m long, 1 m wide, and 10 mm thick and mounted horizontally at a zero angle of attack in the tunnel. The pressure gradient beyond 100 mm from the leading edge was not more than 0.8% per 1 m length. A vibrating ribbon was used to generate T-S waves with specified frequencies and their downstream evolution was studied using the complete spectrum of the signal. The vibrating ribbon was located 250 mm downstream of the leading edge at a height of 0.15-0.2 mm from the plate. The vibrating ribbon was initially excited by a single frequency of 120 Hz and the amplitude of the excitation was gradually increased. At low excitation amplitudes, the spectra showed the development of a broadband of rather low frequencies. As the initial amplitude of the T-S wave increased beyond about 0.163%, the spectra showed

the excitation of a subharmonic wave and incommensurable low-frequency fluctuations, leading to the breakdown of the laminar flow by the filling of the spectrum. As the initial amplitude of the T-S wave approached 1%, the higher harmonics were excited and grew from the very beginning. At the same time, the three-dimensionality of the mean flow and fluctuations grew stronger, leading to the K-breakdown (after Klebanoff) of the laminar flow. They observed a similar behavior for the frequency 96.4 Hz.

To determine the spectral width of the subharmonic resonance, Kachanov and Levchenko (1984) excited the vibrating ribbon with two frequencies f_1 and f_2 simultaneously. They observed the sum $f_1 + f_2$, and the difference $f_1 - f_2$ frequencies as well as other higher-order combinations in the spectra. They fixed the level of excitation, choose $f_1 = 120$ Hz, and varied f_2 from 30 Hz to 70 Hz, with the subharmonic resonance detuning $\delta f = \frac{1}{2} f_1 - f_2$ varying from -30 Hz to $+10$ Hz.

Kachanov and Levchenko (1984) relied on random 3-D disturbances to provide seeding for the subharmonic wave. This resulted in low-frequency meandering of the structures, which made the interpretation of the experimental results difficult. To avoid this problem, Corke and Mangano (1989) simultaneously generated 2-D and 3-D waves having specified frequencies and wave direction using a spanwise array of line heaters suspended just above the wall at a height that approximately corresponds to the critical layer. For a spanwise heating segment of length s, a time series period τ, and a radian phase shift ϕ between adjacent line heaters, they were able to produce spatially propagating waves at equal and opposite angles to the flow direction given by

$$\theta = \pm \tan^{-1} \frac{c\phi\tau}{2\pi s} = \pm \tan^{-1} \frac{\beta}{\alpha}$$

Hence, they were able to produce oblique waves with any desired wave direction and to vary the initial amplitudes and phase differences of the T-S and oblique waves. Their results demonstrate the subharmonic instability. Moreover, their results for large initial amplitudes of the subharmonic wave are helpful in validating any theoretical studies on their nonlinear development and their interaction with the T-S wave.

Mainly there are two analytical models for studying the subharmonic instability in boundary layers. These are the resonant triad model and the Floquet model.

Raetz (1964) and Stuart (1961) established the occurrence of triad resonances for certain waves which are neutrally stable according to linear theory. Craik (1985, 1971, 1975, 1978) established the occurrence of triad resonances over a flat plate. Specifically he found that a 2-D wave

$$u = a\zeta_1(y)e^{2i(\alpha x - \omega t)} + cc$$

forms a resonant triad with the two 3-D waves

$$u_1 = a_1\xi_1(y)e^{i(\alpha x - \beta z - \omega t)} + cc$$

and

$$u_2 = a_2\xi_2(y)e^{i(\alpha x + \beta z - \omega t)} + cc$$

Then using temporal instability analysis he derived the equations governing the modulation of the amplitudes a, a_1, and a_2 with time. He found that the amplitudes become indefinitely large at a finite time, an explosive instability. We note that in the resonant-triad model, the frequencies and streamwise wavenumbers of the 3-D waves are respectively equal to half the frequency and streamwise wavenumber of the 2-D wave. The sum of the spanwise wavenumbers of the 3-D waves is equal to

zero; which means that the 3-D waves form equal but opposite angles with the streamwise direction. Craik analyzed the resonant triad problem for the temporal case. He showed that for a certain frequency and Reynolds number it is always possible to find a spanwise wavenumber such that the 2-D wave and the pair of the 3-D waves are perfectly tuned. Then, by considering a piecewise-linear boundary-layer profile and using asymptotic theory, he determined the order of magnitude of the interaction coefficients. Usher and Craik (1975) extended the temporal case to third order and presented results for the second-order interaction coefficients. Craik and Adam (1978) studied the modulation equations where the wave amplitudes vary with two space variables and time. They assumed that the amplitude of the 2-D wave is much larger than the other two and that the 2-D wave is not affected by the interaction. Lekoudis (1977) derived the equations governing the modulation in space and time of the amplitudes of the waves forming the resonant triad by relaxing the assumption of perfect resonance. Volodin and Zelman (1979) computed the interaction coefficients and presented some results. Nayfeh and Bozatli (1979) analyzed the stability of a 2-D secondary T-S wave whose wavenumber and frequency are nearly one-half those of a primary 2-D T-S wave. They found that the primary wave acts as a parametric exciter for the secondary wave provided that the amplitude of the primary wave exceeds a critical value, which is proportional to the detuning of the two waves.

Starting from the unsteady triple-deck equations and for high-frequency waves and high Reynolds numbers, Smith and Stewart (1987) derived the nonlinear triad equations governing the modulation in time and space of the amplitudes of the 2-D and 3-D waves. They calculated the interaction coefficients as the Reynolds number tends to infinity. Owing to their use of the triple-deck equations which have to be applied at some location, their calculated interaction coefficients are constant. Our

results show that the interaction coefficients depend on the value of the Reynolds number. They solved the temporal form of the modulation equations and found that the solutions have a rather chaotic spiky appearance.

The existence of multi-wave resonances was studied theoretically by Zelman and Maslennikova (see Kachanov (1987)). Their calculations demonstrated the properties of the resonant sets of waves that were discovered experimentally by Kachanov and Levchenko. In particular, a large spectral resonance width was demonstrated as well as the property of symmetrization of resonantly amplified harmonics. Other characteristic features of three- and multi-wave resonance were demonstrated in the theory.

In the parametric instability model, the basic flow is viewed as the sum of the Blasius profile and the 2-D T-S wave, which makes the basic flow almost periodic in the streamwise direction. One method of solution is to apply Floquet theory to derive the equations governing the subharmonic mode and boundary conditions. This will yield an eigenvalue problem which is solved locally to compute the rate of growth and the eigenfunctions of the subharmonic mode. Maseev (1968) was the first to apply Floquet theory to boundary-layer instability. Herbert (1984, 1985, 1988) applied Floquet theory to formulate the subharmonic instability problem. He solved the problem using a collocation method with Chebyshev polynomials; his results are in good agreement with the experimental data of Kachanov and Levchenko (1984). Herbert (1984) traced the eigenvalues of the subharmonic instability problem as the amplitude of the 2-D wave tends to zero. Bertolotti (1985) studied the effect of pressure gradients on the subharmonic instability of incompressible boundary layers. He showed that a decrease in the pressure-gradient coefficient increases the growth rate of both the T-S wave and the subharmonic disturbance. He also showed that a decrease in the pressure-gradient coefficient increases the range of unstable

spanwise wavenumbers and causes dramatic changes in the eigenfunctions; that is, the disturbance velocity profiles. Santos (1987) extended the Floquet model to the case of arbitrary wavelengths, thereby including the subharmonic and fundamental instabilities as special cases. Modes with wavelengths in between the subharmonic and fundamental values are called detuned modes. For the Blasius boundary-layer flow, Santos found the growth rates of modes slightly detuned from the subharmonic mode to be almost as large as the growth rate of the subharmonic itself.

Spalart and Yang (1987) studied the early 3-D stages of transition in the Blasius boundary layer by numerically solving the Navier-Stokes equations. They found that for intermediate amplitudes of the 2-D wave the breakdown is of the subharmonic type and the dominant spanwise wavenumber increases as the amplitude of the 2-D wave increases. Recently, Fasel (1990) numerically simulated solutions of the 3-D Navier-Stokes equations to study the spatial stability of the fundamental and subharmonic resonances. Kloker and Fasel (1990) numerically simulated the 2- and 3-D instability waves in 2-D incompressible boundary layers with streamwise pressure gradients. They studied both the subharmonic and fundamental instabilities. They found that, in the presence of strong adverse pressure gradients, the growth rate of the fundamental resonant wave exceeds that of the subharmonic wave.

In Chapter 2, the subharmonic instability is analyzed using the resonant-triad and Floquet models. Results from both models are presented and compared with each other, with available experimental data, and with numerical simulation.

1.3. Effect of a Bulge on the Subharmonic Instability of Boundary Layers

The performance of natural laminar flow (NLF) airfoils is critically dependent on the location of transition, which may be strongly influenced by surface imperfections. Although modern metal and composite manufacturing techniques can provide smooth surfaces that are compatible with NLF, manufacturing tolerance criteria are needed for other unavoidable surface imperfections. These imperfections include waviness and bulges, steps and gaps at junctions, and 3-D roughness elements, such as flush screw head slots and incorrectly installed flush rivets. Other unavoidable discontinuities arise from the installation of leading-edge panels on wings, nacelles, and empennage surfaces and the installation of access panels, doors, and windows on fuselage noses and engine nacelles (Holmes, et al. 1984; Obara and Holmes 1985; Holmes et al. 1986). Because discontinuities cannot be avoided, a guide is needed for manufacturing tolerances. The guide should not be related to the drag generated by these discontinuities but to their allowable sizes so that laminar flow can be maintained. The mechanisms by which these imperfections cause transition include amplification of T-S waves, Kelvin-Helmholtz instability (for separated flows), enhancement of secondary instabilities, amplification of cross-flow vorticity, Gortler instability, enhancement of receptivity of freestream turbulence and acoustic disturbances, and any interaction between two or more of these mechanisms (Holmes, et al., 1986; Fage, 1943; Goldstein, 1985; Nayfeh, et al., 1988).

Walker and Greening (1942) made wind-tunnel experiments to determine the effect of 2-D smooth bulges and hollows on the transition of the flow over a flat plate. They used surface tubes to determine the location of transition from laminar to

turbulent flow. Their bulges and hollows were mounted on one side of a smooth flat aluminum plate, having an elliptic leading edge. Hislop (1943) carried out similar experiments for narrow spanwise surface-ridge corrugations on a flat plate. Walker and Cox (1942) made wind-tunnel experiments to study the effect of spanwise corrugations on an airfoil. These experiments were made for three forms of narrow corrugations (flat, arch, and wire) situated in the laminar boundary layer of a large symmetric airfoil (EQH 1260 section) mounted at zero angle of attack.

Fage (1943) collected the three previous works (Walker and Greening, 1942; Hislop, 1943; Walker and Cox, 1942) and established criteria for the critical heights of these imperfections that cause transition from laminar to turbulent flow. He found out that the flow conditions near a corrugation that affect transition are associated with a separation of the laminar boundary layer from its surface. The criteria of Fage for steps and gaps did not include the effects of the shapes of these imperfections. However, the flight experiments of Holmes et al. (1986) demonstrate the strong influence of the shapes of steps on the transition location and hence on the allowable heights of such imperfections. They found out that by rounding a forward-facing step the critical Reynolds number increases from 1800 to 2700.

Carmichael, Whites, and Pfenninger (1957) and Carmichael and Pfenninger (1959) performed flight experiments on the wing glove of an F-94A airplane. The modified 652-213 airfoil had 69 suction slots distributed between 41 and 95% chord. They investigated single and multiple sinusoidal waves located at 15%, 28%, and 64% chord. Their results show that the allowable sizes of the waves increase when embedded in the suction region. They found that to maintain laminar flow across the airfoil requires an 8% increase in the suction level over the clear airfoil case. Carmichael (1959) established criteria for allowable single and multiple bulges or sinusoidal waviness for both swept and unswept wing surfaces using the results of

his experiments that partially include the influence of compressibility, suction, pressure gradients, multiple imperfections, and wing sweep. Carmichael's criteria are based on experimental results for waves located more than 25 percent chord downstream of the leading edge, and hence, they underpredict allowable imperfections in the leading-edge region and overpredict allowable imperfections in regions of unaccelerated flows. Spence and Randall (1953) investigated the effect of uniform suction on the stability of boundary layers over plates with sinusoidal surface waves. They derived a closed-form expression for the case of an asymptotic mean profile.

As a first step toward an understanding of the physics of the instability of flows around surface imperfections, Nayfeh et al. (1988) investigated the influence of a 2-D hump on the amplification of 2-D T-S waves for incompressible flows. They correlated their results with the experiments of Walker and Greening (as reported in Fage, 1943) and found that the N factor is in the range of 7.4-10.0. They also found that the most dangerous frequency is different from that for the flow over a flat plate. A similar behavior was confirmed by Cebeci and Egan (1989). Ragab et al. (1990) extended the work of Nayfeh et al. (1988) and investigated the stability of compressible flows over smooth 2-D backward-facing steps. Al-Maaitah et al. (1990a) investigated the effect of wall cooling on the stability of compressible flows over smooth 2-D backward-facing steps. They found that there is an optimal cooling level beyond which more cooling results in destabilizing the flow. Al-Maaitah et al. (1990b) investigated the influence of suction on the stability of compressible flows over backward-facing steps for Mach numbers up to 0.8. They found that continuous suction stabilizes the flow outside the separation bubble, as expected, but it destabilizes the flow inside it. For the same suction flow rate, properly distributed suction strips stabilize the flow more than continuous suction.

In Chapter 3 the influence of a 2-D hump on the 3-D subharmonic incompressible instability on a flat plate is investigated. The mean flow is calculated by using interacting boundary layers, thereby accounting for the viscid/inviscid interaction. The primary wave is taken in the form of a 2-D wave. The secondary wave is taken in the form of a 3-D subharmonic wave. The effect of the hump height and the disturbance frequency on the instability characteristics are studied. In Chapter 7 the effect of a 2-D hump on the 3-D subharmonic compressible instability on a flat plate is studied. The effects of the hump height, the disturbance frequency, the subharmonic disturbance spanwise wavenumber, and compressibility are studied.

1.4. Subharmonic Instability in Compressible Boundary Layers Over an Adiabatic Flat Plate

Due to recent advances in supersonic and hypersonic aerospace technology, there has been a renewed interest in the stability and transition to turbulence of high-speed flows. In contrast with the case of incompressible flows and due to several reasons, rigorous stability experiments are very difficult at supersonic speeds. In addition most of the present experiments related to the stability of high-speed flows measure the onset of turbulence and the extent of the transition region rather than the evolution in space and time of the fluctuations present in the flow. This makes the validation of the proposed theoretical models very difficult. The stability of compressible boundary layers has been recently reviewed by Mack (1984) and Nayfeh (1988).

The linear stability of 2-D compressible boundary layers differs from that of incompressible boundary layers in many ways (Mack, 1984; Nayfeh, 1988). First, whereas the incompressible flat-plate boundary layer has no inflection points and hence is stable to inviscid disturbances, the compressible flat-plate boundary layer has generalized inflection points and hence is unstable to inviscid disturbances. As the Mach number increases, the generalized inflection point moves away from the wall and the inviscid instability increases. Moreover, the viscous instability weakens and disappears when the Mach number exceeds 3. Thus the maximum amplification rate occurs at an infinite Reynolds number and viscosity has a stabilizing rather than a destabilizing effect. Second, whereas there is at most a single unstable wavenumber (frequency) at each Reynolds number and frequency (wavenumber) in the incompressible case, there exist multiple unstable modes whenever there is a region of supersonic flow relative to the disturbance phase velocity. The first unstable mode is similar to the unstable mode existing in incompressible boundary layers and the additional modes do not have any counterpart in the incompressible case. These additional modes were discovered by Mack who called them higher modes and we will call them Mack modes. Mack found that the effect of viscosity on the Mack modes is always stabilizing and hence the maximum amplification rate occurs at an infinite Reynolds number. Third, whereas 2-D modes are the most unstable modes in an incompressible boundary layer, the most unstable first-mode waves in supersonic boundary layers are 3-D. However, the most unstable Mack modes are 2-D.

Nayfeh and Harper (see Nayfeh, 1988) extended the Floquet model and analyzed the spatial and temporal compressible subharmonic instability problem of a flow over an adiabatic wall. They solved the spatial problem by using a shooting technique and presented results for subsonic, transonic, and supersonic flows. They, however,

neglected the interaction terms arising from the equation of state. One of the purposes of this work is to study the effect of neglecting these terms. It is found that their effect is negligible only at low Mach numbers.

El-Hady (1988) solved the spatial subharmonic instability problem for subsonic and transonic flows. He also neglected the interaction terms arising from the equation of state. Later, El-Hady (1989) repeated his analysis and included these terms. He resolved the spatial problem for subsonic and transonic flows by assuming the characteristic exponent to be real. El-Hady concluded that compressibility may be stabilizing or destabilizing, depending on the amplitude of the primary wave and the spanwise wavenumber.

Erlebacher and Hussaini (1987) numerically simulated the full 3-D time-dependent compressible Navier-Stokes equations to study the temporal stability of supersonic flows at $M_\infty = 4.5$. They investigated the interaction between a 2-D wave and a 3-D wave having the same streamwise wavenumber with the wave angle of the 3-D wave being 60°. Their numerical experiments suggest the existence of a secondary instability with a qualitative similarity to the K type breakdown. Thumm, Wolz, and Fasel (1990) numerically simulated spatially growing secondary disturbances in compressible boundary layers and presented results at different Mach numbers.

In Chapter 4, we consider the subharmonic instability in compressible boundary layers over an insulated flat plate. The primary wave is taken to be either a 2-D first- or second (Mack) wave. As discussed above, the most unstable first-mode waves are not 2-D but 3-D. The subharmonic instability problem of compressible boundary layers over a flat plate is solved by using finite differences and the computer code SUPORT. Results are presented for subsonic, transonic, and supersonic flows. The effects of Mach number, spanwise wavenumber, amplitude of the primary wave, Reynolds number, and frequency are studied.

1.5. Effect of Heat Transfer on the Subharmonic Instability of Compressible Boundary Layers Over a Flat Plate

The effect of heat transfer on the primary instability of compressible boundary layers has been studied by many researchers. Using temporal inviscid and viscous theory, Mack (1969, 1975) found that while cooling stabilizes first-mode waves it destabilizes second-mode waves. For moderate Mach numbers, sufficient cooling can be applied to remove the generalized inflection point, which is the source of the first-mode instability. However, the source of the second-mode instability cannot be removed by cooling. Lysenko and Maslov (1984) found both experimentally and by way of calculation that surface cooling: (a) stabilizes first-mode disturbances - the range of unstable frequencies decreases, the amplification rates decrease, and the neutral stability curves are shifted to larger Reynolds numbers; (b) destabilizes second-mode (high frequency) disturbances - the unstable frequency region expands and is shifted to the region of larger frequencies, while the amplification rates increase; and (c) may lead to the region of unstable frequencies of first-mode waves being divided into two. Lysenko and Maslov (1984) found that the experimental results are in a qualitative agreement with the predictions of the theory of hydrodynamic stability. Al-Maaitah et al. (1990c) performed detailed calculations on the effect of heat transfer on the stability of compressible boundary layers. Their calculations confirm the main conclusions of the linear theory of hydrodynamic stability.

In Chapter 5, the effect of heat transfer on the subharmonic instability of 2-D compressible boundary layer over a flat plate is studied, and results for different parameters are presented.

1.6. Effect of Suction on the Subharmonic Instability of Compressible Boundary Layers Over a Flat Plate

Malik (1989) investigated the influence of self-similar suction on the stability of second-mode waves at $M_\infty = 4.5$ and R = 1500. He found that suction shifts the band of unstable frequencies to higher values and reduces the peak amplification. Malik's calculations are for a single Reynolds number and a single Mach number. Al-Maaitah et al. (1990d,e) presented a detailed study on the effect of self-similar as well as nonsimilar suction distributions on the stability of compressible boundary layers. Both first- and second-mode waves of instability were investigated. The results show that the effectiveness of suction decreases by increasing Mach number.

In Chapter 6, the effect of suction on the subharmonic instability of 2-D compressible boundary layer over a flat plate is studied, and results for different parameters are presented.

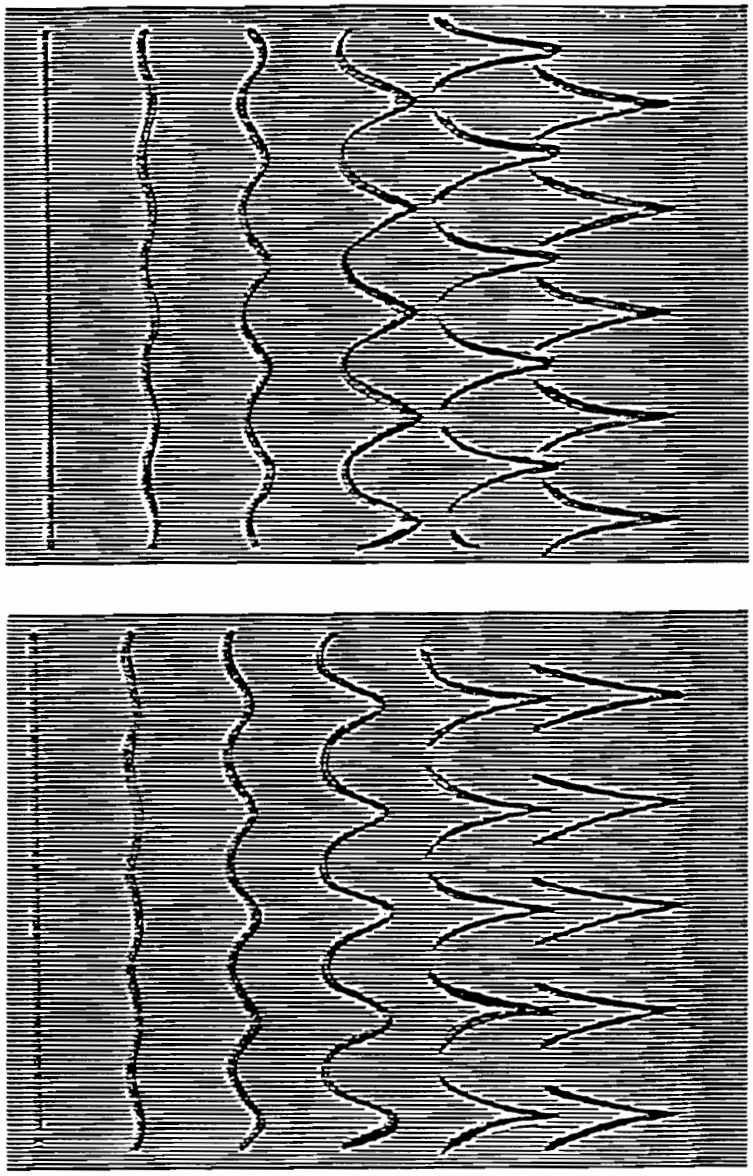

Figure 1.1. Streaklines in Blasius boundary layer. The drawings are a reproduction of photos taken by Saric et al. at the VPI Stability Wind Tunnel. Flow is from left to right, (a) subharmonic disturbance, and (b) fundamental disturbance.

2. SUBHARMONIC INSTABILITY IN INCOMPRESSIBLE BOUNDARY LAYERS OVER A FLAT PLATE

The subharmonic instability in a 2-D boundary layer on a flat plate is analyzed using the Floquet model and the resonant-triad model. The problems arising from both models are solved numerically using a shooting technique and results are presented and compared with each other and with the experimental data of Kachanov and Levchenko and Corke and Mangano. The results are also compared with the numerical simulations of Spalart and Yang. The results of the Floquet model are in good agreement with the experimental data of Kachanov and Levchenko but they are not in as a good agreement with those of Corke and Mangano. The agreement between the results of the resonant-triad model and the experimental data is only qualitative. The results of the Floquet model are in good agreement with the numerical simulations of Spalart and Yang.

2.1. Mathematical Formulation

2.1.1. The stability problem

We consider a 3-D unsteady disturbance represented by the quantities u, v, p, and w imposed on a 2-D basic flow represented by the quantities U, V, and P. Then the equations governing the disturbance are given by

$$\frac{\partial u}{\partial x} + \frac{\partial v}{\partial y} + \frac{\partial w}{\partial z} = 0, \tag{2.1}$$

$$\begin{aligned} \frac{\partial u}{\partial t} + U\frac{\partial u}{\partial x} + v\frac{\partial U}{\partial y} + \frac{\partial p}{\partial x} - \frac{1}{R}\nabla^2 u + \Big[u\,\frac{\partial U}{\partial x} \\ + V\,\frac{\partial u}{\partial y}\Big] + \left\{u\frac{\partial u}{\partial x} + v\frac{\partial u}{\partial y} + w\frac{\partial u}{\partial z}\right\} = 0, \end{aligned} \tag{2.2}$$

$$\begin{aligned} \frac{\partial v}{\partial t} + U\frac{\partial v}{\partial x} + \frac{\partial p}{\partial y} - \frac{1}{R}\nabla^2 v + \Big[u\,\frac{\partial V}{\partial x} \\ + V\,\frac{\partial v}{\partial y} + v\frac{\partial V}{\partial y}\Big] + \left\{u\frac{\partial v}{\partial x} + v\frac{\partial v}{\partial y} + w\frac{\partial v}{\partial z}\right\} = 0, \end{aligned} \tag{2.3}$$

$$\begin{aligned} \frac{\partial w}{\partial t} + U\frac{\partial w}{\partial x} + \frac{\partial p}{\partial z} - \frac{1}{R}\nabla^2 w + \left[V\frac{\partial w}{\partial y}\right] \\ + \left\{u\frac{\partial w}{\partial x} + v\frac{\partial w}{\partial y} + w\frac{\partial w}{\partial z}\right\} = 0, \end{aligned} \tag{2.4}$$

where

$$\nabla^2 = \frac{\partial^2}{\partial x^2} + \frac{\partial^2}{\partial y^2} + \frac{\partial^2}{\partial z^2},$$

and

$$R = U_{\infty}^{*}\delta_{r}^{*}/\nu^{*} \tag{2.5}$$

In the above equations, distances, velocities, the time, and the pressure are made dimensionless using $\delta_r^* = \sqrt{\nu^* L^*/U_\infty^*}$, δ_r^*/U_∞^*, and $\rho^* U_\infty^{*2}$, where ν^* is the kinematic viscosity of the fluid, L^* is the distance from the leading edge of the plate to a reference point, ρ^* is the fluid density, and U_∞^* is the freestream velocity. The terms in the square brackets are due to the growth of the boundary layer (nonparallel terms) and the terms in the curly brackets are due to the nonlinearity.

Along with Eqs. (2.1)-(2.4) we have the boundary conditions

$$u = v = w = 0 \text{ at } y = 0 \tag{2.6}$$

and

$$u, v, p, w \to 0 \text{ as } y \to \infty \tag{2.7}$$

The mean flow is 2-D and steady. An asymptotic solution of the mean-flow problem in the limit of an infinite Reynolds number is given by the Blasius solution

$$U = f'(\eta), \tag{2.8}$$

$$V \approx \frac{1}{2\sqrt{xRe}}\left[\eta f'(\eta) - f(\eta)\right] \tag{2.9}$$

$$P \approx \text{constant}, \tag{2.10}$$

where

$$\eta = y\sqrt{Re/x}\,, \tag{2.11}$$

$$Re = U_\infty^* L^*/\nu^* = R^2, \tag{2.12}$$

and f is governed by the Blasius problem

$$f''' + \frac{1}{2} f f'' = 0, \tag{2.13}$$

$$f = f' = 0 \text{ at } \eta = 0, \tag{2.14}$$

$$f' \to 1 \text{ as } \eta \to \infty. \tag{2.15}$$

The 3-D linear quasiparallel stability problem is derived by neglecting the terms inside the square and curly brackets in Eqs. (2.1)-(2.4) and seeking solutions of the resulting equations in the form

$$(u,v,p) = \cos \beta z \left[\{\xi_1(y), \xi_3(y), \xi_4(y)\} e^{i\theta} + cc \right], \tag{2.16}$$

$$w = \sin \beta z \left[\xi_5(y) e^{i\theta_1} + cc \right], \tag{2.17}$$

where

$$\theta_1 = \int \alpha_1 dx - \omega_1 t, \tag{2.18}$$

and cc stands for the complex conjugate of the preceding terms. In Eqs. (2.16)-(2.18), α_1 is complex and is equal to $\alpha_{1r} + i\alpha_{1i}$, where α_{1r} is the streamwise wavenumber and $-\alpha_{1i}$ is the spatial growth rate, ω_1 is complex and is equal to $\omega_{1r} + i\omega_{1i}$, where ω_{1r} is the frequency of the wave and ω_{1i} is the temporal growth rate, and β is the spanwise wavenumber and it is real for a 2-D boundary layer. For spatial stability analysis, ω is real and α is complex, whereas for temporal stability analysis α is real and ω is

complex. Substituting Eqs. (2.16)-(2.18) into Eqs. (2.1)-(2.4), (2.6), and (2.7) and neglecting the terms inside the square and curly brackets, we obtain

$$i\alpha_1\xi_1 + D\xi_3 + \beta\xi_5 = 0, \tag{2.19}$$

$$-\frac{1}{R}D^2\xi_1 + \frac{\Lambda}{R}\xi_1 + DU\xi_3 + i\alpha_1\xi_4 = 0, \tag{2.20}$$

$$-\frac{1}{R}D^2\xi_3 + \frac{\Lambda}{R}\xi_3 + D\xi_4 = 0, \tag{2.21}$$

$$-\frac{1}{R}D^2\xi_5 + \frac{\Lambda}{R}\xi_5 - \beta\xi_4 = 0, \tag{2.22}$$

$$\xi_1 = \xi_3 = \xi_5 = 0 \text{ at } y = 0, \tag{2.23}$$

$$\xi_n \to 0 \text{ as } y \to \infty, \tag{2.24}$$

where

$$\Lambda = \alpha_1^2 + \beta^2 + iR(\alpha_1 U - \omega_1), \tag{2.25}$$

$D = \partial/\partial y$.

The 2-D linear quasiparallel stability problem can be obtained from Eqs. (2.19)-(2.25) by setting $\beta = \xi_5 = 0$. This yields

$$i\alpha\zeta_1 + D\zeta_3 = 0, \tag{2.26}$$

$$-\frac{1}{R}D^2\zeta_1 + \frac{\Gamma}{R}\zeta_1 + DU\zeta_3 + i\alpha\zeta_4 = 0, \tag{2.27}$$

$$-\frac{1}{R}D^2\zeta_3 + \frac{\Gamma}{R}\zeta_3 + D\zeta_4 = 0, \tag{2.28}$$

$$\zeta_1 = \zeta_3 = 0 \text{ at } y = 0, \tag{2.29}$$

$$\zeta_n \to 0 \text{ as } y \to \infty, \tag{2.30}$$

where

$$\Gamma = \alpha^2 + iR(\alpha U - \omega). \tag{2.31}$$

2.1.2. The resonant-triad problem

In the resonant triad model we consider the disturbance as a superposition of a 2-D wave and two 3-D waves traveling at equal but opposite angles with respect to the downstream direction. Following Nayfeh (1987), we use the method of averaging and consider the combined temporal/spatial instability, including the effect of nonparallelism. Numerical results will however be presented for the spatial quasiparallel case. We seek a solution of Eqs. (2.1)-(2.4) in the form

$$u = \left\{A(x,t)\zeta_1(y,x)e^{i\theta} + 2C(x,t)\cos\beta z\,\xi_1(y,x)e^{i\theta_1}\right\} + cc, \tag{2.32}$$

$$v = \left\{A(x,t)\zeta_3(y,x)e^{i\theta} + 2C(x,t)\cos\beta z\,\xi_3(y,x)e^{i\theta_1}\right\} + cc, \tag{2.33}$$

$$p = \left\{A(x,t)\zeta_4(y,x)e^{i\theta} + 2C(x,t)\cos\beta z\,\xi_4(y,x)e^{i\theta_1}\right\} + cc, \tag{2.34}$$

$$w = 2C(x,t)\sin\beta z\,\xi_5(y,x)e^{i\theta_1} + cc, \tag{2.35}$$

where the ζ_n and ξ_n are, respectively, solutions of the 2-D and 3-D quasiparallel problems corresponding to

$$\theta = \int \alpha dx - \omega t \text{ and } \theta_1 = \int \alpha_1 dx - \omega_1 t. \tag{2.36}$$

We assume that

$$\omega_1 \approx \frac{1}{2}\omega \text{ and } \alpha_1 \approx \frac{1}{2}\alpha. \tag{2.37}$$

Substituting Eqs. (2.32)-(2.36) into Eqs. (2.1)-(2.4) and separating harmonics, we obtain

$$e_1 = -\xi_1 \frac{\partial C}{\partial x} - \frac{\partial \xi_1}{\partial x} C, \tag{2.38}$$

$$\begin{aligned} e_2 = & -(U\xi_1 + \xi_4)\frac{\partial C}{\partial x} - \xi_1 \frac{\partial C}{\partial t} - \left[U \frac{\partial \xi_1}{\partial x} + \frac{\partial \xi_4}{\partial x} + \xi_1 \frac{\partial U}{\partial x} + VD\xi_1\right]C \\ & - \left[i(\alpha - \bar{\alpha}_1)\zeta_1 \bar{\xi}_1 + \zeta_3 D\bar{\xi}_1 + \bar{\xi}_3 D\zeta_1\right] A\bar{C} e^{i(\theta - \theta_1 - \bar{\theta}_1)}, \end{aligned} \tag{2.39}$$

$$\begin{aligned} e_3 = & -U\xi_3 \frac{\partial C}{\partial x} - \xi_3 \frac{\partial C}{\partial t} - \left[U \frac{\partial \xi_3}{\partial x} + VD\xi_3 + \xi_3 DV\right]C \\ & - \left[i(\alpha\zeta_3 \bar{\xi}_1 - \bar{\alpha}_1 \zeta_1 \bar{\xi}_3) + \zeta_3 D\bar{\xi}_3 + \bar{\xi}_3 D\zeta_3\right] A\bar{C} e^{i(\theta - \theta_1 - \bar{\theta}_1)}, \end{aligned} \tag{2.40}$$

$$\begin{aligned} e_4 = & -U\xi_5 \frac{\partial C}{\partial x} - \xi_5 \frac{\partial C}{\partial t} - \left[U \frac{\partial \xi_5}{\partial x} + VD\xi_5\right]C \\ & - \left[-i\bar{\alpha}_1 \zeta_1 \bar{\xi}_5 + \zeta_3 D\bar{\xi}_5\right] A\bar{C} e^{i(\theta - \theta_1 - \bar{\theta}_1)}, \end{aligned} \tag{2.41}$$

$$e_5 = -\zeta_1 \frac{\partial A}{\partial x} - \frac{\partial \zeta_1}{\partial x} A, \tag{2.42}$$

$$e_6 = -(U\zeta_1 + \zeta_4)\frac{\partial A}{\partial x} - \zeta_1 \frac{\partial A}{\partial t} - \left[U \frac{\partial \zeta_1}{\partial x} + \frac{\partial \zeta_4}{\partial x} + \zeta_1 \frac{\partial U}{\partial x} + VD\zeta_1 \right] A - 2\left[i\alpha_1 \xi_1^2 + \xi_3 D\xi_1 - \beta \xi_1 \xi_5 \right] C^2 e^{i(2\theta_1 - \theta)}, \tag{2.43}$$

$$e_7 = -U\zeta_3 \frac{\partial A}{\partial x} - \zeta_3 \frac{\partial A}{\partial t} - \left[U \frac{\partial \zeta_3}{\partial x} + VD\zeta_3 + \zeta_3 DV \right] A - 2\left[i\alpha_1 \xi_1 \xi_3 + \xi_3 D\xi_3 - \beta \xi_3 \xi_5 \right] C^2 e^{i(2\theta_1 - \theta)}, \tag{2.44}$$

where $\bar{\chi}$ denotes the complex conjugate of χ. To derive the equations governing the modulation of the amplitudes C and A with time and space, we demand that the residuals e_1, e_2, e_3, and e_4 be orthogonal to the adjoint functions ξ_4^*, ξ_1^*, ξ_3^*, and ξ_5^*; they are defined in Appendix A. The result is

$$H_1 \frac{\partial C}{\partial t} + H_2 \frac{\partial C}{\partial x} + H_4 C + \Lambda_2 A \bar{C} e^{i(\theta - \theta_1 - \bar{\theta}_1)} = 0, \tag{2.45}$$

where H_1, H_2, H_4, and Λ_2 are defined in Appendix B. Similarly, we demand that the residuals e_5, e_6, and e_7 be orthogonal to ζ_4^*, ζ_1^*, and ζ_3^*; they are also defined in Appendix A. The result is

$$h_1 \frac{\partial A}{\partial t} + h_2 \frac{\partial A}{\partial x} + h_4 A + \Lambda_1 C^2 e^{i(2\theta_1 - \theta)} = 0, \tag{2.46}$$

where h_1, h_2, h_4 and Λ_1 are defined in Appendix B.

2.1.3. Parametric formulation

In the parametric formulation, the basic flow is taken as a superposition of the Blasius flow and a 2-D linear spatial quasiparallel disturbance. Thus we let

$$U_b = U(y) + A\left[\zeta_1(y)e^{i\theta} + cc\right], \tag{2.47}$$

$$V_b = A\left[\zeta_3(y)e^{i\theta} + cc\right], \tag{2.48}$$

where U(y) is the Blasius profile given by Eq. (2.8), A is the local amplitude of the 2-D disturbance, $\theta = \int \alpha_r dx - \omega t$, and the ζ_n satisfy Eqs. (2.26)-(2.30). Substituting Eqs. (2.47) and (2.48) into Eqs. (2.1)-(2.4), linearizing, and neglecting the nonparallel terms, we obtain

$$\frac{\partial u}{\partial x} + \frac{\partial v}{\partial y} + \frac{\partial w}{\partial z} = 0, \tag{2.49}$$

$$\begin{aligned}\frac{\partial u}{\partial t} &+ \left[U + A_0(\zeta_1 e^{i\theta} + cc)\right]\frac{\partial u}{\partial x} + v\left[DU + A_0(D\zeta_1 e^{i\theta} + cc)\right] \\ &+ A_0(i\alpha\zeta_1 e^{i\theta} + cc)u + A_0(\zeta_3 e^{i\theta} + cc)\frac{\partial u}{\partial y} + \frac{\partial p}{\partial x} - \frac{1}{R}\nabla^2 u = 0,\end{aligned} \tag{2.50}$$

$$\begin{aligned}\frac{\partial v}{\partial t} &+ \left[U + A_0(\zeta_1 e^{i\theta} + cc)\right]\frac{\partial v}{\partial x} + A_0\left(i\alpha\zeta_3 e^{i\theta} + cc\right)u \\ &+ A_0(\zeta_3 e^{i\theta} + cc)\frac{\partial v}{\partial y} + A_0(D\zeta_3 e^{i\theta} + cc)v + \frac{\partial p}{\partial y} - \frac{1}{R}\nabla^2 v = 0,\end{aligned} \tag{2.51}$$

$$\begin{aligned}\frac{\partial w}{\partial t} &+ \left[U + A_0(\zeta_1 e^{i\theta} + cc)\right]\frac{\partial w}{\partial x} + A_0(\zeta_3 e^{i\theta} + cc)\frac{\partial w}{\partial y} \\ &+ \frac{\partial p}{\partial z} - \frac{1}{R}\nabla^2 w = 0.\end{aligned} \tag{2.52}$$

Equations (2.49)-(2.52) are linear partial-differential equations whose coefficients are independent of z, periodic in t, and almost periodic in x. If we assume that the coefficients are strictly periodic in x, then it follows from Floquet theory that Eqs. (2.49)-(2.52) have an approximate solution either of the form

$$(u,v,p) = \cos \beta z\, e^{\sigma_x x + \sigma_t t}\Big[\{\psi_1(y), \psi_3(y), \psi_4(y)\} e^{\frac{1}{2} i(\alpha_r x - \omega t)} + \Big\{\hat{\psi}_1(y), \hat{\psi}_3(y), \hat{\psi}_4(y)\Big\} e^{-\frac{1}{2} i(\alpha_r x - \omega t)} + cc \Big], \tag{2.53}$$

$$w = \sin \beta z\, e^{\sigma_x x + \sigma_t t}\Big[\psi_5(y) e^{\frac{1}{2} i(\alpha_r x - \omega t)} + \hat{\psi}_5(y) e^{-\frac{1}{2} i(\alpha_r x - \omega t)} + cc \Big] \tag{2.54}$$

or the form

$$(u,v,p) = \sin \beta z\, e^{\sigma_x x + \sigma_t t}\Big[\{\psi_1(y), \psi_3(y), \psi_4(y)\} e^{\frac{1}{2} i(\alpha_r x + \omega t)} + \Big\{\hat{\psi}_1(y), \hat{\psi}_3(y), \hat{\psi}_4(y)\Big\} e^{-\frac{1}{2} i(\alpha_r x - \omega t)} + cc \Big], \tag{2.55}$$

$$w = \cos \beta z\, e^{\sigma_x x + \sigma_t t}\Big[\psi_5(y) e^{\frac{1}{2} i(\alpha_r x - \omega t)} + \hat{\psi}_5(y) e^{-\frac{1}{2} i(\alpha_r x - \omega t)} cc \Big]. \tag{2.56}$$

Thus, the excited subharmonic wave will be a linear combination of both forms. The form of the solution given by either Eqs. (2.53) and (2.54) or Eqs. (2.55) and (2.56) consists of a pair of 3-D propagating waves that form a spanwise standing wave. They are 90° out of phase. For tuned modes $\hat{\psi}_n = \overline{\psi}_n$ and either σ_t or σ_x is real. Substituting either Eqs. (2.53) and (2.54) or Eqs. (2.55) and (2.56), specialized for tuned modes, into Eqs. (2.49)-(2.52) and equating the coefficients of $\exp\Big[\frac{1}{2} i(\alpha_r x - \omega t)\Big]$ on both sides, we obtain

$$(\sigma_x + \tfrac{1}{2} i\alpha_r)\psi_1 + D\psi_3 + \beta\psi_5 = 0, \tag{2.57}$$

$$\begin{aligned} &\Big[(\sigma_x + \tfrac{1}{2} i\alpha_r)U + \sigma_t - \tfrac{1}{2} i\omega\Big]\psi_1 + DU\psi_3 + (\sigma_x + \tfrac{1}{2} i\alpha_r)\psi_4 \\ &\quad - \frac{1}{R}\Big[D^2 + (\sigma_x + \tfrac{1}{2} i\alpha_r)^2 - \beta^2\Big]\psi_1 + A_0 e^{-\int \alpha_i dx}\big[(\sigma_x + \tfrac{1}{2} i\alpha_r \\ &\quad - \alpha_i)\zeta_1\overline{\psi}_1 + \zeta_3 D\overline{\psi}_1 + D\zeta_1\overline{\psi}_3\big] = 0, \end{aligned} \tag{2.58}$$

$$\left[(\sigma_x + \frac{1}{2} i\alpha_r)U + \sigma_t - \frac{1}{2} i\omega\right]\psi_3 + D\psi_4 - \frac{1}{R}\left[D^2 + (\sigma_x + \frac{1}{2} i\alpha_r)^2 - \beta^2\right]\psi_3 + A_0 e^{-\int \alpha_i dx}\left[(\sigma_x - \frac{1}{2} i\alpha_r)\zeta_1\bar{\psi}_3 + i\alpha\zeta_3\bar{\psi}_1 + \zeta_3 D\bar{\psi}_3 + \bar{\psi}_3 D\zeta_3\right] = 0, \tag{2.59}$$

$$\left[(\sigma_x + \frac{1}{2} i\alpha_r)U + \sigma_t - \frac{1}{2} i\omega\right]\psi_5 + \beta\psi_4 - \frac{1}{R}\left[D^2 + (\sigma_x + \frac{1}{2} i\alpha_r)^2 - \beta^2\right]\psi_5 + A_0 e^{-\int \alpha_i dx}\left[(\sigma_x - \frac{1}{2} i\alpha_r - \alpha_i)\zeta_1\bar{\psi}_5 + \zeta_3 D\bar{\psi}_5\right] = 0, \tag{2.60}$$

The boundary conditions are

$$\psi_1 = \psi_3 = \psi_5 = 0 \text{ at } y = 0, \tag{2.61}$$

$$\psi_n \to 0 \text{ as } y \to \infty. \tag{2.62}$$

2.2. Method of Solution

The 3-D linear quasiparallel stability problem given by Eqs. (2.19)-(2.24) consists of a system of homogeneous differential equations subject to homogeneous boundary conditions. A nontrivial solution to this problem exists only for a certain combination of α_1, β, ω_1, and R. The eigenvalue problem provides a complex dispersion relation of the form

$$\alpha_1 = \alpha_1(\omega_1, \beta, R) \tag{2.63}$$

The solution to this eigenvalue problem is obtained numerically. For spatial stability analysis, we assign real values to ω_1, β and R. Then a complex α_1 can be calculated as an eigenvalue.

To solve the problem given by Eqs. (2.19)-(2.24), we transform the equations into the system of first-order differential equations

$$D\xi = F\xi \tag{2.64}$$

where

$$\xi = \{\xi_1, \xi_2, \xi_3, \xi_4, \xi_5, \xi_6\}^T \tag{2.65}$$

is a 6x1 vector and F is a 6x6 matrix with elements defined in Appendix C.

Equations (2.23) and (2.24) define, respectively, the boundary conditions at y = 0 and as $y \to \infty$. Because we solve the problem over a finite domain, we replace the boundary conditions at infinity with the proper boundary conditions at some finite value $y = y_{max}$ in the form

$$Q\xi = 0 \text{ at } y = y_{max} \tag{2.66}$$

where y_{max} is larger than the boundary-layer thickness. The boundary conditions at $y = y_{max}$ given by Eq. (2.66), the boundary conditions at y = 0 given by Eqs. (2.23), and the system of differential equations given by Eq. (2.64) subject to the boundary conditions (2.23) and (2.66) forms a stiff eigenvalue problem, which we solve using a combination of finite-differences (Pereyra 1976) and a Newton-Raphson scheme.

The 2-D problem governed by Eqs. (2.26)-(2.30) and the adjoint problems defined in Appendix A are solved in the same way described above. We note here that because the adjoint problem has the same eigenvalues as the original problem, no iteration is required to compute the adjoint functions.

Once we find the eigenvalues and the eigenfunctions of the 2-D and 3-D problems and their adjoints, we compute the coefficients describing the modulation of the amplitudes in the resonant triad model at different values of R. Then, we integrate Eqs. (2.45) and (2.46) for certain initial values to compute the variation of A and C with R.

As an alternative to the collocation technique used by Herbert, we use the shooting technique described above to solve the Floquet problem. However, in order to replace the boundary conditions at $y = \infty$ with boundary conditions at some finite value $y = y_{max}$, we note that for a large value of $y(y \geq y_{max})$, the ζ_n are functions of y and are not constants. This means that for any $y \geq y_{max}$, we do not have a system of equations with constant coefficients due to the interaction terms. To overcome this difficulty, we note that the interaction terms are the order $A\zeta\psi$, whereas the rest are order ψ. Because the ζ_n and ψ_n vanish exponentially as $y \to \infty$, the interaction terms decay faster than the rest of the terms. Thus by choosing a large enough y_{max}, the interaction terms can be neglected and the boundary conditions at infinity can be replaced with Eq. (2.66). The error involved can be monitored by choosing a certain value of y_{max} and solving the problem, then increasing y_{max} and solving the problem again and noting the effect of increasing y_{max} on the accuracy of the solution.

2.3. Results

We present results for the spatial quasiparallel case. The frequency F, which is related to ω through $\omega = FR$, is kept constant following a certain wave. The spanwise

wavenumber is defined through $B = 1000\beta/R$ and B is kept constant as the wave propagates downstream.

2.3.1. Results from the Floquet model

Using a collocation method with Chebyshev polynomials, Herbert implemented the Floquet model and presented few sets of results. Using mainly temporal stability concept, Herbert studied the effects of the amplitude of the primary wave, spanwise wavenumber, and Reynolds number on the growth rates and amplification factors of the subharmonic wave. In this work, we use a finite-difference scheme to study the effect of the frequency on the growth rates and the amplification factors of the subharmonic wave.

Figure 2.1 shows the variation of the growth rate of the subharmonic wave with spanwise wavenumber for five different frequencies at R = 600. At this Reynolds number, we note that increasing the frequency results in an increase in the growth rate of the subharmonic wave. We also note that as the frequency increases the most amplified subharmonic wave shifts towards a higher spanwise wavenumber. Figure 2.2 shows the variation of the growth rate of the subharmonic wave with the frequency of the primary wave for four different spanwise wavenumbers at R = 600 and a rms amplitude of the primary wave equals to 0.01. The figure shows that the subharmonic mode is amplified within a wide band of frequencies. It also confirms the conclusion from figure 2.1 that increasing the frequency results in an increase in the spanwise wavenumber of the most amplified subharmonic wave.

Figure 2.3 shows the variation of the growth rate of the subharmonic wave with the frequency of the primary wave for different amplitudes of the primary wave. It

shows that increasing the amplitude of the primary wave results in a widening of the band of unstable subharmonic waves. It also shows a shift in the most amplified subharmonic wave towards a higher frequency as the amplitude of the primary wave increases. However, this shift is reversed as the amplitude of the primary wave gets to be large.

Figure 2.4 shows the variation of the growth rate of the subharmonic wave with the frequency of the primary wave for six different Reynolds numbers at $B = 0.2$ and a rms amplitude of the primary wave equals to 0.01. It shows that increasing the Reynolds number results in a shift of the most amplified subharmonic wave towards a lower frequency. At high frequencies of the primary wave the dependence of the growth rate of the subharmonic wave on Reynolds number is rather complicated. Figure 2.5 shows the variation of the growth rate of the subharmonic wave with Reynolds number for four different frequencies of the primary wave. The spanwise wavenumber is $B = 0.2$ and the initial rms amplitude of the primary wave at $R = 600$ is 0.005. Figure 2.5 shows that although at low Reynolds numbers the high-frequency subharmonic waves are more unstable, they become less unstable at larger Reynolds numbers. This is partially due to the fact that at high frequencies and high Reynolds numbers the primary wave is damped and thus the amplitude of the primary wave is low, which causes the growth rate of the subharmonic wave to decrease.

Figure 2.6 shows the variation of the location of the onset of the subharmonic instability with the rms amplitude of the primary wave for three different frequencies and a spanwise wavenumber $B = 0.2$. Figure 2.6 shows that as the frequency increases, it takes a smaller amplitude of the primary wave to initiate the subharmonic instability. Figure 2.7 shows the variation of the growth rate of the subharmonic wave with Reynolds number starting from the onset of the subharmonic instability and for three different frequencies. The initial rms amplitude of the primary

wave at the onset of the subharmonic instability is 0.005 and the spanwise wavenumber is B = 0.2. Figure 2.7 shows that although the small-frequency wave becomes unstable much further downstream than the high-frequency wave, the growth rate becomes larger than that of the high-frequency wave and the total amplification (figure 2.8) of the low-frequency wave might exceed that of the high-frequency wave as the waves propagate downstream.

Figure 2.9 shows the variation of the growth rate of the subharmonic wave with spanwise wavenumber for different levels of rms amplitude of the primary wave. This variation was studied extensively by Herbert, who showed the presence of a broad band of unstable spanwise wavenumbers and a shift in the most amplified wave towards a higher spanwise wavenumber as the rms amplitude of the primary wave increases. Figure 2.9 is presented for later comparison with the resonant triad model.

2.3.2. Results from the resonant triad model

For the spatial quasiparallel case, the modulation equations (2.45) and (2.46) reduce to

$$\frac{dC}{dx} = -\frac{\Lambda_2}{H_2} A\bar{C} e^{-\int \alpha_i dx} e^{i\int(\alpha_r - 2\alpha_{1_r})dx} \tag{2.67}$$

$$\frac{dA}{dx} = -\frac{\Lambda_1}{h_2} C^2 e^{\int(\alpha_i - 2\alpha_{1_i})dx} e^{i\int(2\alpha_{1_r} - \alpha_r)dx} \tag{2.68}$$

where the terms on the right-hand sides are due to the interaction of the two modes. Figure 2.10 shows the variation of the ratio of the magnitude of Λ_2/H_2 to the magnitude of Λ_1/h_2 with R at $F_{2D} = 124x10^{-6}$ and for the two spanwise wavenumbers B = 0.18 and

B = 0.33. It shows that the magnitude of Λ_2/H_2 is much larger than the magnitude of Λ_1/h_2, which indicates that the interaction affects the pair of the 3-D waves much more than it affects the 2-D wave. With the 2-D wave being only slightly affected by the interaction, the solution of equation (2.67) is dominated by the amplitude of the 2-D wave $Ae^{-\int \alpha_i dx}$ and the magnitude of the interaction coefficient Λ_2/H_2. Thus, studying the magnitude of the interaction coefficient Λ_2/H_2 gives us a good idea about the qualitative features of the resonant triad model.

Figure 2.11 shows the variation of the magnitude of Λ_2/H_2 with the spanwise wavenumber B for four different frequencies at R = 520. The 3-D wave in figure 2.11 is taken as an Orr-Sommerfeld mode. This figure shows that the magnitude of Λ_2/H_2 increases monotonically with increasing B. This leads us to expect that the growth rate of the subharmonic wave predicted by the resonant triad model increases with increasing B. This is a major qualitative disagreement between the resonant triad model and the Floquet model which predicts (figure 2.9) the presence of a peak in the variation of the growth rate of the subharmonic wave with the spanwise wavenumber. Figure 2.12 shows the variation of the magnitude of Λ_2/H_2 with the frequency of the 2-D wave for six different Reynolds numbers at B = 0.2. This figure demonstrates the strong dependence of the magnitude of Λ_2/H_2 on Reynolds number and the presence of a peak which shifts towards a lower frequency as the Reynolds number increases. In figure 2.12 the 3-D wave is taken as an Orr-Sommerfeld mode. Figure 2.13 shows the variation of the magnitude of Λ_2/H_2 with the spanwise wavenumber B when the 3-D wave is a Squire's mode. Figure 2.13 shows the presence of a peak which shifts towards a higher spanwise wavenumber as the frequency increases. The magnitude of Λ_2/H_2 in figure 2.13 remains large at high spanwise wavenumbers. Comparing figure 2.13 with figure 2.11, we note that at R = 520 the magnitude of Λ_2/H_2 for the Squire's mode is of the same order of magnitude as that for the Orr-Sommerfeld

mode, the Squire's mode however is highly damped when compared with the Orr-Sommerfeld mode. Figure 2.14 shows the variation of the magnitude of Λ_2/H_2 with the frequency of the 2-D wave for different Reynolds numbers when the 3-D wave is a Squire's mode. Again, as in the Orr-Sommerfeld mode we note a peak which shifts towards a lower frequency as R increases. Comparing figure 2.14 with figure 2.12 we note that the magnitude of Λ_2/H_2 at high Reynolds numbers is much larger for the Orr-Sommerfeld mode than for the Squire's mode.

Figure 2.15 shows the variation of the growth rate of the subharmonic wave with Reynolds number predicted by the resonant triad model compared with that predicted by the Floquet model. The initial amplitudes are chosen such that the rms amplitude of the primary wave at R = 610 is 0.00237. In this figure the 3-D wave used in the resonant triad model is taken to be an Orr-Sommerfeld mode. This figure shows that the predictions of the resonant triad model depend on the starting point of the integration of the modulation equations. However, the growth rate becomes eventually independent of the starting point of integration. This behavior is typical of nonstationary oscillations (Nayfeh and Mook, 1979) and may qualitatively explain the results obtained experimentally and by numerical simulation. This figure shows that the predictions of the resonant triad model are larger than the predictions of the Floquet model. Figure 2.16 is like figure 2.14 with the 3-D wave used in the resonant triad model being a Squire's mode. The predicted growth rates again depend on the starting point of integration and become eventually independent of it. The growth rates predicted by the resonant triad model are again larger than those predicted by the Floquet model.

2.3.3. Comparison with experimental data

Kachanov and Levchenko (1984) studied experimentally the 3-D resonant interaction of a plane T-S wave having a frequency f_1 with a pair of oblique waves having the frequency $\frac{1}{2}f_1$. In the controlled part of the experiment, the frequency f_1 is equal to 111.4 Hz, which corresponds to $F = 124x10^{-6}$, and the spanwise wavenumber β^* is equal to .195 mm^{-1}, which corresponds to B = 0.33. The amplitudes of the waves were measured at y*/(boundary-layer thickness) = 0.26 where the boundary-layer thickness was determined experimentally from the condition $U^*/U^*_\infty = 0.99$.

Figure 2.17 shows the streamwise variation of the rms amplitudes of the 2-D wave and the 3-D subharmonic wave as predicted by the Floquet model; it also shows the experimental data. The initial amplitude of the 3-D subharmonic wave was chosen such that the theoretical and experimental amplitudes match at branch II of the neutral stability curve of the Blasius flow (i.e., $R_{II} = 606$). The agreement is very good. The y variations of the magnitude and phase of the eigenfunction of the streamwise subharmonic disturbance at $R_{II} = 606$, as predicted by the Floquet model, are shown in figure 2.18. Also shown are the experimental data at R = 608. The agreement is also good.

Figures 2.19 and 2.20 are like figure 2.17 and 2.18, but they compare results predicted by the resonant triad model at B = 0.33 with the corresponding experimental data. In the resonant triad model the 3-D wave is taken to be an Orr-Sommerfeld mode. It is clear that the predictions of the resonant triad model for the amplitudes as well as the phase are not as good as those predicted by the Floquet model. However, there is good agreement between the predicted magnitude of the eigenfunction and the experimentally obtained magnitude. Figure 2.21

compares the predictions of the resonant triad model when the 3-D wave is a Squire's mode with the experimental data. This figure shows that the predictions of the triad in this case are far from the experimental data.

Corke and Mangano (1989) studied experimentally the resonant interaction problem and presented three sets of data corresponding to three different conditions. In one case, which they referred to as case 150P, the frequency of the 2-D wave is equal to 32 Hz, which corresponds to $F = 82.7x10^{-6}$, and the spanwise wavenumber β^* is equal to 0.633 cm^{-1}, which corresponds to B = 0.156. Figure 2.22 shows the streamwise variation of the rms amplitudes of the 2-D wave and the 3-D subharmonic wave as predicted by the Floquet model along with the experimental data of case 150P. The location of the virtual leading edge is taken at x = - 58 cm. The agreement between theory and experiment for the amplitude of the subharmonic is good between R = 800 and R = 890. However, the agreement between theory and experiment for the amplitude of the primary wave is poor. Changing the location of the virtual origin to x = - 38 cm yields a better agreement between the theoretical and experimental data of the 2-D wave, as shown in Figure 2.23. Overall, however, the agreement between the results of the Floquet model and the experimental data of Corke and Mangano is not as good as the agreement between the results of the Floquet model and the experimental data of Kachanov and Levchenko (1984). The discrepancy between theory and experiment for the amplitude of the primary wave is believed to be due to nonlinear effects, which cause mutual interaction between the 2-D primary and 3-D subharmonic waves. Using a perturbation method, Crouch (1988) accounted for the mutual interaction and obtained a reasonable agreement between his theoretical model and the experimental data of Corke and Mangano.

2.3.4. Comparison with numerical simulation

Spalart and Yang (1987) studied the early 3-D stages of transition in the Blasius boundary layer by numerically solving the Navier-Stokes equations. They found that for intermediate amplitudes of the 2-D wave the breakdown is of the subharmonic type, and the dominant spanwise wavenumber increases with the amplitude of the 2-D wave. Figures 2.24 and 2.25 show a comparison between results obtained by the Floquet model with results obtained by numerical simulation for two different spanwise wavenumbers. The agreement is good. We note the initial rise in the amplitude of the subharmonic wave in the numerical simulation, which agrees qualitatively with the experimental data.

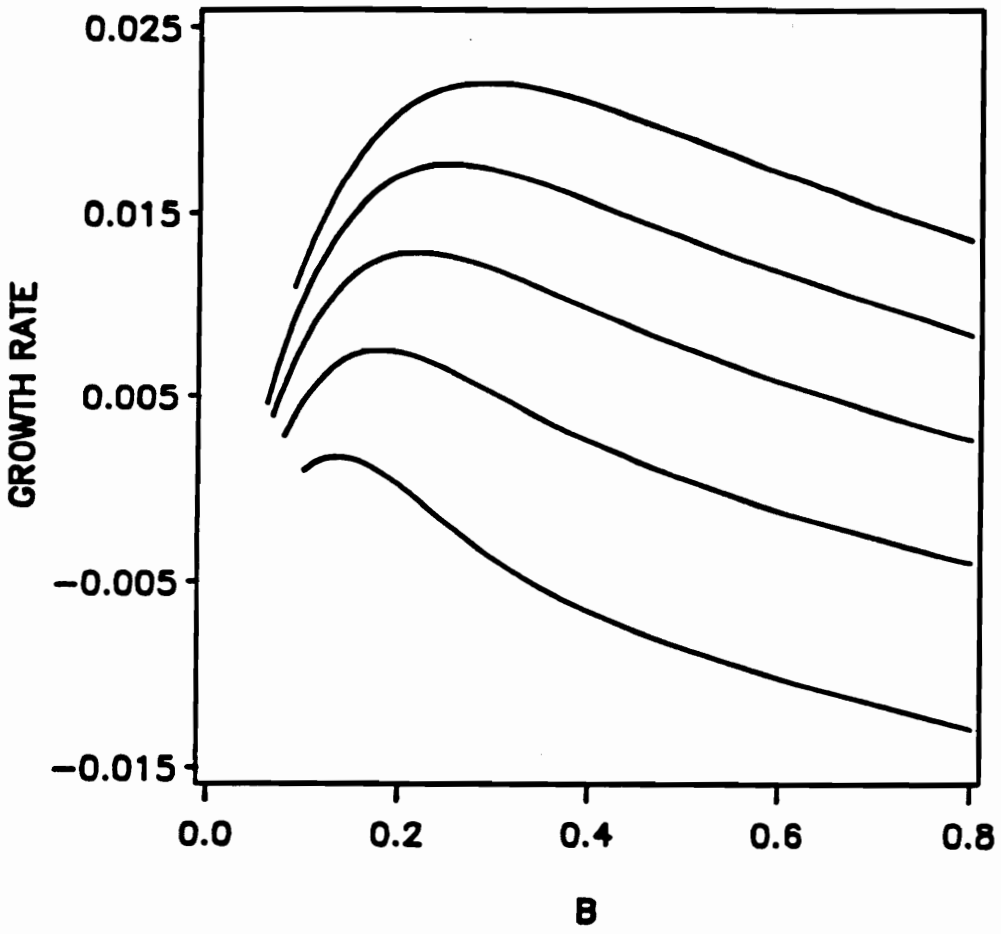

Figure 2.1. Variation of the growth rate of the subharmonic wave as predicted by the Floquet model with the spanwise wavenumber for different frequencies. R = 600, and $A_{rms} = 0.01$,. The frequency of the primary wave proceeding downwards is $Fx10^6$ = 130, 110, 90, 70, and 50.

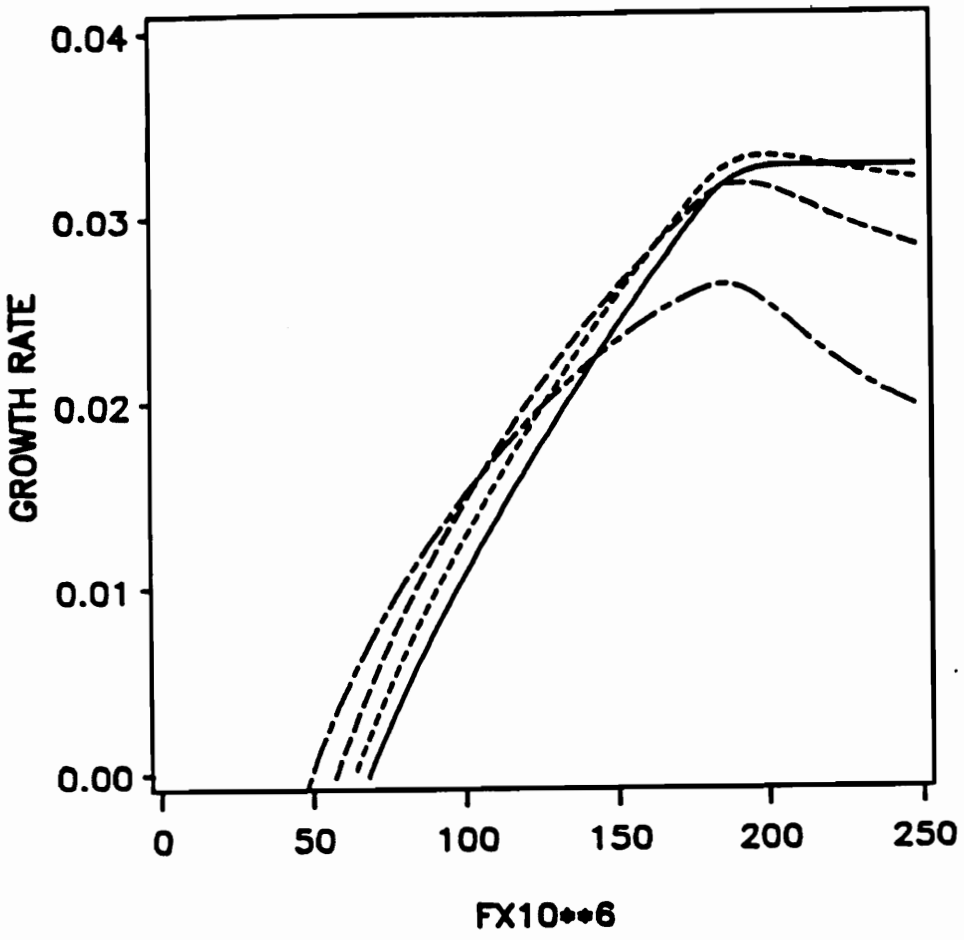

Figure 2.2. Variation of the growth rate of the subharmonic wave as predicted by the Floquet model with the frequency of the primary wave for different spanwise wavenumbers. R = 600, and $A_{rms} = 0.01$ (___) B = 0.5, (...) B = 0.4, (- - -) B = 0.3, and (_._.) B = 0.2.

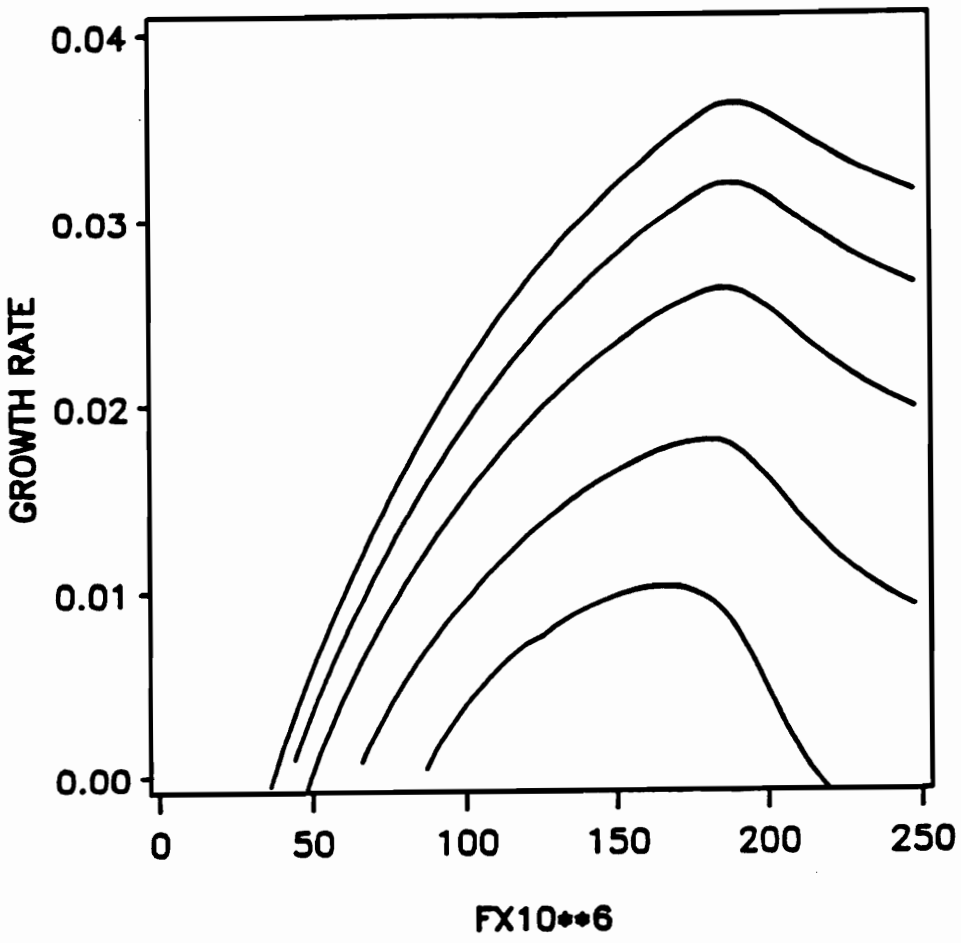

Figure 2.3. Variation of the growth rate of the subharmonic wave as predicted by the Floquet model with the frequency of the primary wave, R = 600, B = 0.2. The rms amplitude of the primary wave proceeding downwards 0.02, 0.015, 0.01, 0.005, and 0.002.

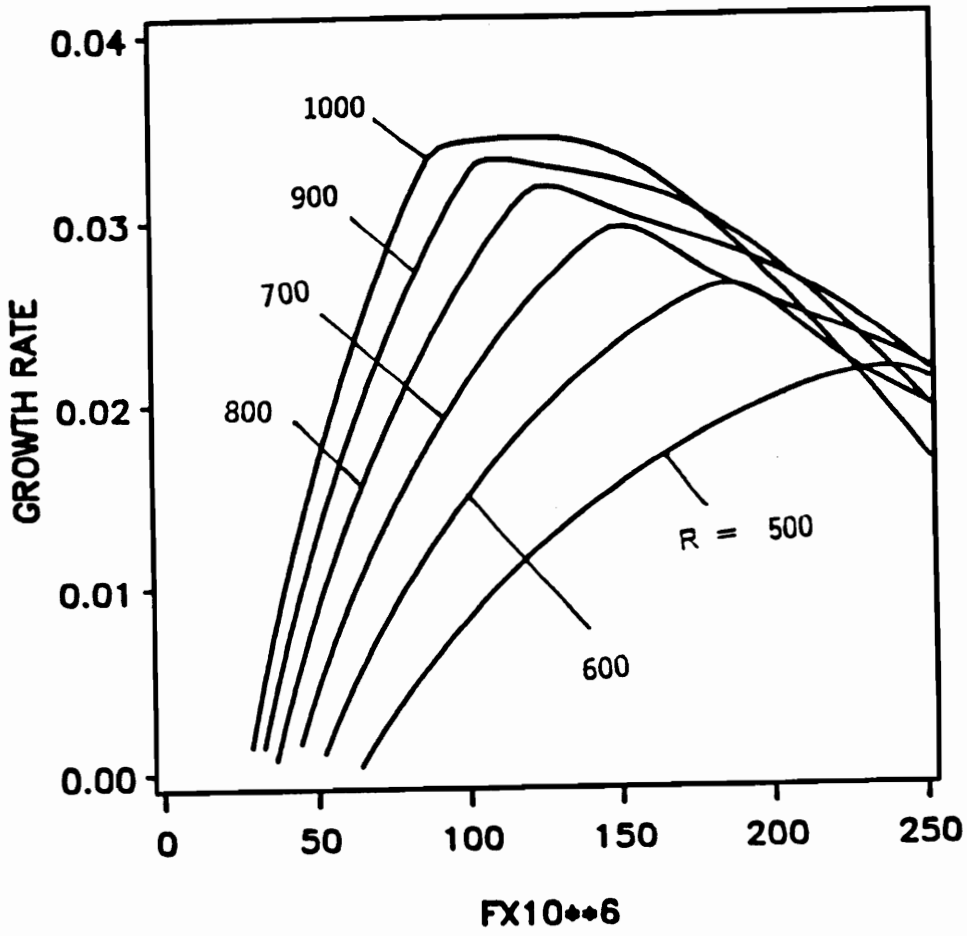

Figure 2.4. Variation of the growth rate of the subharmonic wave as predicted by the Floquet model with the frequency of the primary wave for different Reynolds numbers. B = 0.2, and A_{rms} = 0.01.

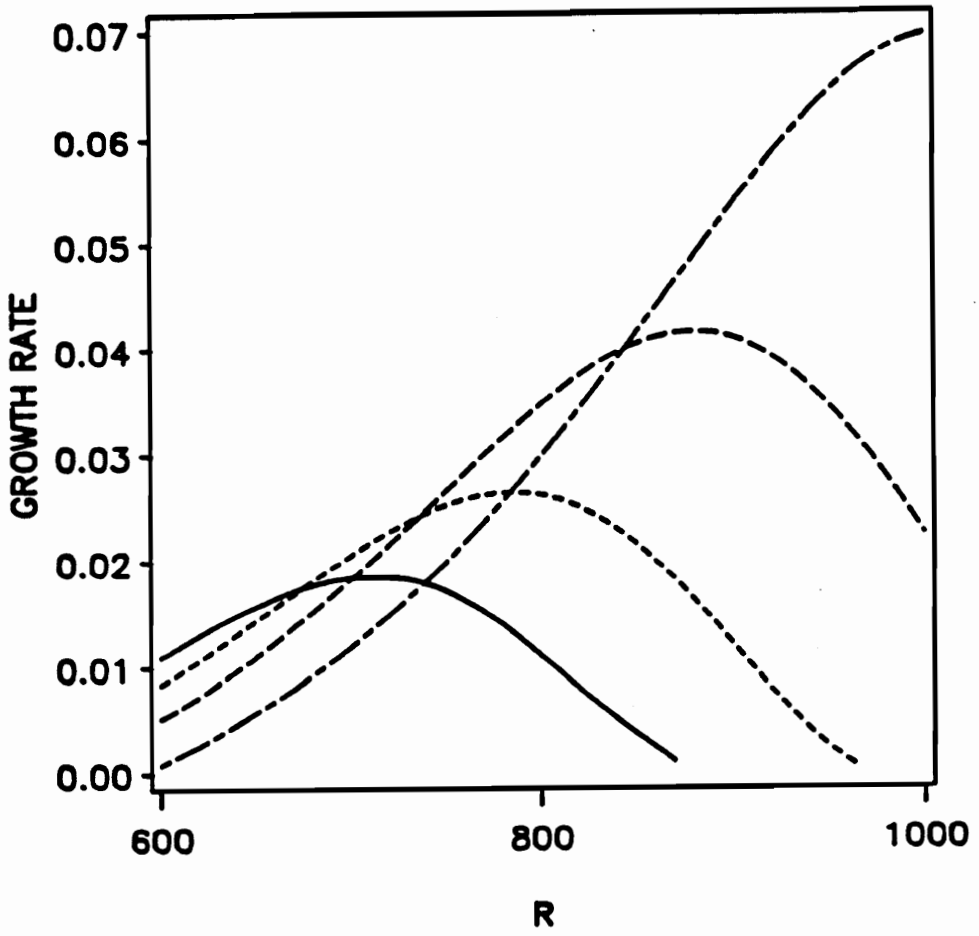

Figure 2.5. Variation of the growth rate of the subharmonic wave as predicted by the Floquet model with Reynolds number for different frequencies. B = 0.2, $A_{rms} = 0.005$ at R = 600. (___) $F_{2D} = 108x10^{-6}$, (...) $F_{2D} = 94x10^{-6}$, (- - -) $F_{2D} = 80x10^{-6}$, and (_._.) $F_{2D} = 66x10^{-6}$.

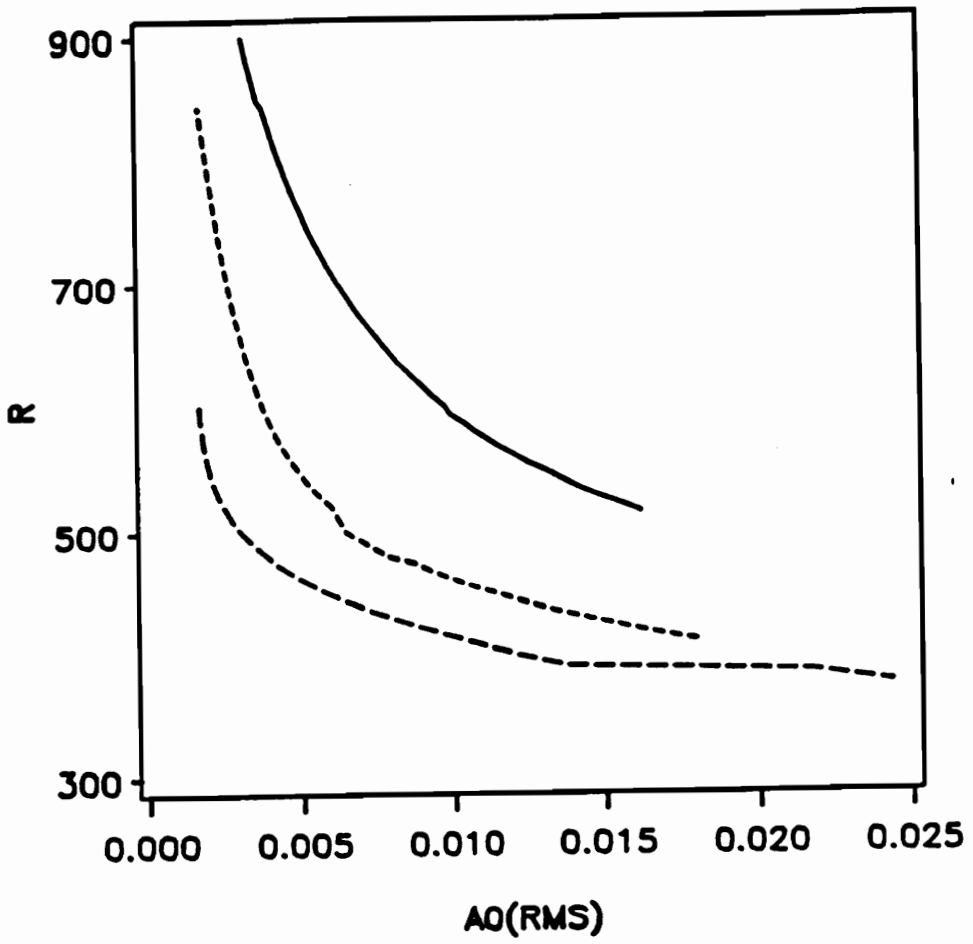

Figure 2.6. Variation of the location of the onset of the subharmonic instability as predicted by the Floquet model with the initial rms amplitude of the primary wave for three different frequencies. B = 0.2, (___) $F_{2D} = 50x10^{-6}$, (...) $F_{2D} = 70x10^{-6}$, and (- - -) $F_{2D} = 90x10^{-6}$.

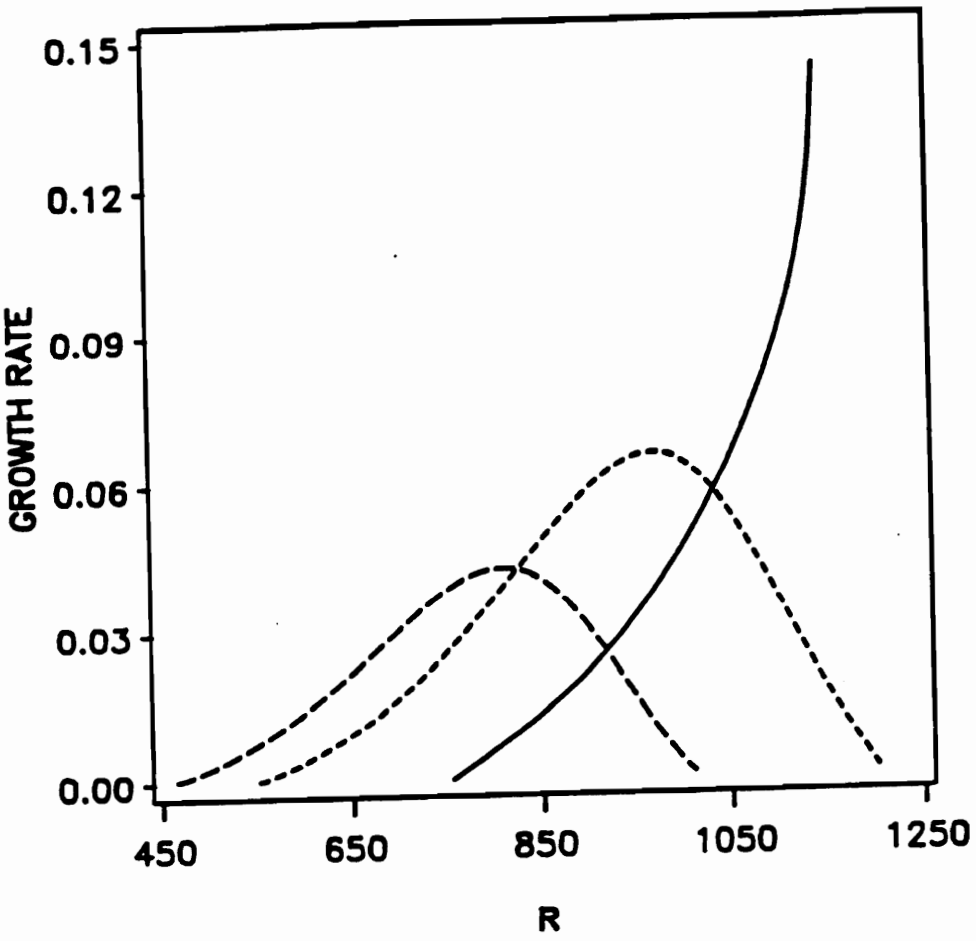

Figure 2.7. Variation of the growth rate of the subharmonic wave as predicted by the Floquet model with Reynolds number starting from the onset of the subharmonic instability. B = 0.2, the initial rms amplitude of the primary wave at the onset of the subharmonic instability is 0.005. (___) $F_{2D} = 50x10^{-6}$, (...) $F_{2D} = 70x10^{-6}$, and (- - -) $F_{2D} = 90x10^{-6}$.

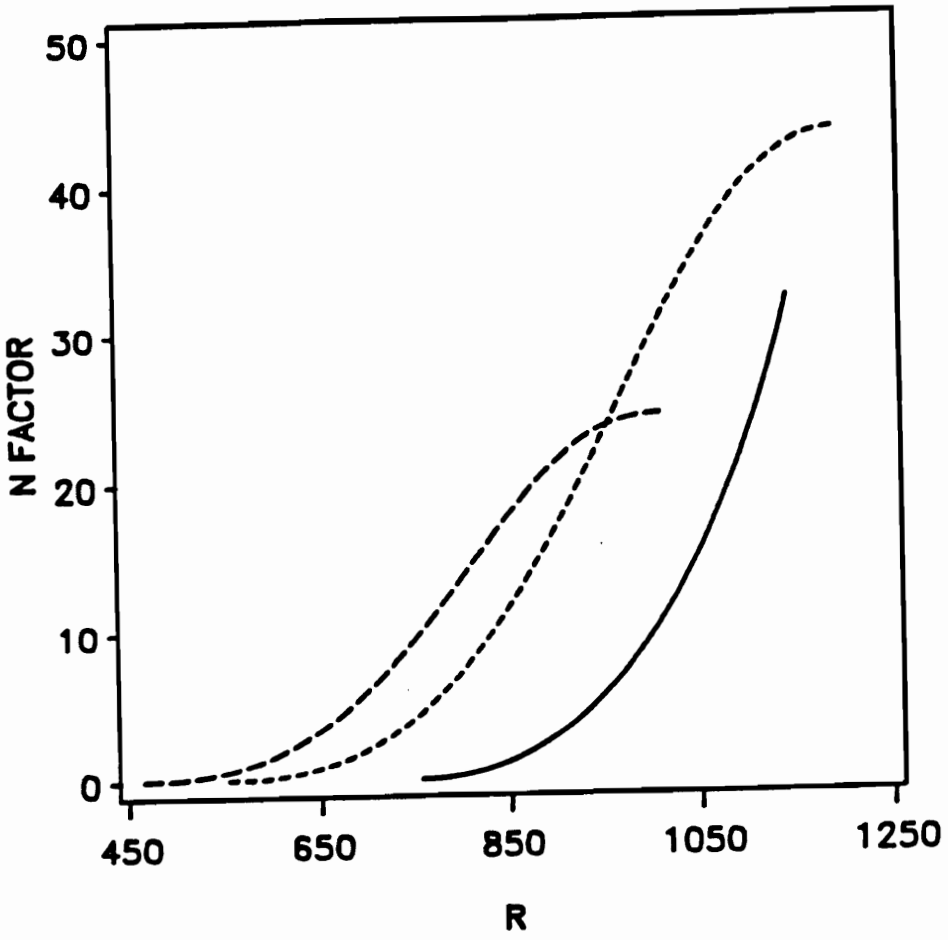

Figure 2.8. Variation of the N-factor of the subharmonic wave as predicted by the Floquet model with Reynolds number starting from the onset of the subharmonic instability. B = 0.2, the initial rms amplitude of the primary wave at the onset of the subharmonic instability is 0.005. (___) $F_{2D} = 50x10^{-6}$, (...) $F_{2D} = 70x10^{-6}$, and (- - -) $F_{2D} = 90x10^{-6}$.

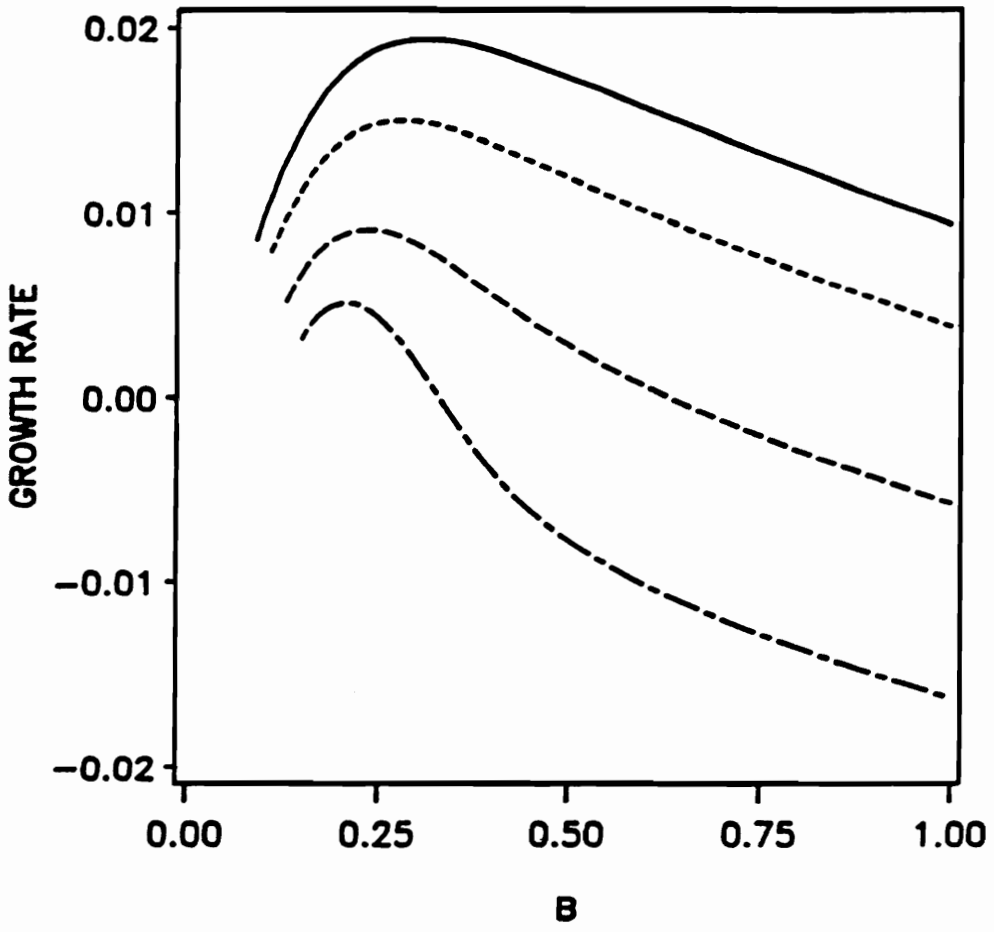

Figure 2.9. Variation of the growth rate of the subharmonic wave as predicted by the Floquet model with the spanwise wavenumber for different rms amplitudes of the primary wave. $F_{2D} = 124x10^{-6}$, R = 520, (___) $A_{rms} = 0.015$, (...) $A_{rms} = 0.01$, (- - -) $A_{rms} = 0.01$, (_._.) $A_{rms} = 0.0025$.

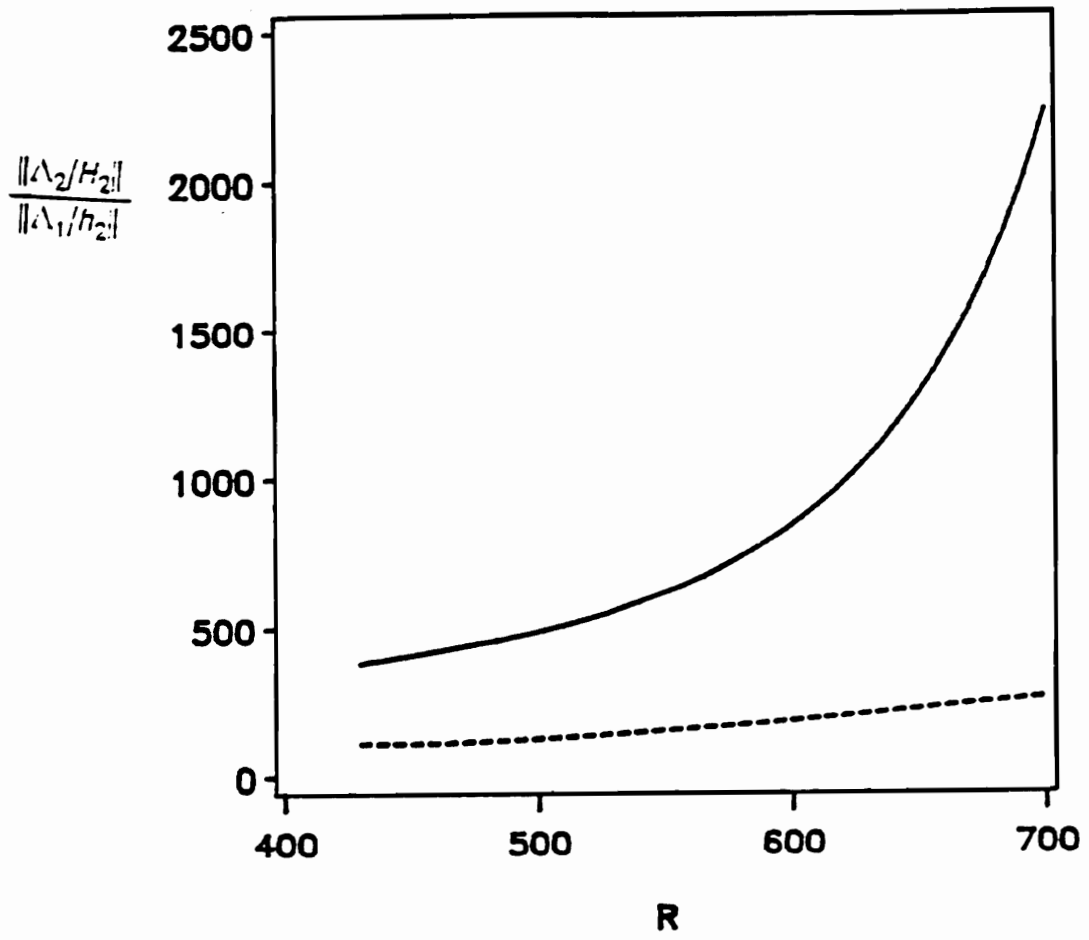

Figure 2.10. Variation of the ratio of the magnitude of Λ_2/H_2 to the magnitude of Λ_1/h_2 with R at $F_{2D} = 124x10^{-6}$: (___), B = 0.33; (...) B = 0.18. The 3-D wave is an Orr-Sommerfeld mode.

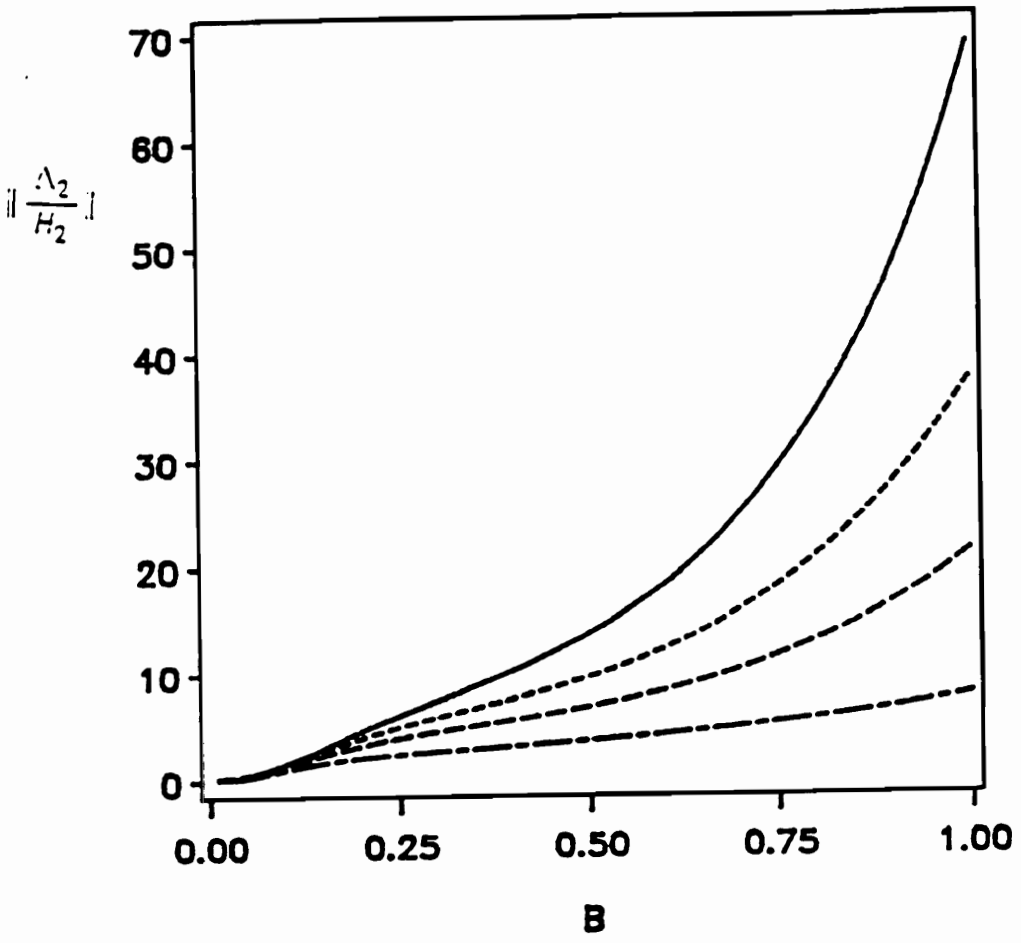

Figure 2.11. Variation of the magnitude of Λ_2/H_2 with the spanwise wavenumber for different frequencies. The 3-D wave is an Orr-Sommerfeld mode. R = 520, (___) $F_{2D} = 124x10^{-6}$, (...) $F_{2D} = 100x10^{-6}$, (- - -) $F_{2D} = 80x10^{-6}$, (_._.) $F_{2D} = 50x10^{-6}$.

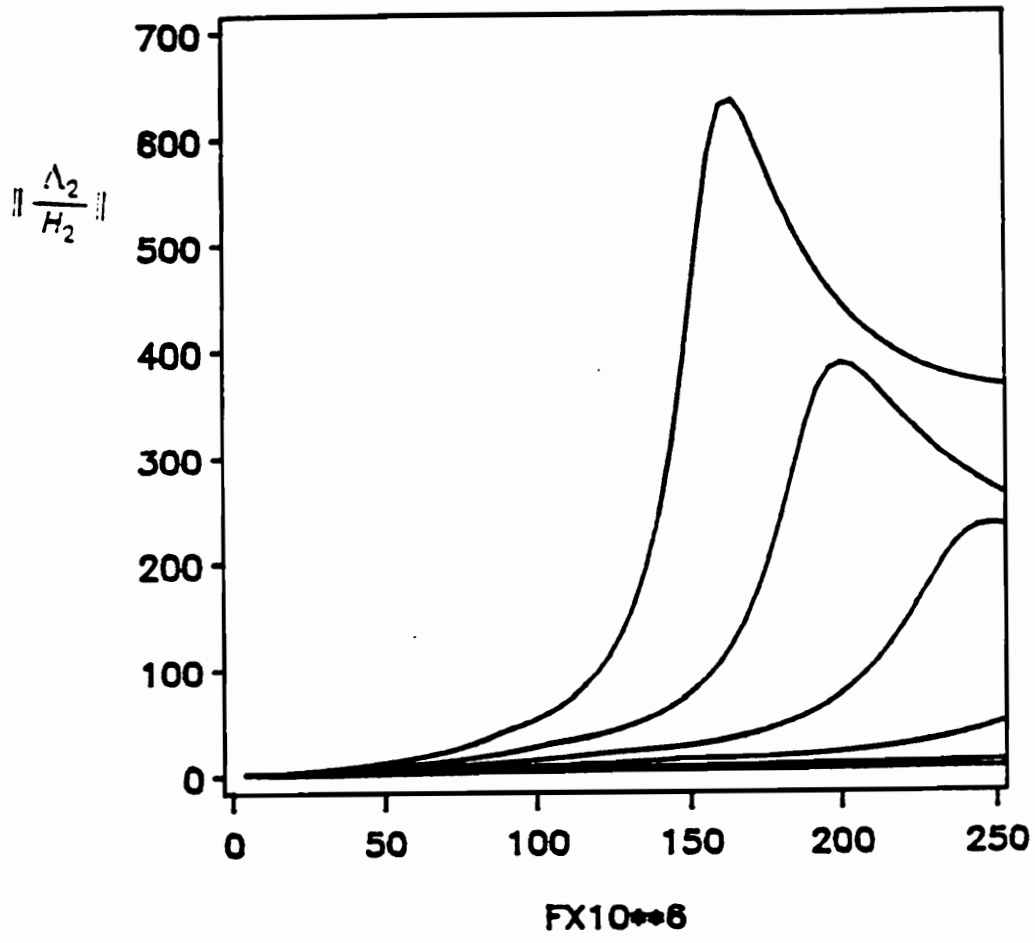

Figure 2.12. Variation of the magnitude of Λ_2/H_2 with the frequency of the primary wave for different Reynolds numbers. The 3-D wave is an Orr-Sommerfeld mode. B = 0.2. Reynolds numbers proceeding downwards are: 1000, 900, 800, 700, 600, and 500.

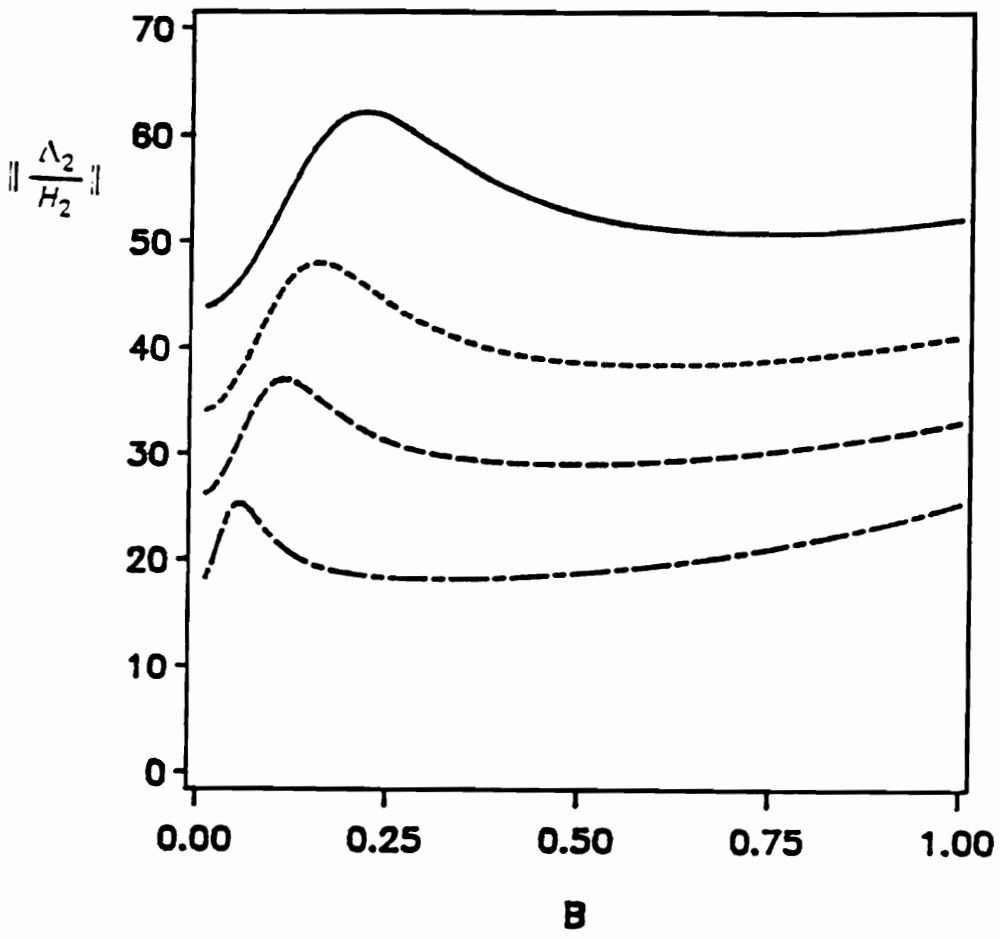

Figure 2.13. Variation of the magnitude of Λ_2/H_2 with the spanwise wavenumber for different frequencies. The 3-D wave is a Squire's mode. R = 520, (___) $F_{2D} = 124x10^{-6}$, (...) $F_{2D} = 100x10^{-6}$, (- - -) $F_{2D} = 80x10^{-6}$, and (_._.) $F_{2D} = 50x10^{-6}$.

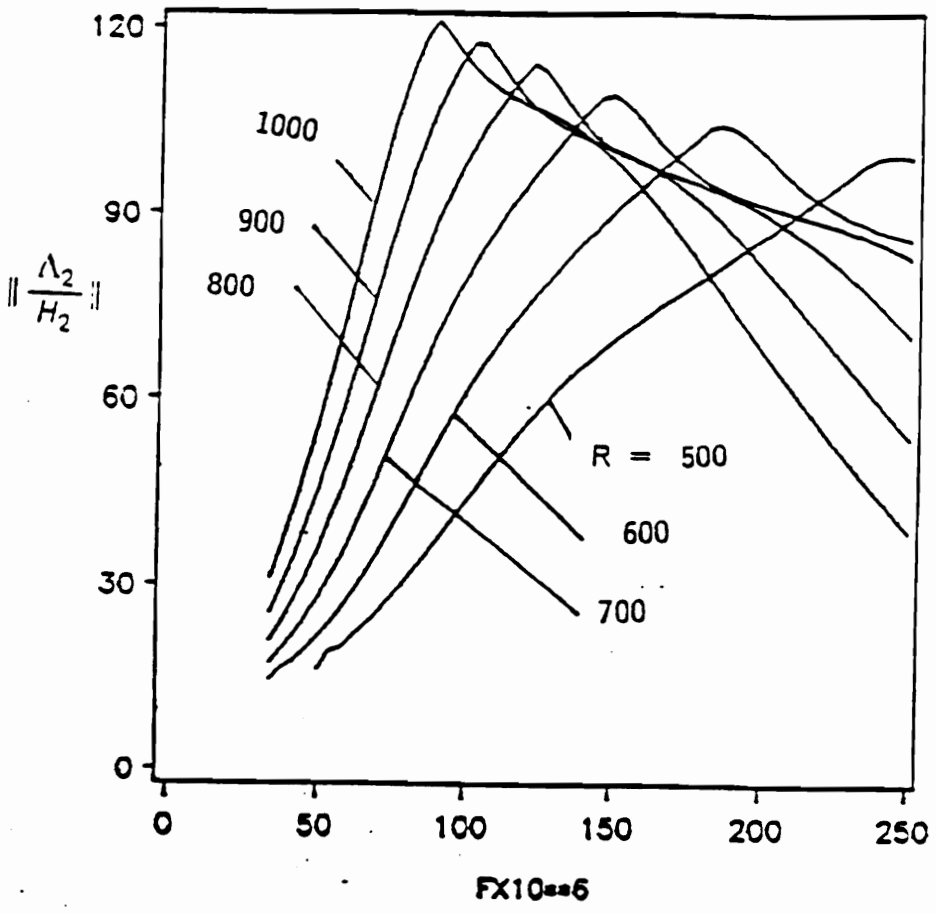

Figure 2.14. Variation of the magnitude of Λ_2/H_2 with the frequency of the primary wave for different Reynolds numbers. The 3-D wave is a Squire's mode. B = 0.2.

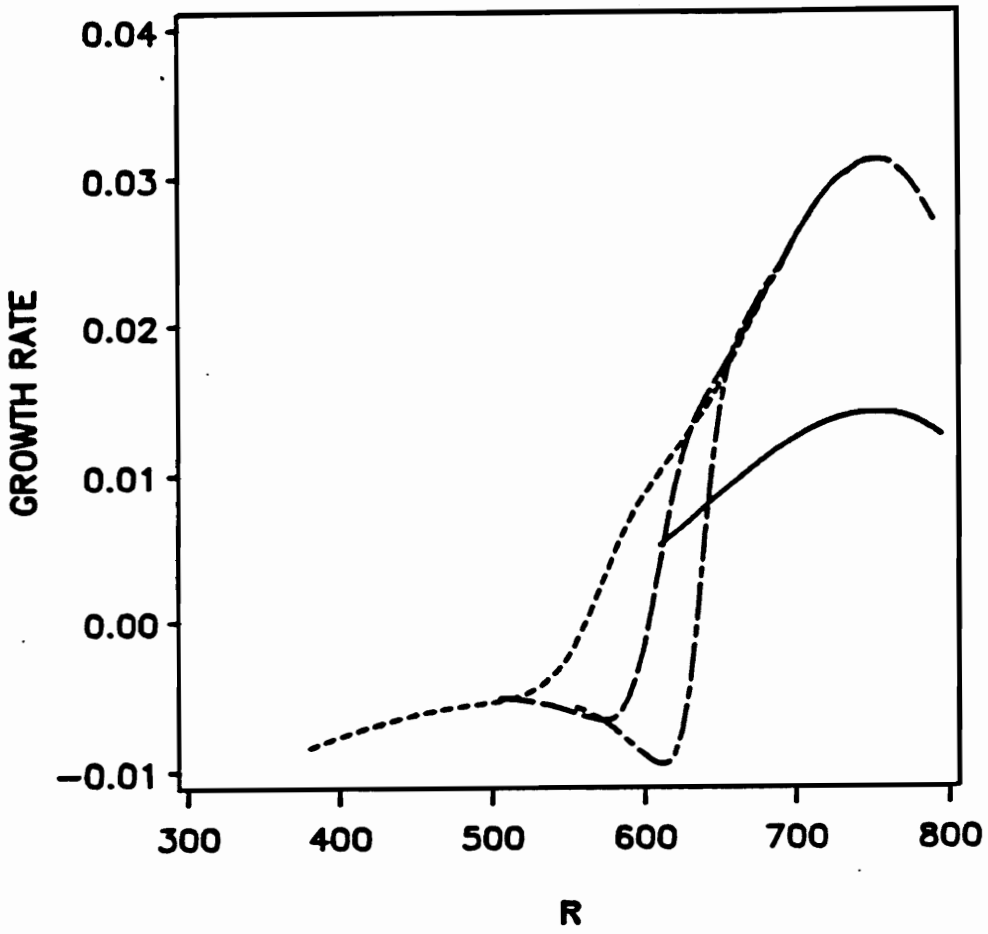

Figure 2.15. Variation of the growth rate of the subharmonic wave as predicted by the resonant triad model compared with the prediction of the Floquet model. The 3-D wave is an Orr-Sommerfeld mode. $F_{2D} = 100x10^{-6}$, $B = 0.2$, $A_{rms} = 0.00237$ at R = 610. (___) Floquet model. Resonant triad model with the integration started at (...) R = 375, (- - -) R = 500, and (_._.) R = 550.

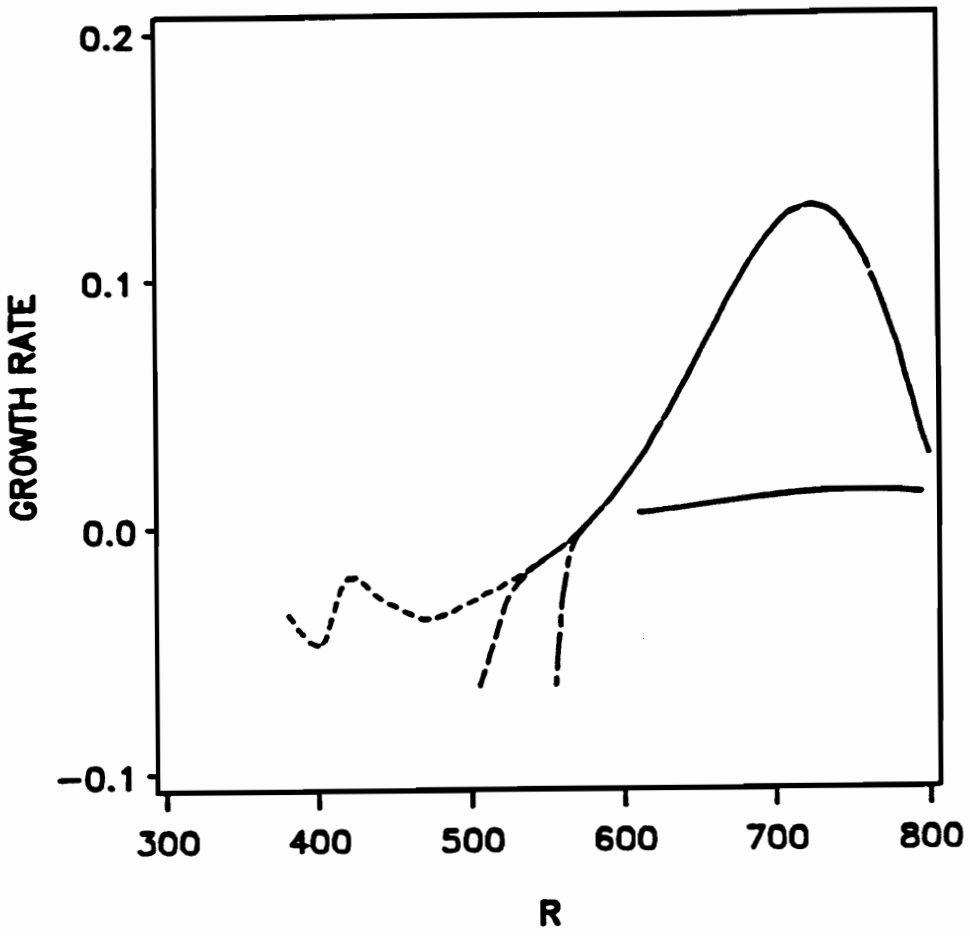

Figure 2.16. Variation of the growth rate of the subharmonic wave as predicted by the resonant triad model compared with the prediction of the Floquet model. The 3-D wave is a Squire's mode. $F_{2D} = 100x10^{-6}$, B = 0.2, $A_{rms} = 0.00237$ at R = 610. (___) Floquet model. Resonant triad model with the integration started at (...) R = 375, (- - -) R = 500, and (_._.) R = 550.

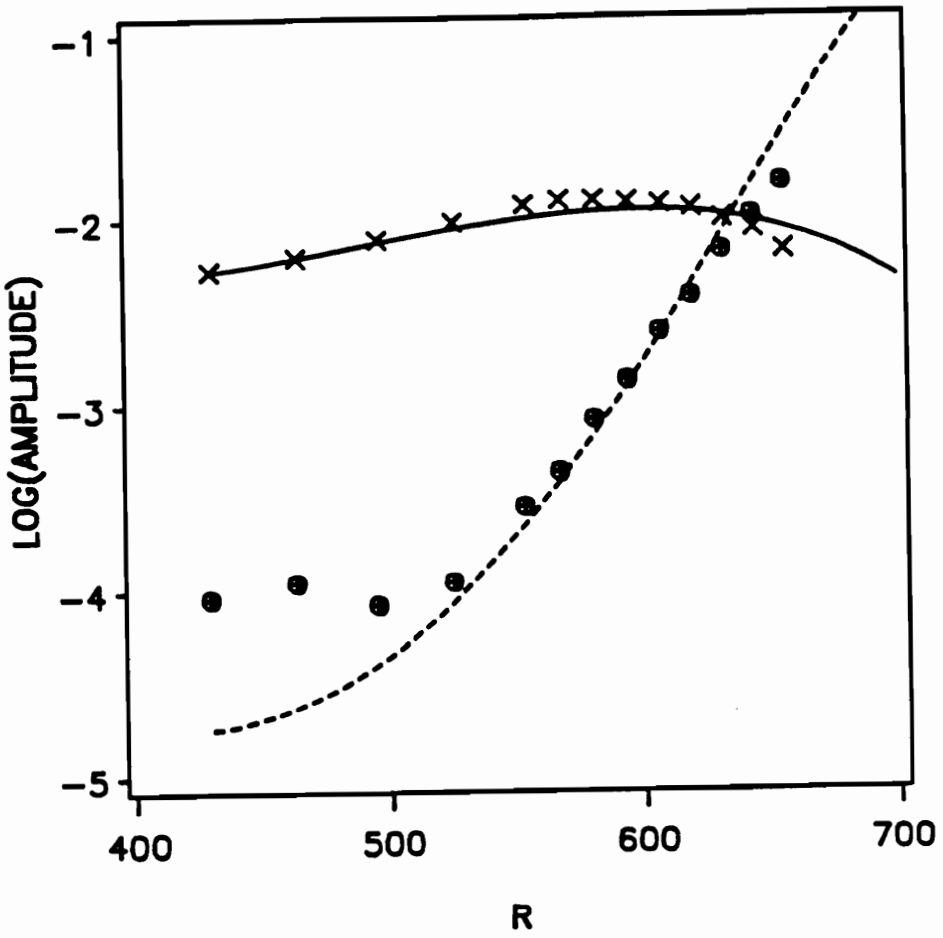

Figure 2.17. Variation with R of the rms amplitudes of the primary (___) and subharmonic (...) waves as predicted by the Floquet model for $F_{2D} = 124x10^{-6}$ and B = 0.33. At R = 430 the rms amplitudes of the primary and subharmonic waves are $5.2x10^{-3}$ and $2.63x10^{-5}$, respectively. (x) and (⊕) are the experimental points of Kachanov and Levchenko (1984).

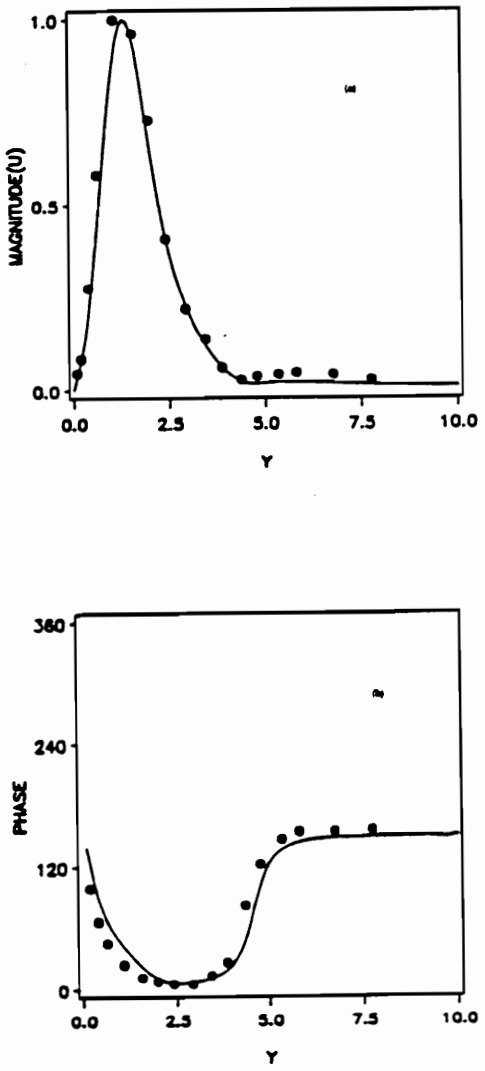

Figure 2.18. The y variation of the magnitude (a) and the phase (b) of the streamwise subharmonic disturbance at R = 606 as predicted by the Floquet model (___) compared with the experimental data (⊕) of Kachanov and Levchenko (1984). for $F_{2D} = 124x10^{-6}$ and B = 0.33 .

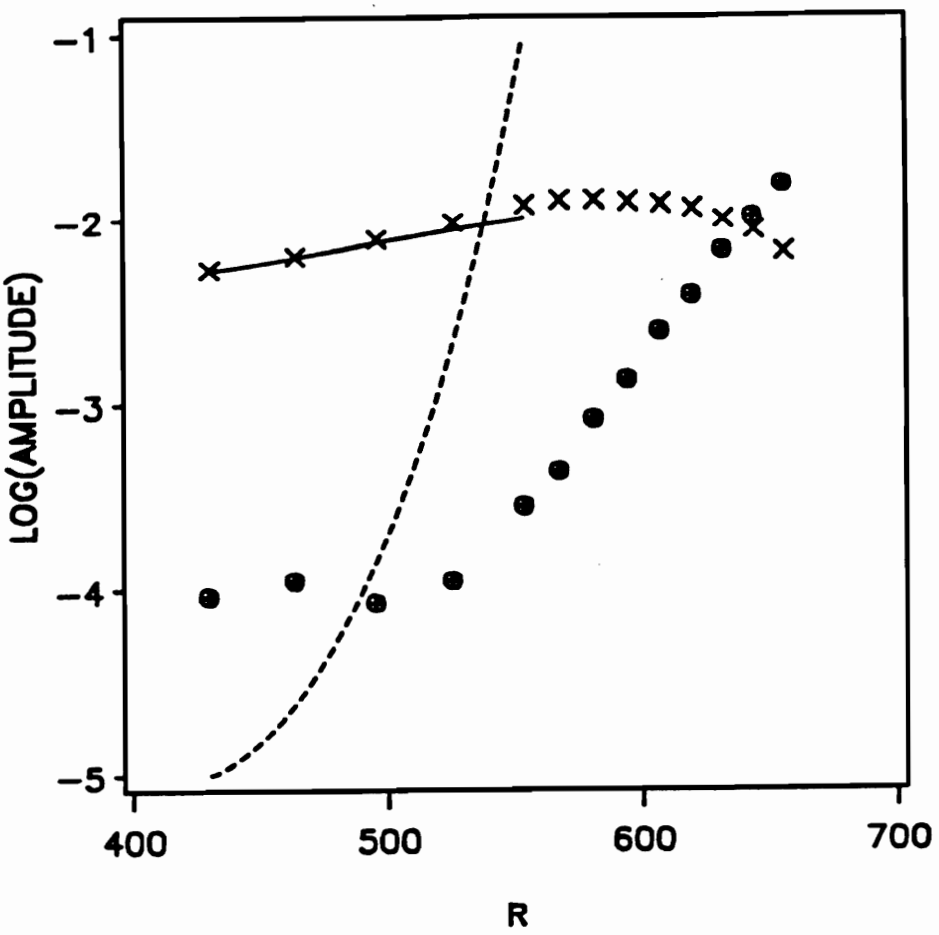

Figure 2.19. Variation with R of the rms amplitudes of the primary (___) and subharmonic (...) waves as predicted by the resonant triad model for $F_{2D} = 124x10^{-6}$ and B = 0.33. The 3-D wave is taken as an Orr-Sommerfeld mode. At R = 430 the rms amplitudes of the primary and subharmonic waves are, respectively, $5.2x10^{-3}$ and 10^{-5}. (x) and (⊕) are the experimental points of Kachanov and Levchenko (1984).

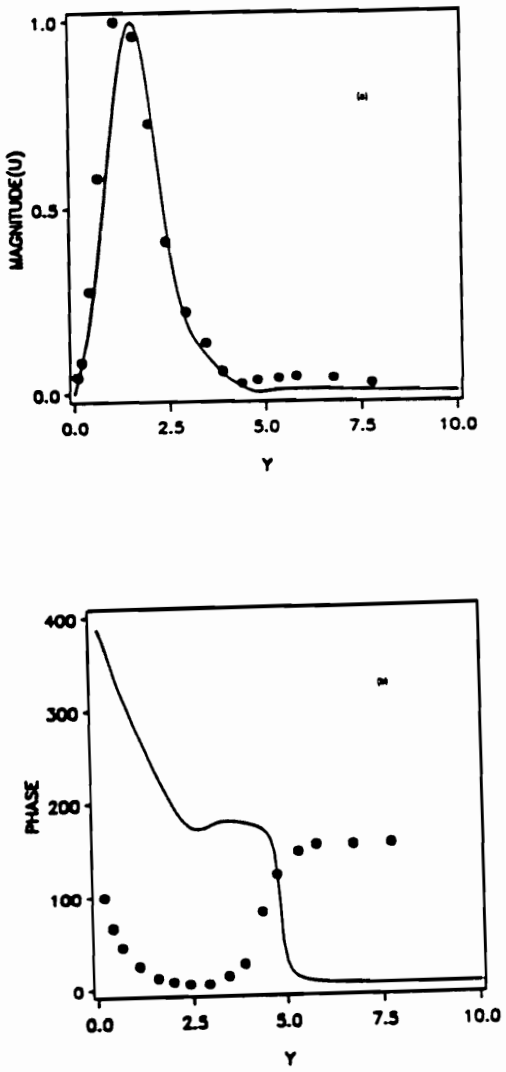

Figure 2.20. The y variation of the amplitude (a) and the phase (b) of the streamwise subharmonic disturbance at R = 606 as predicted by the resonant triad model (___) compared with the experimental data (⊕) of Kachanov and Levchenko (1984). for $F_{2D} = 124x10^{-6}$ and B = 0.33. The 3-D wave is taken as an Orr-Sommerfeld mode.

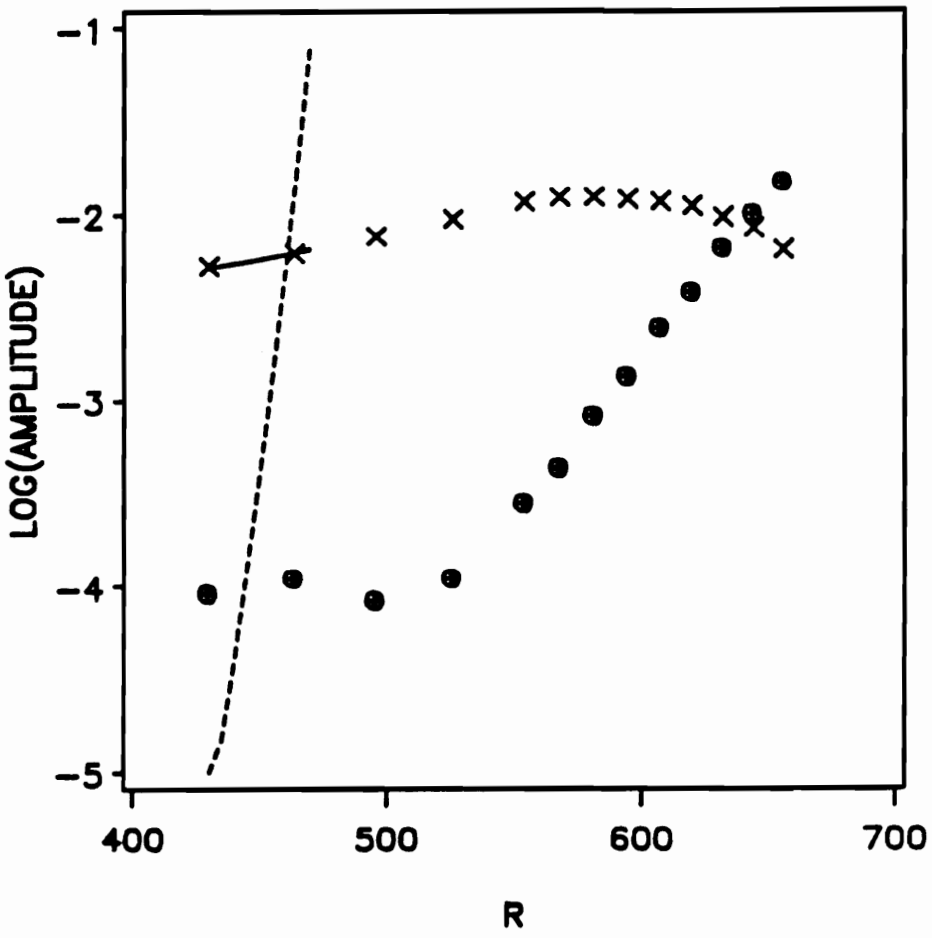

Figure 2.21. Variation with R of the rms amplitudes of the primary (___) and subharmonic (...) waves as predicted by the resonant triad model for $F_{2D} = 124x10^{-6}$ and B = 0.33. The 3-D wave is taken as a Squire's mode. At R = 430 the rms amplitudes of the primary and subharmonic waves are, respectively, $5.2x10^{-3}$ and 10^{-5}. (x) and (⊕) are the experimental points of Kachanov and Levchenko (1984).

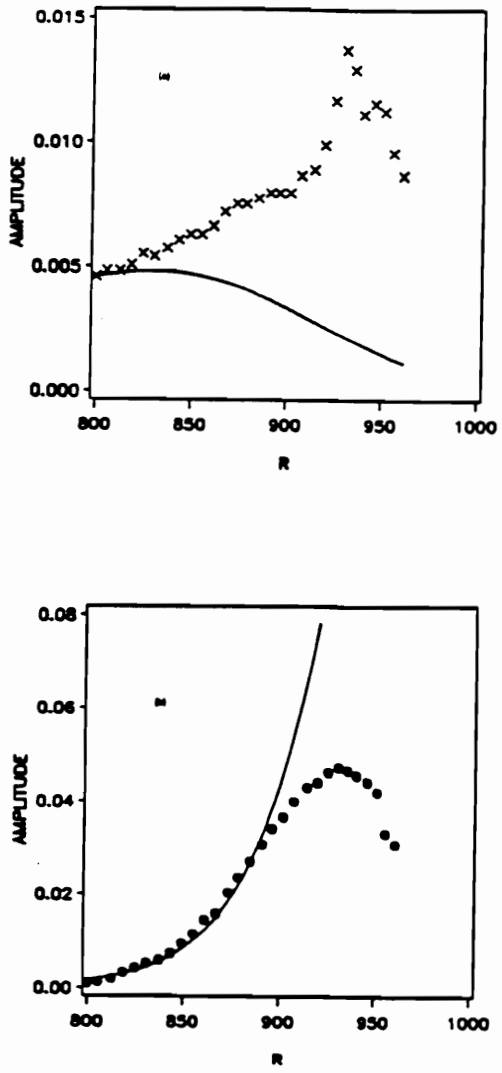

Figure 2.22. Variation with R of the rms amplitudes of the interacting waves as predicted by the Floquet model (___) compared with the experimental data (x, $\oplus$) of Corke and Mangano (1989) for $F_{2D} = 82.7x10 -6$, B = 0.156, and the virtual leading edge in at x = - 58 cm: (a) the primary wave (b) the subharmonic wave.

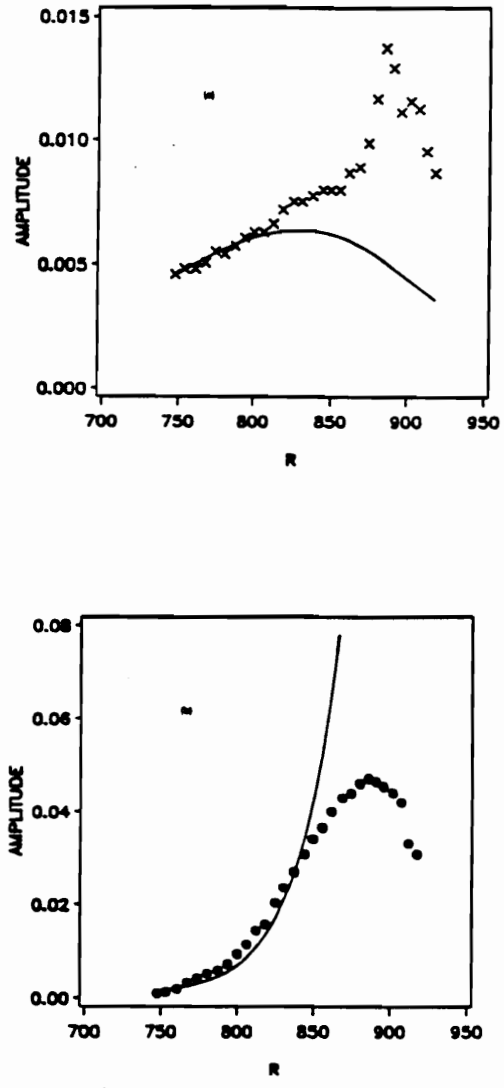

Figure 2.23. Variation with R of the rms amplitudes of the interacting waves as predicted by the Floquet model (___) compared with the experimental data (x, ⊕) of Corke and Mangano (1989) for $F_{2D} = 82.7x10-6$, B = 0.156, and the virtual leading edge in at x = - 38 cm: (a) the primary wave (b) the subharmonic wave.

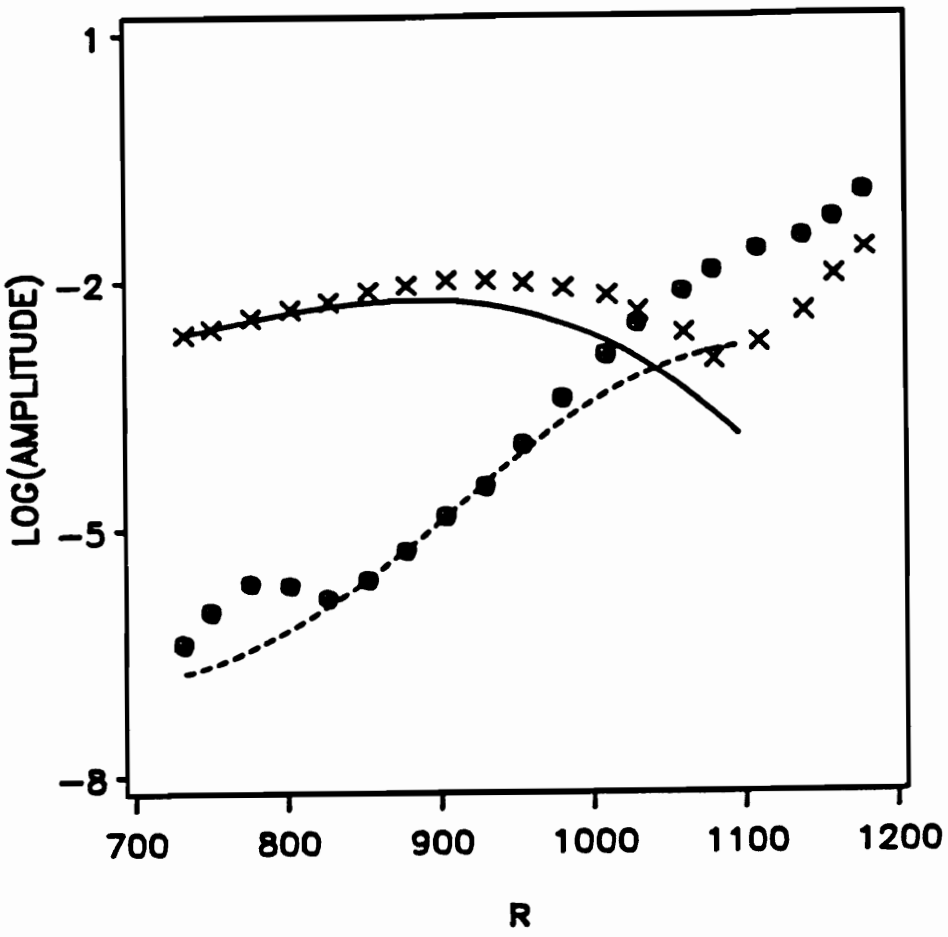

Figure 2.24. Variation with R of the rms amplitudes of the primary (___) and subharmonic (...) waves as predicted by the Floquet model for $F_{2D} = 76x10^{-6}$ and B = 0.14. (x) and (⊕) are the numerical simulation points of Spalart and Yang (1987).

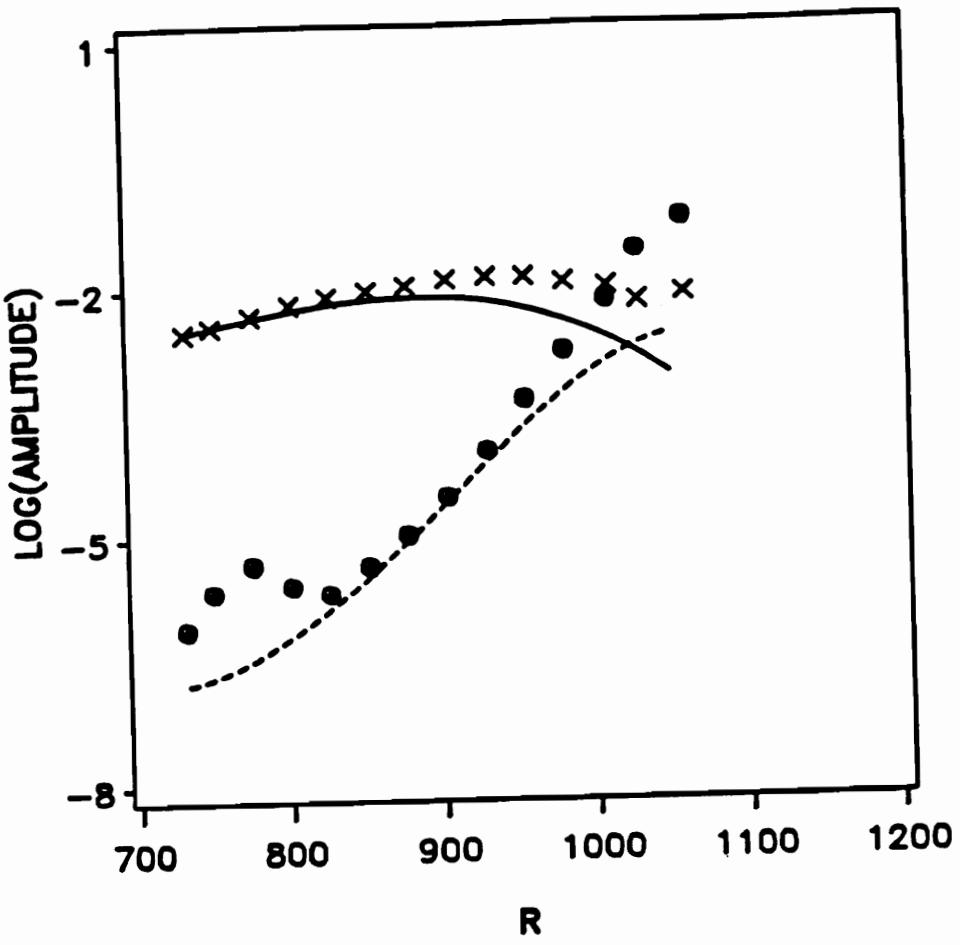

Figure 2.25. Variation with R of the rms amplitudes of the primary (___) and subharmonic (...) waves as predicted by the Floquet model for $F_{2D} = 76 \times 10^{-6}$ and B = 0.2. (x) and (⊕) are the numerical simulation points of Spalart and Yang (1987).

3. EFFECT OF A BULGE ON THE SUBHARMONIC INSTABILITY OF INCOMPRESSIBLE BOUNDARY LAYERS

The influence of a 2-D hump on the 3-D subharmonic instability on a flat plate is investigated. The mean flow is calculated by using interacting boundary layers, thereby accounting for the viscid/inviscid interaction. The primary wave is taken in the form of a 2-D T-S wave. The secondary wave is taken in the form of a 3-D subharmonic wave. The results show that increasing the hump height results in an increase in the amplification factors of the primary and subharmonic waves. When the hump causes separation, the growth rates of both the primary and subharmonic waves are considerably larger than those obtained in the case of no separation.

3.1. Mean Flow

The 2-D incompressible laminar boundary layer over the plate and the hump is determined by solving the interacting boundary-layer equations (Davis and Werle, 1982; Ragab and Nayfeh, 1982). These equations account for upstream influence through the interaction of the viscous flow with the inviscid flow outside the boundary layer. Moreover, they are also capable of capturing separation bubbles without difficulties (Ragab, Nayfeh, and Krishna, 1990). Solutions are obtained by using a second-order finite-difference method in which the grid spacings acknowledge the scaling predicted by triple-deck theory in the interaction region.

Figure 3.1 shows a small symmetric hump of height h^* and width $2b^*$ whose center is located at x_m^*. We introduce dimensionless variables by using L^* and U_∞^*, where L^* is the distance from the leading edge to the center of the hump, as reference quantities. The reference length L^* affects the calculations through Re, which fixes the location of the hump. In terms of dimensionless variables, the hump shape is given by

$$y = \frac{y^*}{L^*} = \frac{h^*}{L^*} f(\zeta) = hf(\zeta), \tag{3.1}$$

where

$$\zeta = \frac{x^* - x_m^*}{b^*} = \frac{x - x_m}{b}. \tag{3.2}$$

We present numerical results for the Walker and Greening hump (Walker and Greening, 1942)

$$f(\zeta) = \begin{cases} h(1 - 12\zeta^2 + 16\zeta^3) & \text{if } \zeta \leq 0.5 \\ 0 & \text{if } |\zeta| > 0.5 \end{cases} \tag{3.3}$$

The flowfield over the plate with the hump is assumed to be governed by the steady, incompressible boundary-layer equations

$$u\frac{\partial u}{\partial x} + v\frac{\partial u}{\partial y} = u_e\frac{du_e}{dx} + \frac{1}{Re}\frac{\partial^2 u}{\partial y^2} \tag{3.4}$$

$$\frac{\partial u}{\partial x} + \frac{\partial v}{\partial y} = 0 \tag{3.5}$$

where u_e is the streamwise edge velocity and

$$Re = U_\infty^* L^*/\nu^* \tag{3.6}$$

with ν^* being kinematic viscosity of the fluid. The no-slip and no-penetration conditions demand that

$$u = v = 0 \text{ at } y = hf[\zeta(x)] \tag{3.7}$$

Away from the wall,

$$u \to u_e \text{ as } y \to \infty \tag{3.8}$$

To solve Eqs. (3.4)-(3.8), we first use the Prandtl transposition theorem, let

$$z = y - hf[\zeta(x)], \quad w = v - hu\frac{df}{dx}[\zeta(x)] \tag{3.9}$$

and rewrite the problem as

$$u\frac{\partial u}{\partial x}+w\frac{\partial u}{\partial z}=u_e\frac{du_e}{dx}+\frac{1}{Re}\frac{\partial^2 u}{\partial z^2} \tag{3.10}$$

$$\frac{\partial u}{\partial x}+\frac{\partial w}{\partial z}=0 \tag{3.11}$$

$$u=w=0 \quad \text{at} \quad z=0 \tag{3.12}$$

$$u\to u_e \quad \text{as} \quad z\to\infty \tag{3.13}$$

Then, we introduce the Levy-Lees variables, specialized for incompressible flow,

$$\xi=\int_0^x u_e dx, \quad \eta=zu_e\sqrt{\frac{Re}{2\xi}} \tag{3.14}$$

$$F=\frac{u}{u_e}, \quad V=\frac{2\xi}{u_e}\left[F\frac{\partial\eta}{\partial x}+w\sqrt{\frac{Re}{2\xi}}\right] \tag{3.15}$$

and rewrite Eqs. (3.10)-(3.13) as

$$2\xi FF_\xi+VF_\eta+\tilde{\beta}(F^2-1)-F_{\eta\eta}=0 \tag{3.16}$$

$$2\xi F_\xi+V_\eta+F=0 \tag{3.17}$$

$$F=V=0 \quad \text{at} \quad \eta=0 \tag{3.18}$$

$$F\to 1 \quad \text{as} \quad \eta\to\infty \tag{3.19}$$

$$F=F(\xi_0,\eta) \quad \text{at} \quad \xi=\xi_0 \tag{3.20}$$

where ξ_0 corresponds to a location upstream of the interaction region and

$$\tilde{\beta} = \frac{2\xi}{u_e}\frac{du_e}{d\xi} \tag{3.21}$$

With u_e specified by the inviscid flow over the hump surface, Eqs. (3.16)-(3.20) represent a conventional boundary-layer theory. However, in the presence of separation or strong viscid/inviscid interactions these equations fail to provide a solution, and one needs to use triple-deck theory or interacting boundary layers or a Navier-Stokes solver. In this thesis, we employ interacting boundary layers. The interaction law relates the edge velocity u_e to the scaled displacement surface $\delta_1\sqrt{Re}$ as

$$\delta = \delta_1\sqrt{Re} = \frac{\sqrt{2\xi}}{u_e}\int_0^\infty (1-F)d\eta \tag{3.22}$$

$$u_e = \tilde{u}_e + \frac{1}{\pi}\int_{L.E.}^\infty \frac{1}{x-t}\frac{d}{dt}\left[\tilde{u}_e\delta(Re)^{-1/2}\right]dt \tag{3.23}$$

where $\tilde{u}_e$ is the inviscid surface velocity in the absence of the boundary layer, which is also given by thin airfoil theory as

$$\tilde{u}_e = 1 + \frac{1}{\pi}\int_{L.E.}^\infty \frac{1}{x-t}d\frac{(hf)}{dt}dt \tag{3.24}$$

The principal values of the Cauchy integrals in Eqs. (3.23) and (3.24) are assumed. If we let $T = \sqrt{Re}\,hf + \tilde{u}_e\delta$, then Eq. (3.23) can be rewritten as

$$u_e = 1 + \frac{1}{\pi\sqrt{Re}} \int_{L.E.}^{\infty} \frac{1}{x - t} \frac{dT}{dt}\, dt \tag{3.25}$$

We follow Veldman (1981) and solve Eqs. (3.16)-(3.20) simultaneously with the interaction law (3.25). The skin-friction coefficient

$$C_f\sqrt{Re} = \frac{2U_e^2}{\sqrt{2\xi}} \frac{\partial F}{\partial \eta}\bigg|_{\eta=0} \tag{3.26}$$

and the displacement surface, Eq. (3.22), will be presented later for different hump heights.

3.2. The Quasiparallel Assumption

We consider the 2-D spatial quasiparallel stability of the mean flow determined by the interacting boundary-layer code. Although the quasiparallel assumption has been justified for conventional aerodynamic surfaces, one might question its validity for the configuration under investigation. Figure 3.2 shows that the wavelengths of the disturbances for the geometrical and flow parameters of our configuration are of the same order of magnitude as those of the Blasius flow at the same Reynolds number and frequency. Consequently, nonparallel effects are second-order quantities and to first order the disturbance can be considered to be quasiparallel. Moreover, the direct numerical simulations of Bestek, Gruber, and Fasel (1989) and the experimental results of Dovgal and Kozlov (1989) support the quasiparallel

assumption. Bestek, Gruber, and Fasel investigated the effect of a 2-D smooth backward-facing step on the spatial development of a T-S wave by numerically integrating the Navier-Stokes equations using a finite-difference scheme. The growth rates obtained by the direct numerical simulation are in excellent agreement with those obtained by a quasiparallel stability analysis. Dovgal and Kozlov experimentally investigated the stability characteristics of flows over humps and backward- and forward-facing steps. The experimentally determined transverse and streamwise developments of the disturbances ahead, inside, and downstream of the separation bubble are similar to those obtained here and by Nayfeh et al. (1988) by a quasiparallel theory.

3.3. Results

3.3.1. Mean flow

We have obtained results for the mean flow over a hump whose shape is defined by Eqs. (3.1)-(3.3), center is at $x_m = 1.0$, and width $2b = 0.2$. We have considered four humps with an increasing height given by $h = (h^*/L^*)\sqrt{Re} = 1.5, 2, 3,$ and 5. The Reynolds number Re is fixed for all humps at $Re = 10^6$. The hump corresponding to $\tilde{h} = 1.5$ does not induce any flow separation, while that corresponding to $\tilde{h} = 2$ shows incipient separation at $x \approx 1.08$. The hump corresponding to $\tilde{h} = 3$ induces a small separation bubble (separation at $x \approx 1.043$, reattachment at $x \approx 1.14$, and a maximum flow reversal of -2.4% u_e). The hump corresponding to $\tilde{h} = 5$ induces a somewhat

larger separation bubble (separation at $x \approx 1.018$, reattachment at $x = 1.33$, and a maximum flow reversal of -11.7% u_e).

The interaction region extends from $x = 0.3$ to $x = 2.6$ for $\tilde{h} = 5$, and from $x = 0.5$ to $x = 2.4$ for the other three humps. The step size in the x-direction is uniform with $\Delta x = 0.2/30$, which results in 30 points equally spaced over the hump width. In the transverse direction, a stretched grid is used with $\Delta\eta_1 = 0.03$ and $\Delta\eta_j = 1.03\Delta\eta_{j-1}$ for $j = 2,...,N$. The matching condition, Eq. (3.19), is applied at $\eta_N = 12.1$ for $\tilde{h} = 5$ and at $\eta_N = 10.3$ for the other three humps.

The hump shapes and the predicted scaled displacement surfaces are depicted in Figs. 3.3, 3.5, and 3.7, and the corresponding distributions of the pressure and scaled skin-friction coefficients are shown in Figs. 3.4, 3.6, and 3.8 for $\tilde{h} = 2, 3$, and 5, respectively. The scaling δ with respect to $\sqrt{Re}$, where Re is fixed, rather than the local Reynolds number, is for convenience and has no effect on the correctness of the numerical results. Figure 3.3 shows that the hump height for the case of incipient separation is slightly larger than the Blasius displacement thickness δ_B at the hump center ($\tilde{h}/\delta_B = 2/1.7208 = 1.16$). The case of $\tilde{h} = 5(\tilde{h}/\delta_B = 5/1.7208 \approx 2.89)$ contains a large separation bubble downstream of the hump as evident from figure 3.8. For all humps, there is an adverse pressure gradient ahead of the hump, and consequently the skin friction drops below the Blasius value. The region of adverse pressure gradient is followed by a region of favorable pressure gradient extending over a very short region (from $x \approx .90$ to $x \approx 1.0$), then the pressure gradient becomes adverse again, causing the boundary layer to separate. Generally speaking, one would expect that the T-S wave will be unstable ahead of the hump, become stable over the short favorable pressure-gradient region, and then turn unstable in the separation region. This general behavior has been predicted for different humps at different Reynolds numbers and over a range of frequencies by Nayfeh et al. (1988).

3.3.2. Primary and subharmonic stability analysis

We have conducted a stability analysis of the calculated mean flows. We used spatial stability theory for both primary and subharmonic waves; ω is real and α is complex. For the case of tuned subharmonic waves, γ is real. The growth rate of the primary wave is given by $-\alpha_i$ and that of the tuned subharmonic wave is given by γ. Throughout this work, the frequency $F = \omega^* \nu^* / U_\infty^{*2}$ is related to ω through $\omega = FR$ and remains constant as the wave propagates downstream. Because the mean flow is 2-D and stationary, the dimensional frequency ω^* and spanwise wavenumber β^* remain constant as the wave propagates downstream. Then, the dimensionless spanwise wavenumber $\beta = \beta^* \delta_r^* = \beta^* \nu^* R / U_\infty^*$. Hence, β is proportional to R and in turn β/R and $B = 1000\beta/R$ remain constant as the wave propagates downstream. We note that B is proportional to the dimensional wavenumber. However, instead of saying that B is proportional to the wavenumber, we will refer to it as the spanwise wavenumber.

To determine the effect of the hump on the most amplified subharmonic mode, particularly when separation is present, we performed a local stability analysis of the velocity profiles at $x = 1.1$ (i.e., $R = 1049$) for humps with $\tilde{h} = 0$ (Blasius flow), 1.5, 2, and 3. For $\tilde{h} = 3$, the velocity profile at $x = 1.1$ has a maximum flow reversal of -2.4% u_e. We define the amplitude a of the primary wave as the root-mean square (rms) of the u' disturbance maximized over y. For $a = 0.01 U_\infty^*$, the variation of the growth rate γ with B is shown in figure 3.9. The spanwise wavenumber B of the most amplified secondary wave shifts towards smaller values of B as $\tilde{h}$ increases from zero to 3. For $\tilde{h} = 3$, the value of B corresponding to the most amplified wave is approximately 0.124.

The mean-flow profile and the eigenfunctions for the u' disturbance of both the primary and secondary waves are shown in figure 3.10. It is interesting to note that the primary wave has local maxima at three locations in the transverse direction. The middle one is related to the shear-layer instability mechanism associated with the inflection point (see Nayfeh et al., 1988).

Next we consider the flow over the hump with $\tilde{h} = 5$. A stability analysis has been performed ahead of the hump only. The analysis in the separation bubble downstream of the hump was unnecessary after finding out that the much smaller separation bubble caused by $\tilde{h} = 3$ considerably increases the growth rate of the primary wave and even more dramatically the growth rate of the subharmonic wave. We start at the initial station $x_0 = 0.68$, where $R_0 = 825$, and assume that $a_0 = 0.01U_\infty^*$ and $B = 0.218$. Then we march downstream and compute simultaneously the primary and subharmonic waves by using the local velocity profiles and local wavenumber α_r and updating a from $a = a_0 \exp(-2\int_{R_0}^{R} \alpha_i dR)$. Also we compute $\ell n(A/A_0) = 2\int_{R_0}^{R} \gamma dR$, where A is the amplitude of the subharmonic wave.

Figure 3.11 shows the growth rates $-\alpha_i$ and γ ahead of the hump. The amplification factors $\ell n(a/a_0)$ and $\ell n(A/A_0)$ are shown in figure 3.12. We note that the primary wave is almost neutral, except near the upstream corner of the hump. The zero growth rate is a result of two counteracting effects. The first is a very weak adverse pressure gradient (see figure 3.8), which is destabilizing. And the second is the increase in the Reynolds number, which is stabilizing (we recall that the Reynolds number and frequency at the initial station correspond to a point on the upper branch of the neutral curve of the Blasius boundary layer). As shown in figure 3.12, the amplification factor of the primary wave is less than 2 at the end of the adverse pressure-gradient region, but the amplification factor of the subharmonic wave is greater than 9. This is alarming if we are concerned about keeping the flow laminar

ahead of the hump. Unfortunately, at the present time, there is no quantitative correlation between the amplification factors of secondary instabilities and transition. Such a correlation, if it exists, must involve the amplitude of the primary wave or a certain measure of the background disturbances as a parameter.

Next we present the results of the stability analysis downstream of the hump for $\tilde{h} = 1.5$, 2, and 3. At the initial station $x = 1.03$ we assume that $a = a_0$ and choose a value of B. Then we march downstream and compute the growth rates and amplification factors for both the primary and subharmonic waves. The variation of the growth rates for the three humps at $F_{2D} = 83x10^{-6}$ are shown in figure 3.13 and the corresponding amplification factors are shown in figure 3.14. For the small hump $\tilde{h} = 1.5$, the growth rate is small and the amplification factor reaches a maximum of 2.2. For the hump $\tilde{h} = 2$, which corresponds to incipient separation, the amplification factor of the primary wave reaches a maximum of 4.2 and then drops downstream. The case with small separation bubble ($\tilde{h} = 3$) shows considerable amplification of the primary wave over a very short distance. Half way through the separation bubble the amplification factor is already greater than 5. The obtained growth rates and amplification factors for the subharmonic wave with $B = 0.124$ and $a_0 = 0.002$ are shown in figure 3.15 and 3.16, respectively. Here again we see considerable growth rates for the separated flow case in comparison with the cases of incipient separation or no separation.

Next, we investigate the influence of the frequency. In figure 3.17, we show the streamwise variation of the growth rate of the primary wave for the small hump $\tilde{h} = 1.5$ for several frequencies. When $F = 120x10^{-6}$, the disturbance is unstable over the narrow range $1039 \leq R \leq 1061$ and the maximum growth rate is approximately 0.012 and occurs at $R \approx 1042$. Consequently, the resulting growth of the disturbance, as measured by the N factor, is very small, as shown in figure 3.18. As the frequency

decreases to $F = 83x10^{-6}$, figure 3.17 shows that the peak growth rate increases to approximately 0.033 and the unstable range increases to $1016 \leq R \leq 1080$, resulting in a maximum N factor of about 2.2 at $R = 1079$, as shown in figure 3.18. As the frequency decreases to $F = 40x10^{-6}$, figure 3.17 shows that the peak growth increases slightly to 0.037 and shifts slightly to the lower Reynolds number 1039. Moreover, the range of unstable streamwise locations increases considerably, resulting in a still larger amplification factor, as shown in figure 3.18. As F decreases to $40x10^{-6}$, figure 3.17 shows that the peak growth rate decreases but the range of unstable locations increases considerably, resulting in still a larger amplification factor, as shown in figure 3.18. As F decreases further, figure 3.17 shows that the growth rates are less than those for $F = 40x10^{-6}$ for all $R \leq 1147$. Beyond this Reynolds number the growth rates corresponding to $F = 30x10^{-6}$ are slightly larger than those corresponding to $F = 40x10^{-6}$. The end result is an amplification factor that is larger in the case of $F = 40x10^{-6}$ than in the case of $F = 30x10$ 6, as shown in figure 3.18.

For $\tilde{h} = 1.5$, $B = 0.2$, and $a_{rms} = 0.003$ at the initial location $x = 1.03$, we show in figure 3.19 the streamwise variation of the growth rate of the subharmonic wave for the frequencies employed in figures 3.17 and 3.18. For all frequencies, initially the growth rate γ of the subharmonic wave increases rapidly with R. In the case of $F = 120x10^{-6}$, the maximum growth rate is approximately 0.038 and occurs at $R \approx 1042$. Consequently, the maximum amplification factor is approximately 4.5 and occurs at $R \approx 1120$, as shown in figure 3.20. As F decreases to $83x10^{-6}$, the maximum growth rate increases to approximately 0.053 and occurs earlier at $R \approx 1075$, resulting in much larger N factors, as shown in figure 3.20. In fact, the N factor exceeds 9 when $R > 1112$, as shown in figure 3.20. When $F = 50x10^{-6}$ or $40x10^{-6}$ or $30x10^{-6}$, the growth rate of the subharmonic wave does not have a maximum in the range of Reynolds numbers investigated. Moreover, the N factors at these frequencies increase rapidly

with increases R, as shown in figure 3.20. It appears that an $F \approx 50x10^{-6}$ is the most critical frequency because it yields the largest N factors when R exceeds 1128. In fact, N exceeds 15 when $R = 1164$.

For the hump $\tilde{h} = 2$, which corresponds to the case of incipient separation, we show in figure 3.21 the streamwise variation of the growth rate of the primary wave for several frequencies. Comparing figures 3.17 and 3.21, we conclude that the growth rates for the case of incipient separation are much larger than those in the case of no separation. It follows from figure 3.21 that $F = 83x10^{-6}$ has the largest growth rate. However, the bandwidth of the peak growth rate is smaller than those corresponding to smaller values of F. Consequently, the frequency that results in the largest amplification factor of the primary wave is approximately $50x10^{-6}$, as shown in figure 3.22.

In figure 3.23, we show the streamwise variation of the growth rates of the subharmonic wave for $\tilde{h} = 2$ for the frequencies employed in figures 3.21 and 3.22 when $B = 0.2$ and $a_{rms} = 0.003$ at $x = 1.03$. Comparing figures 3.19 and 3.23, we conclude that the growth rates of the subharmonic wave in the case of incipient separation are much larger than those in the case of no separation. It appears from figures 3.23 and 3.24 that again an $F \approx 50x10^{-6}$ produces the largest amplification factors when $R > 1077$.

In the case of $\tilde{h} = 3$, which produces a small separation bubble, we show in figure 3.25 the streamwise variation of the growth rates of the primary wave for several frequencies. In this case, $F = 120x10^{-6}$ produces the largest growth rate. Comparing figures 3.21 and 3.25, we note that the separation bubble results in much larger growth rates at all frequencies, resulting in much larger amplification factors at all frequencies as can be seen from comparing figures 3.22 and 3.26.

The streamwise variation of the growth rates of the subharmonic wave for the frequencies employed in figure 3.25 and 3.26 is shown in figure 3.27 for $B = 0.2$ and $a_{rms} = 0.003$. Comparing figures 3.23 and 3.27, we note that the separation bubble produces much larger growth rates at all frequencies, resulting in very large amplification factors in short distances, as shown in figure 3.28. Thus, the presence of separation bubbles can be very detrimental to the maintenance of laminar flow.

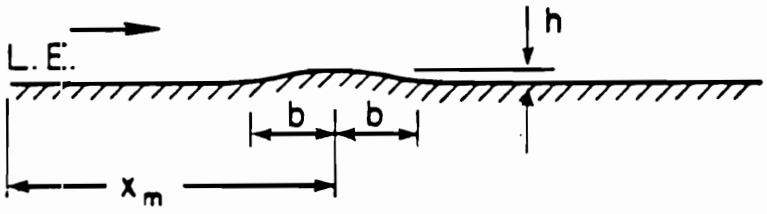
L. E.
h
b
b
x m

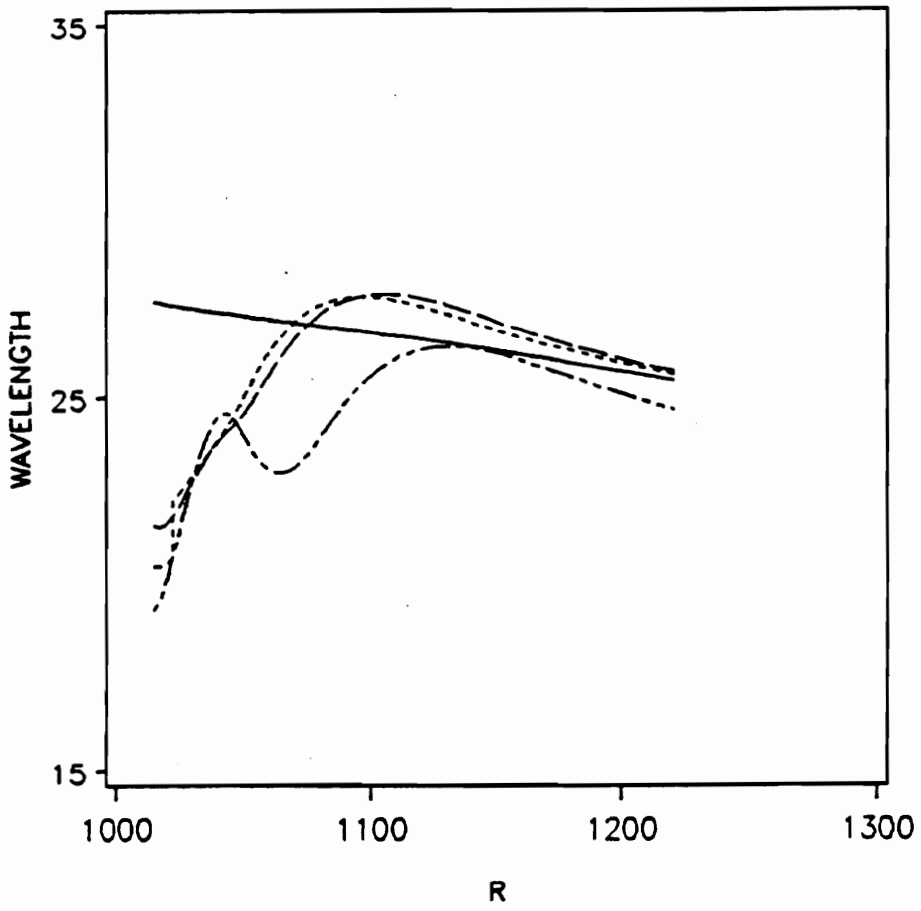

Figure 3.2. Variation of the wavelength of the primary wave with Reynolds number at $F_{2D} = 83x10^{-6}$. (___) $\tilde{h} = 0$ (Blasius), (...) $\tilde{h} = 1.5$, (- - -) $\tilde{h} = 2$, and (__ . __ .) $\tilde{h} = 3$.

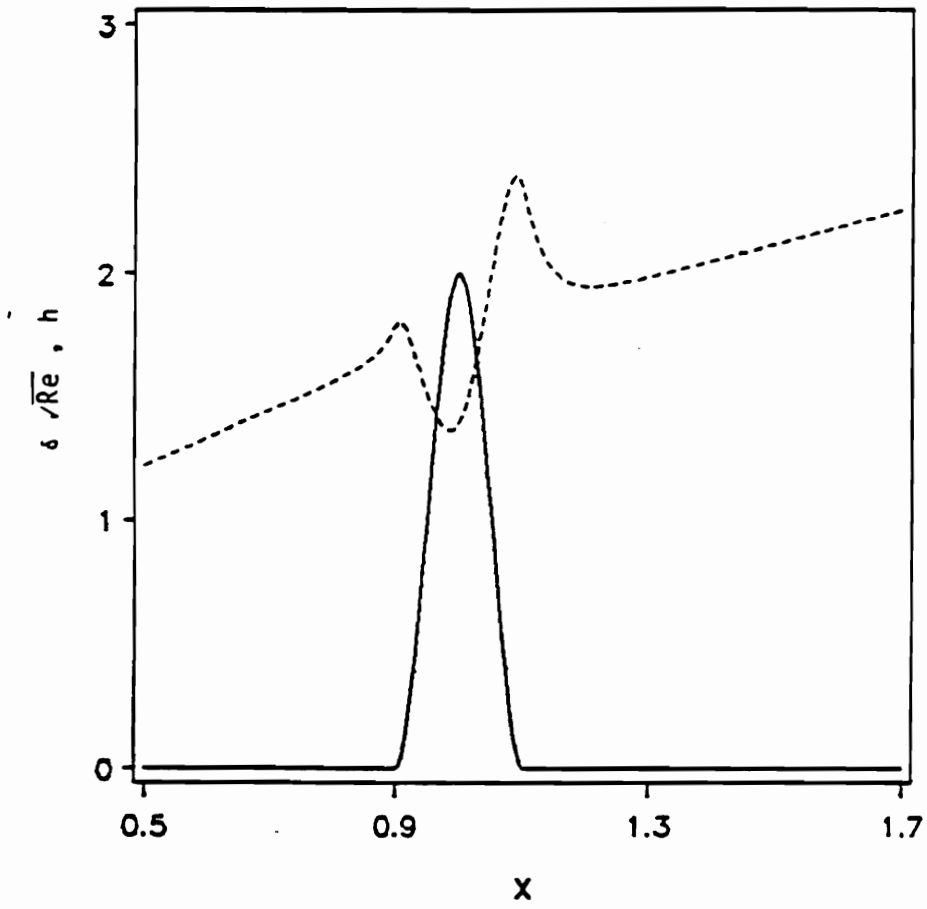

Figure 3.3. (___) Hump shape for $\tilde{h} = 2$ and (...) corresponding scaled displacement surface $\sqrt{Re}$; $Re = 10^6$.

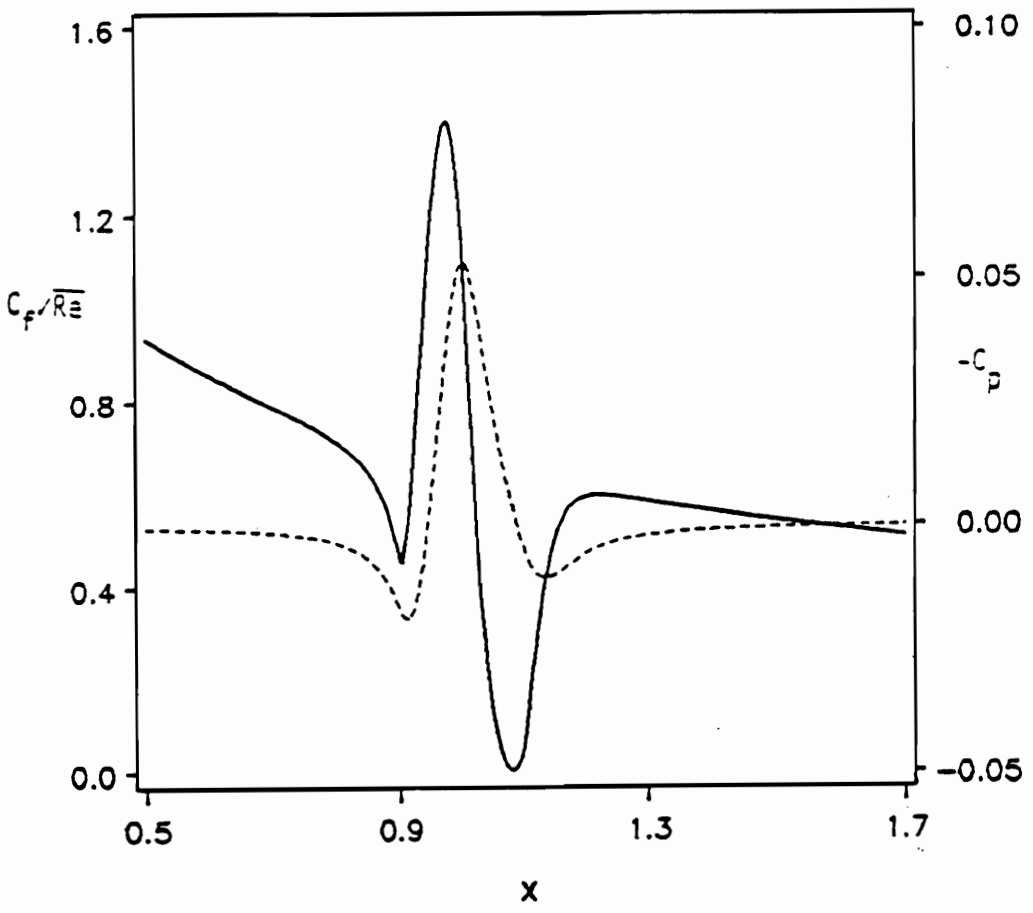

Figure 3.4. Distributions of (___) the scaled skin-friction coefficient $C_f\sqrt{Re}$ and (...) pressure coefficient C_p for $\tilde{h} = 2$ and $Re = 10^6$; case of incipient separation.

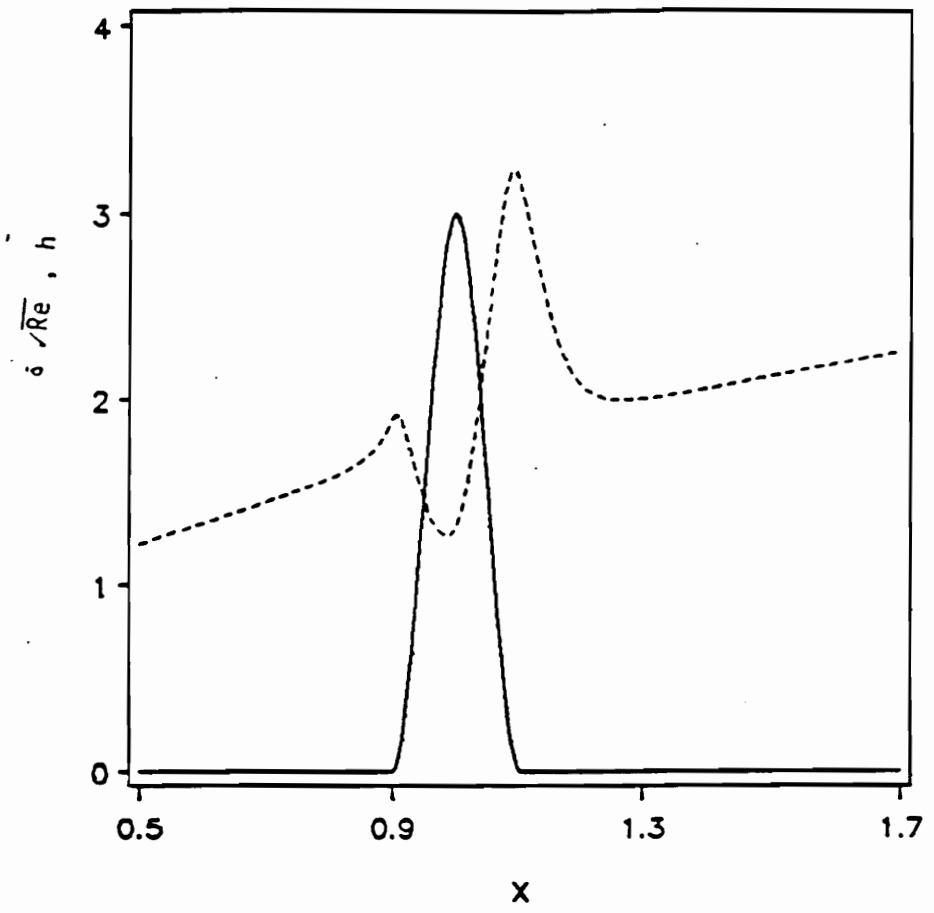

Figure 3.5. (___) Hump shape for $\tilde{h} = 3$ and (...) corresponding scaled displacement surface $\sqrt{Re}$; $Re = 10^6$.

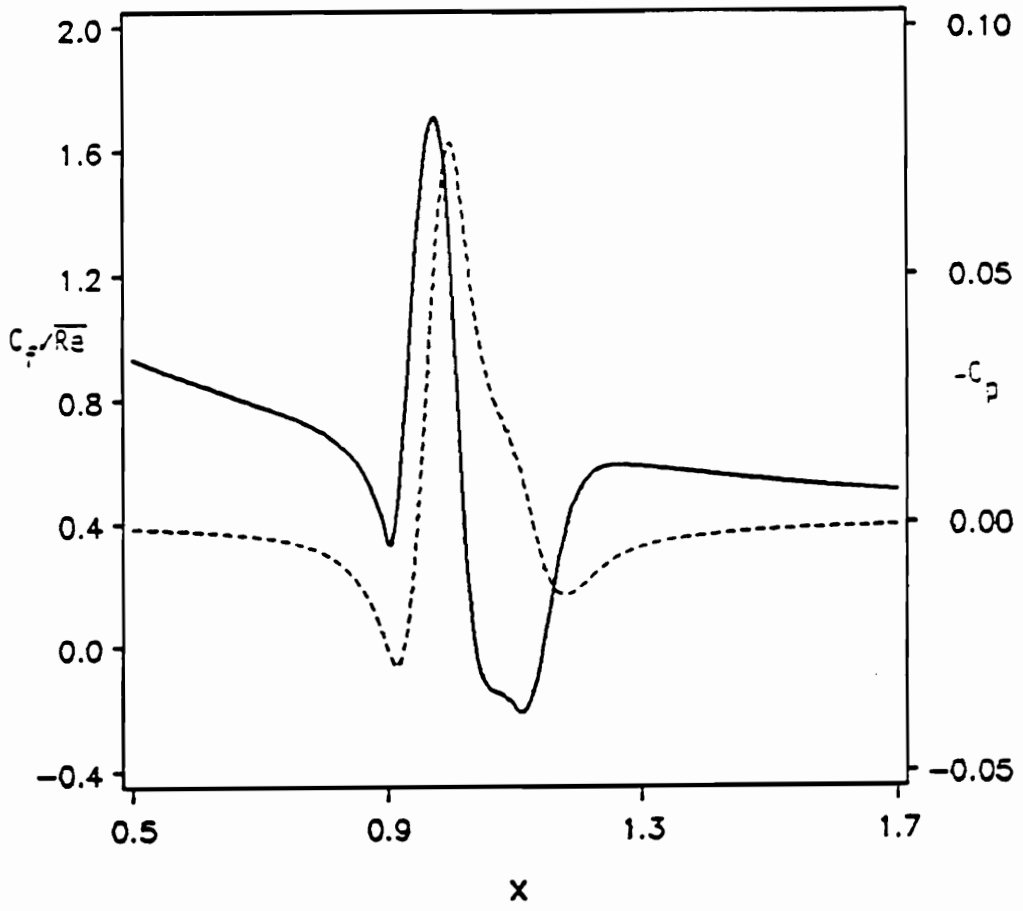

Figure 3.6. Distributions of (___) the scaled skin-friction coefficient $C_f\sqrt{Re}$ and (...) pressure coefficient C_p for $\tilde{h} = 3$ and $Re = 10^6$; small separation bubble.

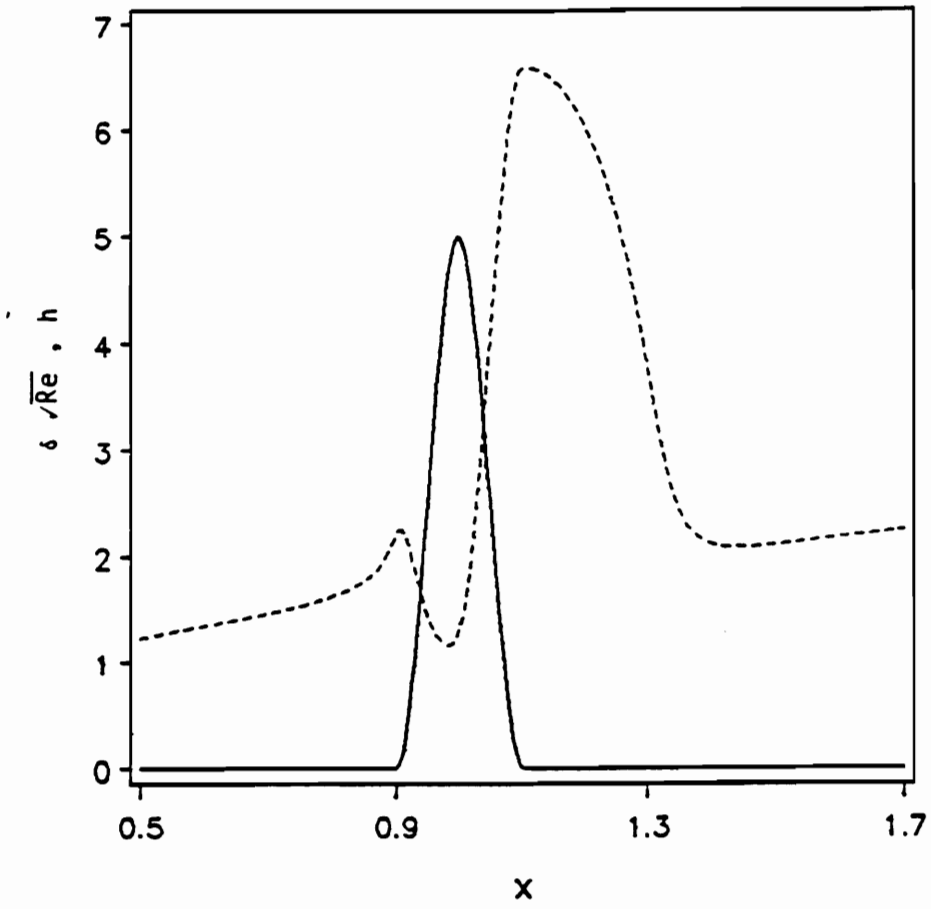

Figure 3.7. (___) Hump shape for $\tilde{h} = 5$ and (...) corresponding scaled displacement surface $\sqrt{Re}$; $Re = 10^6$.

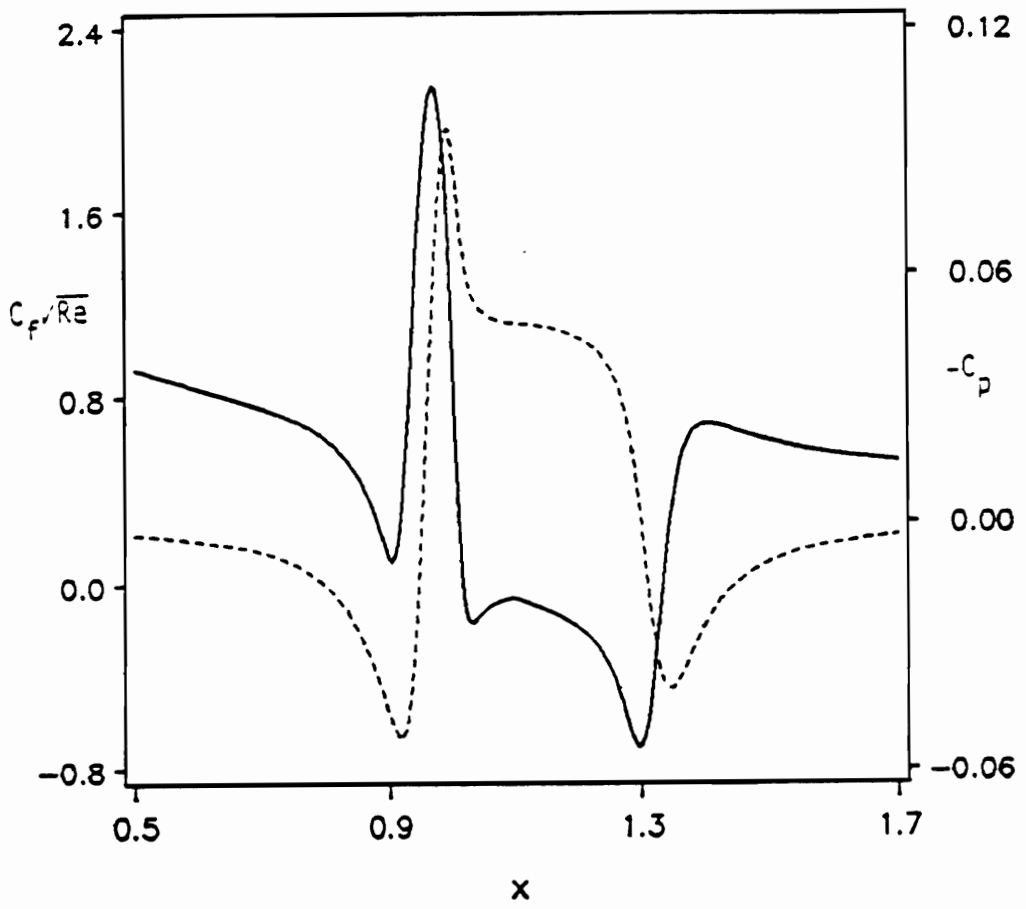

Figure 3.8. Distributions of (___) the scaled skin-friction coefficient $C_f\sqrt{Re}$ and (...) pressure coefficient C_p for $\tilde{h} = 5$ and $Re = 10^6$; large separation bubble.

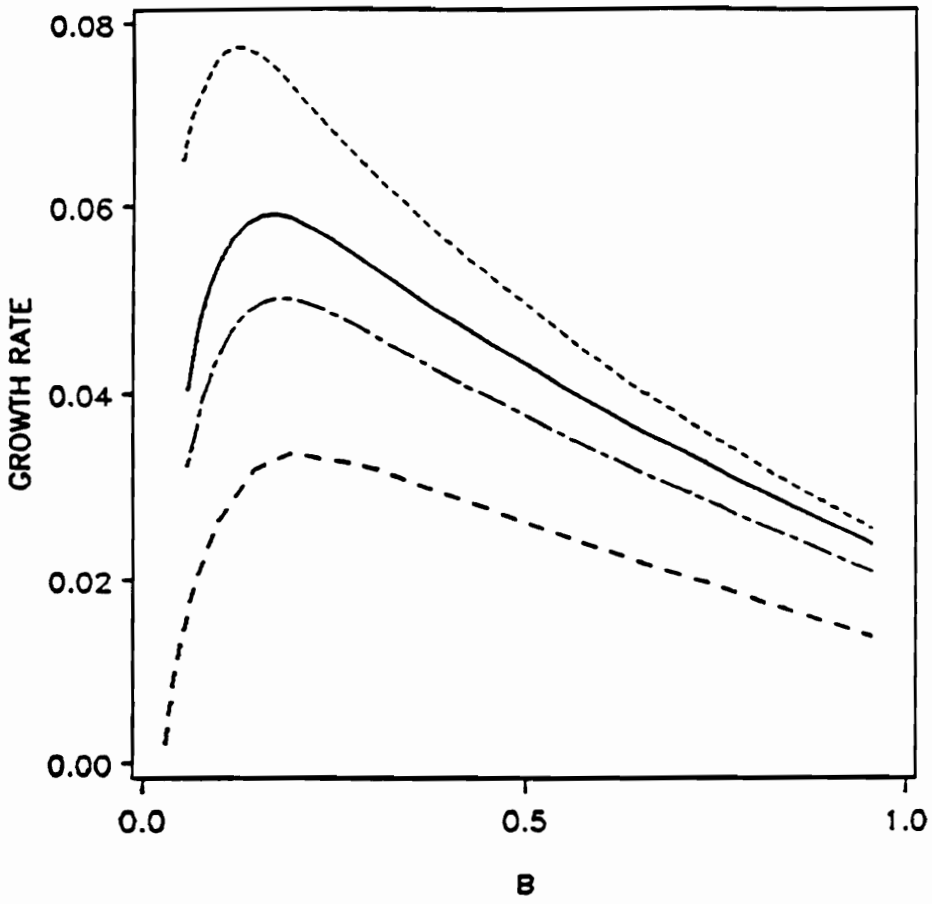

Figure 3.9. Variation of the subharmonic growth rate γ with spanwise wavenumber at R = 1049, $F_{2D} = 83x10^{-6}$, $x = 1.1$ and $a_{rms} = 0.01$: (- - -) $\tilde{h} = 0$ (Blasius), (__ . __ .) $\tilde{h} = 1.5$, (____) $\tilde{h} = 2$, and (...) $\tilde{h} = 3$.

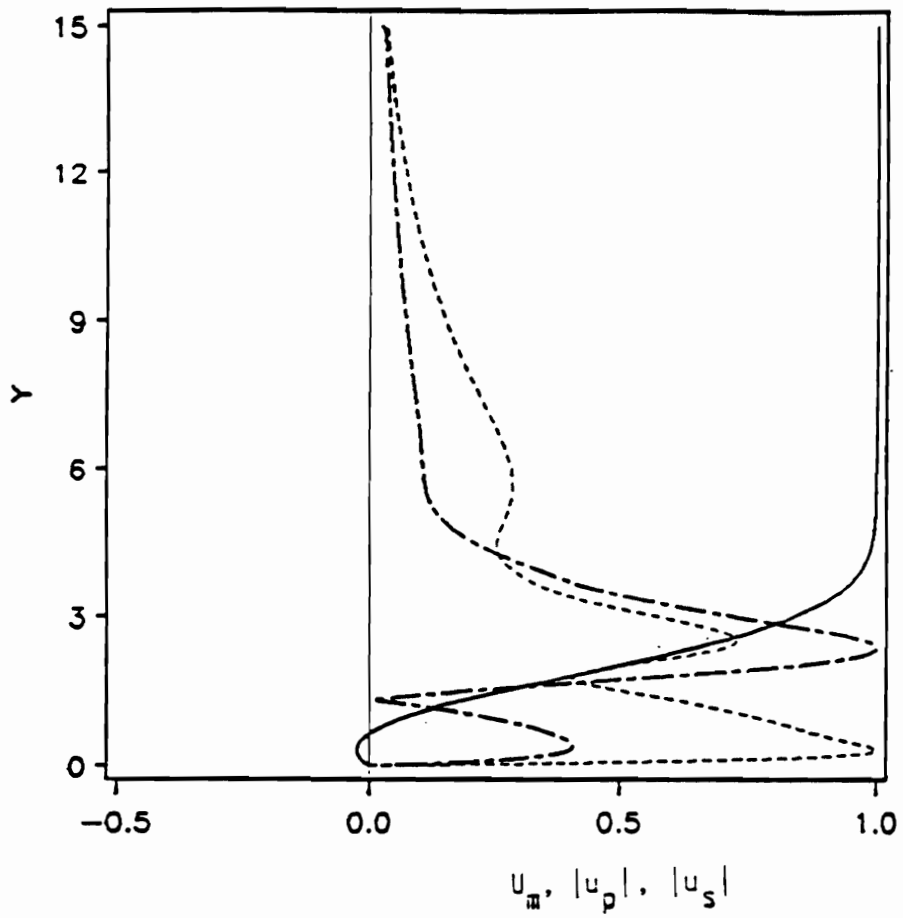

Figure 3.10. (___) Meanflow profile U(y), (...) $|u'(y)|$ for primary wave, and (__ . __ .) $|u'(y)|$ for subharmonic wave: $\tilde{h} = 3, R = 1049, x = 1.1, a_{rms} = 0.01$, and $B = 0.124$.

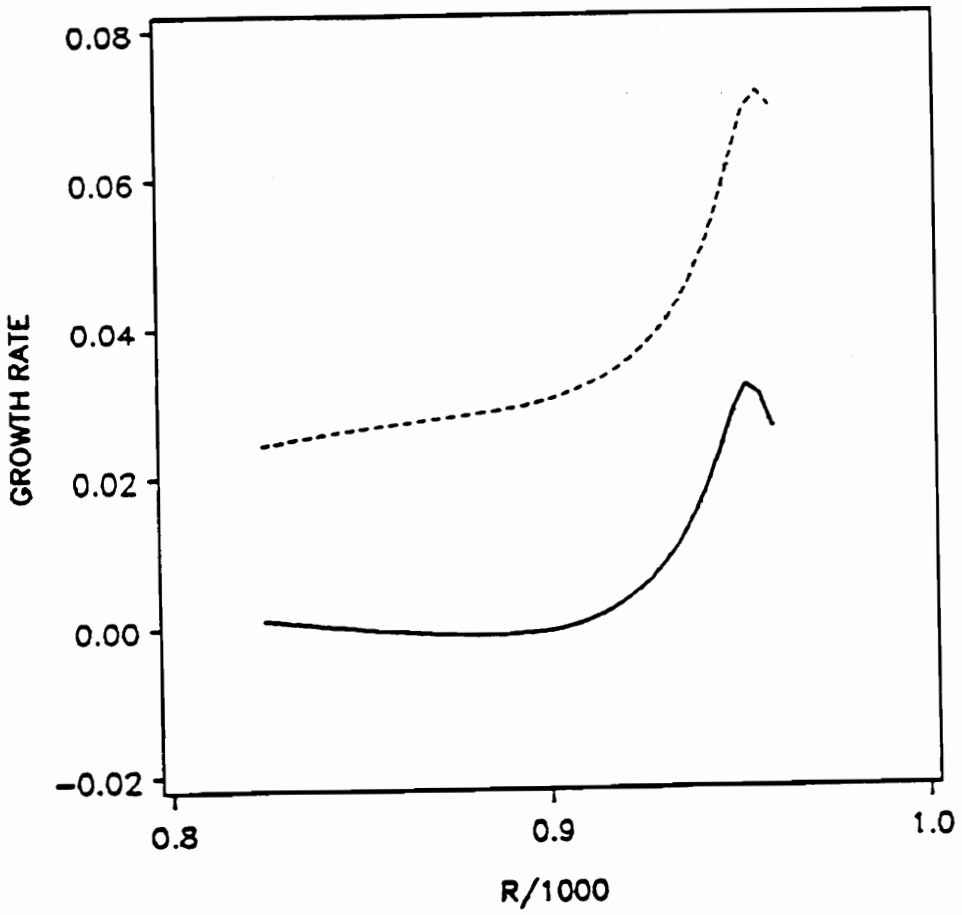

Figure 3.11. Streamwise variation of the growth rate for (___) primary wave ($-\alpha_i$) and (...) subharmonic wave: $\tilde{h} = 5$, $F_{2D} = 83x10^{-6}$, $B = 0.218$, and $a_{rms} = 0.01$ at the initial station x = 0.68.

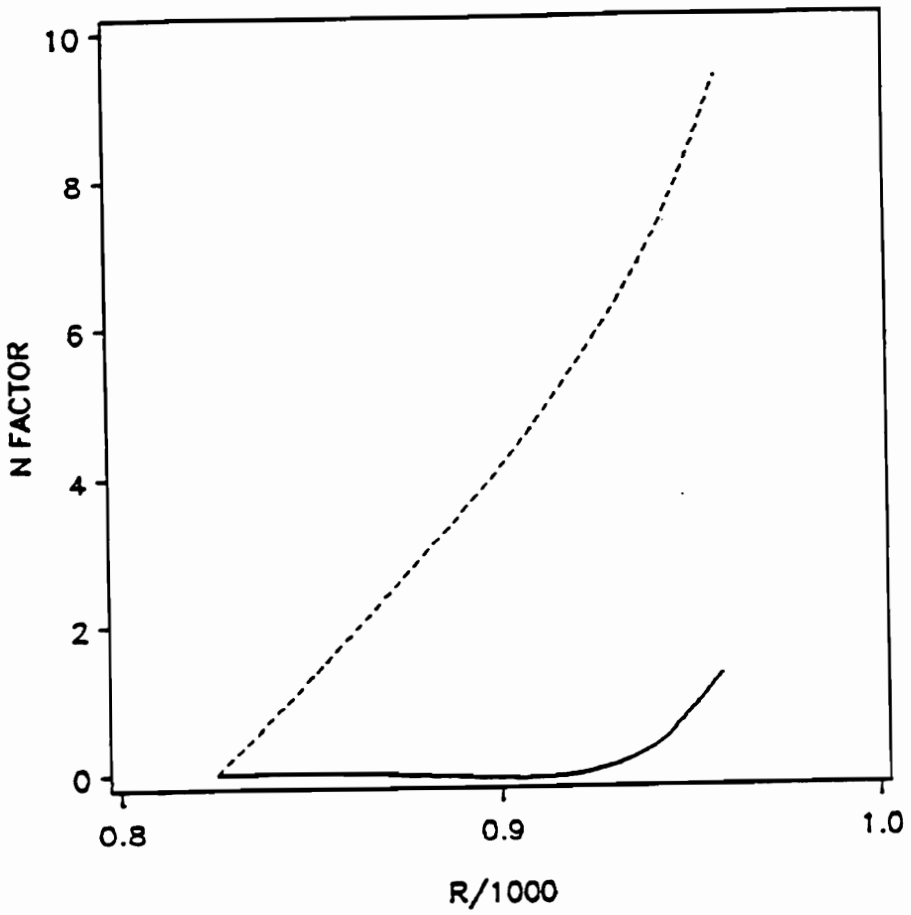

Figure 3.12. Streamwise variation of the amplification factor for (___) primary wave and (...) subharmonic wave: conditions as in figure 3.11.

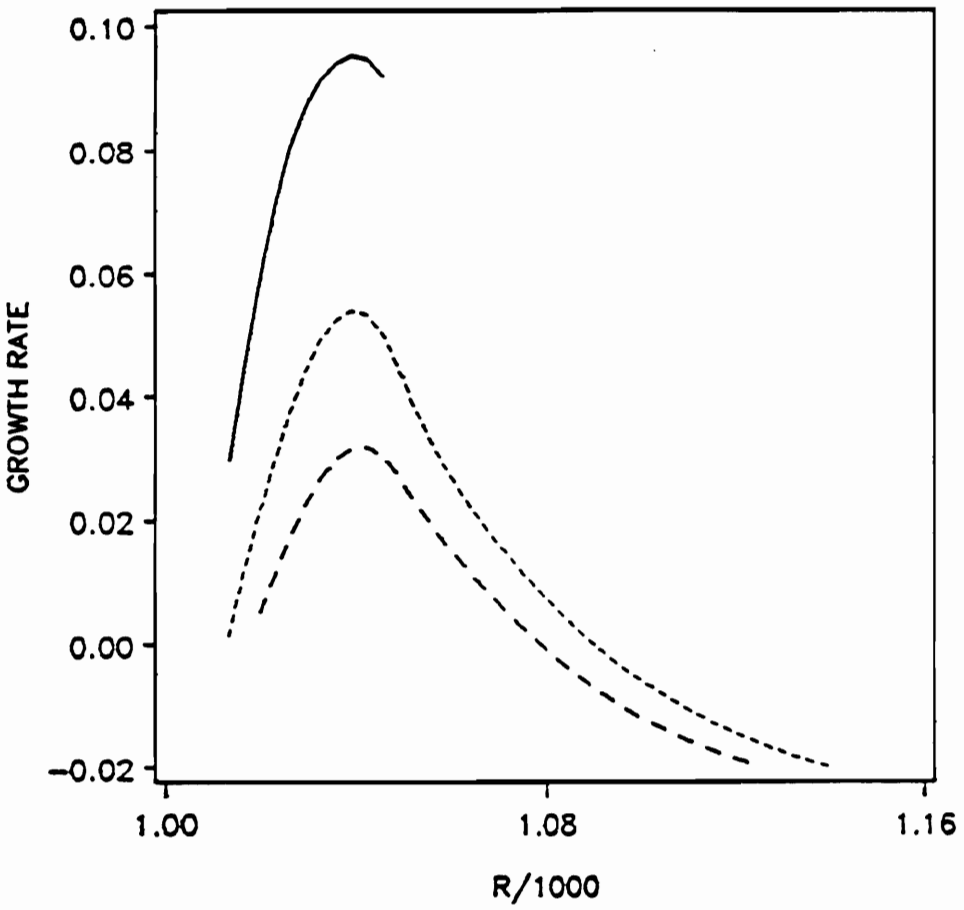

Figure 3.13. Streamwise variation of the growth rate for $-\alpha_i$ of the primary wave at $F_{2D} = 83\text{x}10^{-6}$: (- - -) $\tilde{h} = 1.5$, (...) $\tilde{h} = 2$, and (___) $\tilde{h} = 3$.

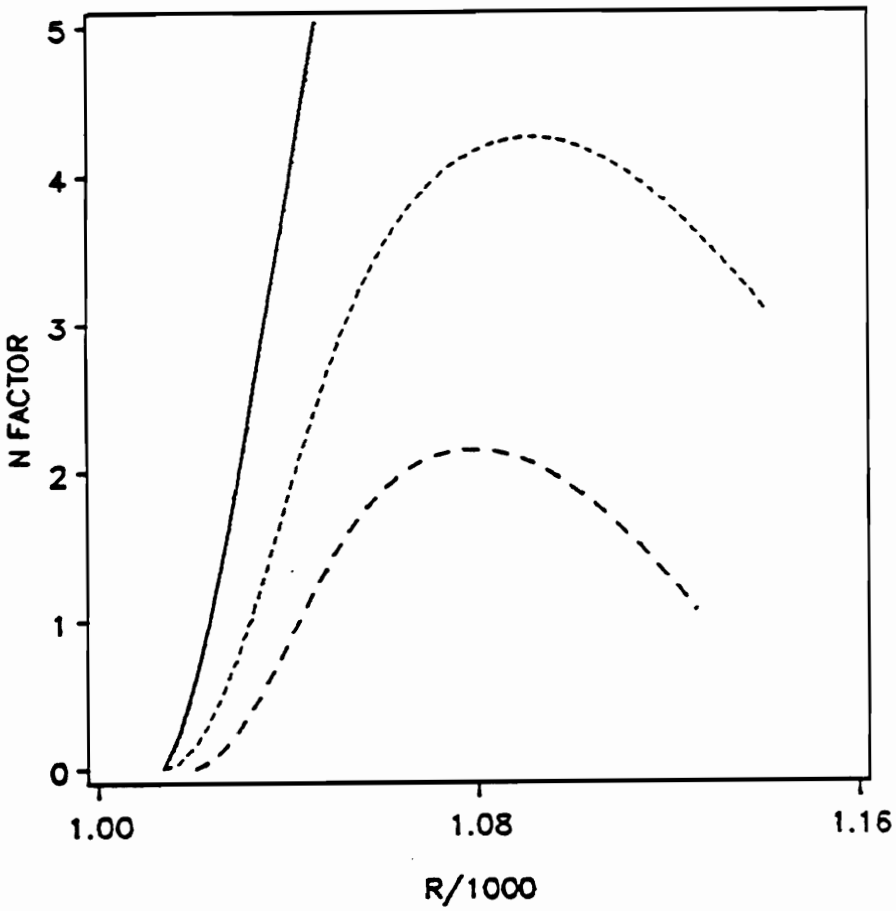

Figure 3.14. Streamwise variation of the amplification factor of the primary wave at $F_{2D} = 83x10^{-6}$: (- - -) $\tilde{h} = 1.5$, (...) $\tilde{h} = 2$, and (___) $\tilde{h} = 3$.

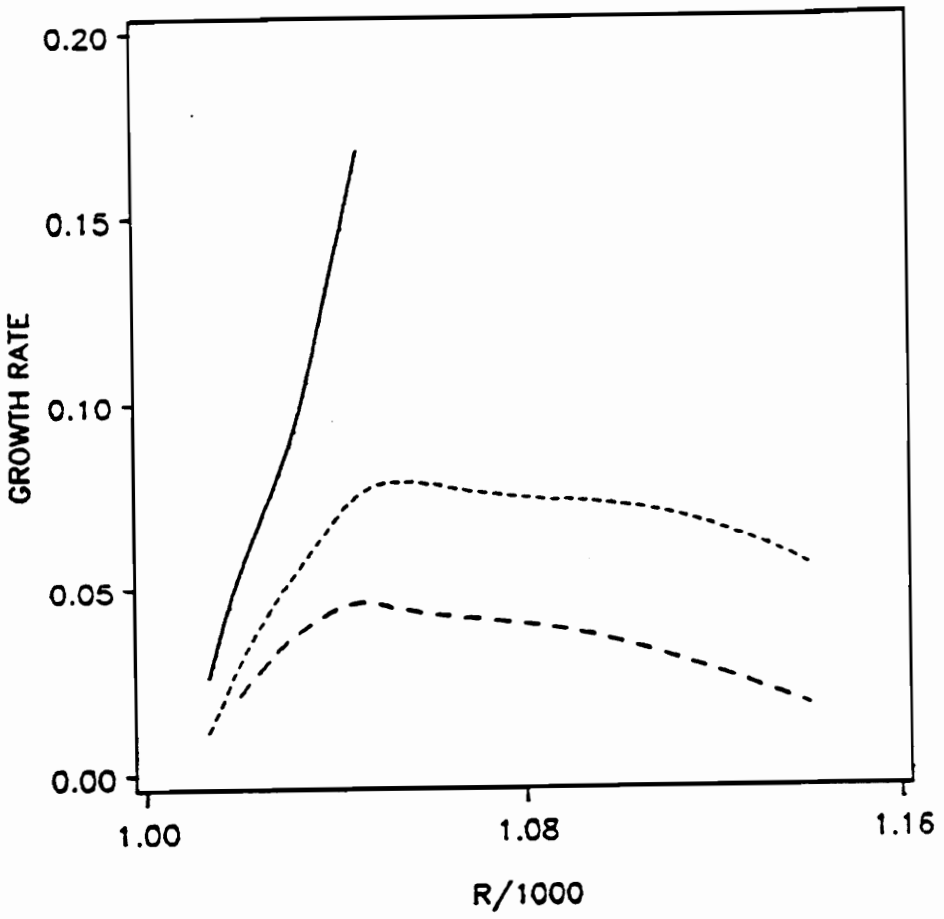

Figure 3.15. Streamwise variation of the growth rate of the subharmonic wave for B = 0.128, $F_{2D} = 83x10^{-6}$, and $a_{rms} = 0.002$ at the initial station x = 1.03: (- - -) $\tilde{h} = 1.5$, (...) $\tilde{h} = 2$, and (___) $\tilde{h} = 3$.

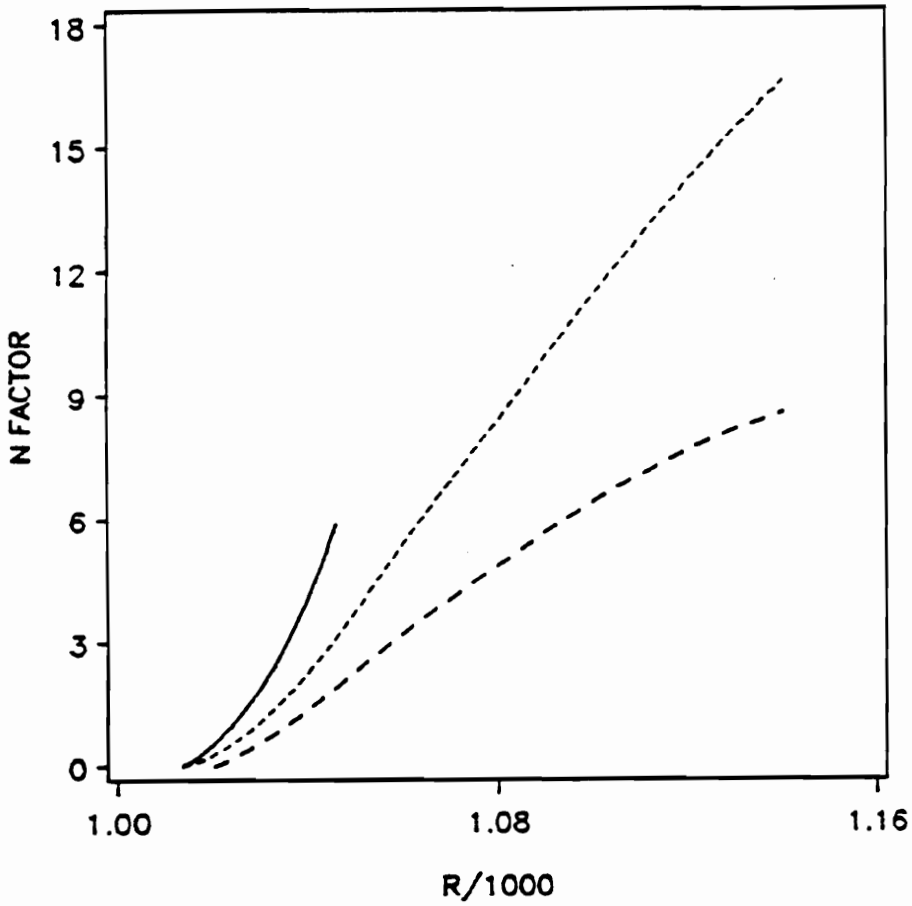

Figure 3.16. Streamwise variation of the amplification factor $\ell n(A/A_0)$ of the subharmonic wave: conditions as in figure 3.15.

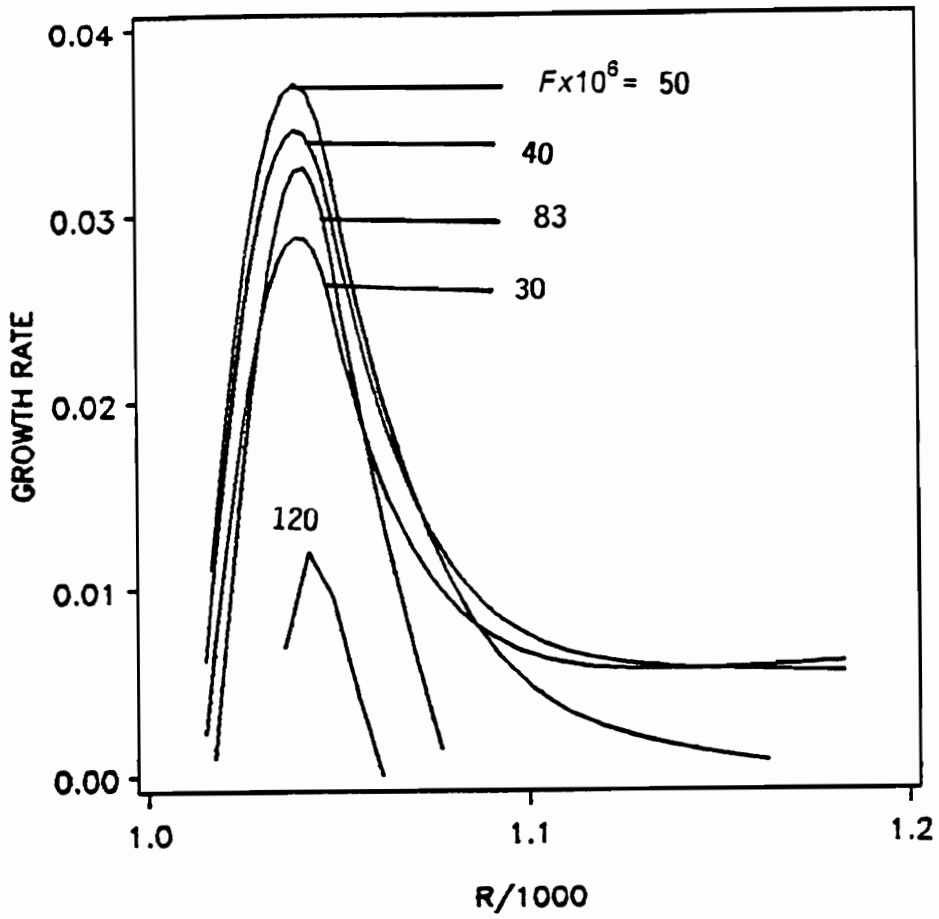

Figure 3.17. Streamwise variation of the growth rate $-\alpha_i$ of the primary wave for the small hump $\tilde{h} = 1.5$ for several frequencies.

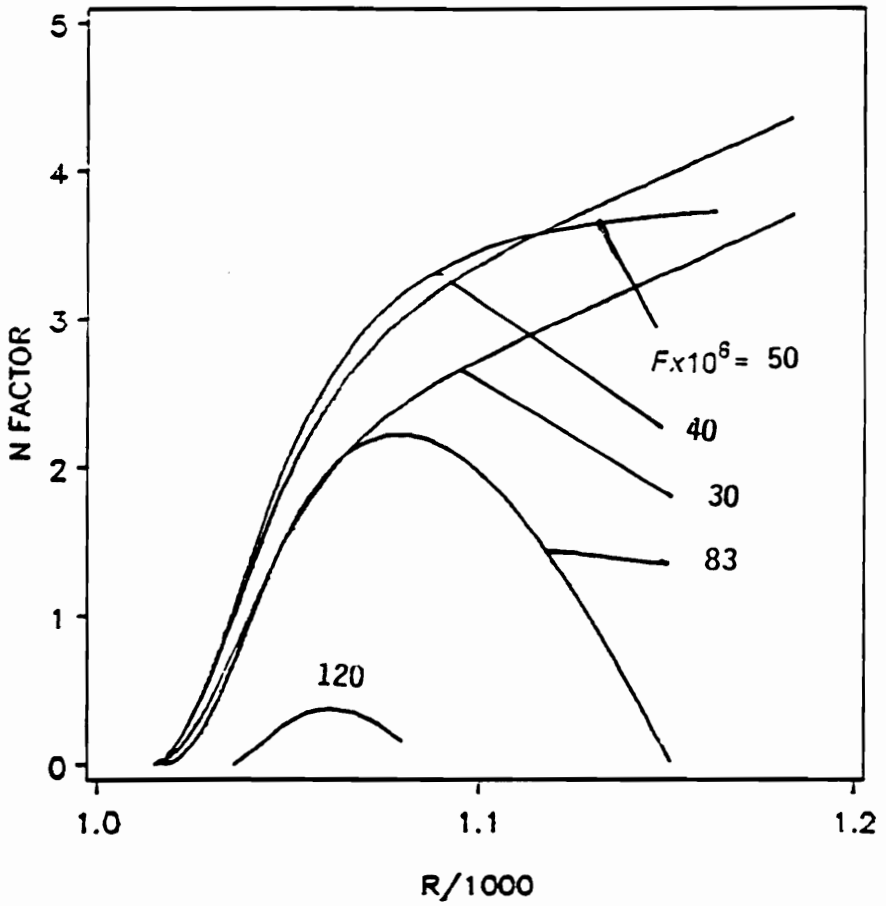

Figure 3.18. Streamwise variation of the amplification factor of the primary wave for the small hump $\tilde{h} = 1.5$ for several frequencies.

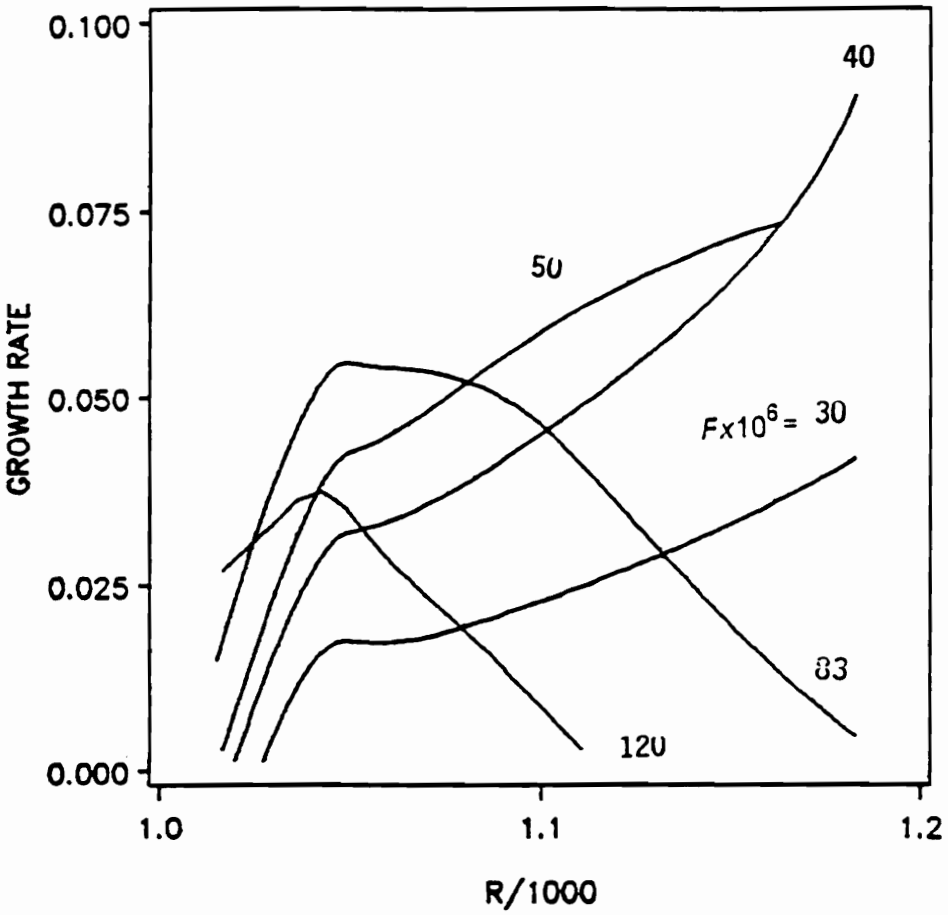

Figure 3.19. Streamwise variation of the growth rate of the subharmonic wave for $\tilde{h} = 1.5$ for several frequencies when B = 0.2 and $a_{rms} = 0.003$ at the initial location x = 1.03.

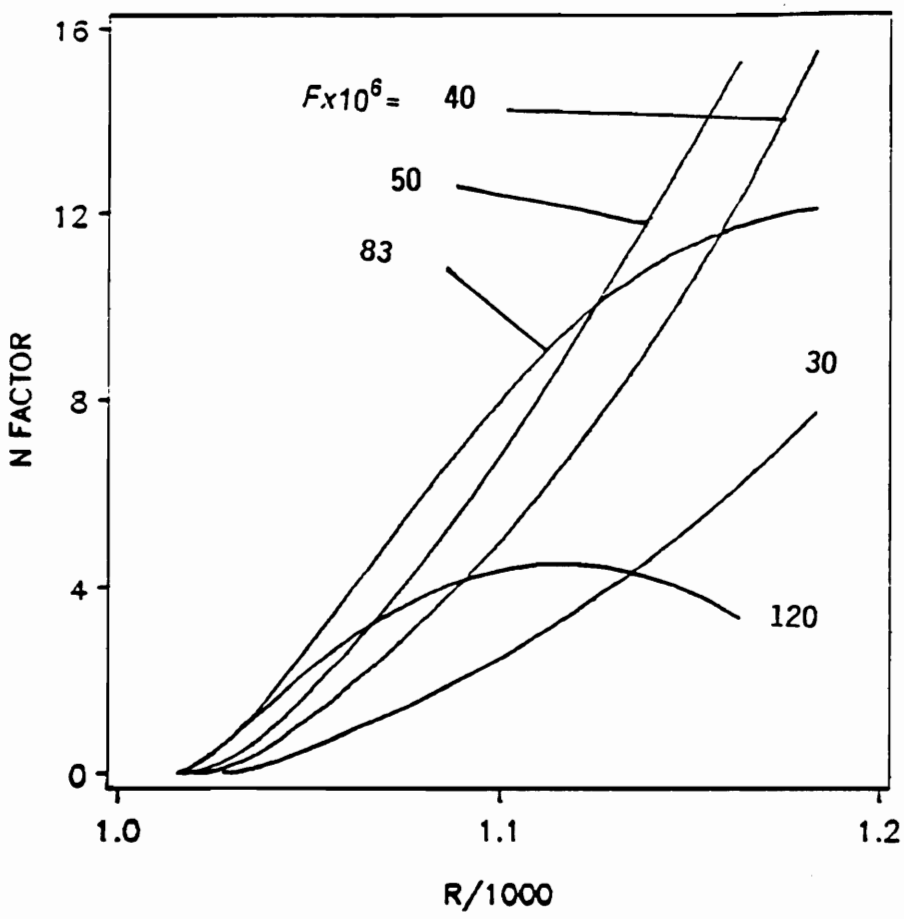

Figure 3.20. Streamwise variation of the amplification factor of the subharmonic wave for $\tilde{h} = 1.5$ for several frequencies when B = 0.2 and $a_{rms} = 0.003$ at the initial location x = 1.03.

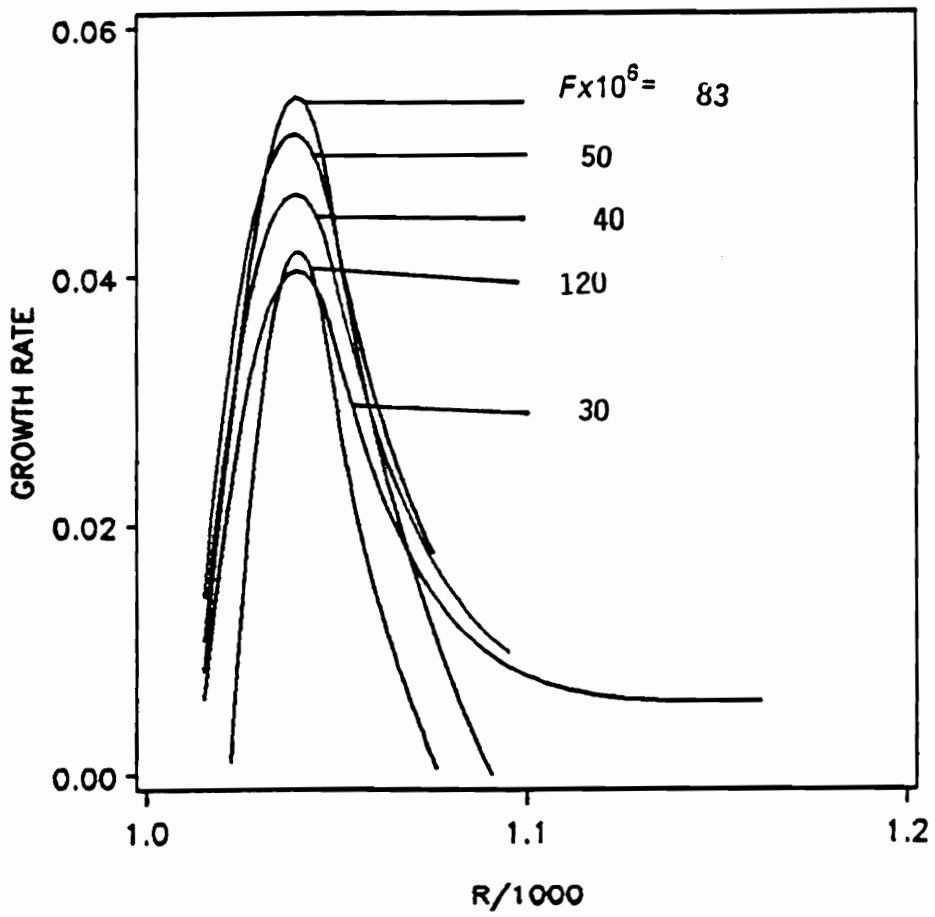

Figure 3.21. Streamwise variation of the growth rate $-\alpha_i$ of the primary wave for the small hump $\tilde{h} = 2$ for several frequencies.

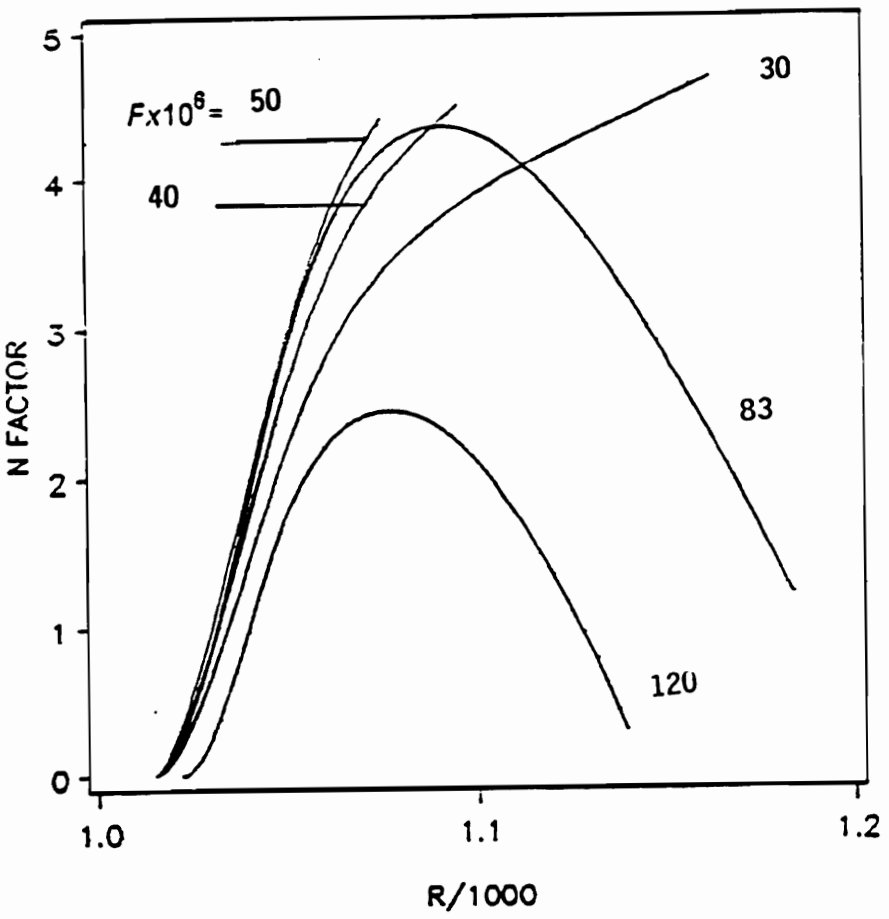

Figure 3.22. Streamwise variation of the amplification factor of the primary wave for $\tilde{h} = 2$ for several frequencies.

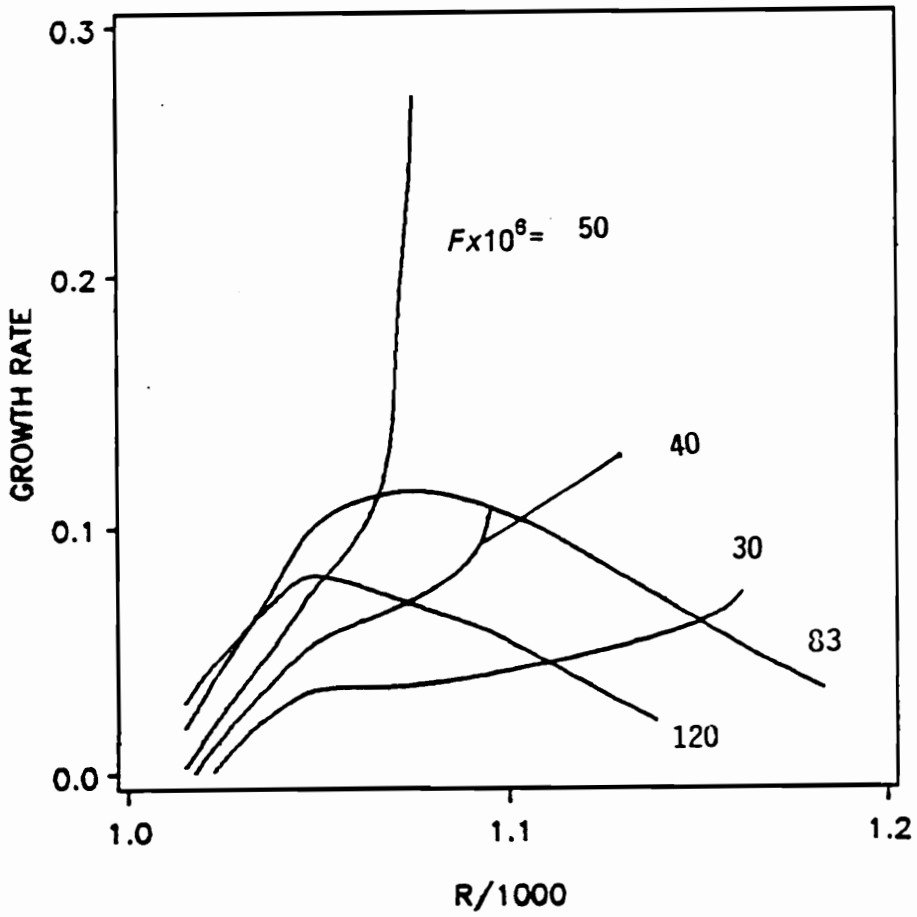

Figure 3.23. Streamwise variation of the growth rate of the subharmonic wave for $\tilde{h} = 2$ for several frequencies when B = 0.2 and $a_{rms} = 0.003$ at the initial location x = 1.03.

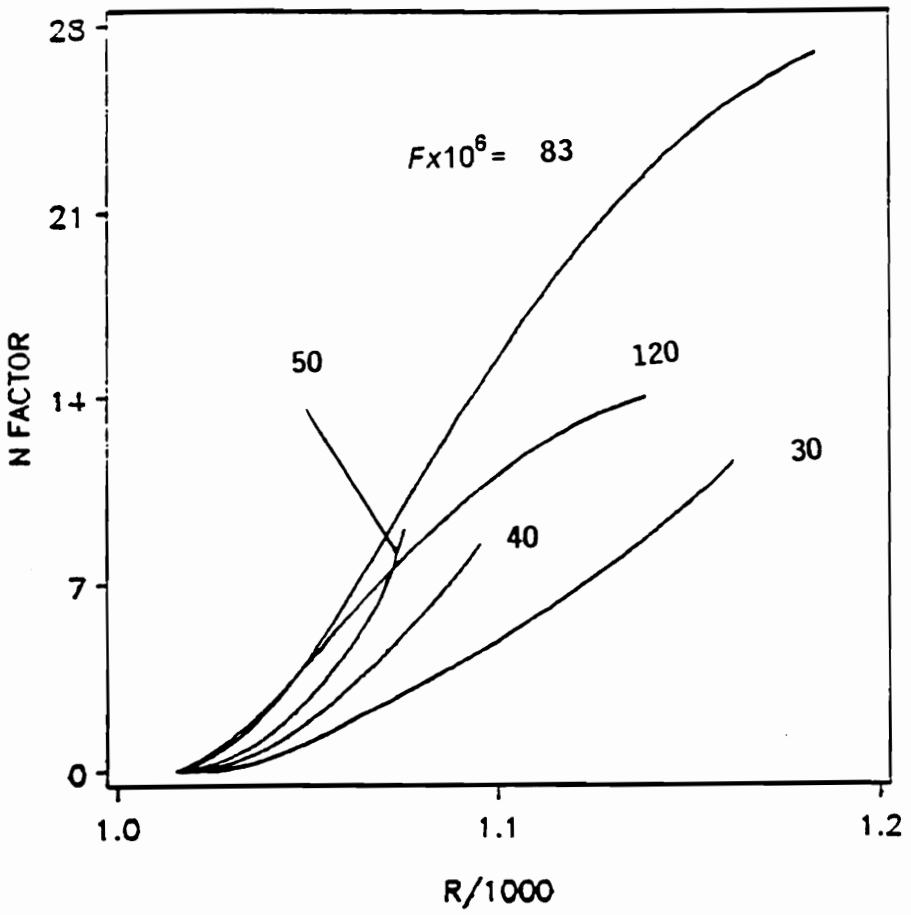

Figure 3.24. Streamwise variation of the amplification factor of the subharmonic wave for $\tilde{h} = 2$ for several frequencies when B = 0.2 and $a_{rms} = 0.003$ at the initial location x = 1.03.

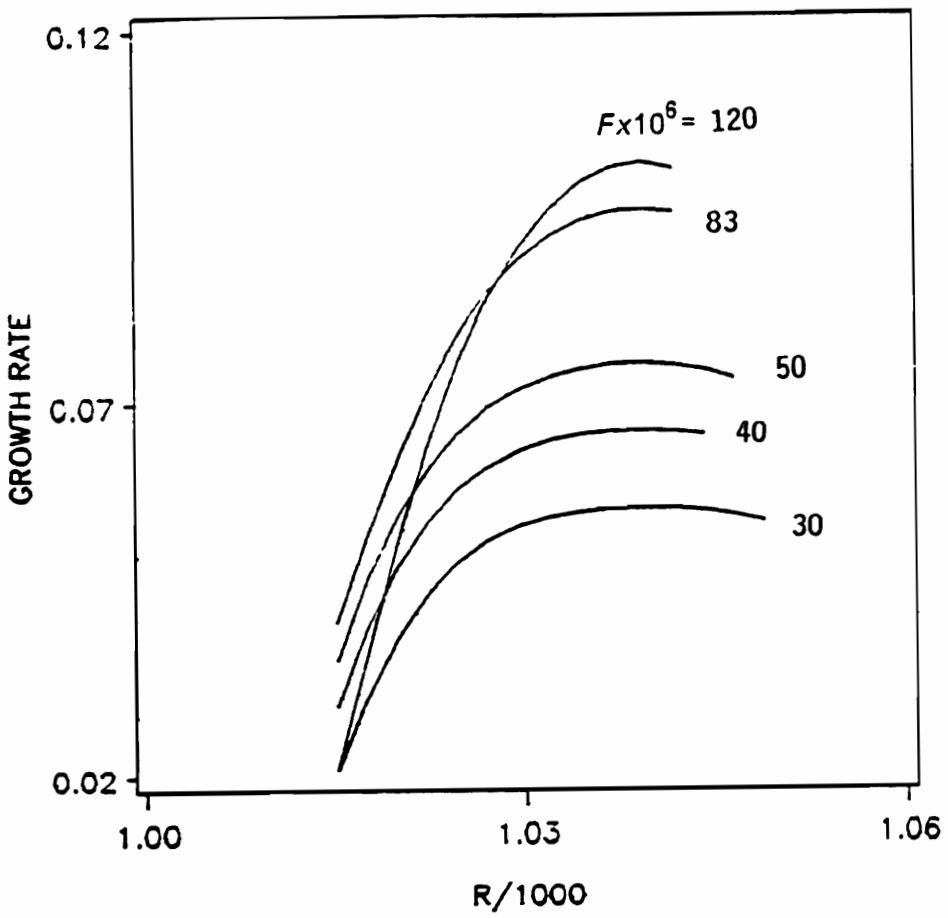

Figure 3.25. Streamwise variation of the growth rate $-\alpha_i$ of the primary wave for the small hump $\tilde{h} = 3$ for several frequencies.

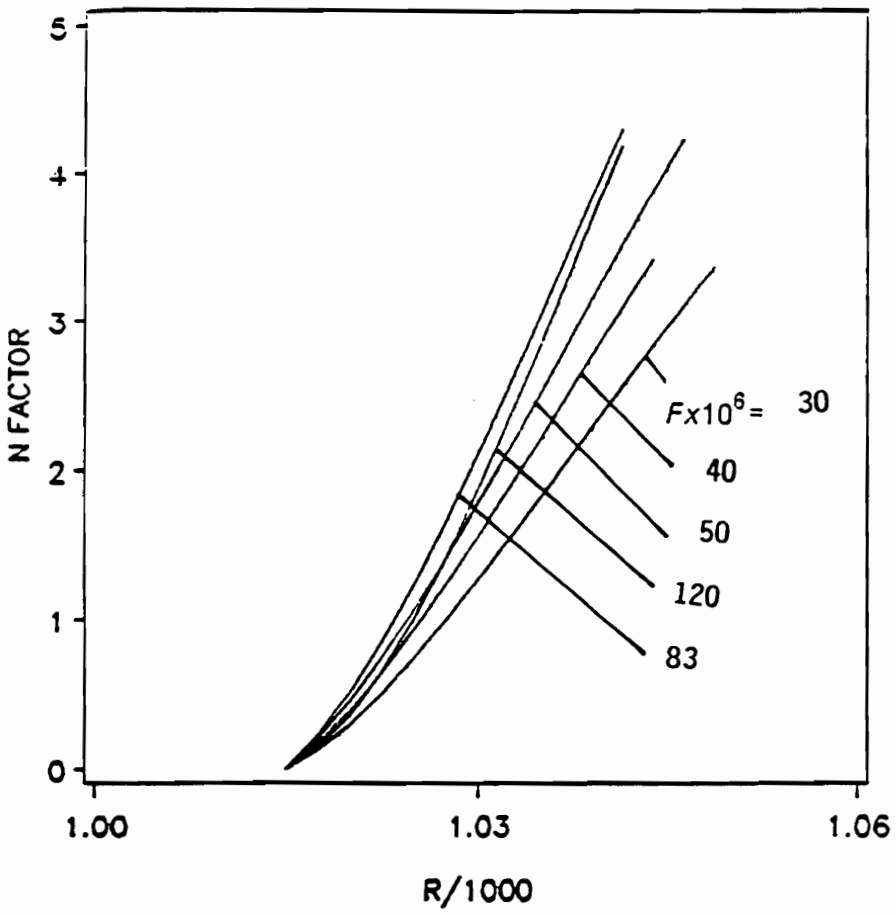

Figure 3.26. Streamwise variation of the amplification factor of the primary wave for $\tilde{h} = 3$ for several frequencies.

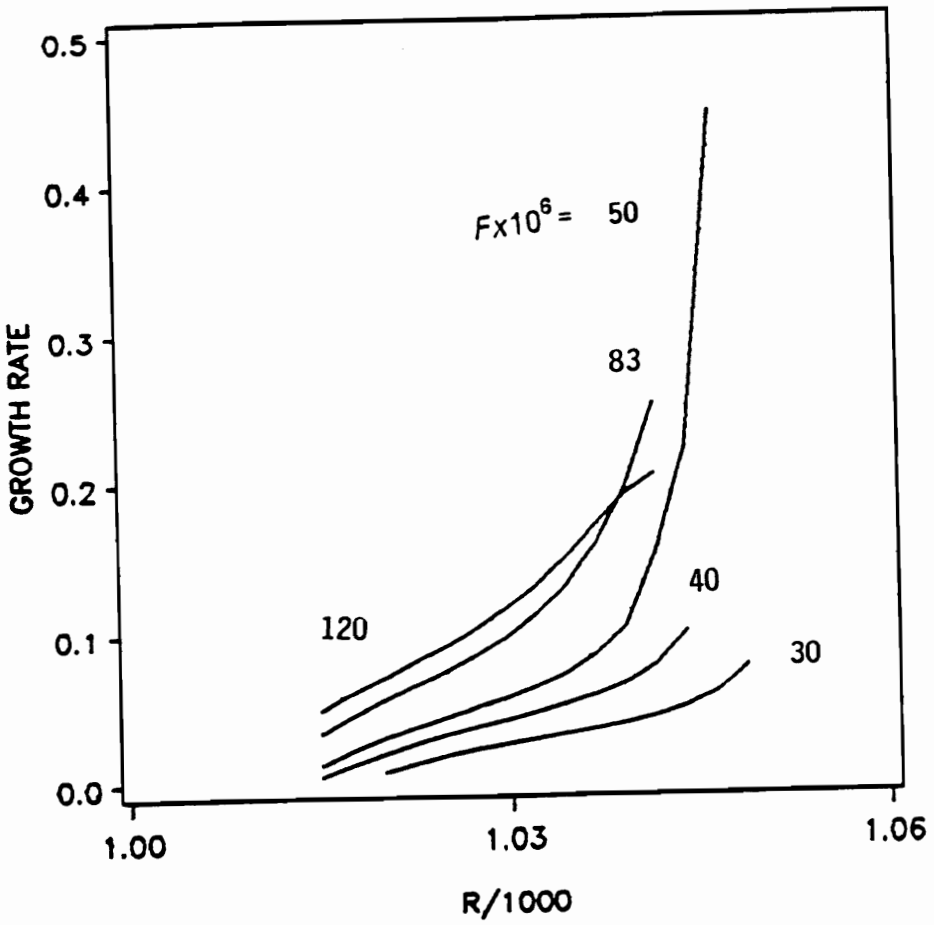

Figure 3.27. Streamwise variation of the growth rate of the subharmonic wave for $\tilde{h} = 3$ for several frequencies when B = 0.2 and $a_{rms} = 0.003$ at the initial location x = 1.03.

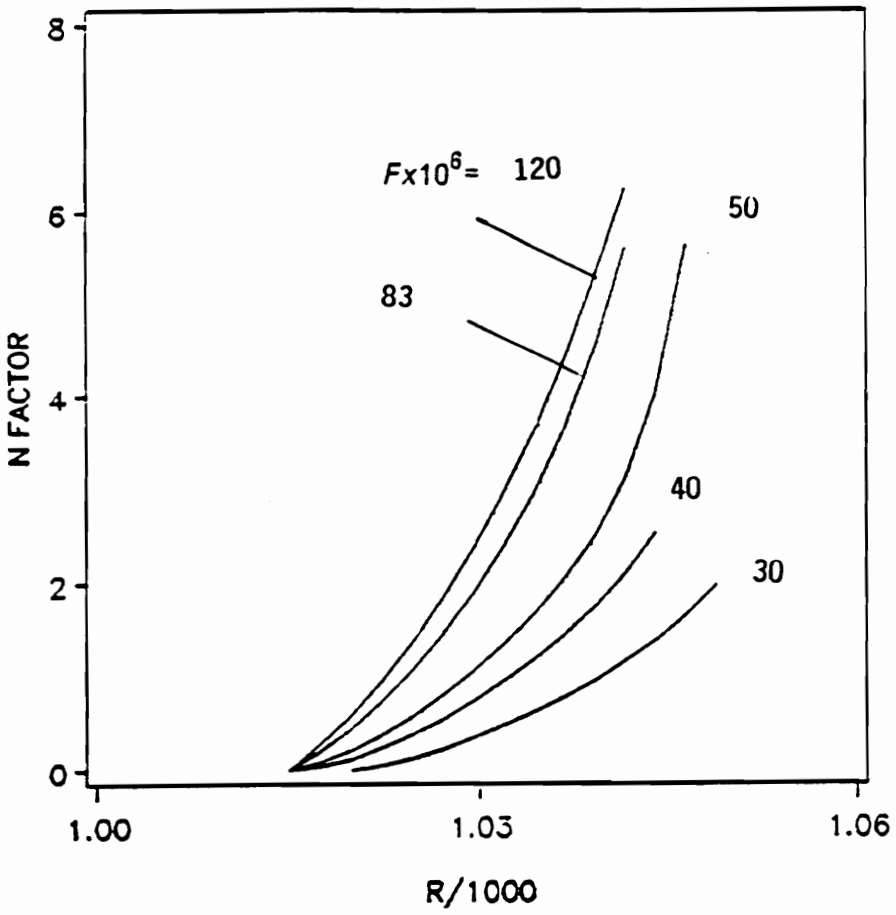

Figure 3.28. Streamwise variation of the amplification factor of the subharmonic wave for $\tilde{h} = 3$ for several frequencies when B = 0.2 and $a_{rms} = 0.003$ at the initial location x = 1.03.

4. SUBHARMONIC INSTABILITY IN COMPRESSIBLE BOUNDARY LAYERS OVER AN ADIABATIC FLAT PLATE

The subharmonic instability of a 2-D compressible boundary layer over an insulated flat plate is analyzed using the Floquet model. The resulting problem is solved numerically by using both finite differences and the computer code SUPORT. Results are presented for subsonic, transonic, and supersonic flows. For supersonic flows results for the first and second modes are presented. The effects of Mach number, spanwise wavenumber, amplitude of the primary wave, Reynolds number, and frequency are studied.

4.1. Formulation

We consider a 3-D unsteady quasiparallel disturbance represented by the quantities q imposed on a 2-D basic flow represented by the quantities q_b. Substituting the total-flow quantities into the Navier-Stokes equations, subtracting the basic state, and linearizing, we find to first order that the disturbance equations are given by

$$\frac{\partial \rho}{\partial t} + \frac{\partial}{\partial x}(\rho_b u + \rho u_b) + \frac{\partial}{\partial y}(\rho_b v + \rho v_b) + \frac{\partial}{\partial z}(\rho_b w) = 0 \tag{4.1}$$

$$\begin{aligned}
\rho_b\Big(\frac{\partial u}{\partial t} + u_b \frac{\partial u}{\partial x} + u \frac{\partial u_b}{\partial x} + v_b \frac{\partial u}{\partial y} + v \frac{\partial u_b}{\partial y} \\
+ w \frac{\partial u_b}{\partial z} \Big) + \rho\Big(\frac{\partial u_b}{\partial t} + u_b \frac{\partial u_b}{\partial x} + v_b \frac{\partial u_b}{\partial y} \Big) = \\
- \frac{\partial p}{\partial x} + \frac{1}{R}\Big\{ \frac{\partial}{\partial x}\Big[\mu_b\Big(r \frac{\partial u}{\partial x} + m \frac{\partial v}{\partial y} + m \frac{\partial w}{\partial z} \Big) \\
+ \mu\Big(r \frac{\partial u_b}{\partial x} + m \frac{\partial v_b}{\partial y} \Big)\Big] + \frac{\partial}{\partial y}\Big[\mu_b\Big(\frac{\partial u}{\partial y} + \frac{\partial v}{\partial x} \Big) \\
+ \mu\Big(\frac{\partial u_b}{\partial y} + \frac{\partial v_b}{\partial x} \Big)\Big] + \frac{\partial}{\partial z}\Big[\mu_b\Big(\frac{\partial w}{\partial x} + \frac{\partial u}{\partial z} \Big)\Big]\Big\}
\end{aligned} \tag{4.2}$$

$$\rho_b\left(\frac{\partial v}{\partial t}+u_b\frac{\partial v}{\partial x}+u\frac{\partial v_b}{\partial x}+v_b\frac{\partial v}{\partial y}+v\frac{\partial v_b}{\partial y}\right)$$
$$+\rho\left(\frac{\partial v_b}{\partial t}+u_b\frac{\partial v_b}{\partial x}+v_b\frac{\partial v_b}{\partial y}\right)=-\frac{\partial p}{\partial y}$$
$$+\frac{1}{R}\left\{\frac{\partial}{\partial x}\left[\mu_b\left(\frac{\partial u}{\partial y}+\frac{\partial v}{\partial x}\right)+\mu\left(\frac{\partial u_b}{\partial y}+\frac{\partial v_b}{\partial x}\right)\right]\right. \tag{4.3}$$
$$+\frac{\partial}{\partial y}\left[\mu_b\left(m\frac{\partial u}{\partial x}+r\frac{\partial v}{\partial y}+m\frac{\partial w}{\partial z}\right)+\mu\left(m\frac{\partial u_b}{\partial x}+r\frac{\partial v_b}{\partial y}\right)\right]$$
$$\left.+\frac{\partial}{\partial z}\left[\mu_b\left(\frac{\partial v}{\partial z}+\frac{\partial w}{\partial y}\right)\right]\right\}$$

$$\rho_b\left(\frac{\partial w}{\partial t}+u_b\frac{\partial w}{\partial x}+v_b\frac{\partial w}{\partial y}\right)=-\frac{\partial p}{\partial z}$$
$$+\frac{1}{R}\left\{\frac{\partial}{\partial x}\left[\mu_b\left(\frac{\partial w}{\partial x}+\frac{\partial u}{\partial z}\right)\right]+\frac{\partial}{\partial y}\left[\mu_b\left(\frac{\partial v}{\partial z}+\frac{\partial w}{\partial y}\right)\right]\right. \tag{4.4}$$
$$\left.+\frac{\partial}{\partial z}\left[\mu_b\left(m\frac{\partial u}{\partial x}+m\frac{\partial v}{\partial y}+r\frac{\partial w}{\partial z}\right)\right]+\frac{\partial}{\partial z}\left[\mu\left(m\frac{\partial u_b}{\partial x}+m\frac{\partial v_b}{\partial y}\right)\right]\right\}$$

$$\rho_b\left[\frac{\partial T}{\partial t}+u\frac{\partial T_b}{\partial x}+u_b\frac{\partial T}{\partial x}+v\frac{\partial T_b}{\partial y}+v_b\frac{\partial T}{\partial y}\right]$$
$$+\rho\left[\frac{\partial T_b}{\partial t}+u_b\frac{\partial T_b}{\partial x}+v_b\frac{\partial T_b}{\partial y}\right]=(\gamma-1)M_\infty^2\left[\frac{\partial p}{\partial t}\right.$$
$$+u\frac{\partial p_b}{\partial x}+u_b\frac{\partial p}{\partial x}+v\frac{\partial p_b}{\partial y}+v_b\frac{\partial p}{\partial y} \tag{4.5}$$
$$\left.+\frac{1}{R}\phi\right]+\frac{1}{RPr}\left\{\frac{\partial}{\partial x}\left(\mu_b\frac{\partial T}{\partial x}+\mu\frac{\partial T_b}{\partial x}\right)\right.$$
$$\left.+\frac{\partial}{\partial y}\left(\mu_b\frac{\partial T}{\partial y}+\mu\frac{\partial T_b}{\partial y}\right)+\frac{\partial}{\partial z}\left(\mu_b\frac{\partial T}{\partial z}\right)\right\}$$

$$p=\frac{1}{\gamma M_\infty^2}(\rho_b T+T_b\rho) \tag{4.6}$$

where γ is the gas specific heat ratio and ϕ is the perturbation dissipation function defined by

$$\begin{aligned}\phi = \mu_b \Bigg\{ & 2r\left(\frac{\partial u_b}{\partial x}\frac{\partial u}{\partial x} + \frac{\partial v_b}{\partial y}\quad\frac{\partial v}{\partial y} \right) \\ & + 2m\left[\frac{\partial u_b}{\partial x}\left(\frac{\partial v}{\partial y} + \frac{\partial w}{\partial z} \right) + \frac{\partial v_b}{\partial y}\left(\frac{\partial u}{\partial x} + \frac{\partial w}{\partial z} \right) \right] \\ & + 2\left(\frac{\partial u}{\partial y} + \frac{\partial v}{\partial x} \right)\left(\frac{\partial u_b}{\partial y} + \frac{\partial v_b}{\partial x} \right) \Bigg\} \\ & + \mu \Bigg\{ r\left[\left(\frac{\partial u_b}{\partial x} \right)^2 + \left(\frac{\partial v_b}{\partial y} \right)^2 \right] \\ & + 2m\frac{\partial u_b}{\partial x}\frac{\partial v_b}{\partial y} + \left(\frac{\partial u_b}{\partial y} + \frac{\partial v_b}{\partial x} \right)^2 \Bigg\}\end{aligned} \tag{4.7}$$

The constants r and m are given by

$$r = m + 2 \text{ and } m = \frac{\lambda}{\mu} \tag{4.8}$$

where λ is the second coefficient of viscosity. The Reynolds number R and Prandtl number Pr are given by

$$R = \frac{U_\infty^* \delta_r^*}{\nu_\infty^*}, \quad Pr = \frac{\mu_\infty^* C_p^*}{\kappa_\infty^*} \tag{4.9}$$

where ν_∞^*, μ_∞^*, and κ_∞^* are the freestream kinematic viscosity, dynamic viscosity, and thermal conductivity, respectively, and C_p^* is the dimensional specific heat at constant pressure. In the above equations, distances, velocities, the time, and the pressure are made dimensionless by using $\delta_r^* = \sqrt{\nu_\infty^* L^* / U_\infty^*}$, U_∞^*, δ_r^*/U_∞^*, and $\rho_\infty^* U_\infty^{*2}$, where L^* is the distance from the leading edge of the plate to a reference point. The temperature,

density, specific heats, viscosity, and thermal conductivity are made dimensionless by using their corresponding freestream values. The gas is assumed to be perfect. Because the pressure is constant across the boundary layer,

$$\rho_m T_m = 1 \text{ and } P_m = \frac{1}{\gamma M_\infty^2} \tag{4.10}$$

where the subscript m refers to mean-flow quantities and M_∞ is the freestream Mach number. We assume that the dynamic viscosity is a function of temperature only so that

$$\mu = \frac{d\mu_b}{dT}\bigg|_{T_b} T \tag{4.11}$$

The boundary conditions at the wall are

$$u = v = w = T = 0 \text{ at } y = 0 \tag{4.12}$$

and the boundary conditions as $y \to \infty$ are

$$u, v, w, p, \text{ and } T \text{ are bounded as } y \to \infty \tag{4.13}$$

4.2. The Mean Flow

The mean flow is a 2-D steady flow over an insulated flat plate. It is governed by

$$\frac{d}{d\eta}\left(\rho\mu\frac{du}{d\eta}\right)+g\frac{du}{d\eta}=0 \tag{4.14}$$

$$\frac{1}{Pr}\frac{d}{d\eta}\left(\rho\mu\frac{dT}{d\eta}\right)+g\frac{dT}{d\eta}+(\gamma-1)M_\infty^2\rho\mu\left(\frac{du}{d\eta}\right)^2=0 \tag{4.15}$$

where

$$\eta=\sqrt{\frac{Re}{x}}\int_0^y\rho dy\,,\quad Re=\frac{U_\infty^{\cdot}L^{\cdot}}{\nu_\infty^{\cdot}}\,,\quad g=V_w+\frac{1}{2}\int_0^\eta u d\eta \tag{4.16}$$

and V_w is the suction velocity. It is positive for suction and negative for blowing. The boundary conditions as $\eta\to\infty$ are

$$u\to 1 \quad \text{and} \quad T\to 1 \quad \text{as} \quad \eta\to\infty \tag{4.17}$$

At the wall, the boundary conditions for an adiabatic wall are

$$u=0,\frac{dT}{d\eta}=0 \ \text{and} \ g=V_w \ \text{at} \ \eta=0 \tag{4.18}$$

whereas in the case of heat transfer we have

$$u=0,\ g=V_w \ \text{and} \ \frac{T_w}{T_{ad}} \ \text{is specified at} \ \eta=0 \tag{4.19}$$

where T_w is the wall temperature and T_{ad} is the adiabatic wall temperature. In this Chapter we present results for an impermeable, adiabatic wall. In Chapter 5 we present results for impermeable wall with heat transfer, whereas in Chapter 6 we present results for an adiabatic wall with suction.

4.3. Primary Instability

We take the primary instability to be a linear 2-D quasiparallel T-S wave. To calculate this wave, we let $u_b = U_m(y)$, $v_b = 0$, $T_b = T_m(y)$, $\rho_b = \rho_m(y)$, and $\mu_b = \mu_m(y)$. Then, we seek a solution of Eqs. (4.1)-(4.7), (4.12), and (4.13) in the form

$$(u,v,p,T) = [\zeta_1(y), \zeta_3(y), \zeta_4(y), \zeta_5(y)]e^{i(\int \alpha dx - \omega t)} \tag{4.20}$$

For the case of spatial stability, the frequency ω is real and $\alpha = \alpha_r + i\alpha_i$ is complex with α_r being the streamwise wavenumber and $-\alpha_i$ being the growth rate of the primary wave. Substituting Eq. (4.20) into Eqs. (4.1)-(4.7), (4.12), and (4.13), we obtain a set of equations and boundary conditions governing ζ_1, ζ_3, ζ_4, and ζ_5. These equations can be recast into the following set of six coupled first-order ordinary-differential equations:

$$D\zeta_n - \sum_{m=1}^{6} a_{nm}\zeta_m = 0, \; n = 1, 2, \ldots, 6 \tag{4.21}$$

where $D = d/dy$, $\zeta_2 = D\zeta_1$, $\zeta_6 = D\zeta_5$, and the coefficients a_{nm} are defined in Appendix D. The boundary conditions are

$$\zeta_1 = \zeta_3 = \zeta_5 = 0 \text{ at } y = 0 \tag{4.22}$$

$$\zeta_n \text{ are bounded as } y \to \infty \tag{4.23}$$

Whereas neutral subsonic disturbances are unique in the case of incompressible flows, they are unique in the case of compressible flows only when the mean flow

relative to the phase velocity is everywhere subsonic. Using extensive numerical calculations, Mack (1984) showed that there are an infinite number of neutral wavenumbers or modes having the same phase velocity if the mean flow relative to the phase velocity is supersonic somewhere in the boundary layer. The first mode is the same as in incompressible flow and the additional modes (Mack modes) do not have incompressible counterparts. Moreover, whereas the most amplified incompressible modes are 2-D, the most amplified first-mode waves in supersonic boundary layers are 3-D. Mack (1984) also established that the most amplified second-mode waves are 2-D. In our analysis, we present calculations for primary waves that are either 2-D first- or second-mode waves.

4.4. Subharmonic Instability

To formulate the subharmonic instability problem, we take the basic flow as the sum of the mean steady flow and a 2-D quasiparallel T-S wave; that is,

$$u_b = U_m(y) + A\left[\zeta_1(y)e^{i\theta} + cc\right] \tag{4.24}$$

$$v_b = A\left[\zeta_3(y)e^{i\theta} + cc\right] \tag{4.25}$$

$$p_b = P_m + A\left[\zeta_4(y)e^{i\theta} + cc\right] \tag{4.26}$$

$$T_b = T_m(y) + A\left[\zeta_5(y)e^{i\theta} + cc\right] \tag{4.27}$$

$$\frac{\partial\theta}{\partial x} = \alpha_r \text{ and } \frac{\partial\theta}{\partial t} = -\omega \tag{4.28}$$

where cc stands for the complex conjugate of the preceding terms, α_r and ω are real, and A and α_r are approximated locally by constant values. Here, A is the root-mean square (rms) amplitude of the primary wave. Substituting Eqs. (4.24)-(4.28) into Eqs. (4.1)-(4.7), (4.12), and (4.13) yields a system of partial-differential equations whose coefficients are independent of z and periodic in x and t. Consequently, the z-variation can be separated and by using Floquet theory, one can represent the solution of the problem either in the form

$$(u,v,p,T,\rho) = e^{\sigma_x x + \sigma_t t} \cos \beta z(\chi_1, \chi_3, \chi_4, \chi_5, \chi_9) \tag{4.29}$$

$$w = e^{\sigma_x x + \sigma_t t} \sin \beta z(\chi_7) \tag{4.30}$$

or in the form

$$(u,v,p,T,\rho) = e^{\sigma_x x + \sigma_t t} \sin \beta z(\chi_1, \chi_3, \chi_4, \chi_5, \chi_9) \tag{4.31}$$

$$w = e^{\sigma_x x + \sigma_t t} \cos \beta z(\chi_7) \tag{4.32}$$

where σ_x and σ_t are called the characteristic exponents and the χ_n are periodic in x and t. For the subharmonic case, the χ_n have a period that is twice the period of the primary wave. Hence, to the first approximation, Eqs. (4.29) and (4.30) become

$$\begin{aligned}(u,v,p,T,\rho) = e^{\sigma_x x + \sigma_t t} \cos \beta z \Big[&\{\xi_1, \xi_3, \xi_4, \xi_5, \xi_9\} e^{\frac{1}{2} i\theta} \\ &+ \left\{\hat{\xi}_1, \hat{\xi}_3, \hat{\xi}_4, \hat{\xi}_5, \hat{\xi}_9\right\} e^{-\frac{1}{2} i\theta} \Big] + cc\end{aligned} \tag{4.33}$$

$$w = e^{\sigma_x x + \sigma_t t} \sin \beta z \left[\xi_7 e^{\frac{1}{2} i\theta} + \hat{\xi}_7 e^{-\frac{1}{2} i\theta} \right] + cc \tag{4.34}$$

whereas Eqs. (4.31) and (4.32) become

$$(u,v,p,T,\rho) = e^{\sigma_x x + \sigma_t t} \sin \beta z \Big[\{\xi_1, \xi_3, \xi_4, \xi_5, \xi_9\} e^{\frac{1}{2} i\theta} + \left\{\hat{\xi}_1, \hat{\xi}_3, \hat{\xi}_4, \hat{\xi}_5, \hat{\xi}_9\right\} e^{-\frac{1}{2} i\theta} \Big] + cc \tag{4.35}$$

$$w = e^{\sigma_x x + \sigma_t t} \cos \beta z \Big[\xi_7 e^{\frac{1}{2} i\theta} + \hat{\xi}_7 e^{-\frac{1}{2} i\theta} \Big] + cc \tag{4.36}$$

For the case of temporal stability, $\sigma_x = 0$ and $\sigma_t = \sigma_{tr} + i\sigma_{ti} \neq 0$ with σ_{tr} being the growth rate and σ_{ti} representing the frequency detuning. On the other hand, for the case of spatial stability $\sigma_t = 0$ and $\sigma_x = \sigma_{xr} + i\sigma_{xi} \neq 0$ with σ_{xr} being the growth rate and σ_{xi} representing the wavenumber detuning. The excited subharmonic wave is a linear combination of the forms given by Eqs. (4.33) and (4.34) and Eqs. (4.35) and (4.36). The form of the solution given by either of these sets of equations consists of a pair of 3-D propagating waves that form a spanwise standing wave. They are 90° out of phase. In the case of tuned modes, we take σ_x or σ_t to be real and $\hat{\xi}_n$ is then equal to $\bar{\xi}_n$; the complex conjugate of ξ_n. This is the case that we consider in this work.

Substituting Eqs. (4.24)-(4.28) and Eqs. (4.33) and (4.34) into Eqs. (4.1)-(4.7), (4.12), and (4.13) and equating the coefficients of $\exp(\frac{1}{2} i\theta)$ and $\exp(-\frac{1}{2} i\theta)$ on both sides leads to the following problem governing the ξ_n and either σ_x or σ_t:

$$\begin{aligned} &\left(\sigma_t - \tfrac{1}{2} i\omega\right)\xi_9 + \left(\sigma_x + \tfrac{1}{2} i\alpha_r\right)\left[\rho_m \xi_1 + U_m \xi_9 + A\left(\zeta_9 \bar{\xi}_1 + \zeta_1 \bar{\xi}_9\right)\right] \\ &+ D\rho_m \xi_3 + \rho_m D\xi_3 + A\left(D\zeta_9 \bar{\xi}_3 + \zeta_9 D\bar{\xi}_3 + D\zeta_3 \bar{\xi}_9 + \zeta_3 D\bar{\xi}_9\right) \\ &+ \beta\left(\rho_m \xi_7 + A\zeta_9 \bar{\xi}_7\right) = 0 \end{aligned} \tag{4.37}$$

$$
\begin{aligned}
&\rho_m \Lambda \xi_1 + A\left(\sigma_t + \frac{1}{2} i\omega\right)\zeta_9 \bar{\xi}_1 \\
&+ A\left[\rho_m\left(\sigma_x + \frac{1}{2} i\alpha_r\right)\zeta_1 \bar{\xi}_1 + U_m\left(\sigma_x - \frac{1}{2} i\alpha_r\right)\zeta_9 \bar{\xi}_1 + i(\alpha_r U_m - \omega)\zeta_1 \bar{\xi}_9\right] \\
&+ \rho_m D U_m \xi_3 + A\left[\rho_m \zeta_3 \bar{\xi}_2 + \rho_m \zeta_2 \bar{\xi}_3 + D U_m \zeta_9 \bar{\xi}_3 + D U_m \zeta_3 \bar{\xi}_9\right] \\
&+ \left(\sigma_x + \frac{1}{2} i\alpha_r\right)\xi_4 - \frac{1}{R}\left\{r\left(\sigma_x + \frac{1}{2} i\alpha_r\right)^2 \mu_m \xi_1 \quad + (1+m)\mu_m(\sigma_x\right. \\
&+ \frac{1}{2}\ i\alpha_r) D\xi_3 + (1+m)\beta\mu_m\left(\sigma_x + \frac{1}{2} i\alpha_r\right)\xi_7 + \mu_m D\xi_2 + \frac{d\mu_m}{dT_m} D^2 U_m \xi_5 + D\mu_m \xi_2 \\
&+ D U_m \frac{d(D\mu_m)}{dT_m}\xi_5 + D U_m \frac{d\mu_m}{dT_m}\xi_6 + \left(\sigma_x + \frac{1}{2} i\alpha_r\right) D\mu_m \xi_3 \\
&- \beta^2 \mu_m \xi_1 = 0
\end{aligned}
\tag{4.38}
$$

$$
\begin{aligned}
&\rho_m \Lambda \xi_3 + \left(\sigma_t + \frac{1}{2} i\omega\right) A\zeta_9 \bar{\xi}_3 \\
&+ \rho_m A\zeta_1\left(\sigma_x - \frac{1}{2} i\alpha_r\right)\bar{\xi}_3 + \rho_m A i\alpha_r \zeta_3 \bar{\xi}_1 \\
&+ \left(\sigma_x - \frac{1}{2} i\alpha_r\right) U_m A\zeta_9 \bar{\xi}_3 + i(\alpha_r U_m - \omega) A\zeta_3 \bar{\xi}_9 \\
&+ A\rho_m \zeta_3 D\bar{\xi}_3 + A\rho_m D\zeta_3 \bar{\xi}_3 + D\xi_4 \\
&- \frac{1}{R}\left\{(1+m)\left(\sigma_x + \frac{1}{2} i\alpha_r\right)\ \mu_m \xi_2 + \left(\sigma_x + \frac{1}{2} i\alpha_r\right) D U_m \frac{d\mu_m}{dT_m}\xi_5\right. \\
&+ \left(\sigma_x + \frac{1}{2} i\alpha_r\right)^2 \mu_m \xi_3 + r\mu_m D^2 \xi_3 + r D\mu_m D\xi_3 \\
&+ m\left(\sigma_x + \frac{1}{2} i\alpha_r\right) D\mu_m \xi_1 + (1+m)\beta\mu_m \xi_8 \\
&\left. + m\beta D\mu_m \xi_7 - \beta^2 \mu_m\ \xi_3\right\} = 0
\end{aligned}
\tag{4.39}
$$

$$
\begin{aligned}
&\rho_m \Lambda \xi_7 + A\left(\sigma_t + \frac{1}{2} i\omega\right)\zeta_9 \bar{\xi}_7 + \rho_m A\zeta_1\left(\sigma_x - \frac{1}{2} i\alpha_r\right)\bar{\xi}_7 \\
&+ U_m A\zeta_9\left(\sigma_x - \frac{1}{2} i\alpha_r\right)\bar{\xi}_7 - \beta\xi_4 + \rho_m A\zeta_3 \bar{\xi}_8 \\
&- \frac{1}{R}\left\{-\beta(1+m)\left(\sigma_x + \frac{1}{2} i\alpha_r\right)\mu_m \xi_1 + \left(\sigma_x + \frac{1}{2} i\alpha_r\right)^2 \mu_m \xi_7\right. \\
&\left. - \beta D\mu_m \xi_3 - \beta\mu_m(1+m)D\xi_3 + D\mu_m \xi_8 + \mu_m D\xi_8 - \beta^2 \mu_m r\xi_7 = 0\right.
\end{aligned}
\tag{4.40}
$$

$$
\begin{aligned}
&\rho_m \Lambda \xi_5 + A\left(\sigma_t + \frac{1}{2} i\omega\right)\zeta_9 \bar{\xi}_5 \\
&+ A\left[\rho_m\left(\sigma_x - \frac{1}{2} i\alpha_r\right)\ \zeta_1 \bar{\xi}_5 + U_m\left(\sigma_x - \frac{1}{2} i\alpha_r\right)\zeta_9 \bar{\xi}_5\right. \\
&\left. + i\alpha_r \rho_m\ \zeta_5 \bar{\xi}_1\right] + \rho_m DT_m \xi_3 \\
&+ A\left[\rho_m \zeta_3 \bar{\xi}_6 + \rho_m \zeta_6 \bar{\xi}_3 + DT_m\ \zeta_9 \bar{\xi}_3\right. \\
&\left. + i(\ \alpha_r U_m - \omega)\zeta_5 \bar{\xi}_9 + DT_m \zeta_3 \bar{\xi}_9\right] \\
&- (\gamma - 1)M_\infty^2 \{\Lambda \xi_4\ + \left(\sigma_x - \frac{1}{2} i\alpha_r\right) A\zeta_1 \bar{\xi}_4 \\
&+ i\alpha_r\ A\zeta_4 \bar{\xi}_1 + A\zeta_3 D\bar{\xi}_4 + AD\zeta_4 \bar{\xi}_3\} \\
&- \frac{(\gamma - 1)M_\infty^2}{R} \left\{(DU_m)^2\ \frac{d\mu_m}{dT_m}\ \xi_5\right. \\
&\left. + 2\mu_m DU_m \xi_2 + 2\left(\sigma_x + \frac{1}{2} i\alpha_r\right) DU_m \mu_m \xi_3\right\} \\
&- \frac{1}{RPr} \left\{\left(\sigma_x + \frac{1}{2} i\alpha_r\right)^2 \mu_m \xi_5\ \ + \mu_m D\xi_6\right. \\
&+ D^2 T_m \frac{d\mu_m}{dT_m}\ \xi_5 + D\mu_m \xi_6 \\
&\left. + DT_m \frac{d(D\mu_m)}{dT_m}\ \xi_5 + \ \ \frac{d\mu_m}{dT_m}\ DT_m \xi_6 - \beta^2 \mu_m \xi_5\right\} = 0
\end{aligned}
\tag{4.41}
$$

$$
-\gamma M_\infty^2 \rho_m \xi_4 + \rho_m^2 \xi_5 + \xi_9 + \rho_m A\zeta_9 \bar{\xi}_5 + \rho_m A\zeta_5 \bar{\xi}_9 = 0 \tag{4.42}
$$

where

$$
\Lambda = \sigma_t - \frac{1}{2} i\omega + U_m\left(\sigma_x + \frac{1}{2} i\alpha_r\right) \tag{4.43}
$$

and $\xi_2 = D\xi_1$, $\xi_6 = D\xi_5$, and $\xi_8 = D\xi_7$. The boundary conditions are

$$
\xi_1 = \xi_3 = \xi_5 = \xi_7 = 0 \ \text{ at } \ y = 0 \tag{4.44}
$$

$$
\xi_n \text{ are bounded as } y \to \infty \tag{4.45}
$$

In arriving at Eqs. (4.37)-(4.42), we neglected terms of order A^2 and A/R.

4.5. Method of Solution

The spatial subharmonic instability problem given by Eqs. (4.37)-(4.45) with σ_t being zero consists of a system of homogeneous differential equations subject to homogeneous boundary conditions. It has a nontrivial solution only for a certain combination of σ_x, β, ω, A,and R. The eigenvalue problem provides a complex dispersion relation of the form

$$\sigma_x = \sigma_x(\beta, \omega, A, R)$$

The solution to this eigenvalue problem is obtained numerically.

To solve the problem given by Eqs. (4.37)-(4.45), we eliminate the density disturbance and transform the equations into the system of first-order differential equations

$$D\xi = F\xi \tag{4.46}$$

where

$$\xi = \{\xi_1, \xi_2, \xi_3, \xi_4, \xi_5, \xi_6, \xi_7, \xi_8\}^T \tag{4.47}$$

is an 8x1 vector and F is an 8x8 matrix.

Equations (4.44) and (4.45) define, respectively, the boundary conditions at y = 0 and ∞. Because we solve the problem over a finite domain, we replace the

boundary conditions at infinity with the proper boundary conditions at some finite value of y, say $y = y_{max}$, so that

$$Q\xi = 0 \text{ at } y = y_{max} \tag{4.48}$$

We note that the interaction terms in the governing equations are the order $A\zeta\xi$ whereas the rest are order ξ. For the case when the ζ_n and ξ_n vanish exponentially as $y \to \infty$, the interaction terms decay faster than the rest of the terms. Thus by choosing a large enough y_{max}, we can neglect the interaction terms and replace the boundary conditions at infinity with those of the corresponding 3-D linear quasiparallel disturbance problem. The error involved can be monitored by choosing a certain value of y_{max} and solving the problem, then increasing y_{max} and resolving the problem, and noting the effect of increasing y_{max} on the accuracy of the solution.

The boundary conditions at $y = y_{max}$ given by equation (4.48), the boundary conditions at y = 0 given by Eqs. (4.44), and the system of differential equations given by Eq. (4.46) form a stiff eigenvalue problem. It is solved by using a combination of finite differences (Pereyra, 1976) and a Newton-Raphson scheme or a combination of SUPORT (Scott and Watts, 1977) and a Newton-Raphson scheme. Without a sacrifice in the accuracy, the finite-difference scheme is considerably faster than SUPORT; however the convergence is not guaranteed. Most of the results in this work were produced by using the finite-difference scheme.

4.6. Results

Because experiments are not available for comparison with our numerical results and because the direct numerical simulations of Erlebacher and Hussaini (1987) are for the case of fundamental secondary instability only, we validated our code by comparing its results with the incompressible results of Herbert (1984) and Chapter 2 of this study and the compressible results of El-Hady (1989), Nayfeh and Harper (see Nayfeh, 1988). The results obtained by using the present code for the case of incompressible flows are in excellent agreement with those of Herbert (1984) and the results in Chapter 2 of this study. Moreover, when $M_\infty = 4.5$, the results obtained for the case of first- and second-mode primary waves by using the present code with the interaction terms in the equation of state being neglected are in excellent agreement with those obtained by Nayfeh and Harper (see Nayfeh, 1988). Furthermore, the results obtained by using the present code for $M_\infty = 0.8$ are in reasonable agreement with those obtained by El-Hady (1989) as shown in figure 4.1.

Next, we investigated the influence of the interaction terms in the equation of state. Figure 4.2 shows the effect of neglecting the interaction terms in the equation of state at $M_\infty = 0.8$. It is clear from this figure that at such a low Mach number the effect is negligible. However, the effect of the interaction terms in the equation of state increases as the Mach number increases. For example, at $M_\infty = 4.5$, figure 4.3 shows that the effect of these interaction terms is not negligible.

Next, we present results for the spatial stability of subsonic, transonic, and supersonic flows, including the effect of the interaction terms in the equation of state. The frequency F, which is related to ω through $\omega = FR$, is kept constant when following a certain wave. The spanwise wavenumber is defined as $B = 1000\beta/R$ and

B is kept constant as the wave propagates downstream. For all the results presented in this chapter, T_∞ is kept constant and equal to 120°K, the Prandtl number Pr is kept constant and equal to 0.72, $m = \lambda/\mu = -0.2/3.0$, $\gamma = 1.4$, the variation of viscosity with temperature is given by the Sutherland formula, and σ_x is taken to be real, which corresponds to a perfectly tuned subharmonic mode.

Figure 4.4 shows the variation of the spatial growth rate of the subharmonic wave with spanwise wavenumber for the three Mach numbers 0.0, 0.8, and 1.6 and two r.m.s. amplitudes (0.01 and 0.02) of the primary wave. We note that the 2-D first-mode waves, which are used as primary waves, are not the most amplified first-mode waves; the most amplified first-mode waves are 3-D (see Mack, 1984). The variation in the case of compressible flows shares a lot of features with the incompressible case: the broadband character of the unstable spanwise wavenumbers, the sharp cutoff at low spanwise wavenumbers, and the shift in the most amplified spanwise wavenumber towards a higher value as the amplitude of the primary wave increases. As the Mach number increases, we note from figure 4.4 that (a) the bandwidth of unstable spanwise wavenumbers decreases, (b) the most amplified spanwise wavenumber shifts to a lower value, and (c) the growth rates decrease for all values of spanwise wavenumber. Figure 4.5 shows the variation of the growth rate of the 3-D free or primary waves (linear oblique waves having a frequency that is one-half that of the 2-D primary waves), corresponding to the data of figure 4.4. We note from this figure that in the presence of no interaction, the 3-D wave is damped for all spanwise wavenumbers when $M_\infty = 1.6$ and damped over most of the range of spanwise wavenumbers when $M_\infty = 0.0$ and 0.8. Comparing figures 4.4 and 4.5, we conclude that the subharmonic instability dominates the primary instability at all Mach numbers.

Figure 4.6 shows the rate of growth of the 2-D primary wave at $F = 45x10^{-6}$ for the three Mach numbers $M_\infty = 0.0, 1.0$ and 2.0. It shows that as the Mach number increases (a) the onset of the primary instability shifts towards a lower Reynolds number, (b) the maximum growth rate decreases, and (c) the second neutral point shifts to a lower Reynolds number. It is clear that the total amplification, as measured by the area under the growth-rate curve, decreases as the Mach number increases. In figure 4.7, we compare the streamwise variation of the N factor of the 2-D primary wave at $F_{2D} = 45x10^{-6}$ and $M_\infty = 1.0$ with that of the subharmonic wave having the spanwise wavenumber B = 0.2. It is clear that the subharmonic wave dominates the instability.

Next, we investigate the influence of viscosity on the growth rate of the secondary instability. In figure 4.8, we show the variation of the growth rate of the subharmonic wave with Reynolds number and amplitude of the primary wave for $M_\infty = 1.0$, $F_{2D} = 45x10^{-6}$, and B = 0.2. It is clear that increasing the initial amplitude of the primary wave results in an upstream shift of the onset of the subharmonic instability. Moreover, initially the growth rate increases approximately linearly with Reynolds number. However, at large Reynolds numbers, the growth rate increases only slightly with Reynolds number. As expected, increasing the initial amplitude of the primary waves results in an increase in the growth rate of the subharmonic wave at all streamwise locations.

El-Hady (1989) concluded from his numerical results for disturbances having the frequency $F = 60x10^{-6}$ at Mach numbers between 0 and 2.2 that the effect of compressibility on the local growth rates of subharmonic waves at a given streamwise location can be misleading because the local growth rates depend on the amplitude of primary waves and the spanwise wavelength of the subharmonic wave. However, the overall effect of compressibility is stabilizing. Next, we reinvestigate

the influence of compressibility on the subharmonic instability for supersonic as well as subsonic and transonic Mach numbers. We note that the subharmonic growth rate is a function of Mach number, spanwise wavenumber, Reynolds number, and frequency. In figure 4.9, we show the variation of the location of the onset of the subharmonic instability with the initial amplitude of the primary wave for B = 0.2, $F_{2D} = 45x10^{-6}$, and $M_\infty = 0.0$, 1.0, 2.0, and 4.5. For a given Mach number, as the initial amplitude of the primary wave increases the onset of the subharmonic instability shifts rapidly towards a lower Reynolds number. Figure 4.9 also shows that for the same initial amplitude of the primary wave, increasing the Mach number shifts the onset of the subharmonic instability towards a lower Reynolds number. Figure 4.10 shows the variation of the growth rate of the subharmonic wave with Reynolds number for a constant value of the amplitude of the primary wave and the three Mach numbers $M_\infty = 0.0$, 1.0, and 2.0. It shows that, although the onset of the subharmonic instability shifts towards a lower value of Reynolds number as the Mach number increases, the rate of increase of the growth rate of the subharmonic wave with Reynolds number decreases with increasing Mach number so that eventually the growth rate of the subharmonic wave decreases as the Mach number increases. Consequently, at low Reynolds numbers, the amplification factor increases with increasing Mach number but at large Reynolds numbers the amplification factor decreases with increasing Mach number, as shown in figure 4.11. Figure 4.11 also shows that the subharmonic wave dominates the primary instability at all Mach numbers

Figure 4.12 shows the variation of the growth rate of the subharmonic wave with the frequency of the primary wave when $M_\infty = 0.0$, 1.0, 2.0, and 3.0. The subharmonic wave is unstable over a very wide range of frequencies and the growth rate has a broad maximum. Moreover, except for a small range of frequencies near the left

neutral values, increasing the Mach number results in decreasing the growth rate of the subharmonic wave. Furthermore, the maximum growth rate decreases as the Mach number increases.

Figure 4.13 shows the variation of the growth rates of the subharmonic wave and the 3-D free or primary wave with Mach number at R = 1150, $F_{2D} = 120x10^{-6}$, a r.m.s. amplitude of the primary wave equal to 0.01, and B = 0.2. The 3-D free or primary wave is damped but the subharmonic wave grows over the whole considered range of Mach numbers. Again, the subharmonic instability dominates the primary instability at all Mach numbers. At this location and initial amplitude of the primary wave, the growth rate of the subharmonic wave decreases as the Mach number increases. Figures 4.13, 4.14, and 4.10 suggest that compressibility decreases the growth rate of the subharmonic mode at large Reynolds numbers and large initial amplitudes of the primary wave. At small Reynolds numbers and small initial amplitudes of the primary wave compressibility may increase the growth rate of the subharmonic wave. However, the overall effect of compressibility as measured by the maximum amplification factor is stabilizing, as shown in figure 4.11.

One feature of compressible instability is the presence of more than one mode of instability. The first mode is similar to the T-S instability mode of incompressible flows, while the second and higher unstable (Mack) modes are unique to compressible flows. In contrast with the first mode, the most unstable second mode is 2-D. As the Mach number increases to the hypersonic regime, the second mode displays growth rates that are higher than those of the 3-D first mode (Mack, 1984).

Figure 4.15 shows the variation of the growth rate of the subharmonic wave with spanwise wavenumber at $M_\infty = 4.5$, $R = 1950$, and $F_{2D} = 120x10^{-6}$ when the primary wave is a second-mode wave, while figure 4.16 shows the variation of the growth rate of the 3-D free or primary wave corresponding to the data of figure 4.15. As in the

case of first-mode-subharmonic instability, the second-mode-subharmonic instability dominates the primary second-mode wave. In fact, whereas the 3-D free or primary wave is damped for all spanwise wavenumbers, the subharmonic wave displays large growth rates over all the considered spanwise wavenumbers. In contrast with the incompressible case, the maximum amplified wave has a narrower bandwidth. Figure 4.17 shows the variation of the growth rate of the subharmonic wave with spanwise wavenumber at $M_\infty = 5.0$ and for different amplitudes of the first-mode primary wave. The figure confirms some of the trends noted in figure 4.4, where the primary wave was also a first-mode wave. In particular we note that as the amplitude of the primary wave increases, there is a shift in the most amplified spanwise wavenumber towards a higher value. However, figure 4.18 shows that the shift is towards a lower value when the primary wave is a second-mode wave.

Figure 4.19 shows the variation of the growth rate of the subharmonic wave with the frequency of the primary wave when $M_\infty = 4.5$, $R = 1950$, $B = 0.1$, and $A_{rms} = 0.01$. We note a wider band of frequencies receiving amplification and the presence of two peaks. To determine the reason for the presence of the two peaks, we calculated the variation of the growth rate of the 2-D primary wave with frequency. The results are shown in figure 4.20. It is clear that for this Mach number and streamwise location there are two modes of instability. The left branch corresponds to first-mode waves and the right branch corresponds to second-mode (first Mack) waves. The pressure-fluctuation amplitude functions shown in figure 4.21 confirm this conclusion. Consequently, the left peak in figure 4.19 is the maximum growth rate of first-mode subharmonic mode of instability, whereas the second peak is the maximum growth rate of second-mode subharmonic mode of instability. To investigate the interval between these two peaks, we calculated the pressure-fluctuation amplitude functions for several frequencies, as shown in figure 4.21. It is clear that there is a continuous

transition from first-to-second 2-D primary waves as the frequency increases. To confirm this conclusion, we calculated the subharmonic eigenfunctions for several frequencies. The results are shown in figure 4.22. It is clear that the mode shape changes continuously from that corresponding to the left peak (first-mode subharmonic mode) to that corresponding to the right peak (second-mode subharmonic mode) in figure 4.19. In other words, first-mode-subharmonic modes merge with second-mode subharmonic modes.

Figure 4.23a shows the spanwise vorticity contours in the presence of the meanflow, the 2-D primary wave, and the 3-D subharmonic wave. The primary wave is a first mode and $M_\infty = 2$. The initial amplitude of the 2-D primary wave at $R = 600$ is 0.01, whereas that of the subharmonic wave is 0.001. We note from the figure that the vorticity is concentrated in a small region which is adjacent to the wall. The vorticity contours in this figure are very similar to the vorticity contours in the presence of the mean flow and the 2-D primary wave, which were reported by Herbert (1984) for the incompressible case. As the initial amplitude of the subharmonic wave is increased to 0.01, we obtain the contours shown in figure 4.23b. At such an amplitude of the subharmonic wave, the vorticity starts to spread in the normal direction, and at the same time we note some convection of the vorticity in the streamwise direction. In figure 4.23c the initial amplitude of the subharmonic wave is further increased to 0.1. At such an amplitude, we note that the vorticity is strongly convected downstream and spread in the normal direction. Thus, figure 4.23 shows that the presence of the subharmonic changes drastically the vortex structure of the original basic flow. We note that the situation in figure 4.23c is similar to that reported by Fasel (1989) for the incompressible case and computed using numerical simulation.

Figure 4.24 shows the normal vorticity contours at y = 1.0 in the presence of the mean flow, the 2-D wave, and the 3-D wave. We note the periodicity in the spanwise direction and the presence of a pattern of vortex cells in that direction. Figure 4.25 shows the streamwise vorticity contours. We note that in the spanwise direction we have two patterns of vorticity contours which repeat themselves due to the spanwise periodicity.

Figure 4.26a shows the spanwise vorticity contours in the presence of the mean flow, the 2-D primary wave, and 3-D subharmonic wave. The primary wave is a second mode and $M_\infty = 4.5$. The initial amplitude of the 2-D primary wave at R = 1550 is 0.01, whereas that of the subharmonic wave is 0.001. We note from this figure that the pattern here is somewhat different from that obtained when the primary wave is a first mode, which is shown in figure 4.23a. As the initial amplitude of the subharmonic wave is increased to 0.01, we obtain the contours shown in figure 4.26b. At such an amplitude of the subharmonic wave, the vorticity spreads far in the normal direction, and at the same time we note that the vorticity is being convected in the streamwise direction. In figure 4.26c the initial amplitude of the subharmonic wave is further increased to 0.1. At such an amplitude, we note that the vorticity is strongly convected downstream and spread further in the normal direction. Figure 4.27 shows the normal vorticity contours at y = 0.3, in the presence of the mean flow, the 2-D wave, and the 3-D wave. We note that the contours shown in this figure are very similar to those shown in figure 4.24, where the primary wave is a first mode. Figure 4.28 shows the streamwise vorticity contours. These contours are very much different from those shown in figure 4.25 for the case in which the primary wave is a first mode.

By solving both the temporal and spatial subharmonic instability problems of incompressible flow over a flat plate, Bertolotti (1985) has shown that the temporal

subharmonic growth rate can be converted within a good accuracy into a spatial growth rate by dividing it by C_r; the real part of the phase speed. His results have shown that the accuracy of this transformation gets better as the growth rate decreases. Tables 4.1 and 4.2 show that this transformation is fairly accurate for the subharmonic growth rate of compressible boundary layers with the error being equal to 2.28% at $M_\infty = 8$. In Table 4.1, the primary wave is a first mode and the error decreases as the growth rate decreases. However, the primary wave in Table 4.2 is a second mode and there is no consistent trend in the relation between the error and the growth rate.

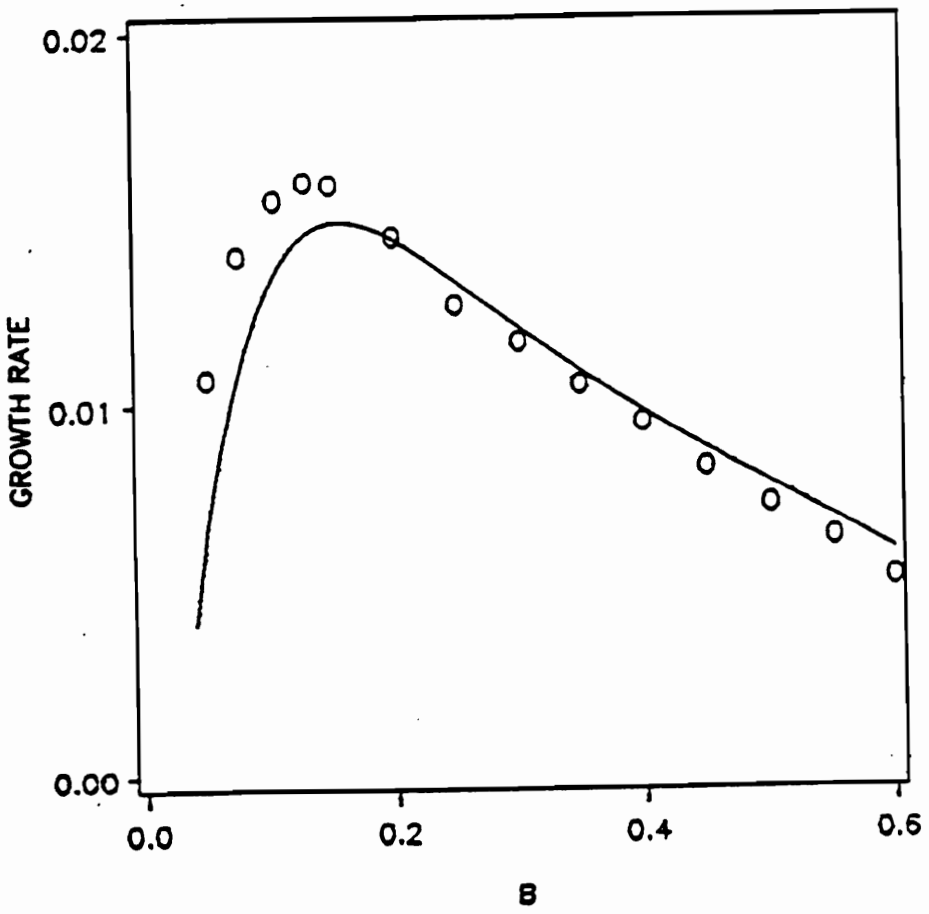

Figure 4.1. Variation of the growth rate of the subharmonic wave with the spanwise wavenumber at $F_{2D} = 60x10^{-6}$, $A_{rms} = 0.01$, $M_\infty = 0.8$, and R = 850: (___) present results and (0) El-Hady's (1989) results.

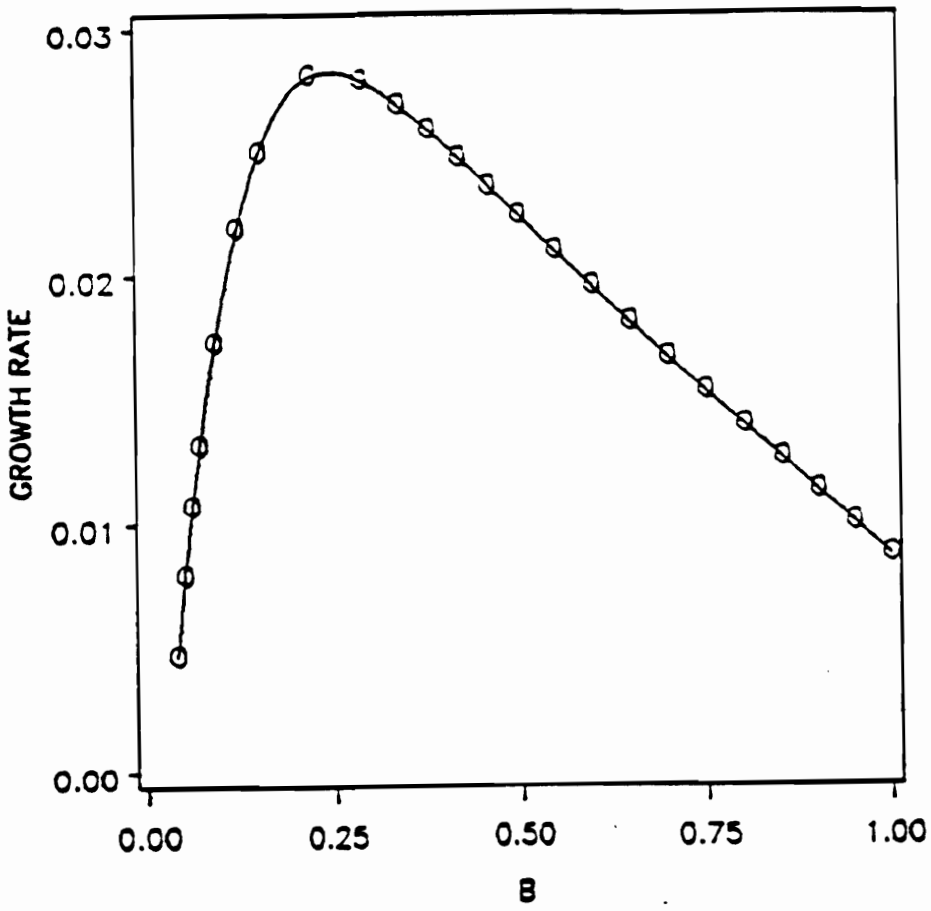

Figure 4.2. Variation of the growth rate of the subharmonic wave with spanwise wavenumber when $M_\infty = 0.8$, $F_{2D} = 120x10^{-6}$, R = 1150, and A_{rms} = 0.01. The interaction terms in the disturbance equation of state are (___) included and (0) neglected.

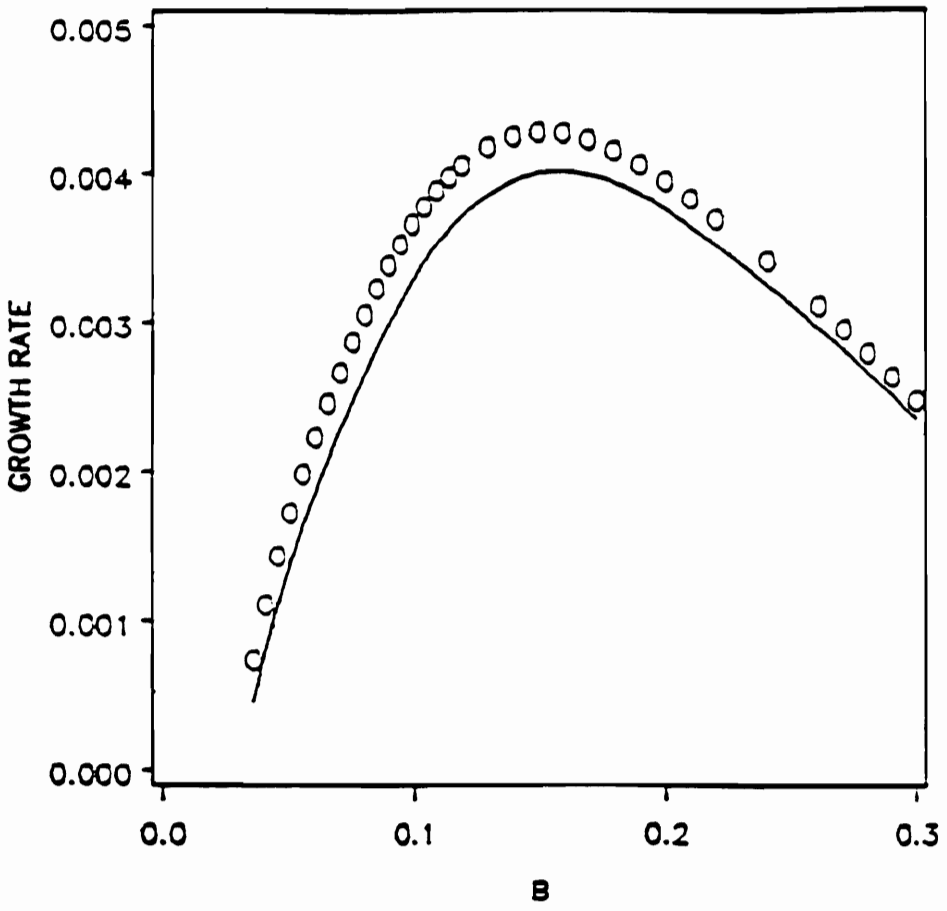

Figure 4.3. Variation of the growth rate of the subharmonic wave with spanwise wavenumber when $M_\infty = 4.5$, $F_{2D} = 120x10^{-6}$, R = 1150, and $A_{rms} = 0.01$. Perfectly tuned mode with the interaction terms in the disturbance equation of state (___) included and (0) neglected.

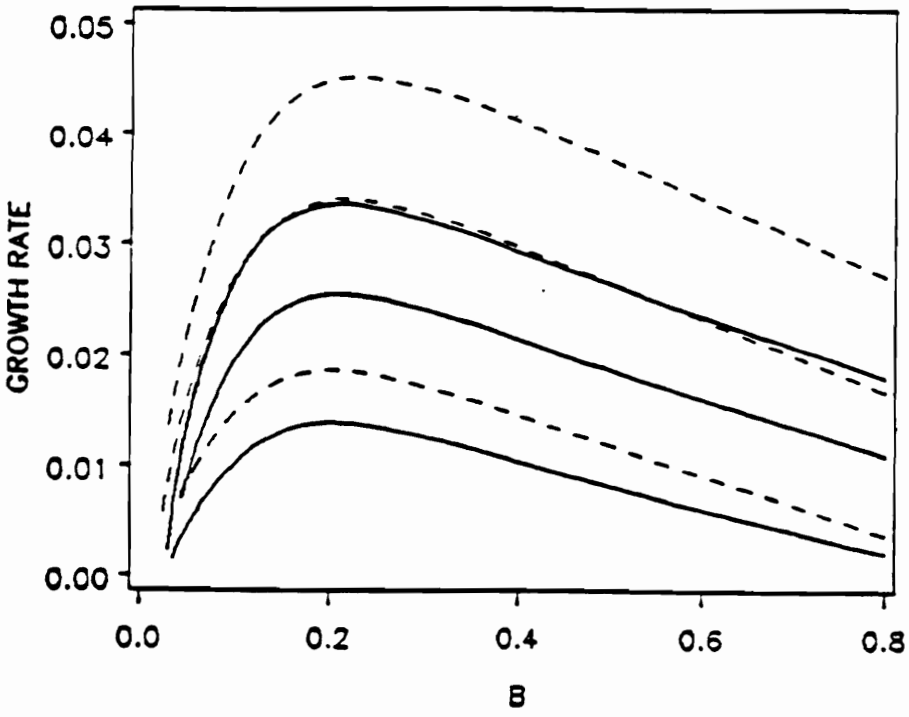

Figure 4.4. Variation of the growth rate of the subharmonic wave with spanwise wavenumber for three Mach numbers and two amplitudes A of the primary wave at R = 1050 and an $F_{2D} = 83x10^{-6}$. Dashed curves - $A_{rms} = 0.02$ and solid curves – $A_{rms} = 0.01$. The Mach numbers for each set proceeding downward are $M_\infty = 0.0$, 0.8, and 1.6.

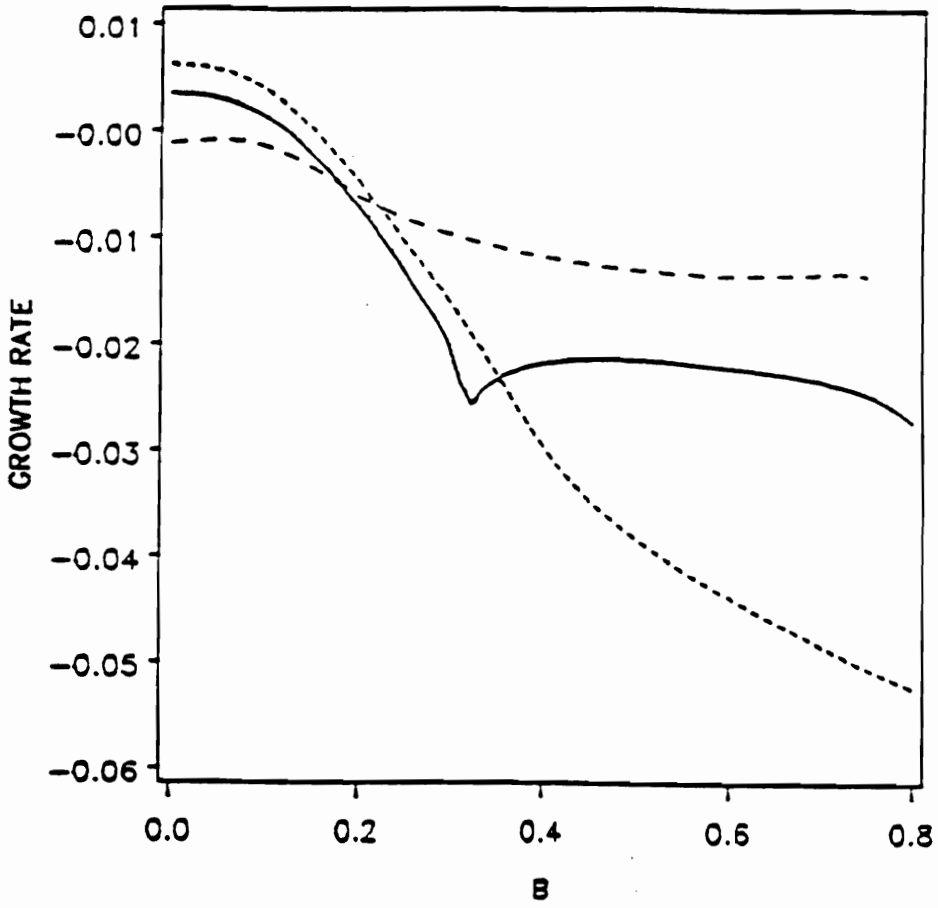

Figure 4.5. Variation of the growth rate of the three-dimensional free waves with spanwise wavenumber at R = 1050 and an $F = 42.5x10^{-6}$: (...) $M_\infty = 0.0$, (___) $M_\infty = 0.8$, and (- - -) $M_\infty = 1.6$.

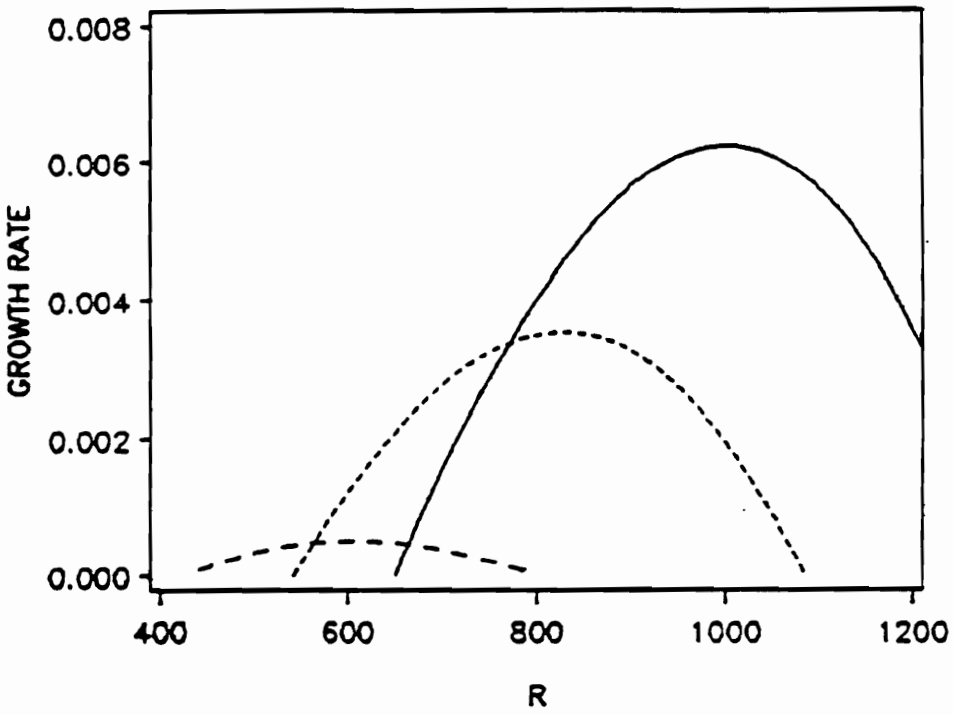

Figure 4.6. Variation of the growth rate of the primary wave with Reynolds number at $F = 45x10^{-6}$: (___) $M_\infty = 0.0$, (...) $M_\infty = 1.0$, and (- - -) $M_\infty = 2.0$.

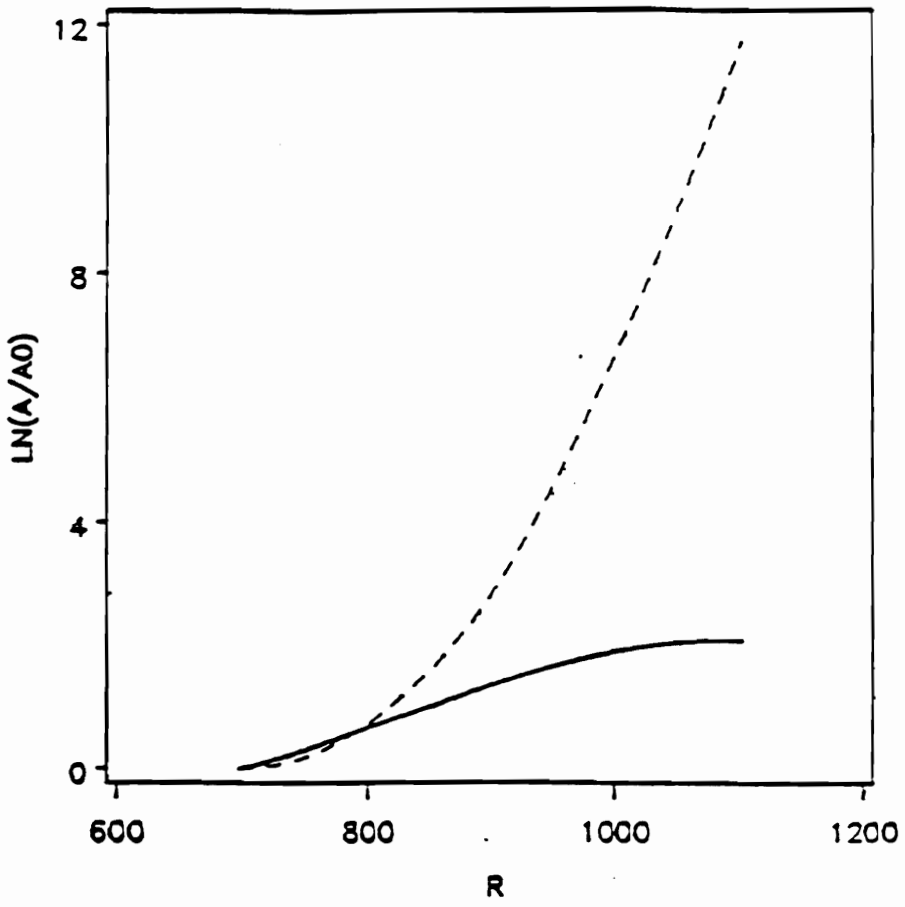

Figure 4.7. Variation of the N-factor of the subharmonic and primary waves with Reynolds number starting from the onset (R = 694) of the subharmonic instability when $F_{2D} = 45x10^{-6}$, $M_\infty = 1.0$, $B = 0.2$, and $A_{rms} = 0.005$: (___) primary wave and (- - -) subharmonic wave.

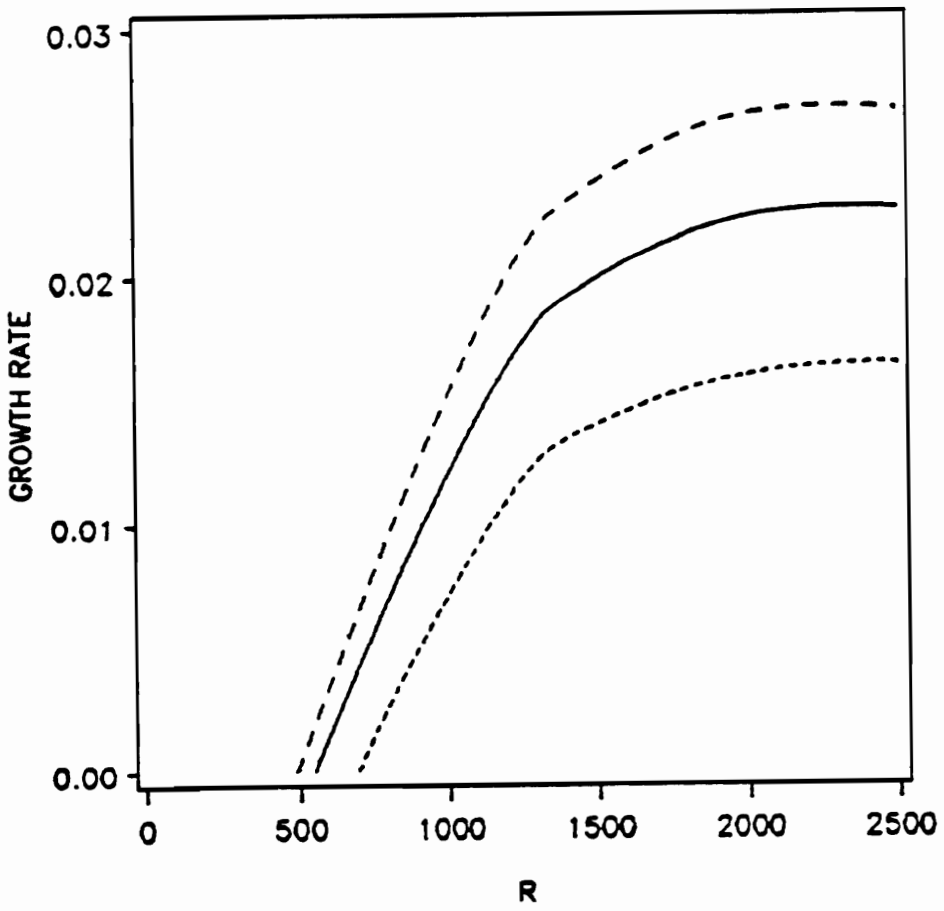

Figure 4.8. Variation of the growth rate of the subharmonic wave with Reynolds number at a constant amplitude of the primary wave when $M_\infty = 1.0$, $F_{2D} = 45x10^{-6}$, $B = 0.2$: (...) $A_{rms} = 0.005$, (___) $A_{rms} = 0.01$ and (- - -) $A_{rms} = 0.015$.

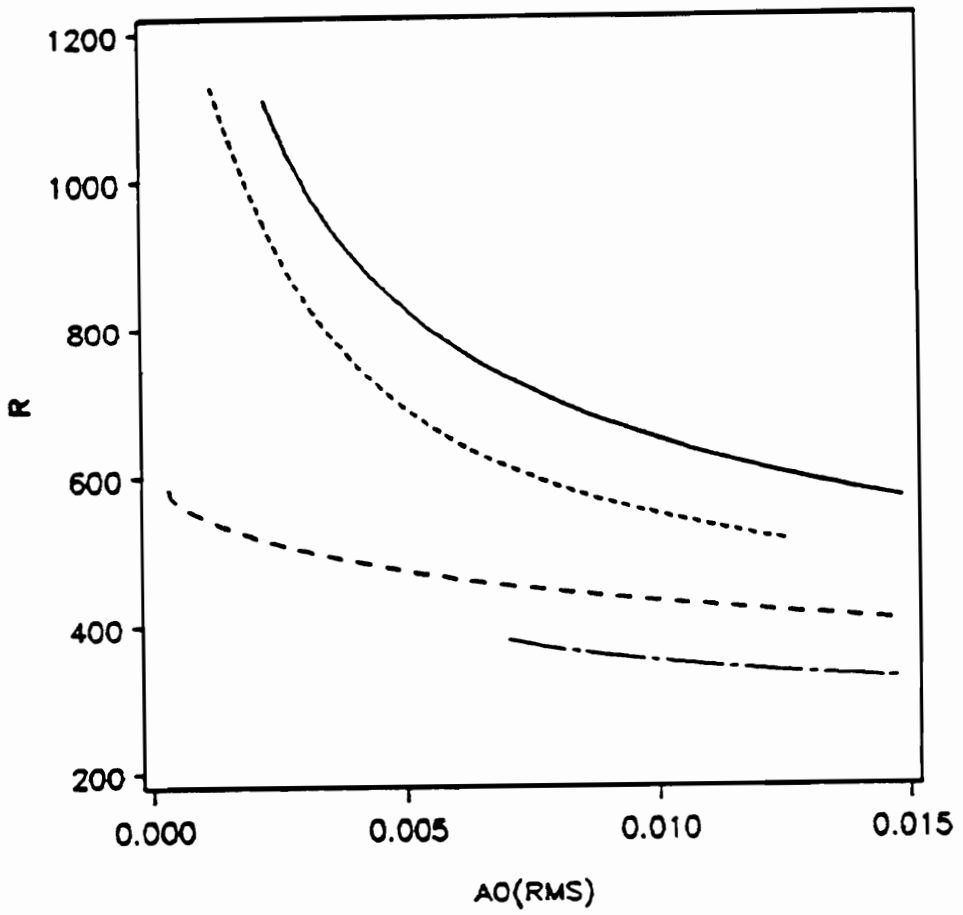

Figure 4.9. Variation of the location of the onset of the subharmonic instability with the amplitude of the primary wave when $F_{2D} = 45x10^{-6}$ and B = 0.2: (___) $M_\infty = 0.0$, (...) $M_\infty = 1.0$, (- - -) $M_\infty = 2.0$, and (_._.) $M_\infty = 4.5$.

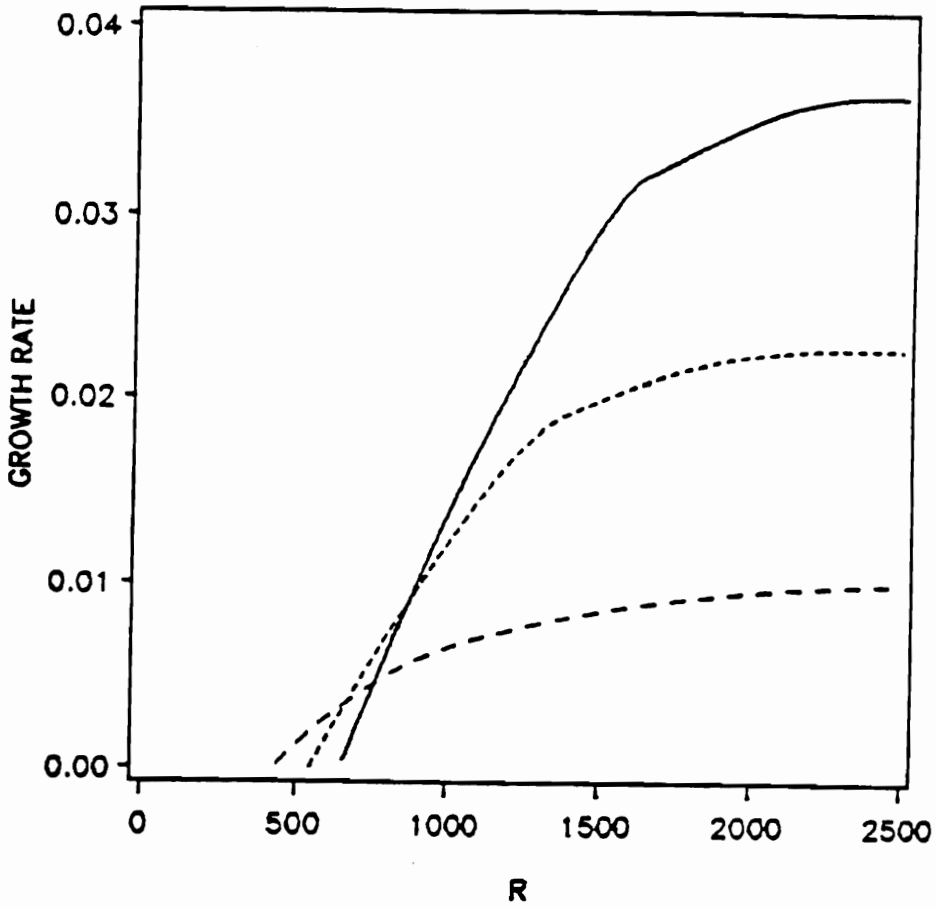

Figure 4.10. Variation of the growth rate of the subharmonic wave with Reynolds number at a constant amplitude of the primary wave when $A_{rms} = 0.01$, $F_{2D} = 45x10^{-6}$, $B = 0.2$: (___) $M_\infty = 0.0$, (...) $M_\infty = 1.0$, and (- - -) $M_\infty = 2.0$.

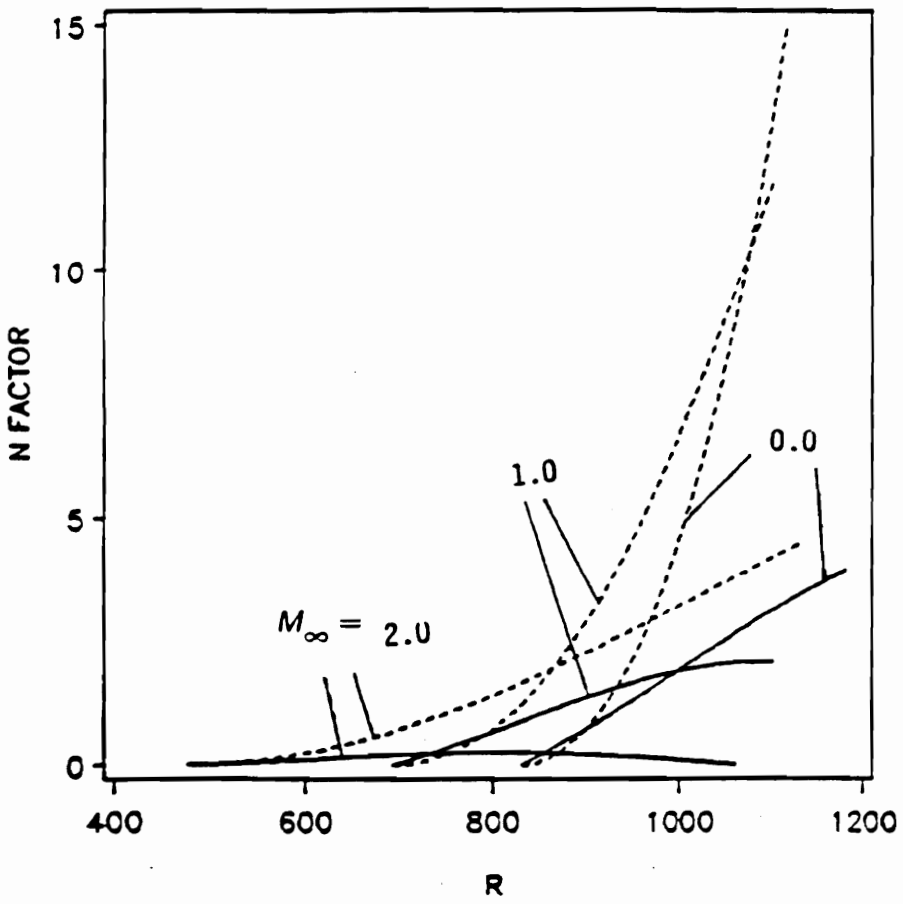

Figure 4.11. Variation of the N-factor of the subharmonic (...) and primary (---) waves with Reynolds number starting from the onset of the subharmonic instability when $F_{2D} = 45x10^{-6}$, $B = 0.2$, and an $A_{rms} = 0.005$ at the onset of the subharmonic instability.

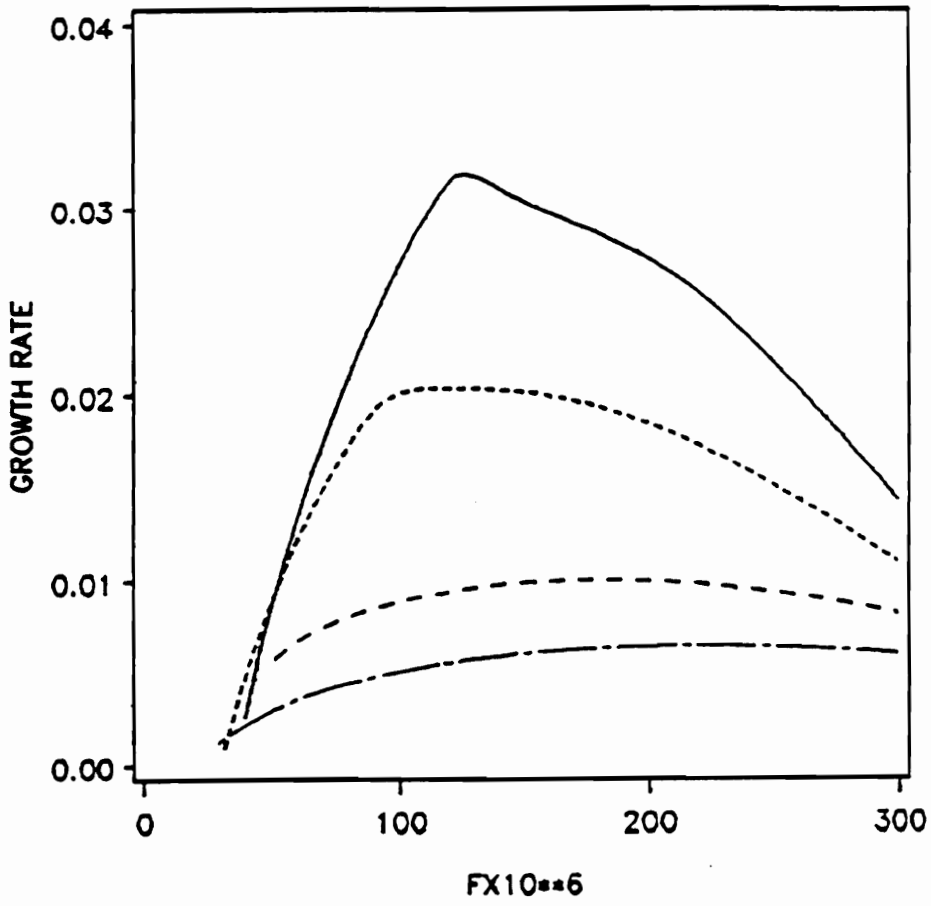

Figure 4.12. Variation of the growth rate of the subharmonic wave with the frequency of the primary wave at R = 800, B = 0.2, and $A_{rms} = 0.01$: (___) $M_\infty = 0.0$, (...) $M_\infty = 1.0$, (- - -) $M_\infty = 2.0$, and (_._.) $M_\infty = 3.0$.

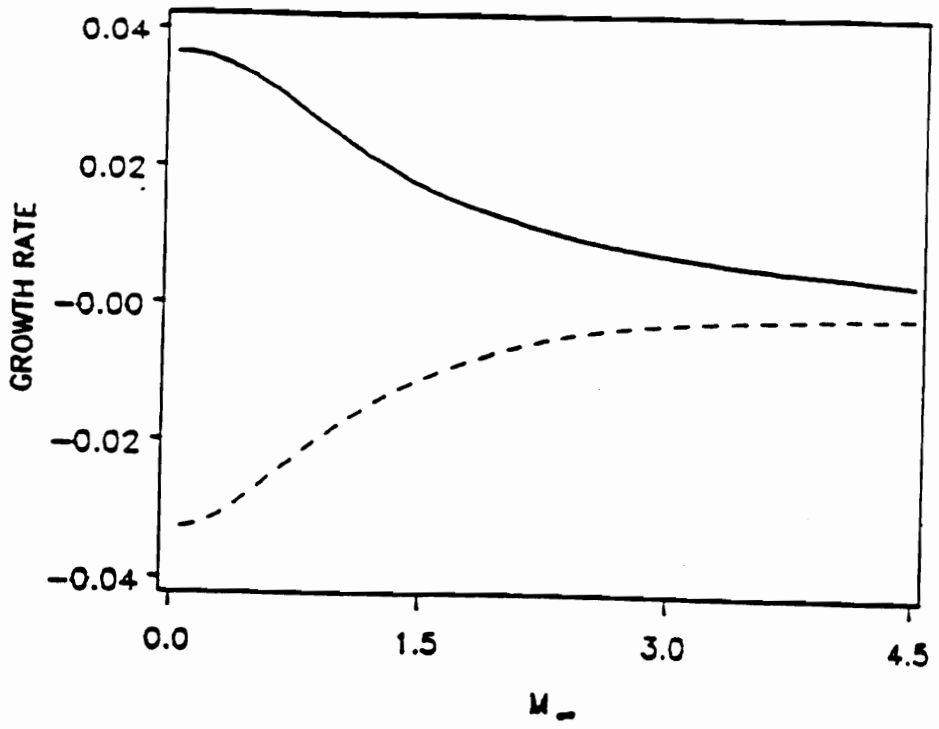

Figure 4.13. Variation of the growth rates of the subharmonic wave and the three-dimensional free or primary wave with Mach number when $F_{2D} = 120x10^{-6}$, R = 1150, B = 0.2, and $A_{rms} = 0.01$: (___) subharmonic wave and (- - -) three-dimensional free or primary wave.

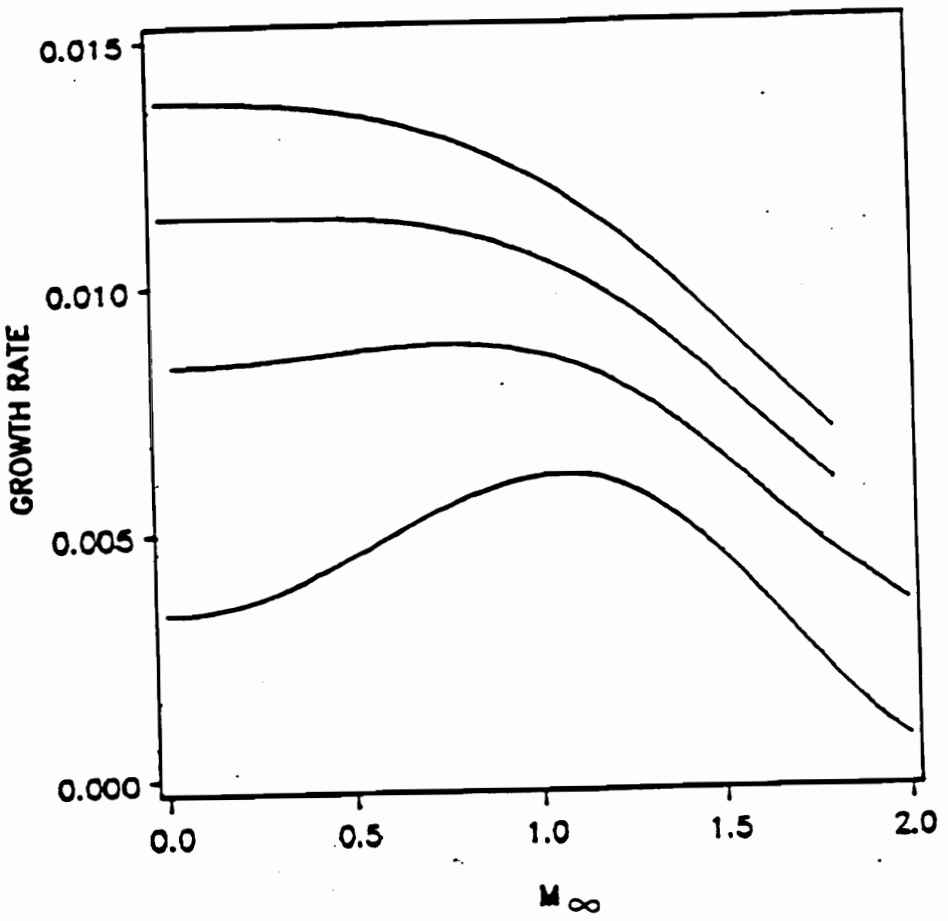

Figure 4.14. Variation of the growth rate of the subharmonic wave with Mach number when $F_{2D} = 60x10^{-6}$, R = 850, and B = 0.15. The r.m.s. amplitudes of the primary wave proceeding downward are 0.008, 0.006, 0.004, and 0.002.

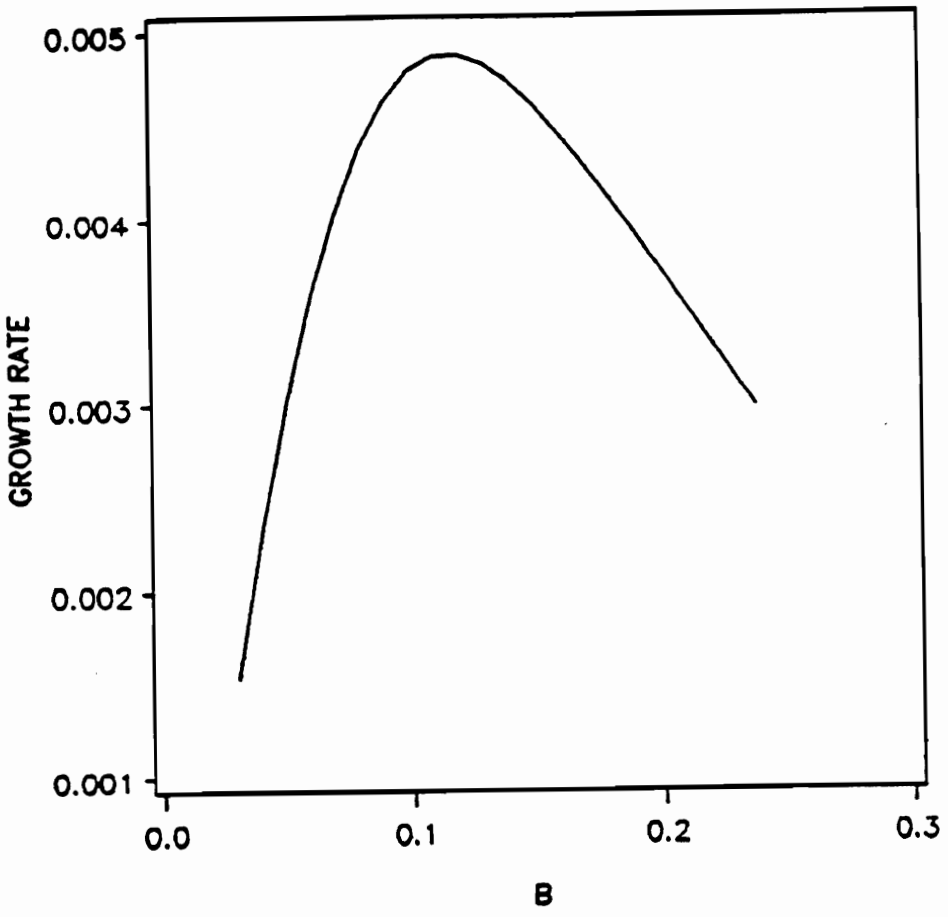

Figure 4.15. Variation of the growth rate of the subharmonic wave with spanwise wavenumber at $F_{2D} = 120x10^{-6}$, $M_\infty = 4.5$, R = 1950, and $A_{rms} = 0.01$ when the primary wave is a second-mode wave.

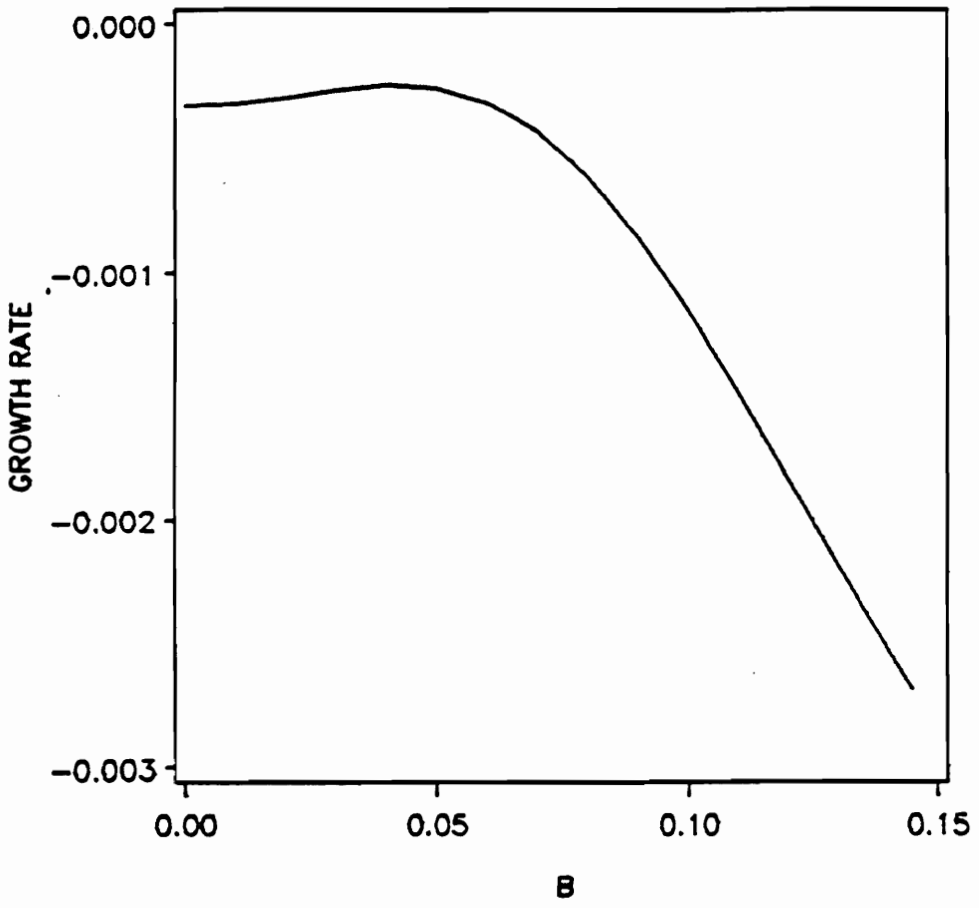

Figure 4.16. Variation of the growth rate of the three-dimensional free wave with spanwise wavenumber at $F = 60x10^{-6}$, R = 1950, and $M_\infty = 4.5$.

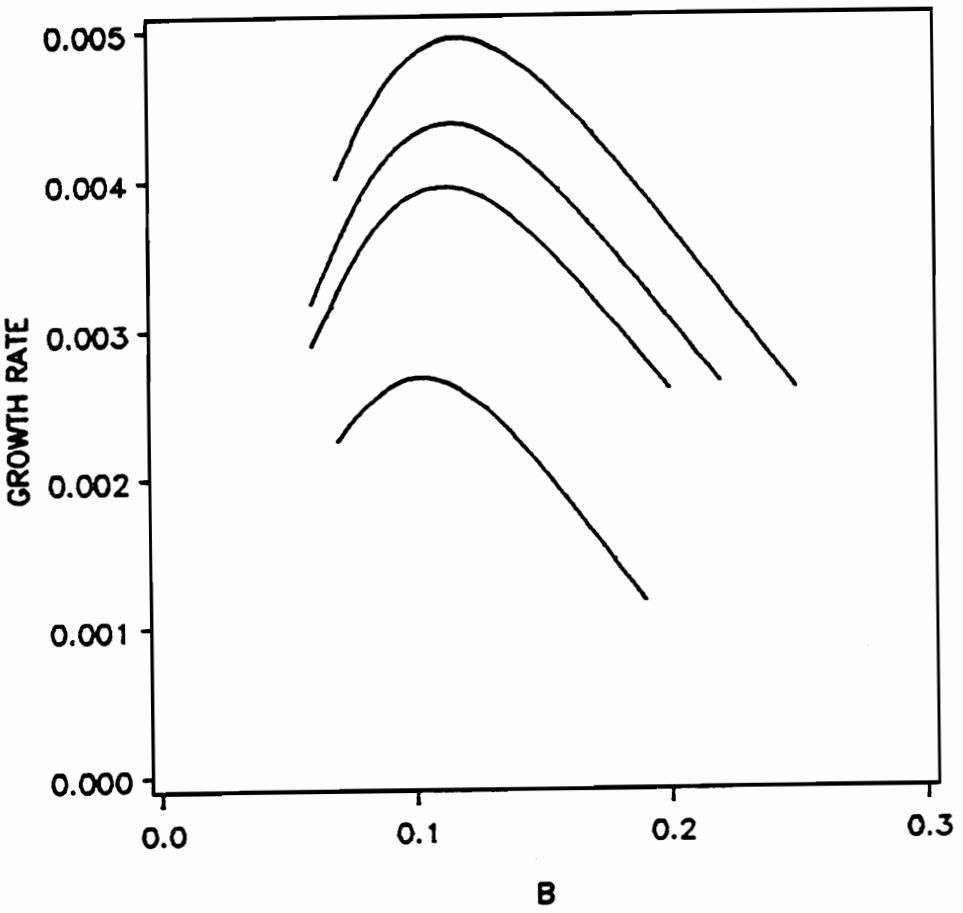

Figure 4.17. Variation of the growth rate of the subharmonic wave with the spanwise wavenumber at $M_\infty = 5.0$, $F_{2D} = 135x10^{-6}$, and R = 1500. The rms amplitudes of the first-mode primary wave proceeding downward are 0.015, 0.012, 0.01, and 0.005.

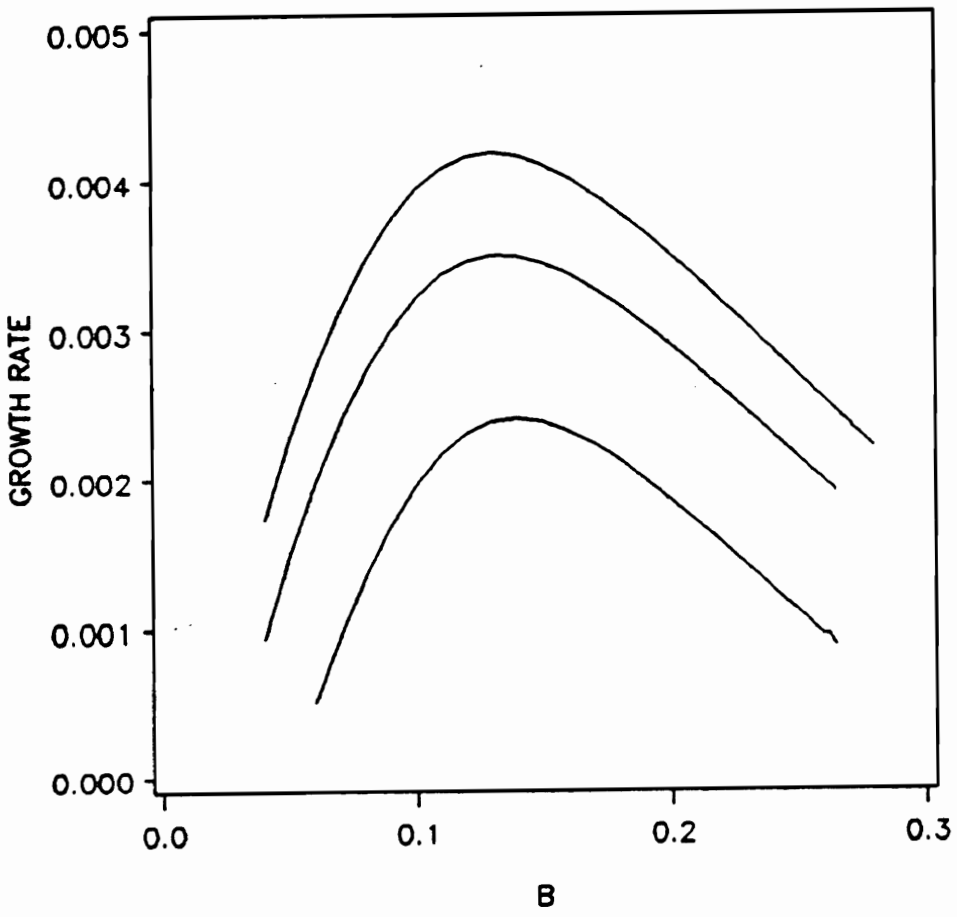

Figure 4.18. Variation of the growth rate of the subharmonic wave with the spanwise wavenumber at $M_\infty = 5.0$, $F_{2D} = 126x10^{-6}$, and R = 1500. The rms amplitudes of the second-mode primary wave proceeding downward are 0.015, 0.01, and 0.005.

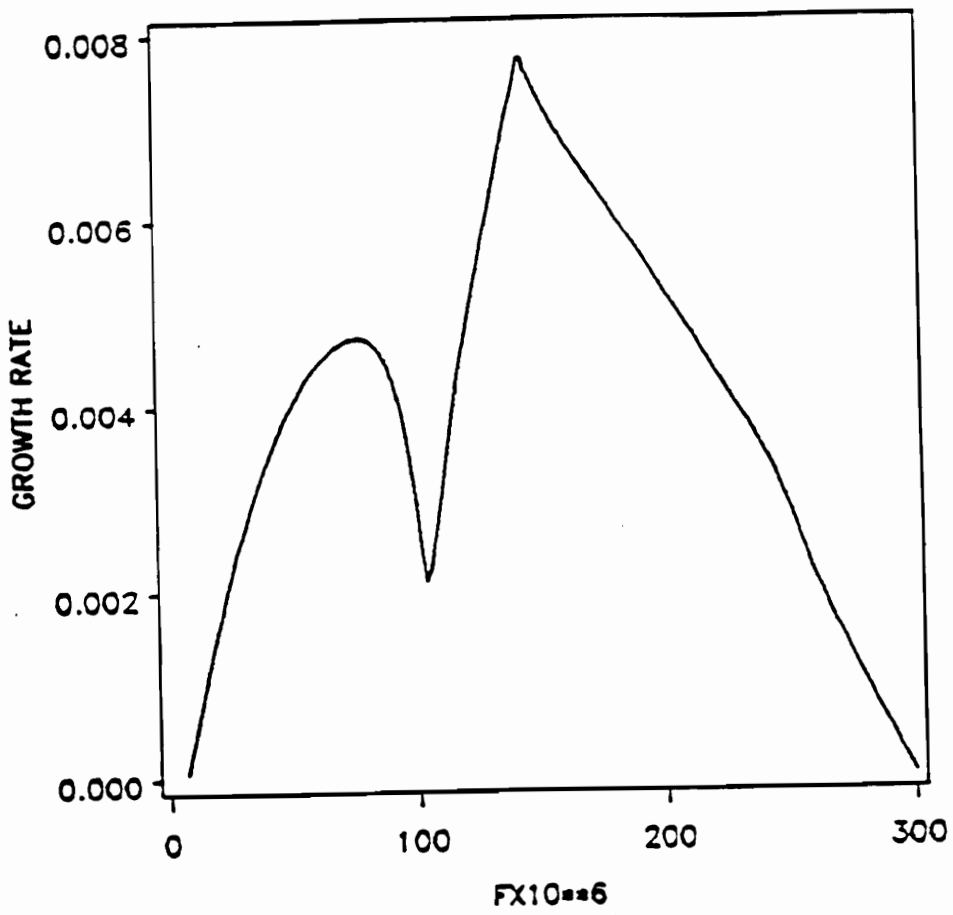

Figure 4.19. Variation of the growth rate of the subharmonic wave with the frequency of the primary wave at $M_\infty = 4.5$, $B = 0.1$, $R = 1950$, and $A_{rms} = 0.01$. The primary wave is (___) a first- and (...) second-mode wave.

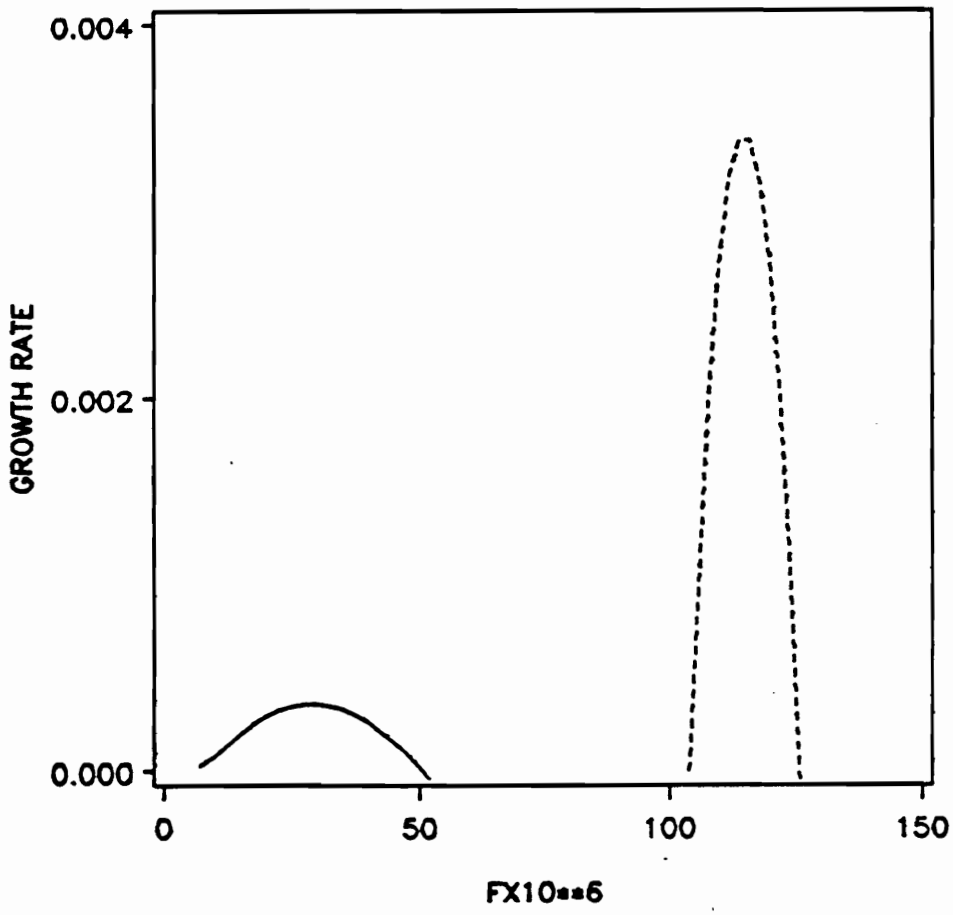

Figure 4.20. Variation of the growth rate of the primary wave with frequency at $M_\infty = 4.5$, and $R = 1950$: (___) first- and (...) second-mode wave.

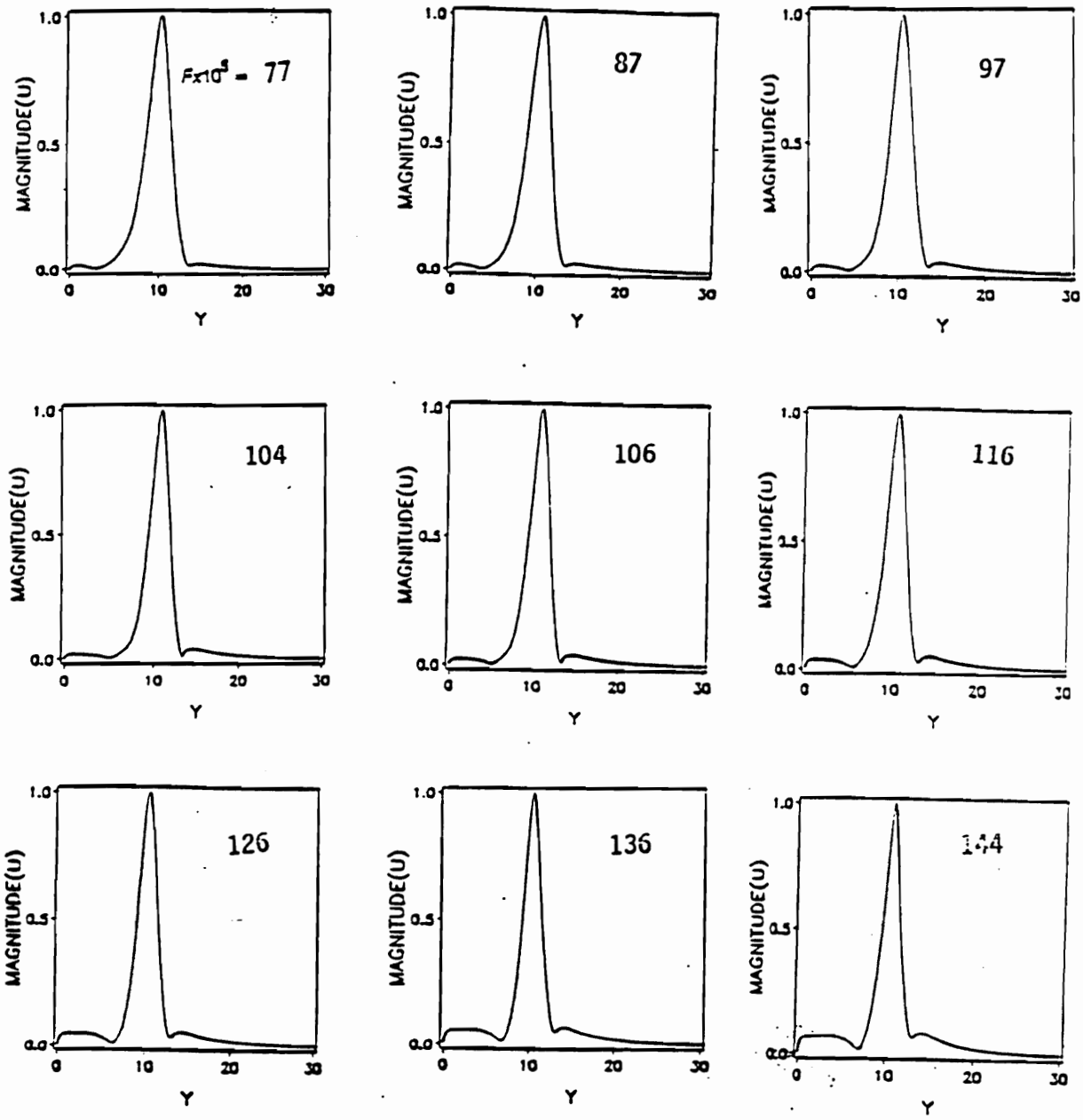

Figure 4.21. Pressure-fluctuation amplitude function of the primary wave for different frequencies: R = 1950 and $M_\infty = 4.5$.

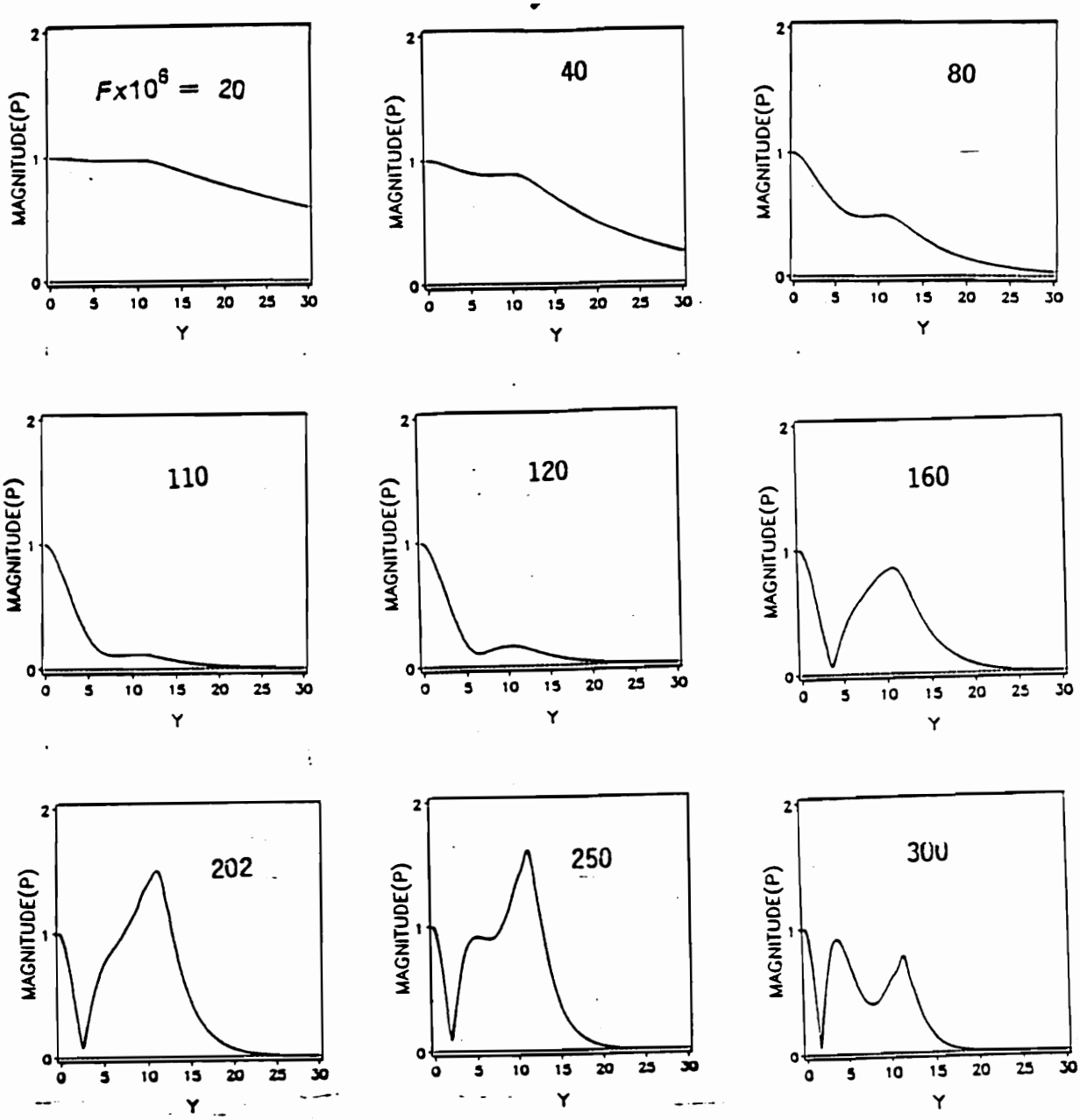

Figure 4.22. Variation of the magnitude of the streamwise component of the subharmonic velocity disturbance with transverse direction for several frequencies when $M_\infty = 4.5$, $B = 0.1$, $R = 1950$, and $A_{rms} = 0.01$.

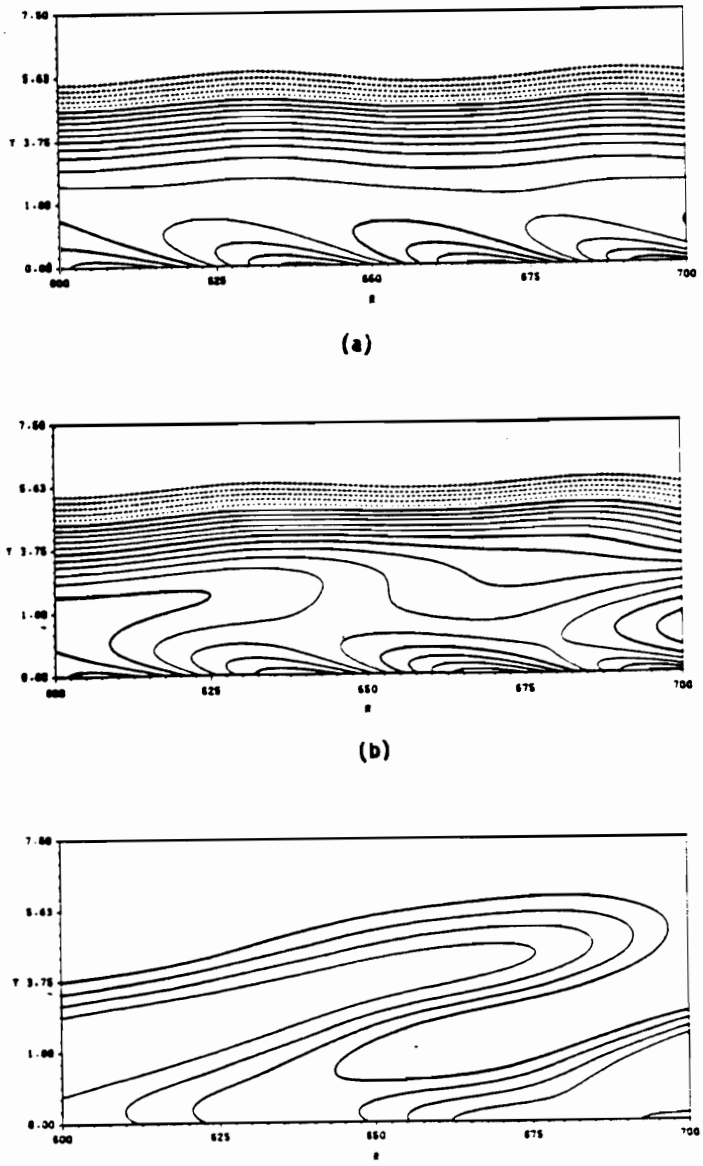

Figure 4.23. The spanwise vorticity contours in the presence of the mean flow, the 2-D primary wave and the 3-D subharmonic wave. The primary wave is a first-mode and $M_\infty = 2.0$, $F_{2D} = 46x10^{-6}$ and B = 0.2. The initial rms amplitude of the primary wave at R = 600 is 0.01, whereas that of the subharmonic wave is (a) 0.001, (b) 0.01, and (c) 0.1.

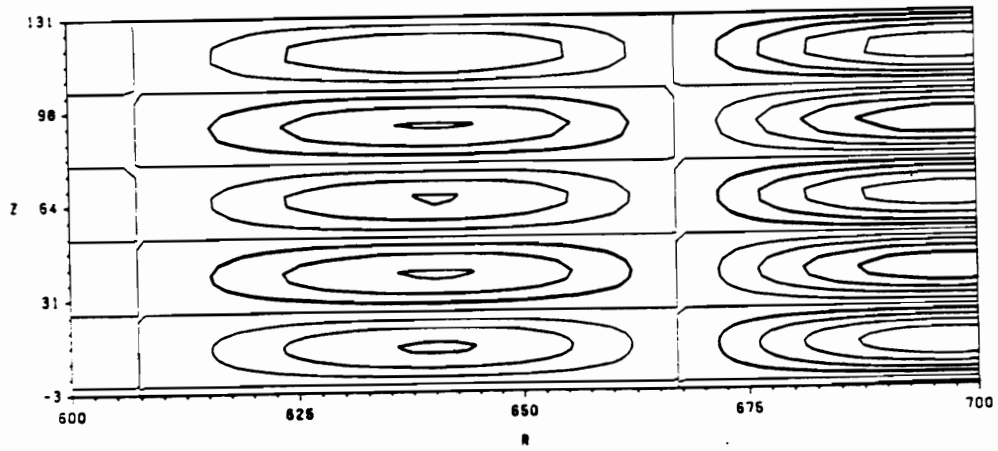

Figure 4.24. The normal vorticity contours in the presence of the mean flow, the 2-D primary wave and the 3-D subharmonic wave at y = 1.0. The primary wave is a first-mode and $M_\infty = 2.0$, $F_{2D} = 46x10^{-6}$ and B = 0.2. The initial rms amplitude of the primary wave at R = 600 is 0.01, whereas that of the subharmonic wave is 0.001.

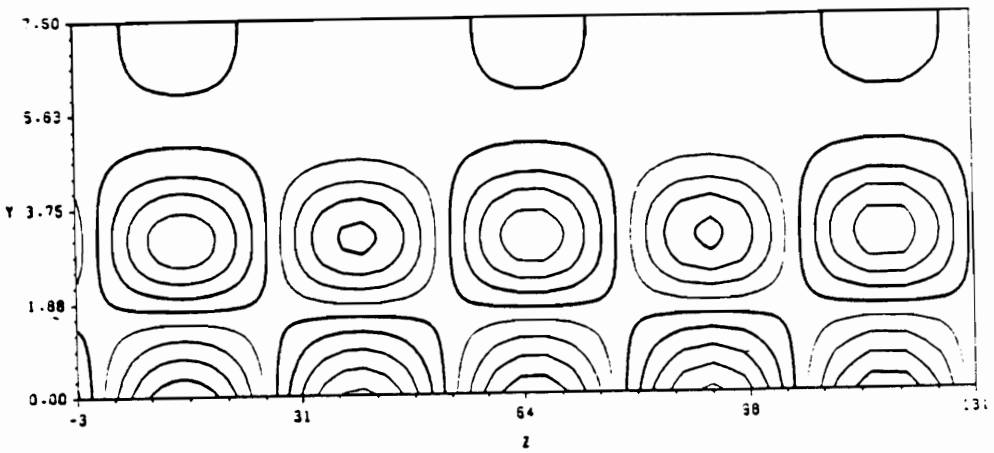

Figure 4.25. The streamwise vorticity contours in the presence of the mean flow, the 2-D primary wave and the 3-D subharmonic wave. The primary wave is a first-mode and $M_\infty = 2.0$, $F_{2D} = 46x10^{-6}$ and B = 0.2, and R = 600. The rms amplitude of the primary wave is 0.01, whereas that of the subharmonic wave is 0.001.

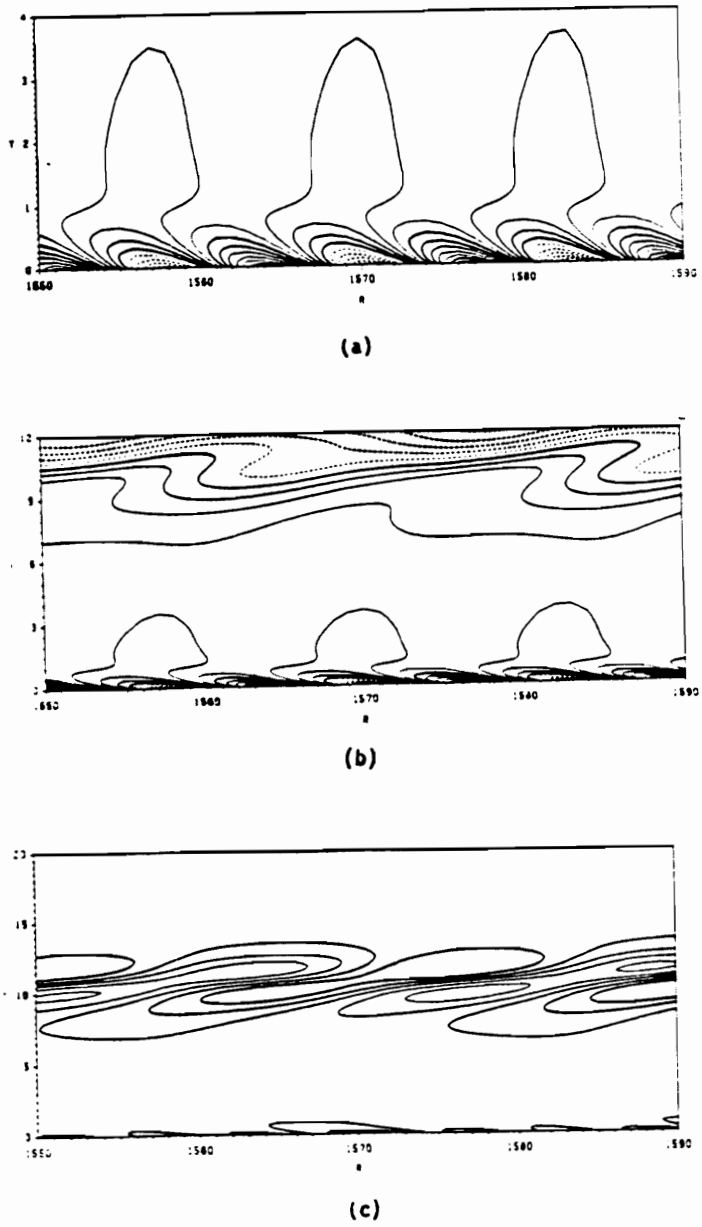

Figure 4.26. The spanwise vorticity contours in the presence of the mean flow, the 2-D primary wave and the 3-D subharmonic wave. The primary wave is a second-mode and $M_\infty = 4.5$, $F_{2D} = 144x10^{-6}$ and B = 0.1. The initial rms amplitude of the primary wave at R = 1550 is 0.01, whereas that of the subharmonic wave is (a) 0.001, (b) 0.01, and (c) 0.1.

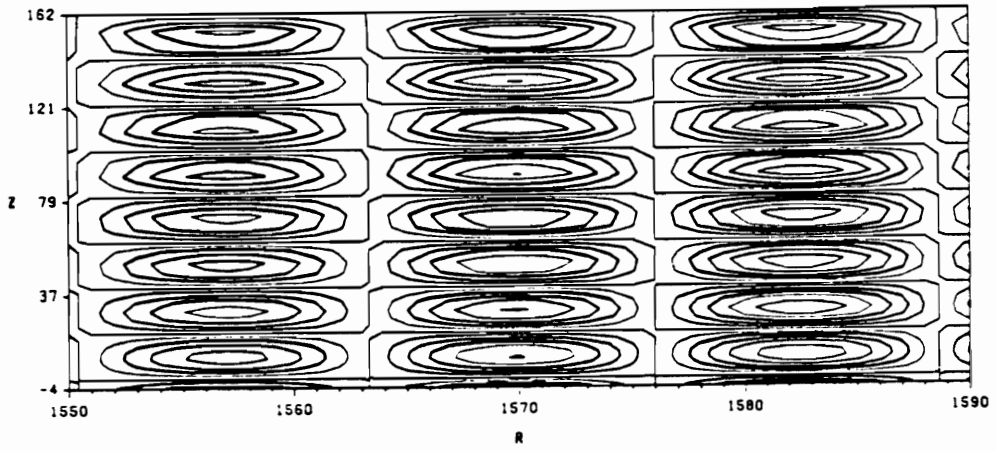

Figure 4.27. The normal vorticity contours in the presence of the mean flow, the 2-D primary wave and the 3-D subharmonic wave at y = 0.3. The primary wave is a second-mode and $M_\infty = 4.5$, $F_{2D} = 144x10^{-6}$ and B = 0.1. The initial rms amplitude of the primary wave at R = 1550 is 0.01, whereas that of the subharmonic wave is 0.001.

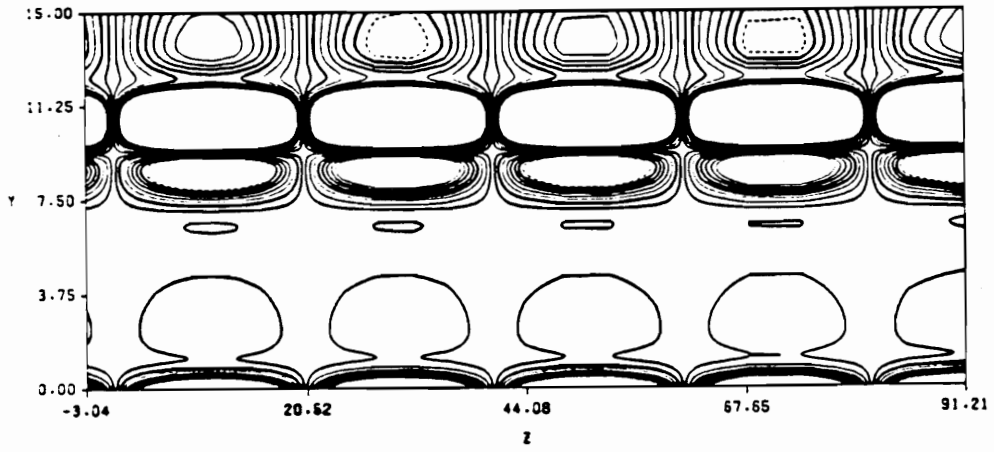

Figure 4.28. The streamwise vorticity contours in the presence of the mean flow, the 2-D primary wave and the 3-D subharmonic wave. The primary wave is a second-mode and $M_\infty = 4.5$, $F_{2D} = 144x10^{-6}$, B = 0.1 and R = 1550. The rms amplitude of the primary wave is 0.01, whereas that of the subharmonic wave is 0.001.

M_∞	α		σ_t	σ_t/C_r	σ_s	% error
3.00	0.074113	-0.000011	0.003523	0.004782	0.004946	3.31
3.10	0.073198	-0.000057	0.003394	0.004550	0.004699	3.18
3.20	0.072351	-0.000098	0.003270	0.004334	0.004470	3.06
3.30	0.071566	-0.000135	0.003152	0.004132	0.004256	2.93
3.40	0.070836	-0.000167	0.003039	0.003942	0.004056	2.80
3.50	0.070155	-0.000196	0.002930	0.003765	0.003868	2.67
3.60	0.069519	-0.000221	0.002825	0.003597	0.003691	2.54
3.70	0.068923	-0.000244	0.002724	0.003439	0.003524	2.42
3.80	0.068365	-0.000265	0.002626	0.003289	0.003366	2.29
3.90	0.067841	-0.000283	0.002530	0.003144	0.003213	2.16
4.00	0.067347	-0.000299	0.002437	0.003005	0.003068	2.03
4.10	0.066882	-0.000313	0.002346	0.002874	0.002930	1.91
4.20	0.066443	-0.000326	0.002259	0.002749	0.002799	1.79
4.30	0.066028	-0.000337	0.002174	0.002630	0.002674	1.67
4.40	0.065634	-0.000347	0.002093	0.002516	0.002556	1.56
4.50	0.065262	-0.000355	0.002014	0.002408	0.002443	1.45

Table 4.1. A comparison of the spatial growth rate of the subharmonic wave as computed directly with the transformed growth rate $\sigma_s = \sigma_t/C_r$. The primary wave is a first-mode, R = 1950, $A_{rms} = 0.01$, B = 0.1 and $F_{2D} = 28x10^{-6}$.

M_∞	α		σ_t	σ_t/C_r	σ_x	% error
3.50	0.081553	-0.000051	0.002298	0.002914	0.002941	0.91
4.00	0.078413	-0.000199	0.002103	0.002563	0.002594	1.20
4.50	0.076073	-0.000281	0.001953	0.002309	0.002344	1.47
5.00	0.074266	-0.000323	0.001844	0.002129	0.002167	1.74
5.50	0.072831	-0.000339	0.001754	0.001986	0.002026	1.99
6.00	0.071662	-0.000338	0.001664	0.001853	0.001895	2.17
6.50	0.070686	-0.000327	0.001561	0.001716	0.001755	2.26
7.00	0.069849	-0.000309	0.001440	0.001564	0.001600	2.27
7.50	0.069107	-0.000291	0.001296	0.001392	0.001424	2.25
8.00	0.068408	-0.000292	0.001116	0.001187	0.001215	2.28

Table 4.2. A comparison of the spatial growth rate of the subharmonic wave as computed directly with the transformed growth rate $\sigma_x = \sigma_t/C_r$. The primary wave is a second-mode, R = 1550, $A_{rms} = 0.01$, B = 0.05 and $F_{2D} = 41.5 \times 10^{-6}$.

5. EFFECT OF HEAT TRANSFER ON THE SUBHARMONIC INSTABILITY OF BOUNDARY LAYERS OVER A FLAT PLATE

The effect of heat transfer on the subharmonic instability of a 2-D boundary layer over a flat plate is analyzed using the Floquet model. The resulting problem is solved numerically by using both finite differences and the computer code SUPORT. Results are presented for different Mach numbers. For supersonic flows results for first- and second-mode primary waves are presented.

5.1. Results

We present results for the case of spatial stability at different Mach numbers. The frequency F, which is related to ω through $\omega = FR$, is kept constant when

following a certain wave. The spanwise wavenumber is defined as $B = 1000\beta/R$ and B is kept constant as the wave propagates downstream. For all the results presented in this chapter, T_∞ is kept constant and equal to 120°K, the Prandtl number Pr is kept constant and equal to 0.72, $m = \lambda/\mu = -0.2/3.0$, $\gamma = 1.4$, and the variation of viscosity with temperature is given by the Sutherland formula. The mean-flow boundary condition in which we specify $\frac{T_w}{T_{ad}}$ (equation 4.19) is imposed by using the formula

$$T_{ad} = 1 + \frac{\gamma - 1}{2} \sqrt{Pr}\, M_\infty^2 \tag{5.1}$$

Equation (5.1) is an approximate expression for the adiabatic wall temperature. The accuracy of this approximation is demonstrated in Table 5.1 for different Mach numbers when $T_\infty = 120°K$. We note from this table that the formula is reasonably accurate, and that the error involved increases by increasing Mach number.

The effect of heat transfer on the instability of compressible boundary layers has been studied by many researchers. Using temporal inviscid and viscous theories, Mack (1969, 1975) found that while cooling stabilizes first-mode waves it destabilizes second-mode waves. For moderate Mach numbers, sufficient cooling can be applied to remove the generalized inflection point, which is the source of the first-mode instability. However, the source of the second-mode instability cannot be removed by cooling. Lysenko and Maslov (1984) found, both experimentally and theoretically, that surface cooling: (a) stabilizes first-mode disturbances - the range of unstable frequencies decreases, the amplification rates decrease, and the neutral stability curves are shifted to larger Reynolds numbers; (b) destabilizes second-mode (high-frequency) disturbances - the unstable frequency region expands and is shifted to larger frequencies, while the amplification rates increase; and (c) may lead to the region of unstable frequencies of the first-mode being divided into two. Lysenko and

Maslov (1984) found that the experimental results are in qualitative agreement with the predictions of the theory of hydrodynamic stability. Al-Maaitah et al. (1990c) performed detailed calculations on the effect of heat transfer on the stability of compressible boundary layers.

Figure 5.1 shows the variation of the growth rate of the second-mode primary wave with frequency for different levels of heat transfer at $M_\infty = 4.5$ and R = 1550. This figure shows that the most amplified mode (the peak) is destabilized by cooling, in agreement with the literature (Mack, 1984). Figure 5.2 shows the variation of the growth rate of the subharmonic wave with frequency for the primary waves shown in figure 5.1. This figure shows that when the primary wave is a second mode, the subharmonic wave is strongly stabilized by cooling. Figures 5.3 and 5.4 are like figures 5.1 and 5.2, but at $M_\infty = 6.5$ and $B = 0.05$. They confirm the trends in figures 5.1 and 5.2.

So far, we have seen that when the primary wave is a second mode the most amplified primary wave is destabilized whereas the subharmonic wave is stabilized by cooling. This means that if we follow a certain wave as it propagates downstream we will have two counter effects. First cooling increases the amplitude of the primary wave and thus the growth rate of the subharmonic wave. Second, cooling stabilizes the subharmonic wave and thus decreases its growth rate. The two combined effects are shown in figures 5.5 and 5.6. Figure 5.5 shows that cooling shifts the onset of the subharmonic instability towards a higher Reynolds number. The growth rate of the cooled wall, however, catches up with the growth rate of the heated wall and exceeds it. Figure 5.6 shows that the N factor of the subharmonic wave when the plate is cooled is less than that when the plate is heated, which means that as a net result cooling stabilizes the subharmonic wave when the primary wave is a second-mode wave.

Figure 5.7 shows the variation of the growth rate of the subharmonic wave with the spanwise wavenumber when the primary wave is a second-mode wave at $M_\infty = 4.5$. This figure demonstrates the strong stabilizing effect of cooling on the subharmonic wave. It also shows a shift in the most amplified subharmonic mode towards a higher spanwise wavenumber as the cooling level increases.

Figure 5.8 shows the variation of the growth rate of the first-mode primary wave with frequency for different levels of heat transfer. As known in the literature (Mack, 1984) cooling stabilizes first-mode waves and shifts the most amplified wave (the peak) to a lower frequency. Figure 5.9 shows the variation of the growth rate of the subharmonic wave with frequency for the primary waves shown in figure 5.8. This figure shows that at the corresponding parameters, the effect of heat transfer on the subharmonic wave is small and might be stabilizing or destabilizing depending on the frequency. Figures 5.10 and 5.11 are like figures 5.8 and 5.9, but at $M_\infty = 2.0$, $R = 600$, and $B = 0.2$. They confirm the trends noted in figures 5.8 and 5.9.

Figure 5.12 shows the variation of the growth rate of the subharmonic wave with spanwise wavenumber when the primary wave is a first mode at $M_\infty = 4.5$. Two things can be noted in the figure. First, cooling tends to stabilize the subharmonic mode at lower spanwise wavenumbers but it destabilizes it at higher spanwise wavenumbers. Second, the most amplified subharmonic mode shifts towards a higher spanwise wavenumber as the cooling level increases.

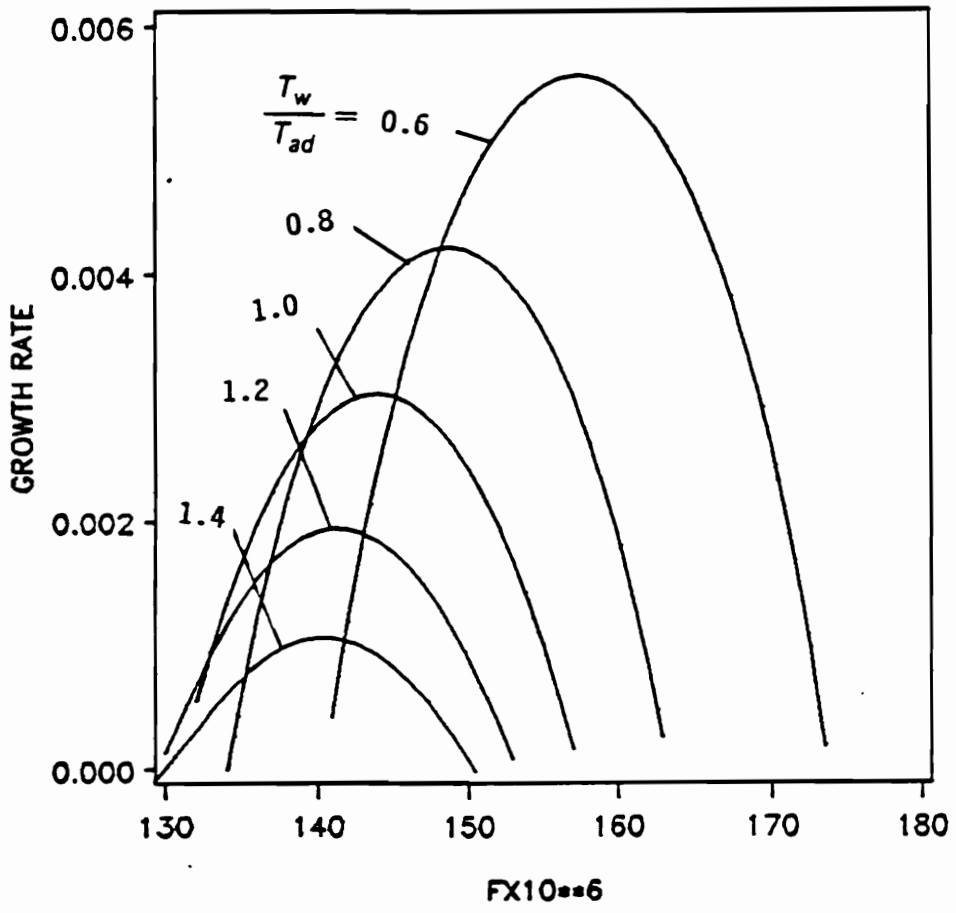

Figure 5.1. Variation of the growth rate of the second-mode wave with frequency for different levels of heat transfer at $M_\infty = 4.5$ and R = 1550.

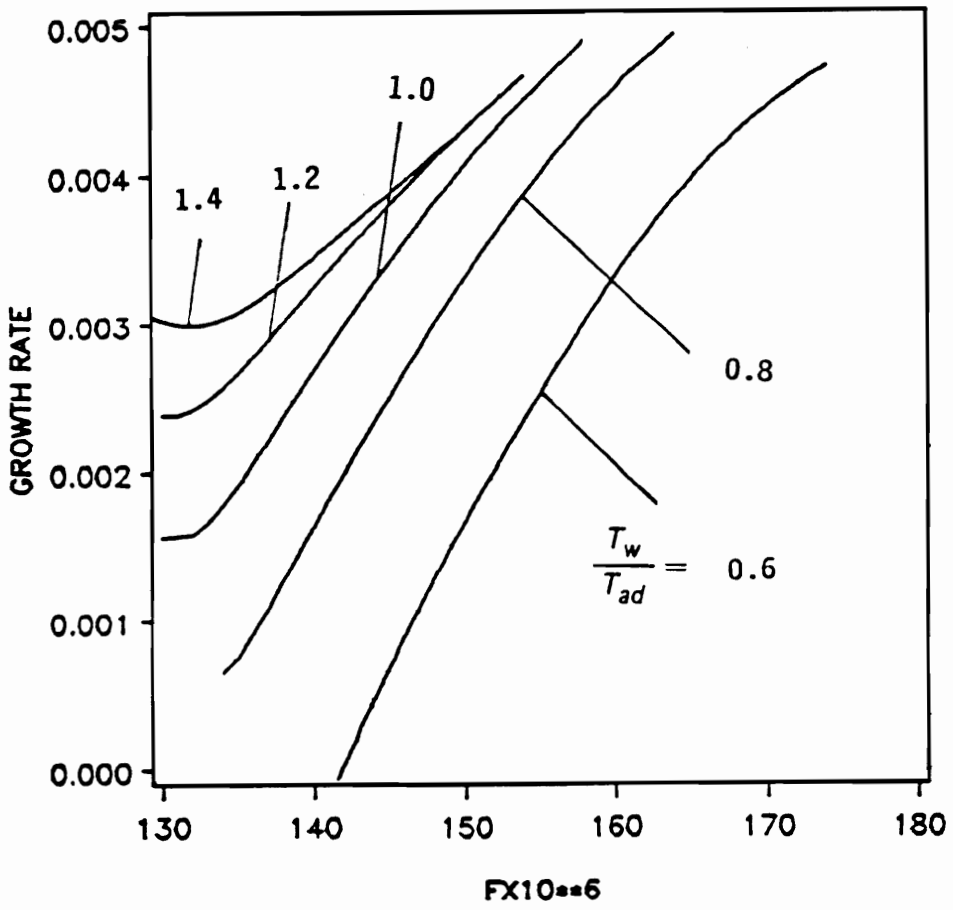

Figure 5.2. Variation of the growth rate of the subharmonic wave with the frequency of the primary wave when the primary wave is a second mode: $M_\infty = 4.5$, $R = 1550$, $\beta = 0.155$, and $A_{rms} = 0.01$.

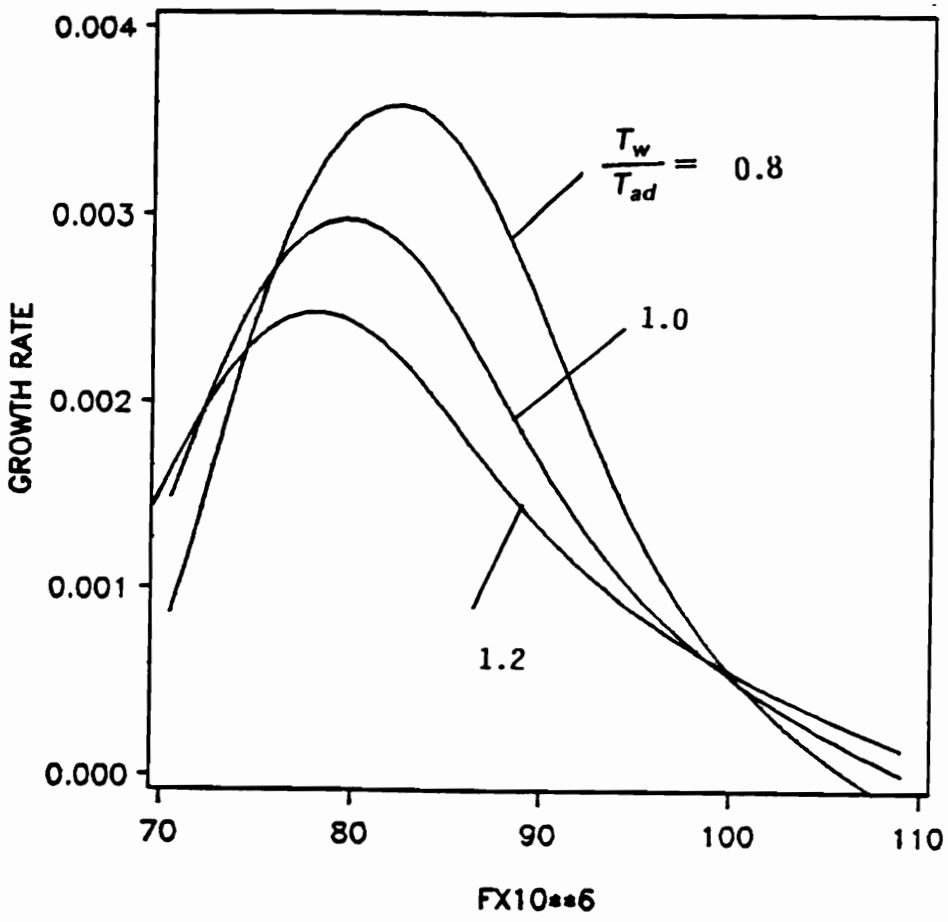

Figure 5.3. Variation of the growth rate of the second-mode primary wave with frequency for different levels of heat transfer at $M_\infty = 6.5$ and R = 1550.

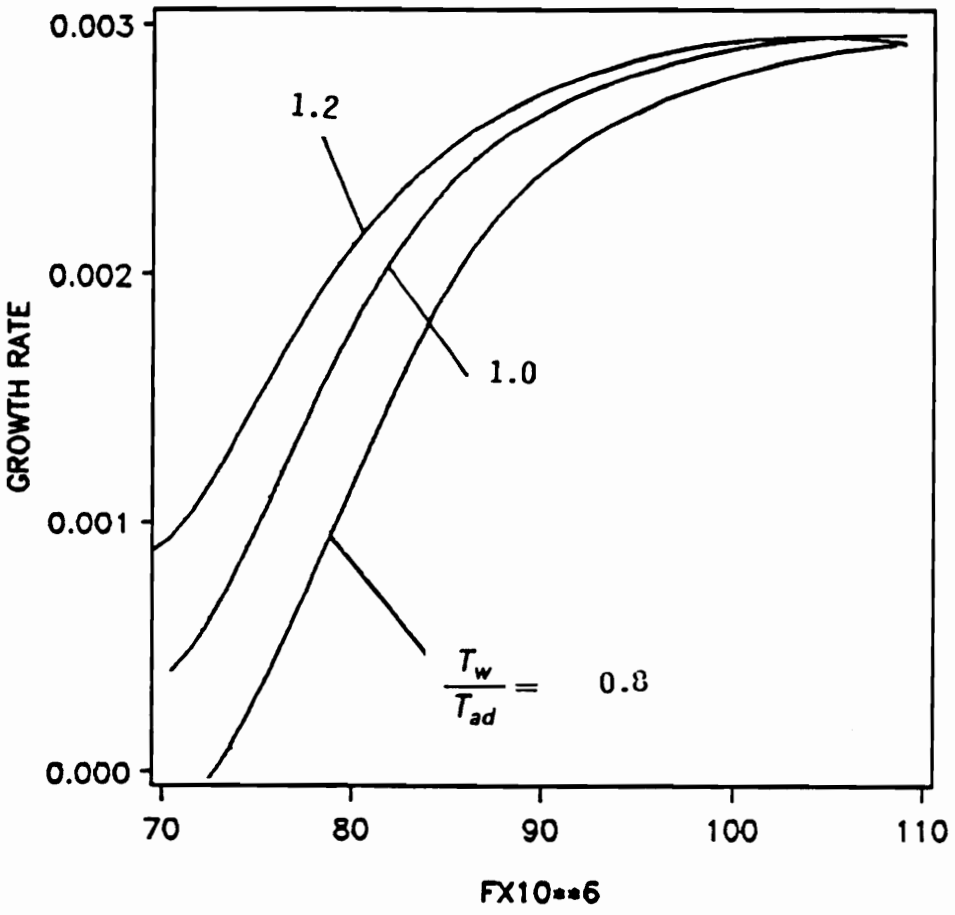

Figure 5.4. Variation of the growth rate of the subharmonic wave with the frequency of the primary wave when the primary wave is a second mode: $M_\infty = 6.5$, $R = 1550$, $\beta = 0.0775$, and $A_{rms} = 0.01$.

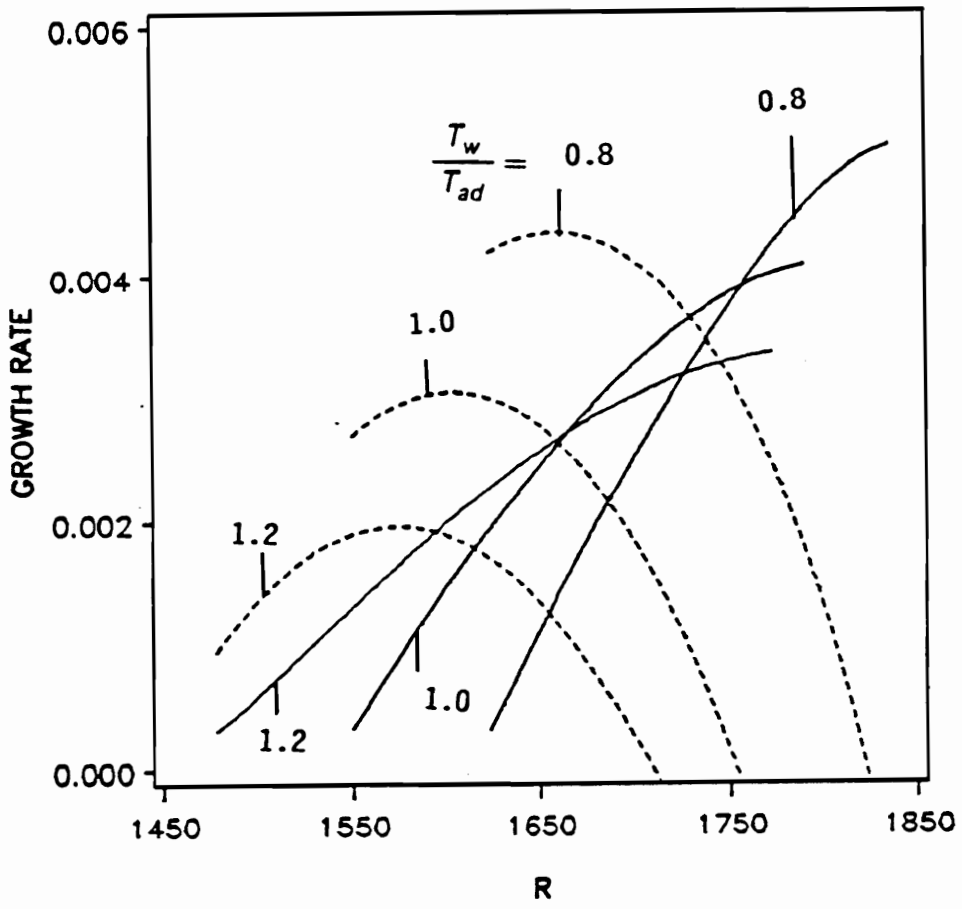

Figure 5.5. Variation of the growth rate of the second-mode primary wave (...) and the corresponding subharmonic wave (___) with Reynolds number from the onset of the subharmonic instability and for different levels of heat transfer: $M_\infty = 4.5$, $F_{2D} = 140x10^{-6}$, $B = 0.15$, and $A_{rms} = 0.002$ at the onset of the subharmonic instability.

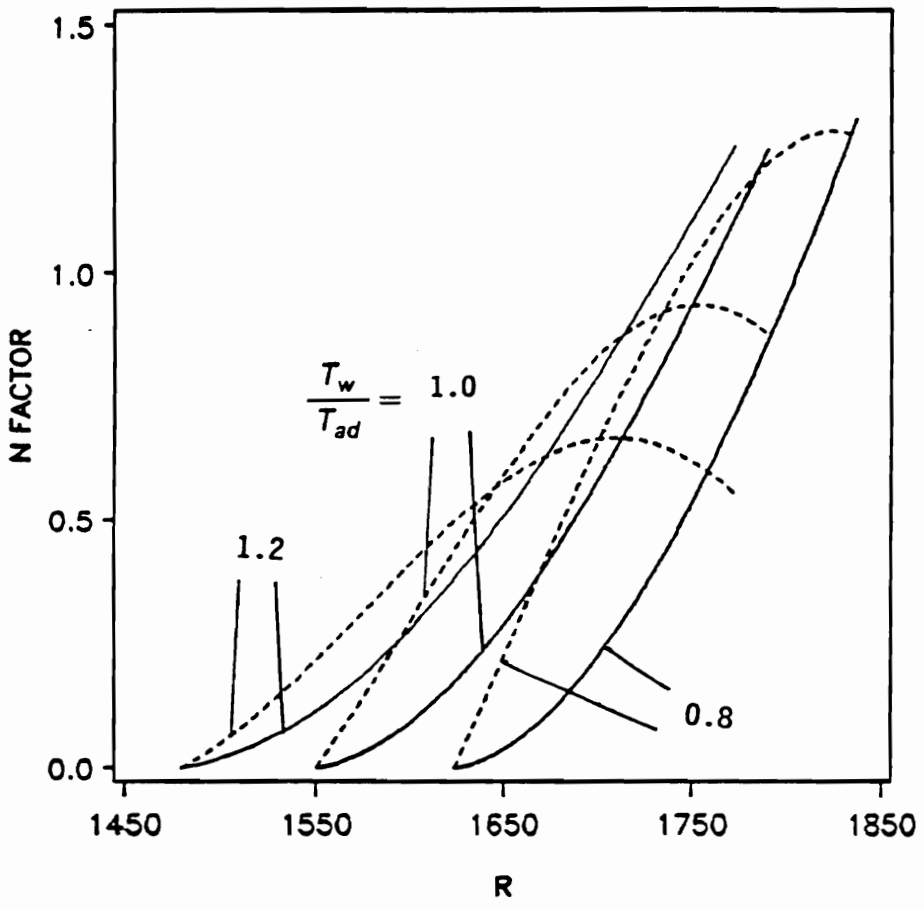

Figure 5.6. Variation of the N-factor of the second-mode primary wave (...) and the corresponding subharmonic wave (___) with Reynolds number from the onset of the subharmonic instability and for different levels of heat transfer: $M_\infty = 4.5$, $F_{2D} = 140x10^{-6}$, $B = 0.15$, and $A_{rms} = 0.002$ at the onset of the subharmonic instability.

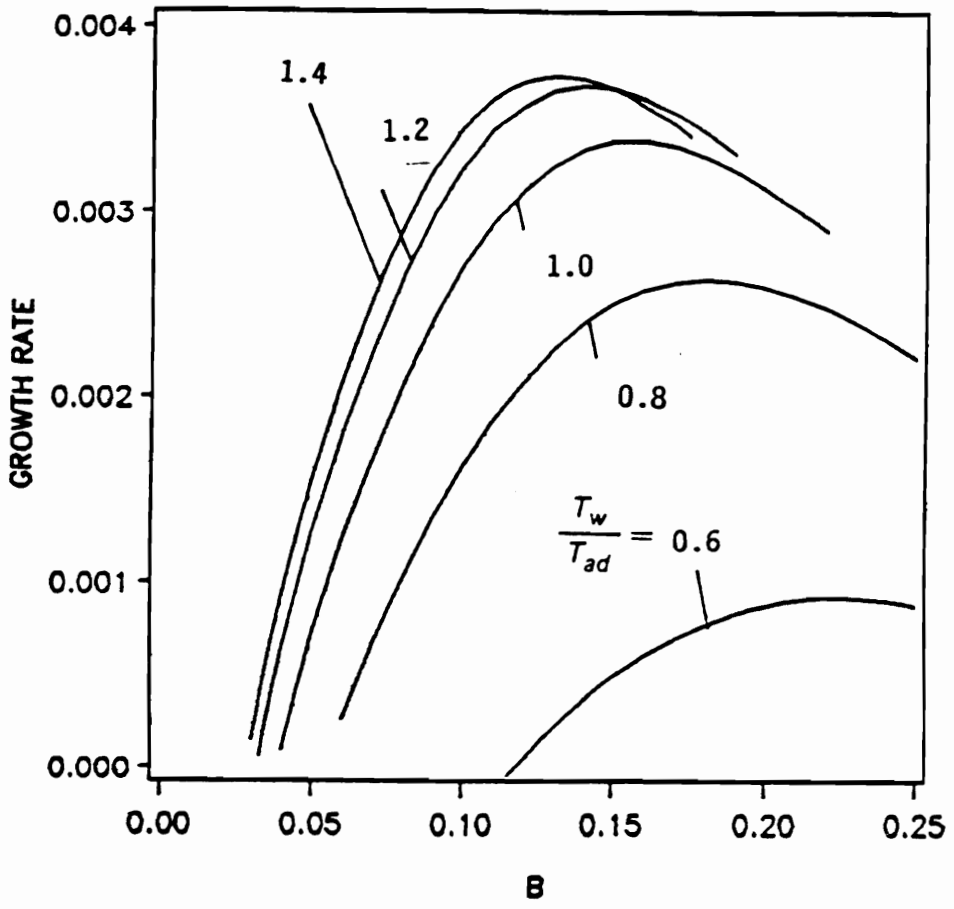

Figure 5.7. Variation of the growth rate of the subharmonic wave with spanwise wavenumber when the primary wave is a second mode: $M_\infty = 4.5$, $R = 1550$, $F_{2D} = 140x10^{-6}$, and $A_{rms} = 0.01$.

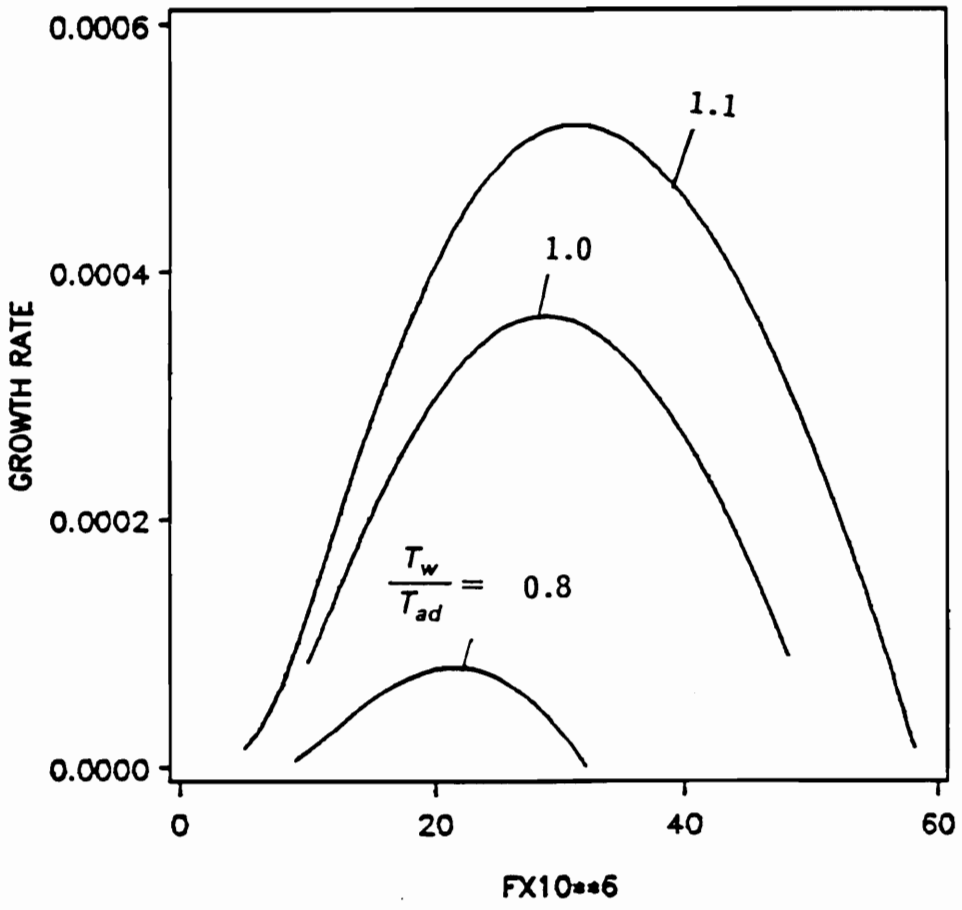

Figure 5.8. Variation of the growth rate of the first-mode primary wave with frequency for different levels of heat transfer at $M_\infty = 4.5$ and R = 1950.

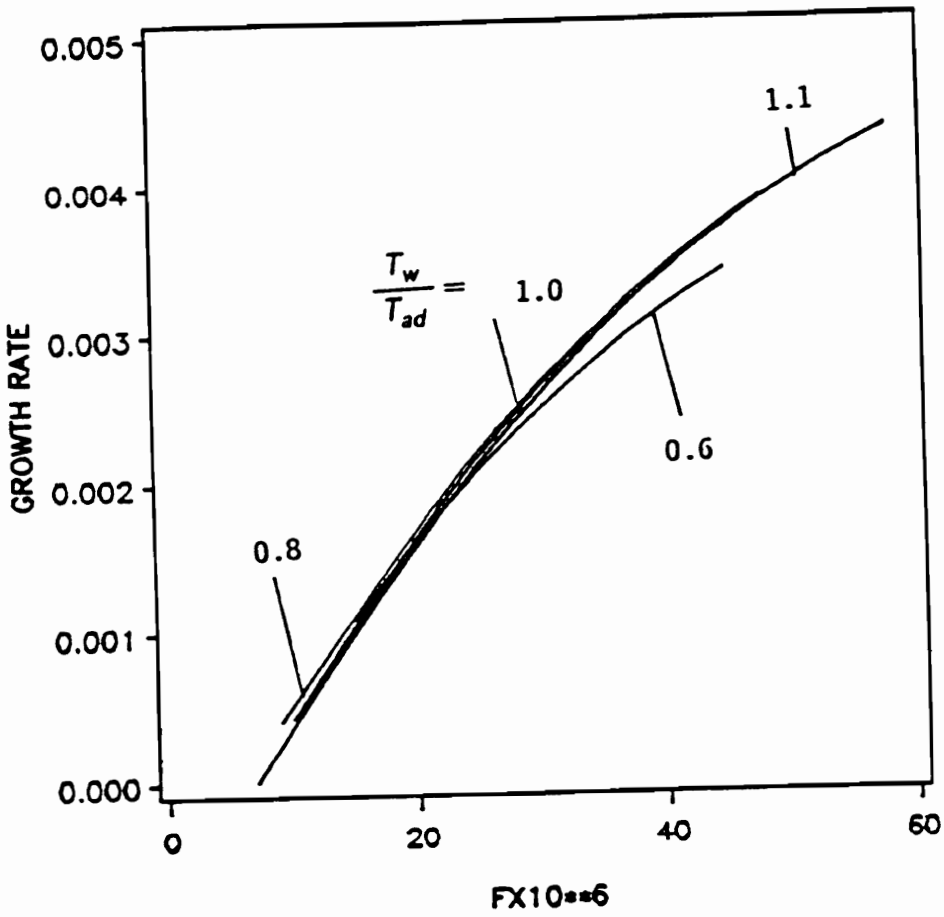

Figure 5.9. Variation of the growth rate of the subharmonic wave with the frequency of the primary wave when the primary wave is a first-mode wave: $M_\infty = 4.5$, $R = 1950$, $\beta = 0.195$, and $A_{rms} = 0.01$.

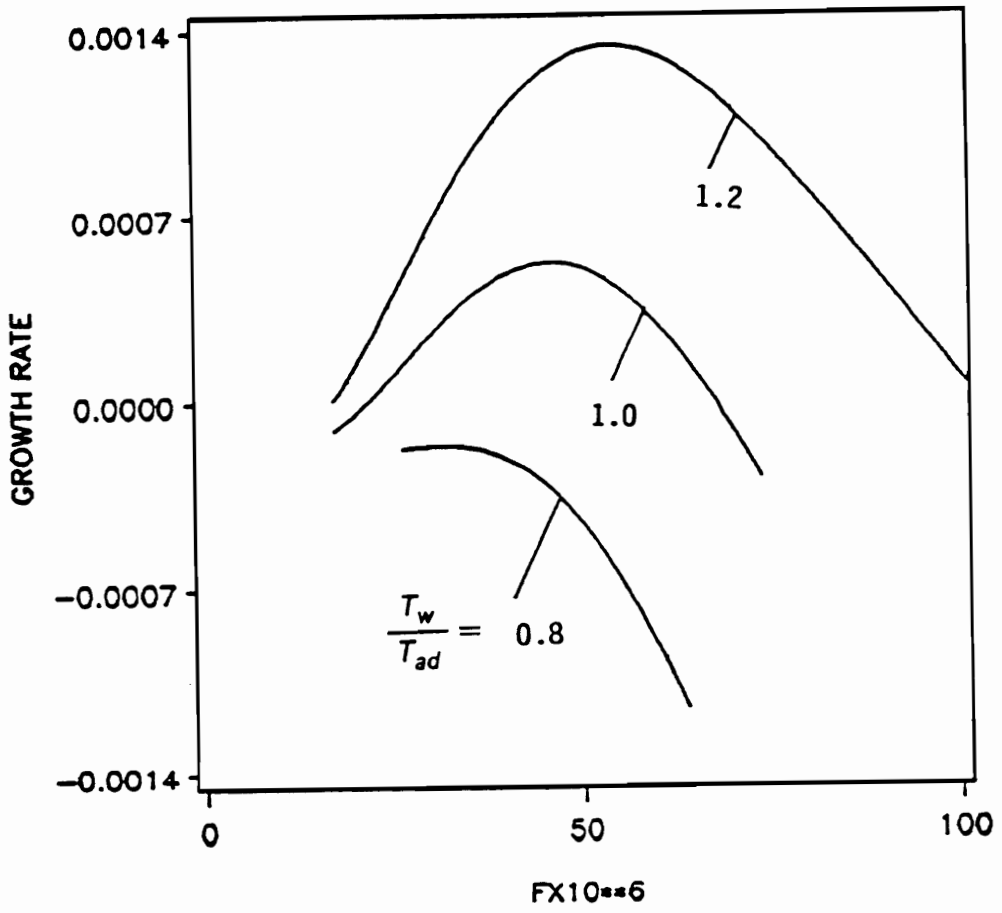

Figure 5.10. Variation of the growth rate of the first-mode primary wave with frequency for different levels of heat transfer at $M_\infty = 2.0$ and R = 600.

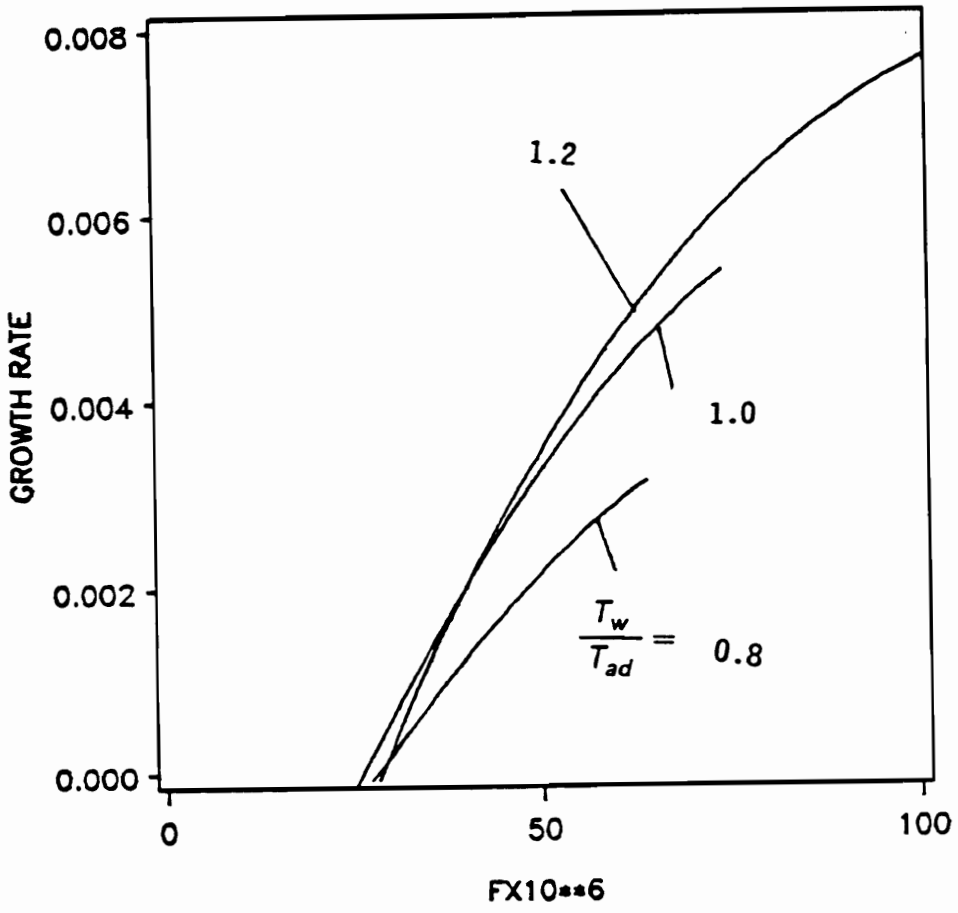

Figure 5.11. Variation of the growth rate of the subharmonic wave with the frequency of the primary wave when the primary wave is a first-mode wave: $M_\infty = 2.0$, $R = 600$, $\beta = 0.12$, and $A_{rms} = 0.01$.

M_∞	exact	formula	% error
1.00	1.16952	1.16971	-0.016
2.00	1.67751	1.67882	-0.078
3.00	2.52175	2.52735	-0.222
4.00	3.69920	3.71529	-0.435
5.00	5.20745	5.24264	-0.676
6.00	7.04500	7.10940	-0.914
7.00	9.21103	9.31558	-1.135
8.00	11.70507	11.86116	-1.334
9.00	14.52691	14.74616	-1.509
10.00	17.67643	17.97056	-1.664

Table 5.1. A comparison of the adiabatic wall temperature as computed directly with the adiabatic wall temperature calculated from the formula $T_{ad} = 1 + (\gamma - 1)\sqrt{Pr}\, M_\infty^2/2$. $T_\infty = 120°K$ and Pr = 0.72.

6. EFFECT OF SUCTION ON THE SUBHARMONIC INSTABILITY OF COMPRESSIBLE BOUNDARY LAYERS

The effect of suction on the subharmonic instability of a two-dimensional compressible boundary layer over an insulated flat plate is analyzed using the Floquet model. The resulting problem is solved numerically by using finite differences. Results are presented for different Mach numbers. For supersonic flows results for first- and second-mode primary waves are presented.

6.1. Results

We present results for the spatial stability at different Mach numbers. The frequency F, which is related to ω through $\omega = FR$, is kept constant when following a

certain wave. The spanwise wavenumber is defined as $B = 1000\beta/R$ and B is kept constant as the wave propagates downstream. For all the results presented in this chapter, T_∞ is kept constant and equal to 120°K, the Prandtl number Pr is kept constant and equal to 0.72, $m = \lambda/\mu = -0.2/3.0$, $\gamma = 1.4$, and the variation of viscosity with temperature is given by the Sutherland formula.

Figure 6.1 shows the variation of the growth rate of the second-mode primary wave with frequency for different levels of suction at $M_\infty = 4.5$. As was pointed out by Malik (1989), suction affects the second-mode primary wave by shifting the band of unstable frequencies to higher values and reduces the peak amplification. Figure 6.2 shows the variation of the growth rate of the subharmonic mode with the frequency of the primary wave for the primary waves shown in figure 6.1. Clearly, suction stabilizes the subharmonic mode when the primary wave is a second mode. At $M_\infty = 6.5$, figures 6.3 and 6.4 confirm the trends noted in figures 6.1 and 6.2.

Figure 6.5 shows the variation of the growth rate of the subharmonic wave with the spanwise wavenumber at $M_\infty = 4.5$ for different levels of suction, when the primary wave is a second-mode. This figure shows that as suction increases, (a) the subharmonic growth rate decreases, (b) the band of unstable spanwise wavenumbers decreases, and (c) the most amplified (the peak) subharmonic mode shifts towards a higher spanwise wavenumber.

Figure 6.6 shows the variation of the growth rate of the first-mode primary wave with frequency for different levels of suction at the subsonic Mach number $M_\infty = 0.1$. It shows that suction stabilizes first-mode waves, consisting with the known result. Figure 6.7 shows the variation of the growth rate of the subharmonic mode with the frequency of the primary wave, for the primary waves shown in figure 6.6. The subharmonic mode is clearly stabilized by suction. Figures 6.8 and 6.9 show that the trends noted in figures 6.6 and 6.7 still hold at $M_\infty = 2.0$. This is not the case,

however, at $M_\infty = 4.5$ as shown in figures 6.10 and 6.11. Figure 6.11 shows that at such a Mach number suction very slightly stabilizes the subharmonic mode at low frequencies and very slightly destabilizes it at relatively high frequencies. Overall, the effect of suction on the growth rate of the subharmonic wave at $M_\infty = 4.5$ when the primary wave is a first mode is negligible, and the three curves in figure 6.11 can hardly be distinguished from each other.

Figure 6.12 shows the variation of the growth rate of the subharmonic wave with the spanwise wavenumber at $M_\infty = 2.0$, for different levels of suction when the primary wave is a first mode. This figure shows that (a) the maximum growth rate decreases by suction, (b) the band of unstable spanwise wavenumbers decreases by increasing suction, and (c) there is a sharp cutoff at low spanwise wavenumbers.

Figure 6.13 shows the variation of the growth rate of the primary wave with frequency at $M_\infty = 4.5$. The peaks on the right correspond to second-mode waves whereas those on the left correspond to first-mode waves. The second mode merges with the first mode as the frequency decreases. Mack was the first one to demonstrate the merging of modes. Corresponding to figure 6.13 we have figure 6.14 which shows the variation of the growth rate of the subharmonic wave with the frequency of the primary wave. In figure 6.14 we note three regions. At high frequencies, the primary wave is a second mode, and the subharmonic wave is stabilized by suction. At low frequencies; the primary wave is a first mode, and the effect of suction is negligible. At moderate frequencies, the second mode merges with the first mode, and the subharmonic mode is strongly destabilized by suction. Figures 6.15 and 6.16 at $M_\infty = 6.5$ confirm the trends noted in figures 6.13 and 6.14. Figure 6.16 also shows that the effect of suction on the subharmonic mode when the primary wave is a first-mode is negligible, which leads us to believe that the effect

of suction on the growth rate of the subharmonic mode when the primary wave is a first mode is negligible at high Mach numbers.

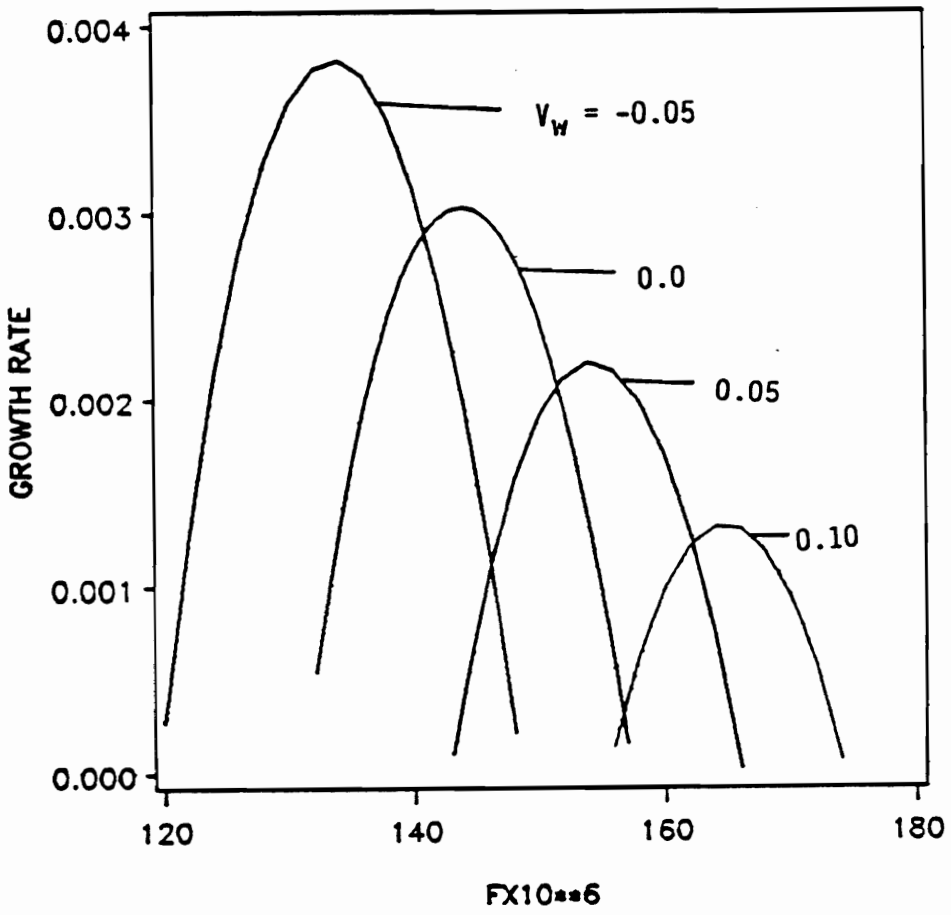

Figure 6.1. Variation of the growth rate of the second-mode primary wave with frequency for different levels of suction. $M_\infty = 4.5$ and R = 1550.

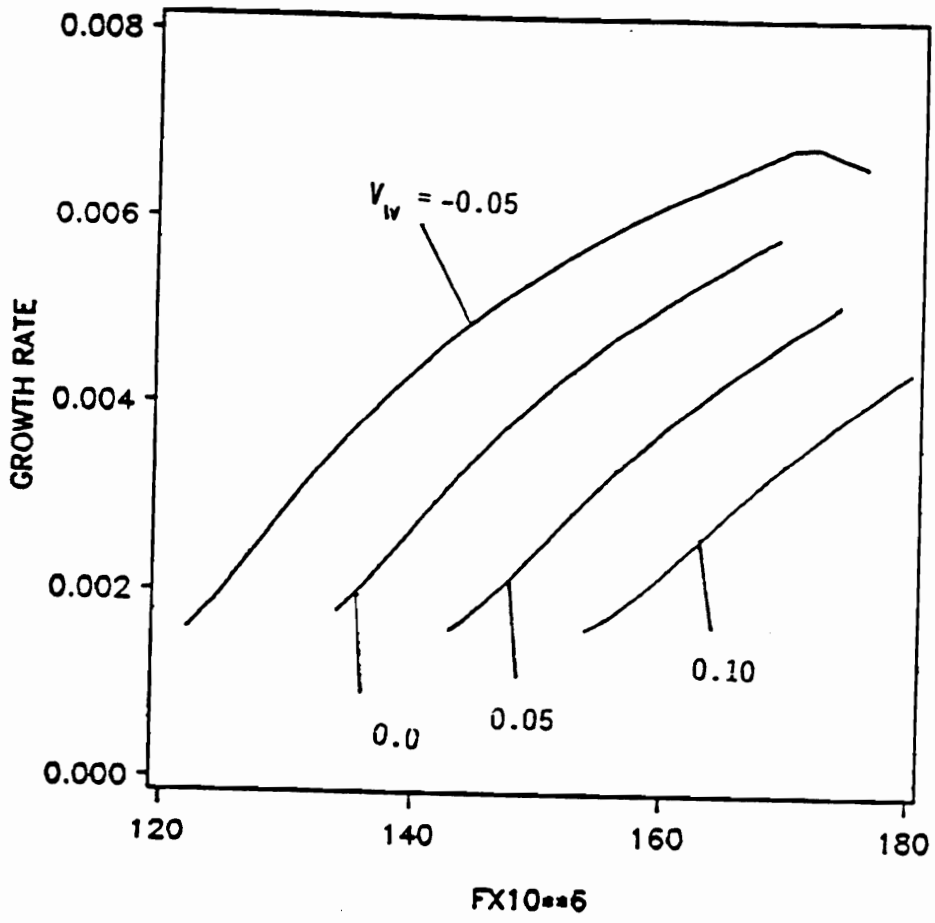

Figure 6.2. Variation of the growth rate of the subharmonic wave with the frequency of the primary wave when the primary wave is a second-mode and for different levels of suction. $M_\infty = 4.5$, R = 1550, $A_{rms} = 0.01$, and B = 0.1.

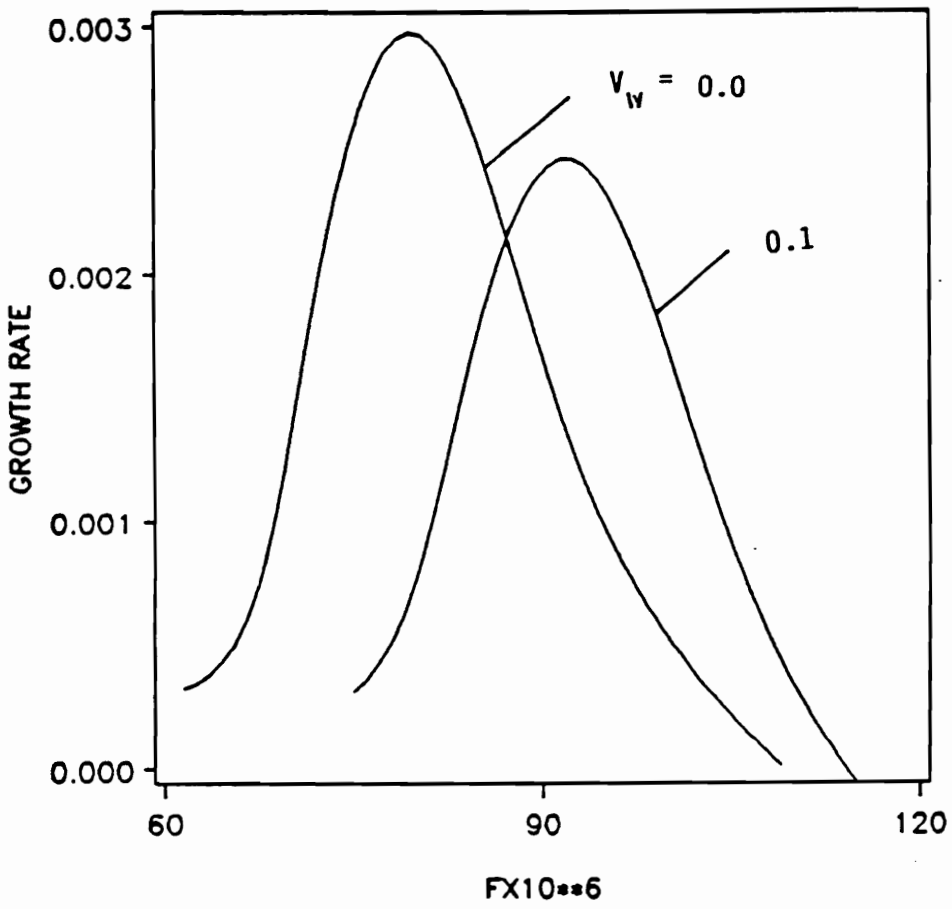

Figure 6.3. Variation of the growth rate of the second-mode primary wave with frequency for different levels of suction. $M_\infty = 6.5$ and R = 1550.

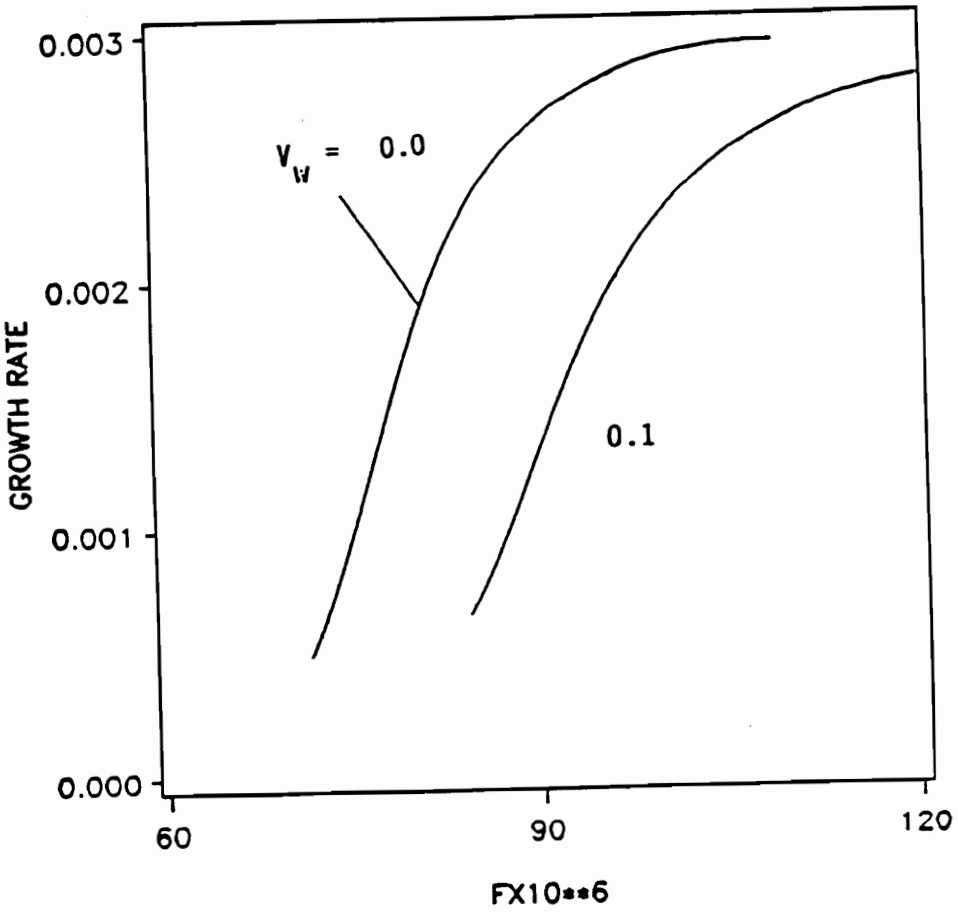

Figure 6.4. Variation of the growth rate of the subharmonic wave with the frequency of the primary wave when the primary wave is a second-mode and for different levels of suction. $M_\infty = 6.5$, R = 1550, $A_{rms} = 0.01$, and B = 0.05.

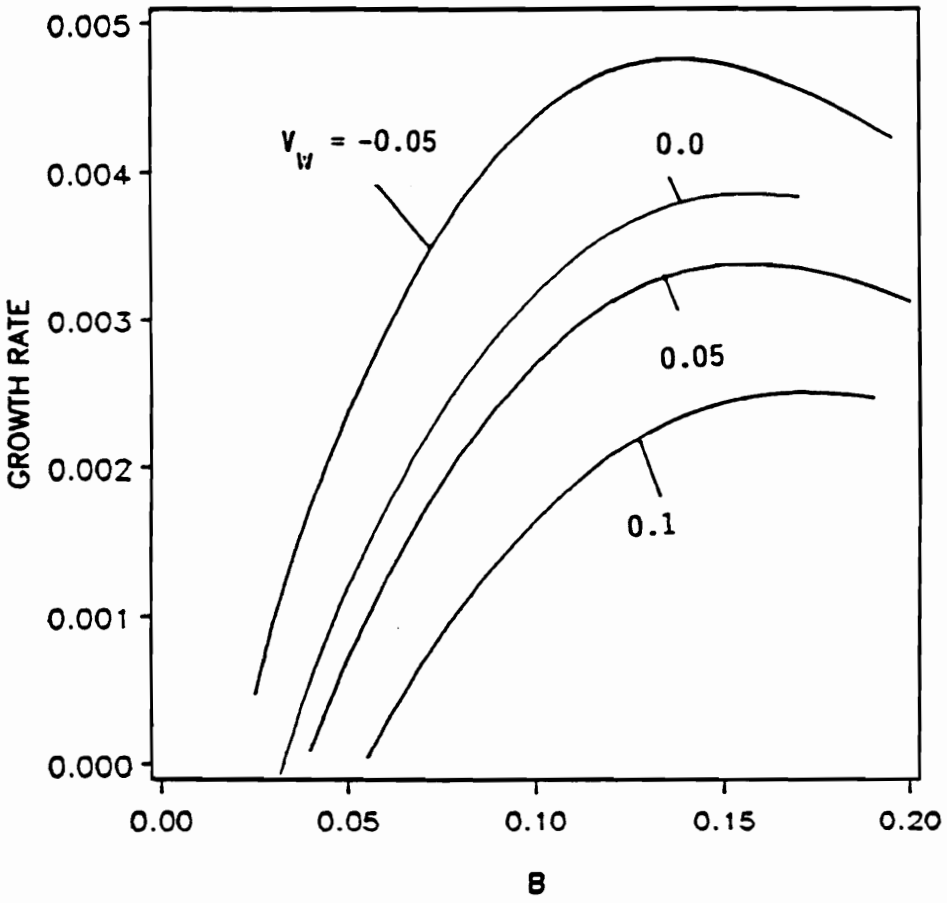

Figure 6.5. Variation of the growth rate of the subharmonic wave with the spanwise wavenumber for different levels of suction when the primary wave is a second mode. $M_\infty = 4.5$, $F_{2D} = 140x10^{-6}$, R = 1550, and $A_{rms} = 0.01$.

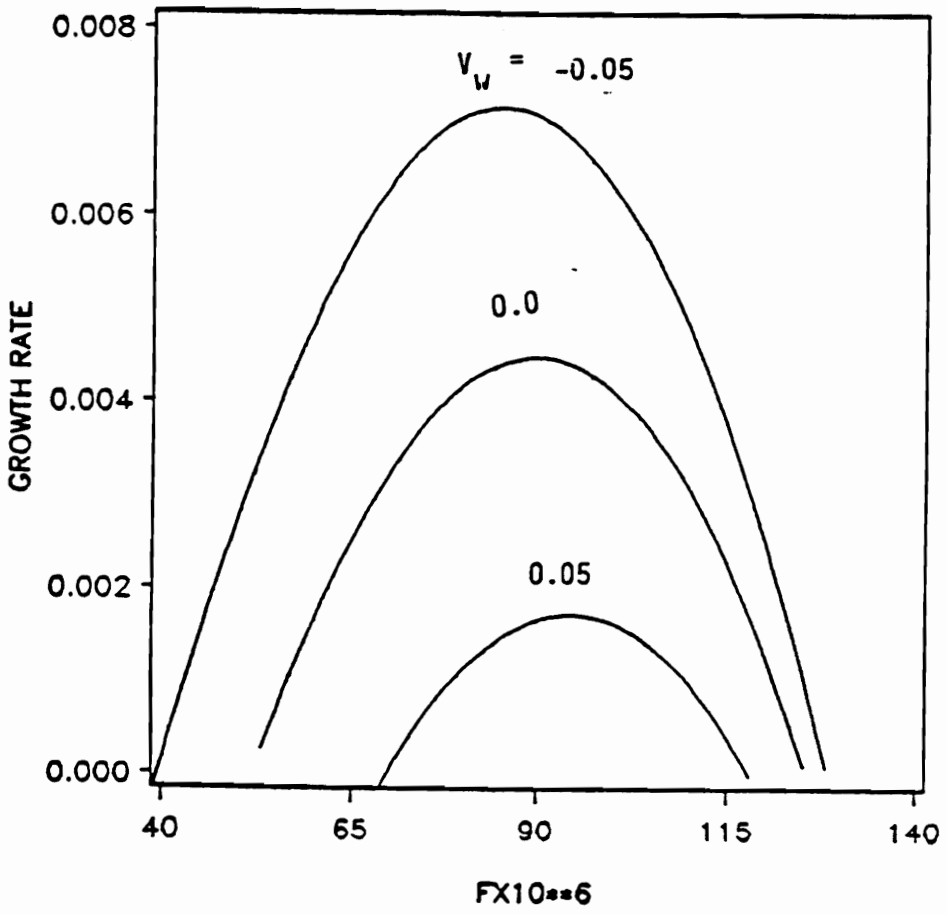

Figure 6.6. Variation of the growth rate of the first-mode primary wave with frequency for different levels of suction. $M_\infty = 0.1$ and R = 600.

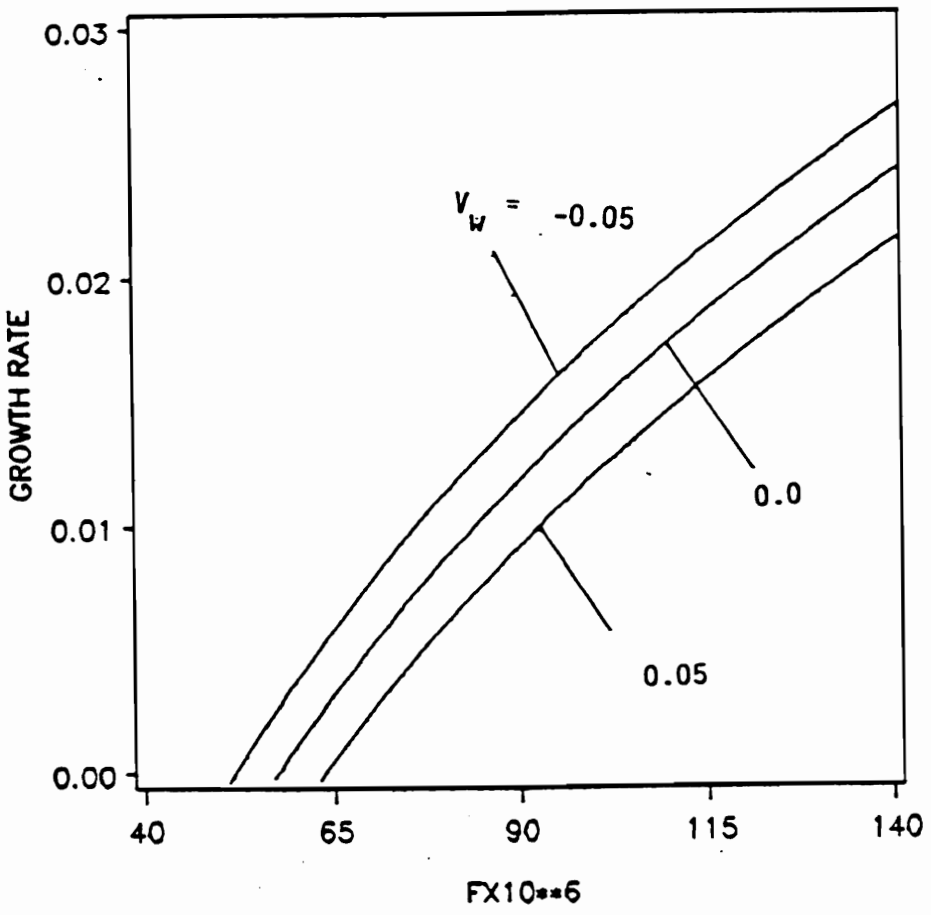

Figure 6.7. Variation of the growth rate of the subharmonic wave with the frequency of the primary wave when the primary wave is a first-mode and for different levels of suction. $M_\infty = 0.1$, R = 600, $A_{rms} = 0.01$, and B = 0.3.

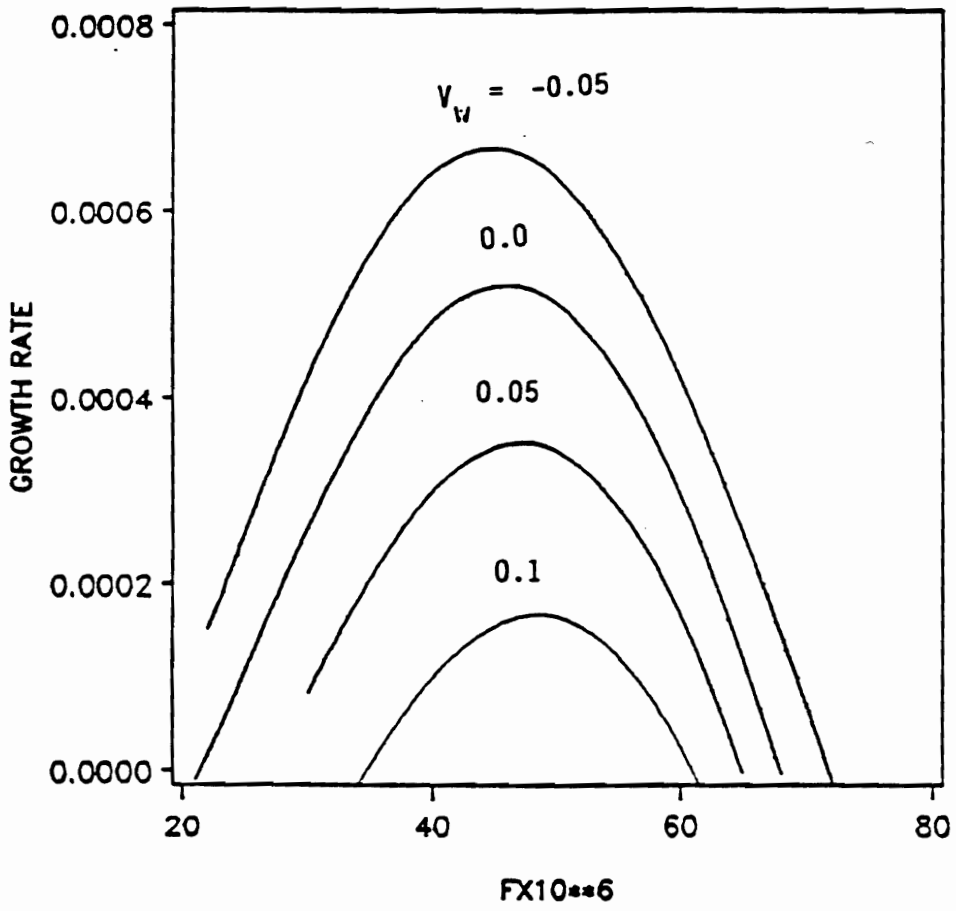

Figure 6.8. Variation of the growth rate of the first-mode primary wave with frequency for different levels of suction. $M_\infty = 2.0$ and R = 600.

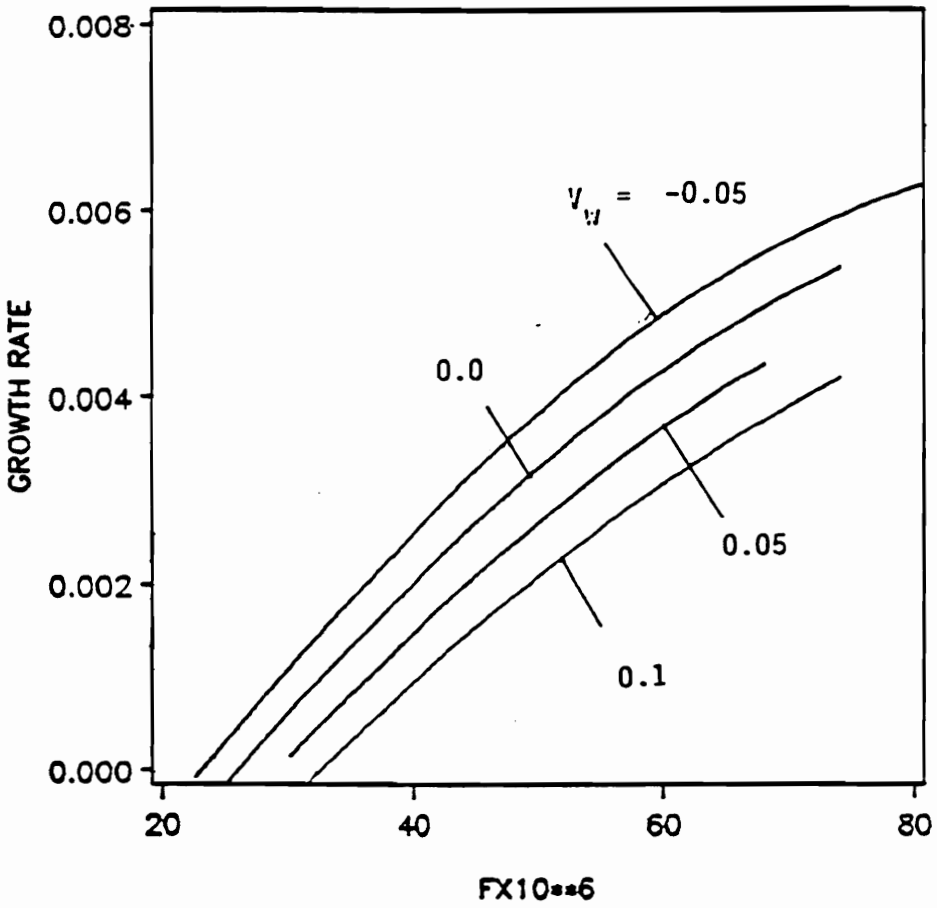

Figure 6.9. Variation of the growth rate of the subharmonic wave with the frequency of the primary wave when the primary wave is a first-mode and for different levels of suction. $M_\infty = 2.0$, R = 600, $A_{rms} = 0.01$, and B = 0.2.

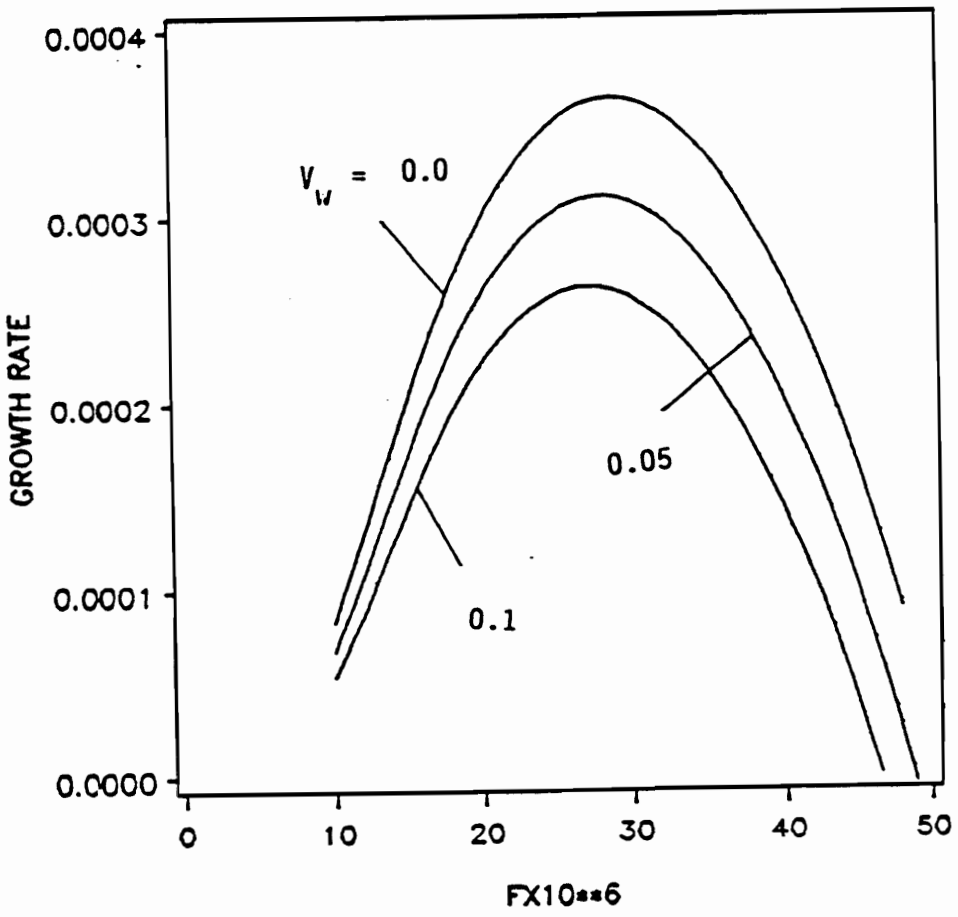

Figure 6.10. Variation of the growth rate of the first-mode primary wave with frequency for different levels of suction. $M_\infty = 4.5$ and R = 1950.

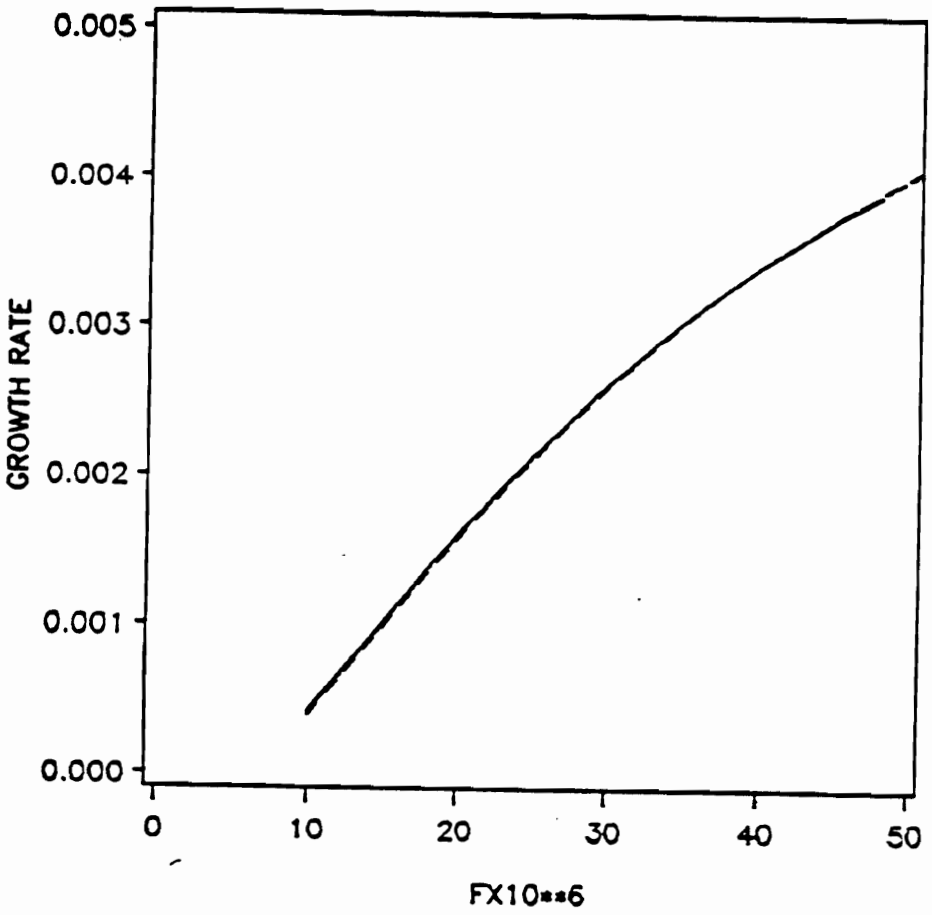

Figure 6.11. Variation of the growth rate of the subharmonic wave with the frequency of the primary wave when the primary wave is a first-mode and for different levels of suction. (___) $V_w = 0.0$, (...) $V_w = 0.05$, and (- - -) $V_w = 0.1$. $M_\infty = 4.5$, $R = 1950$, $A_{rms} = 0.01$, and B = 0.1.

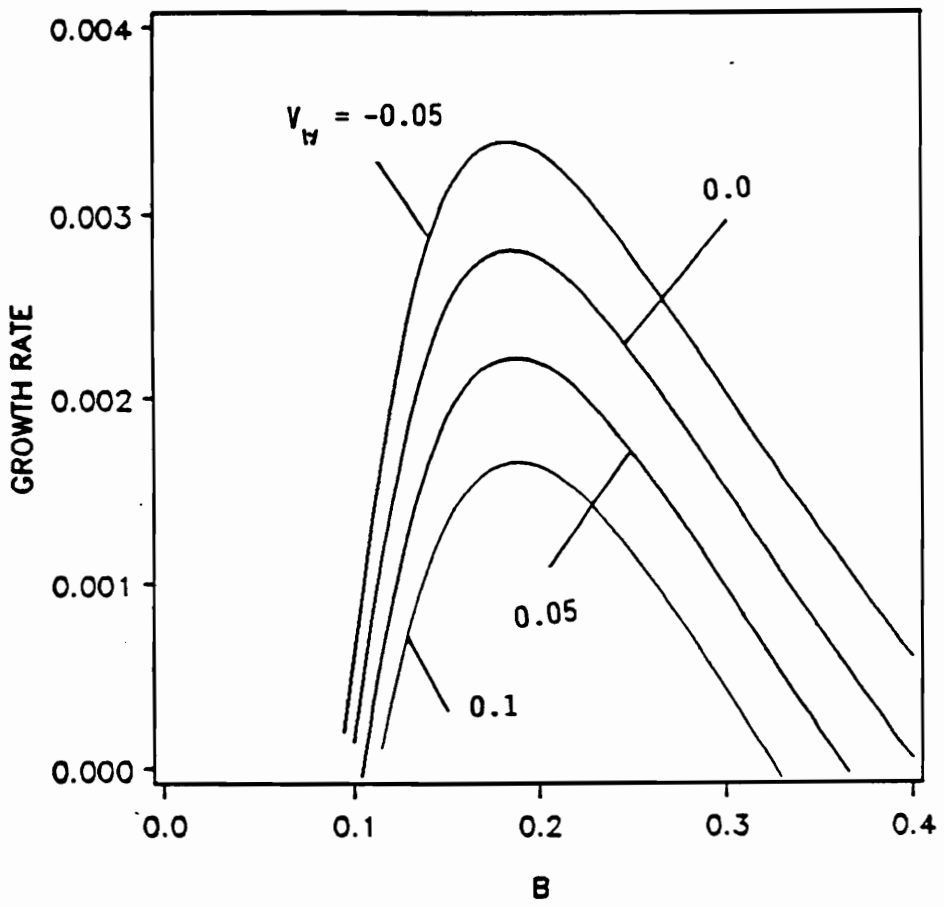

Figure 6.12. Variation of the growth rate of the subharmonic wave with the spanwise wavenumber for different levels of suction when the primary wave is a first mode. $M_\infty = 2.0$, $F_{2D} = 46x10^{-6}$, R = 600, and $A_{rms} = 0.01$.

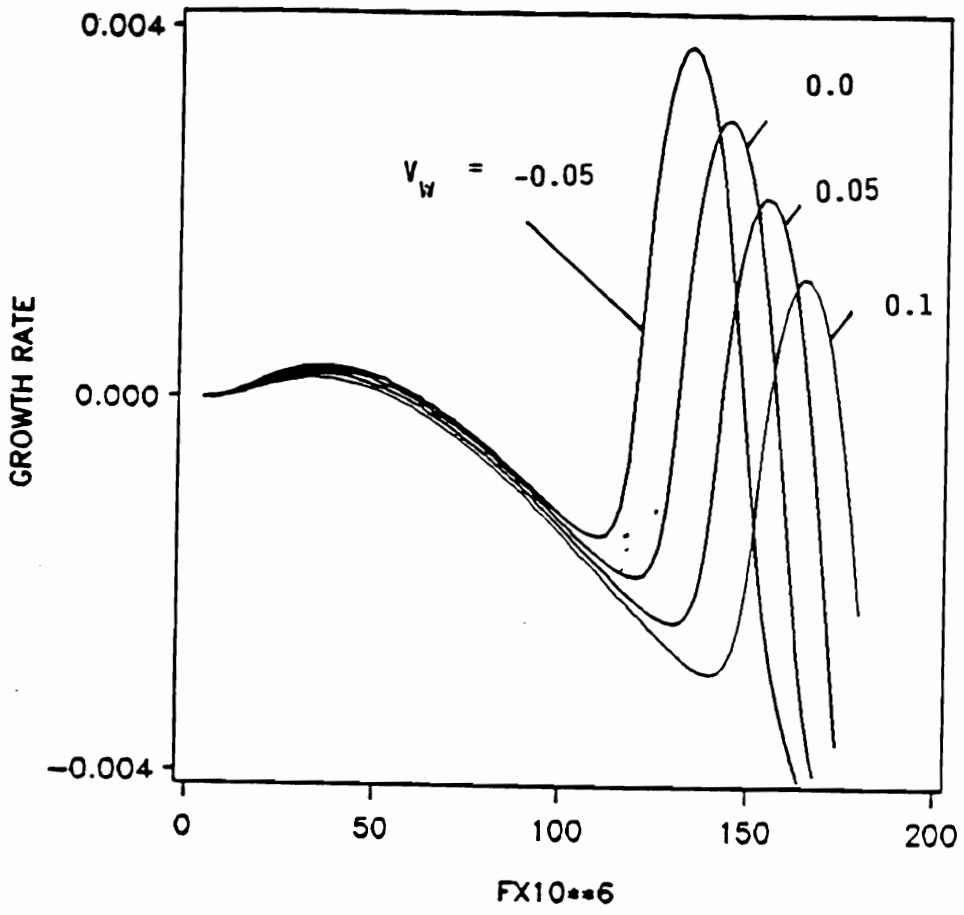

Figure 6.13. Variation of the growth rate of the primary wave with frequency for different levels of suction. $M_\infty = 4.5$ and R = 1550.

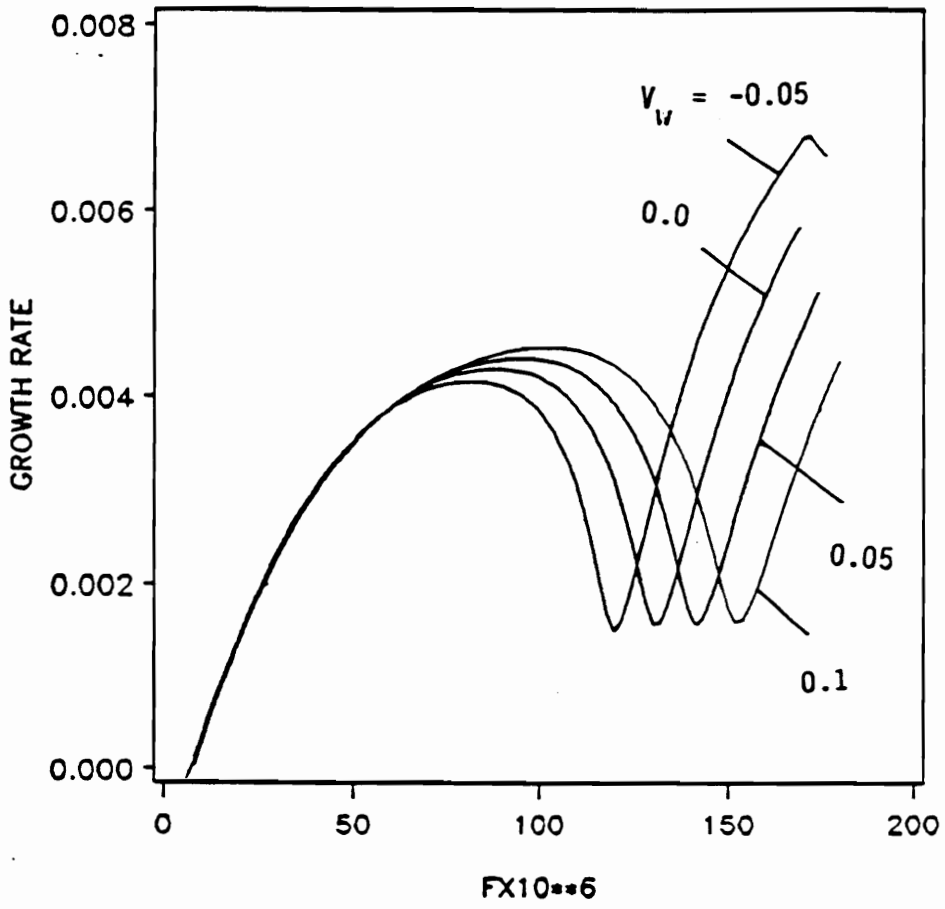

Figure 6.14. Variation of the growth rate of the subharmonic wave with the frequency of the primary wave when the primary wave is that considered in figure 13, and for different levels of suction. $M_\infty = 4.5$, R = 1550, $A_{rms} = 0.01$, and B = 0.1.

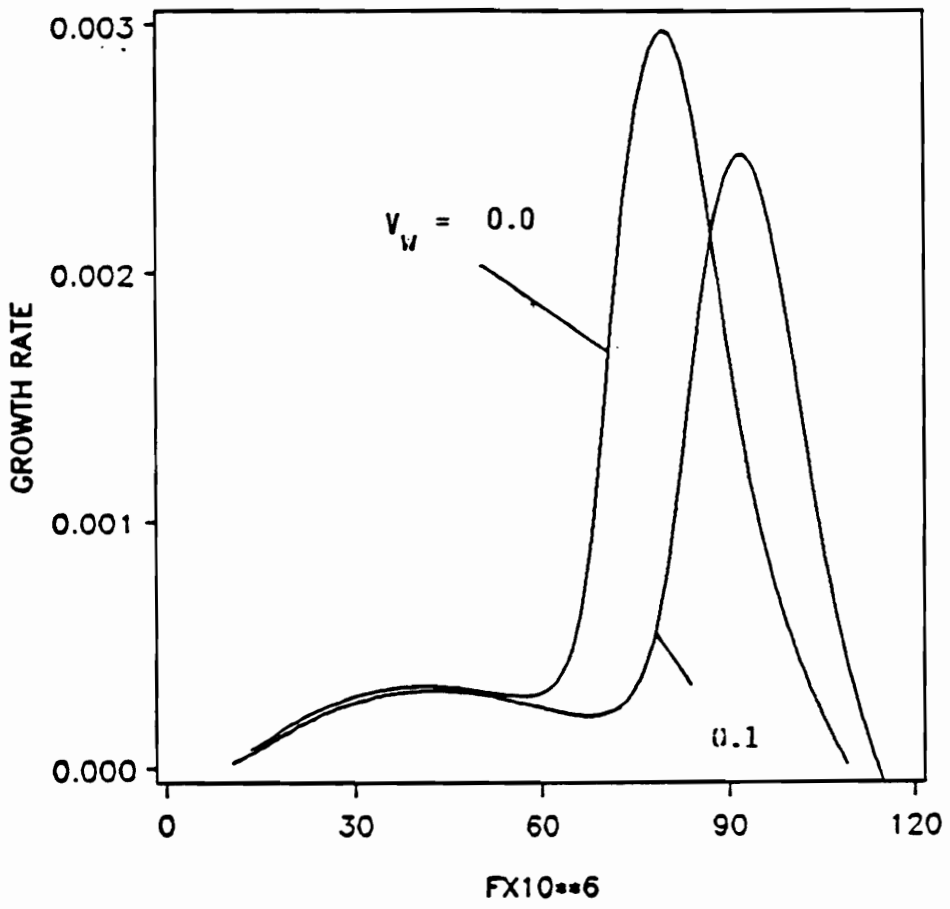

Figure 6.15. Variation of the growth rate of the primary wave with frequency for different levels of suction. $M_\infty = 6.5$ and R = 1550.

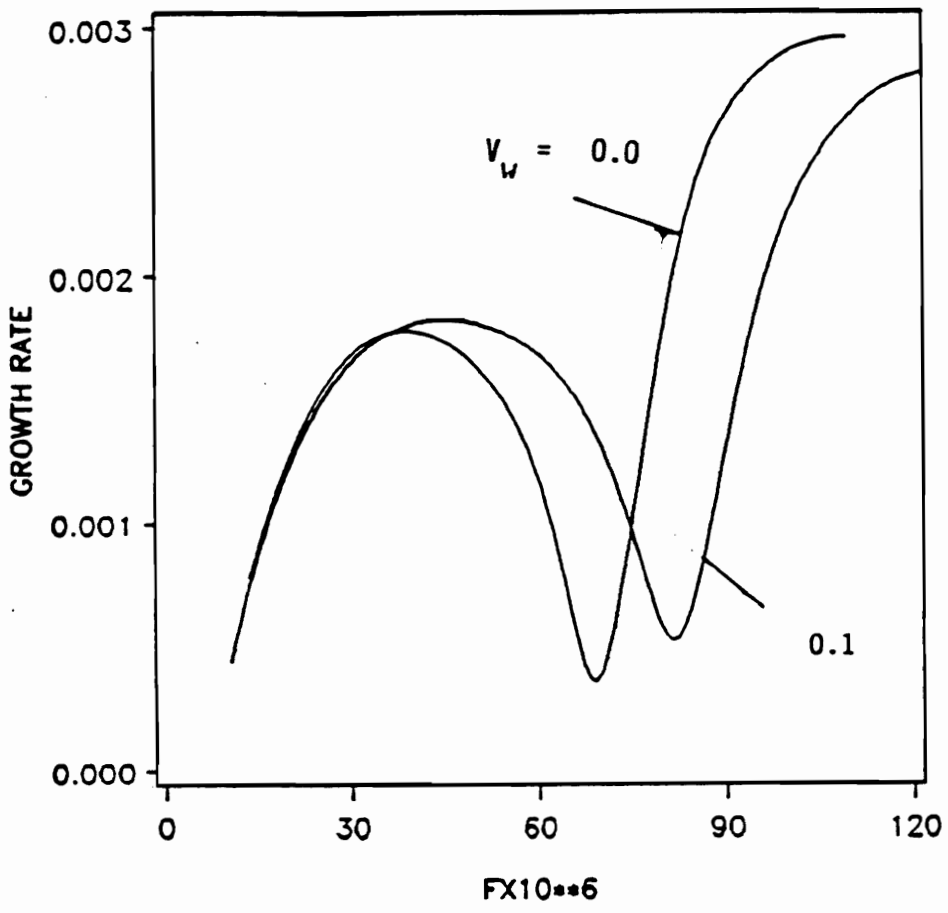

Figure 6.16. Variation of the growth rate of the subharmonic wave with the frequency of the primary wave when the primary wave is that considered in figure 15, and for different levels of suction. $M_\infty = 6.5$, R = 1550, $A_{rms} = 0.01$, and B = 0.05.

7. EFFECT OF A BULGE ON THE SUBHARMONIC INSTABILITY OF COMPRESSIBLE BOUNDARY LAYERS

The effect of a 2-D hump on the 3-D compressible subharmonic instability on a flat plate is investigated. The mean flow is calculated by using interacting boundary layers, thereby accounting for viscid/inviscid interactions. The results show that increasing the hump height produces an increase in the amplification factors of both the primary and subharmonic waves. When the hump causes separation, the growth rates of both the primary and subharmonic waves are considerably larger than those in the case of no separation. The effect of compressibility on reducing the amplification factors of the primary and subharmonic waves decreases as the hump height increases.

7.1. Mean Flow

The 2-D compressible laminar boundary layer over the plate and the hump is determined by solving the interacting boundary-layer equations (Davis and Werle, 1982; Ragab and Nayfeh, 1982). These equations account for upstream influence through the interaction of the viscous flow with the inviscid flow outside the boundary layer. Moreover, they are also capable of capturing separation bubbles without difficulties. Solutions are obtained by using a second-order finite-difference method in which the grid spacings acknowledge the scalings predicted by triple-deck theory in the interaction region.

Figure 3.1 shows a small symmetric hump of height h^* and width $2b^*$ whose center is located at x_m^*. We introduce dimensionless variables by using L^* and U_∞^*, where L^* is the distance from the leading edge of the plate to a reference point, as reference quantities. In terms of dimensionless variables, the hump shape is given by

$$y = \frac{y^*}{L^*} = \frac{h^*}{L^*} f(\zeta) = hf(\zeta) \tag{7.1}$$

where h^* is the height of the hump and

$$\zeta = \frac{x^* - x_m^*}{b^*} = \frac{x - x_m}{b} \tag{7.2}$$

We present numerical results for the Walker and Greening hump

$$f(\zeta) = \begin{cases} h(1 - 12\zeta^2 + 16\zeta^3), & \text{if } \zeta \le 0.5 \\ 0 & \text{if } \zeta > 0.5 \end{cases} \tag{7.3}$$

The flowfield over the plate with the hump is assumed to be governed by the steady 2-D compressible boundary-layer equations

$$\frac{\partial(\rho u)}{\partial x} + \frac{\partial(\rho v)}{\partial y} = 0 \tag{7.4}$$

$$\rho u \frac{\partial u}{\partial x} + \rho v \frac{\partial u}{\partial y} = u_e \frac{du_e}{dx} + \frac{1}{Re} \frac{\partial}{\partial y}\left(\mu \frac{\partial u}{\partial y}\right) \tag{7.5}$$

$$\begin{aligned} \rho u \frac{\partial T}{\partial x} + \rho v \frac{\partial T}{\partial y} &= -(\gamma - 1) M_\infty^2 u u_e \frac{du_e}{dx} \\ &+ \frac{1}{RePr} \frac{\partial}{\partial y}\left(\kappa \frac{\partial T}{\partial y}\right) + \frac{(\gamma - 1)}{Re} M_\infty^2 \mu \left(\frac{\partial u}{\partial y}\right)^2 \end{aligned} \tag{7.6}$$

where u_e is the streamwise edge velocity and

$$Re = \frac{U_\infty^* L^* \rho_\infty^*}{\mu_\infty^*}, \; M_\infty = \frac{U_\infty^*}{\sqrt{\gamma R^* T_\infty^*}}, \; Pr = \frac{\mu_\infty^* C_p^*}{\kappa_\infty^*} \text{ and } \gamma = \frac{C_p^*}{C_v^*} \tag{7.7}$$

Here, R^* is the gas constant and C_p^* and C_v^* are the gas specific heat coefficients at constant pressure and volume, respectively. For perfect gas the dimensionless equation of state has the form

$$\rho T = \rho_e T_e \tag{7.8}$$

At the wall, the boundary conditions are

$$u = 0, \; v = 0, \text{ and } \frac{\partial T}{\partial y} = 0 \text{ at } y = hf[\zeta(x)] \tag{7.9}$$

Away from the wall,

$$u \to u_e \text{ and } T \to T_e \text{ as } y \to \infty \tag{7.10}$$

To solve Eqs. (7.4)-(7.10), we first use the Prandtl transposition theorem, let

$$z = y - hf[\zeta(x)],\ w = v - hu\frac{df}{dx}[\zeta(x)] \tag{7.11}$$

and rewrite the problem as

$$\frac{\partial(\rho u)}{\partial x} + \frac{\partial(\rho w)}{\partial z} = 0 \tag{7.12}$$

$$\rho u\frac{\partial u}{\partial x} + \rho w\frac{\partial u}{\partial z} = u_e\frac{du_e}{dx} + \frac{1}{Re}\frac{\partial}{\partial z}\left(\mu\frac{\partial u}{\partial z}\right) \tag{7.13}$$

$$\begin{aligned}\rho u\frac{\partial T}{\partial x} + \rho w\frac{\partial T}{\partial z} &= -(\gamma-1)M_\infty^2 u u_e\frac{du_e}{\partial x} \\ &+ \frac{1}{RePr}\frac{\partial}{\partial z}\left(\kappa\frac{\partial T}{\partial z}\right) + \frac{(\gamma-1)M_\infty^2}{Re}\mu\left(\frac{\partial u}{\partial z}\right)^2\end{aligned} \tag{7.14}$$

$$u = w = \frac{\partial T}{\partial z} = 0 \text{ at } z = 0 \tag{7.15}$$

$$u \to u_e \text{ and } T \to T_e \text{ as } z \to \infty \tag{7.16}$$

Then, we introduce the Levy-Lees variables

$$\xi = \int_0^x \rho_e\mu_e u_e dx,\ \eta = u_e\sqrt{\frac{Re}{2\xi}}\int_0^z \rho dz \tag{7.17}$$

$$F = \frac{u}{u_e},\ Q = \frac{T}{T_e},\ V = \frac{\sqrt{2\xi}}{\rho_e u_e\mu_e}\left[\sqrt{Re}\,\rho w + \eta_x\sqrt{2\xi}\,F\right] \tag{7.18}$$

and rewrite Eqs. (7.12)-(7.16) as

$$2\xi FF_\xi + VF_\eta - \frac{\partial}{\partial\eta}(\theta F_\eta) + \beta_0(F^2 - Q) = 0 \tag{7.19}$$

$$2\xi F_\xi + V_\eta + F = 0 \tag{7.20}$$

$$2\xi FQ_\xi + VQ_\eta - \frac{\partial}{\partial\eta}\left(\frac{\theta}{Pr}Q_\eta\right) - (\gamma - 1)M_\infty^2 \frac{u_e^2}{T_e}\theta F_\eta^2 = 0 \tag{7.21}$$

$$F = V = Q_\eta = 0 \text{ at } \eta = 0 \tag{7.22}$$

$$F \to 1 \text{ and } Q \to 1 \text{ as } \eta \to \infty \tag{7.23}$$

$$F = F(\xi_0, \eta) \text{ and } Q = Q(\xi_0, \eta) \text{ at } \xi = \xi_0 \tag{7.24}$$

where ξ_0 corresponds to a location upstream of the interaction region and

$$\theta = \frac{\rho\mu}{\rho_e\mu_e}, \beta_0 = \frac{2\xi}{u_e}\frac{du_e}{d\xi} \tag{7.25}$$

With u_e specified by the inviscid flow over the hump surface, Eqs. (7.19)-(7.24) represent a conventional boundary-layer theory. However, in the presence of separation or strong viscid/inviscid interactions, these equations fail to provide a solution, and one needs to use triple-deck theory or interacting boundary layers or the Navier-Stokes equations. The hump sizes of interest in the present study induce strong viscid/inviscid interaction. Hence, one needs to employ interacting boundary layers or the Navier-Stokes equations. To economize the computer effort, we use interacting boundary layers. The interaction law relates the edge velocity u_e to the scaled displacement surface $\delta\sqrt{Re}$ as

$$\delta\sqrt{Re} = \frac{\sqrt{2\xi}}{\rho_e u_e}\int_0^\infty (Q - F)d\eta \tag{7.26}$$

Using thin airfoil theory, we have

$$u_e = \bar{u}_e + \frac{1}{\beta\pi}\int_{L.E.}^{\infty} u_e\delta\,\frac{d(\ell_n\rho_e)/dt}{x-t}\,dt + \frac{1}{\beta\pi}\int_{L.E.}^{\infty}\frac{d(u_e\delta)/dt}{x-t}\,dt \tag{7.27}$$

where $\beta = \sqrt{1 - M_\infty^2}$ and $\bar{u}_e$ is the inviscid surface velocity in the absence of the boundary layer, which is also given by thin airfoil theory as

$$\bar{u}_e = 1 + \frac{1}{\beta\pi}\int_{L.E.}^{\infty}\frac{d(f)/dt}{x-t}\,dt \tag{7.28}$$

The principal values of the Cauchy integrals in Eqs. (7.27) and (7.28) are assumed. If we let $\chi = f + u_e\delta$, then Eq. (7.27) can be rewritten as

$$u_e = 1 + \frac{1}{\beta\pi}\int_{L.E.}^{\infty} u_e\delta\,\frac{d(\ell_n\rho_e)/dt}{x-t}\,dt + \frac{1}{\beta\pi}\int_{L.E.}^{\infty}\frac{d\chi/dt}{x-t}\,dt \tag{7.29}$$

We follow Veldman (1981) and solve Eqs. (7.19)-(7.24) simultaneously with the interaction law (7.29). The skin-friction coefficient

$$C_f\sqrt{Re} = \frac{2u_e^2\mu(T_w)}{\sqrt{2\xi}\,T_w}\frac{\partial F}{\partial\eta}\bigg|_{\eta=0}, \tag{7.30}$$

and the scaled displacement surface, Eq. (7.26), are presented in the next section for different hump heights.

7.2. Results

7.2.1. Mean Flow

We have obtained results for the mean flow over a hump whose shape is defined by Eqs. (7.1)-(7.3), center is at $x_m = 1.0$, and width $2b = 0.2$. We have considered three humps with an increasing height given by $\tilde{h} = (h^*/L^*)\sqrt{Re} = 1$, 1.65, and 2.5. The Reynolds number Re is fixed for all humps at $Re = 10^6$. The hump corresponding to $\tilde{h} = 1$ does not induce any flow separation, while that corresponding to $\tilde{h} = 1.65$ shows incipient separation at $M_\infty = 0.8$. The hump corresponding to $\tilde{h} = 2.5$ induces a separation bubble.

The interaction region extends from $x = 0.5$ to $x = 2.4$ for the three humps. The step size in the x-direction is uniform with $\Delta x = 0.005$. In the transverse direction, a stretched grid is used with $\Delta\eta_1 = 0.03$ and $\Delta\eta_j = 1.03\Delta\eta_{j-1}$ for $j = 2,3,...,N$. The matching condition, Eq. (7.23), is applied at $\eta_N = 10.3$ for the three humps.

Figure 7.1 shows the variation of the locations of separation and reattachment with hump height for $M_\infty = 0.0$ and $M_\infty = 0.8$. For a given Mach number M_∞ and a given hump height $\tilde{h}$, the left branch corresponds to the separation location, whereas the right branch corresponds to the reattachment location. As the Mach number increases, the hump height that induces separation decreases. Moreover, as the

Mach number increases, the separation location moves slightly upstream, whereas the reattachment location moves significantly downstream. Therefore, increasing the Mach number results in an increase in the size and extent of the separation bubble. Figure 7.2 shows the variation of the percentage of maximum flow reversal with streamwise distance for $\tilde{h} = 2.5$ and $M_\infty = 0.0$ and $M_\infty = 0.8$. This figure shows that the maximum flow reversal when $M_\infty = 0.8$ is much larger than that when $M_\infty = 0.0$.

The hump shapes and predicted displacement surfaces are depicted in figure 7.3, 7.6, and 7.9, and the corresponding distributions of the skin-friction and pressure coefficients are shown in figures 7.4, 7.6, 7.7, 7.8, 7.10, and 7.11. For all humps, there is an adverse pressure gradient ahead of the hump, and consequently the skin friction drops below the Blasius value. The region of adverse pressure gradient is followed by a region of favorable pressure gradient extending over a very short region; the pressure gradient becomes adverse again, causing the boundary layer to separate. Generally speaking, one expects the disturbance wave to be unstable ahead of the hump, become stable over the short favorable pressure-gradient region, and then turn unstable in the separation region. This general behavior has been predicted for different humps at different Reynolds numbers and over a wide range of frequencies by Nayfeh et al. (1988).

7.2.2. Stability Results

We have conducted a stability analysis of the calculated mean flows. We have used spatial stability theory for both primary and subharmonic waves; that is, ω is real and α is complex. The growth rate of the primary wave is given by $-\alpha_i$, the imaginary part of α, and that of the subharmonic wave is given by σ_r.

The frequency $F = \omega^* \nu^* / U_\infty^{*2}$ is related to ω through $\omega = FR$ and remains constant as the wave propagates downstream. Because the mean flow is 2-D and stationary, the dimensional frequency ω^* and spanwise wavenumber β^* remain constant as the wave propagates downstream. Then, the dimensionless spanwise wavenumber $\beta = \beta^* \delta_r^* = \beta^* \nu^* R / U_\infty^*$. Hence, β is proportional to R and in turn β/R and $B = 1000\beta/R$ remain constant as the wave propagates downstream. For all the results presented in this chapter, T_∞ is kept constant and equal to 120°K, the Prandtl number is kept constant and equal to 0.72, $m = \lambda/\mu = -0.2/3.0$, $\gamma = 1.4$, the variation of viscosity with temperature is given by the Sutherland formula, and σ_x is taken to be real, which corresponds to a perfectly tuned subharmonic mode.

To determine the effect of the hump on the most amplified subharmonic mode, particularly when separation is present, we performed a local stability analysis of the velocity profiles at x = 1.1 (i.e., R = 1049) for humps with $\tilde{h} = 0$, 1.0, 1.65, and 2.5. We define the amplitude A of the primary wave as the root-mean square (rms) of the u′ disturbance maximized over y. For $A = 0.01\ U_\infty^*$, the variation of the growth rate of the subharmonic wave with B is shown in figure 7.12. It shows the common features of the variation of the subharmonic growth rate with the spanwise wavenumber: the broadband character of the unstable spanwise wavenumbers and the sharp cutoff at low spanwise wavenumbers. It shows that increasing the height of the hump results in an increase in the growth rate of the subharmonic wave, and a shift in the most amplified spanwise wavenumber towards a lower value. It also shows that compressibility has a strong stabilizing influence at $\tilde{h} = 0.0$; however, its effect decreases in the presence of the considered humps.

Figure 7.13 shows the variation of the growth rate of the subharmonic wave with the frequency of the 2-D wave. It shows a sharp cutoff at low frequencies and a broadband of unstable frequencies. It also shows a shift in the most amplified

frequency towards a higher value and a diminishing effect of compressibility as the height of the hump increases.

The mean-flow profile and the eigenfunctions for the u′ disturbance of both the primary and secondary waves at $M_\infty = 0.8$ are shown in figure 7.14. We note from this figure that the primary wave has three local maxima in the transverse direction, as in the incompressible case discussed in Chapter 3. The middle one is again related to the shear-layer instability mechanism associated with the inflection point (see Nayfeh et al., 1988).

Next we present the results of the stability analysis downstream of the humps $\tilde{h}$ = 1.0, 1.65, and 2.5. At the initial station corresponding to x = 1.03, we assume that $A = A_0$ and choose a value of B. Then we march downstream and compute the growth rates and amplification factors for both the primary and subharmonic waves. The variation of the growth rates of the primary waves for the three humps at $F_{2D} = 45x10^{-6}$ are shown in figure 7.15 and the corresponding amplification factors are shown in figure 7.16. For the small hump $\tilde{h}$ = 1.0 the growth rate is small. However, increasing the hump height results in an increase in the growth rate. The case with a separation bubble ($\tilde{h} = 2.5$) shows considerable amplification of the primary wave over a very short distance. These results are in agreement with those obtained by Nayfeh et al. (1988) and Ragab et al. (1990). The obtained growth rates and amplification factors for the subharmonic wave with B = 0.2 and A_0 = 0.003 are shown in figures 7.17 and 7.18, respectively. Here again we see considerable growth rates for the separated flow case in comparison with the cases of incipient separation or no separation. Figures 7.16 and 7.18 show a consistent diminishing effect of compressibility on the N-factor for both the primary and subharmonic waves as the hump height increases.

Figures 7.19-7.22 show the variation of the growth rates and amplification factors of the primary and subharmonic waves with streamwise position for $F_{2D} = 90x10^{-6}$, $B = 0.2$, and $A_0 = 0.003$. For the small hump $\tilde{h} = 1.0$, the primary wave is damped over most of the streamwise range and the amplification factor is zero. As before, the case with a separation bubble ($\tilde{h} = 2.5$) shows considerable amplification in comparison with the cases of incipient separation or no separation. Figures 7.20 and 7.22 also show a decrease in the effect of compressibility on the amplification factors as the hump height increases.

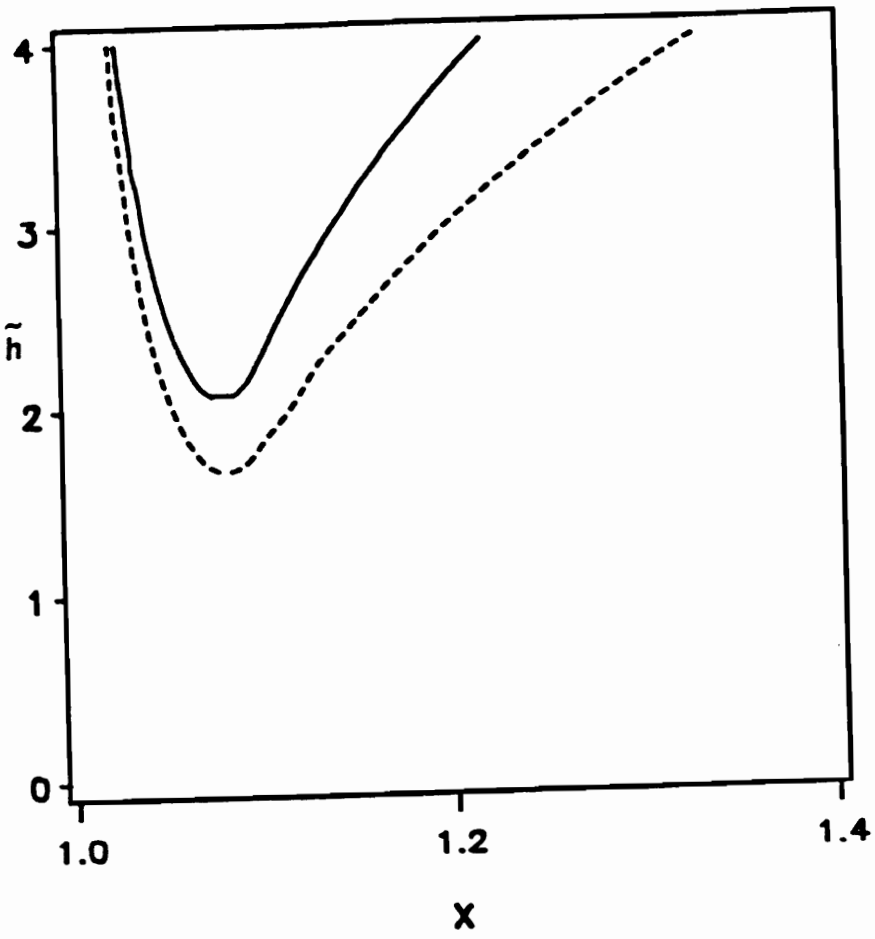

Figure 7.1. Variation of the locations of separation and reattachment with the hump height where $Re = 10^6$: (___) $M_\infty = 0.0$ and (...) $M_\infty = 0.8$.

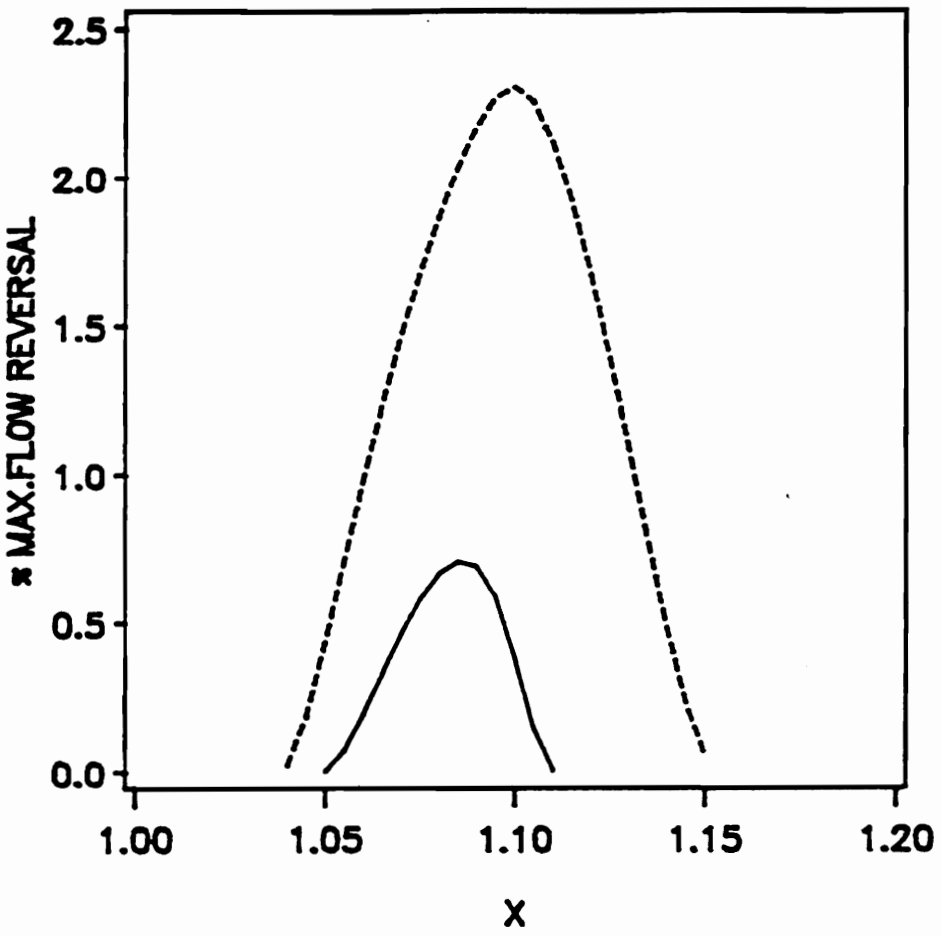

Figure 7.2. Variation of the percentage of the maximum flow reversal with streamwise distance. $\tilde{h} = 2.5$, (___) $M_\infty = 0.0$, and (...) $M_\infty = 0.8$.

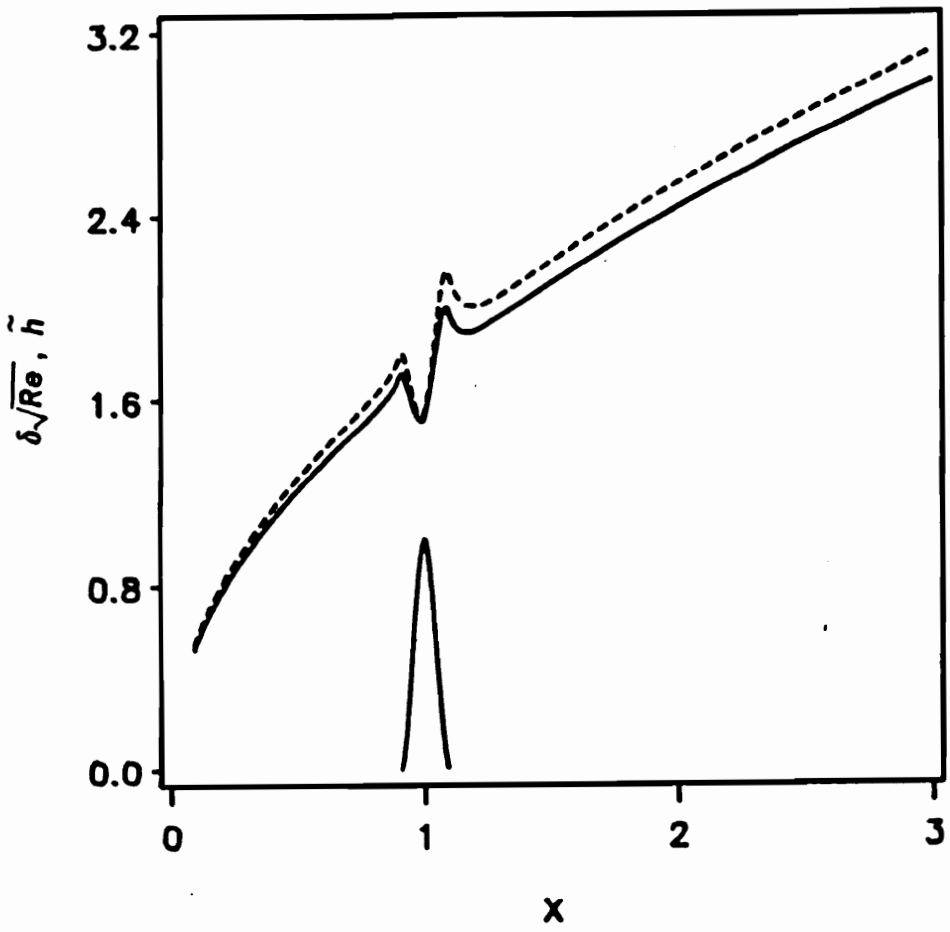

Figure 7.3. Hump shape for $\tilde{h} = 1.0$ and corresponding scaled displacement surface $\delta\sqrt{Re}$ when $Re = 10^6$: (___) $M_\infty = 0.0$ and (...) $M_\infty = 0.8$.

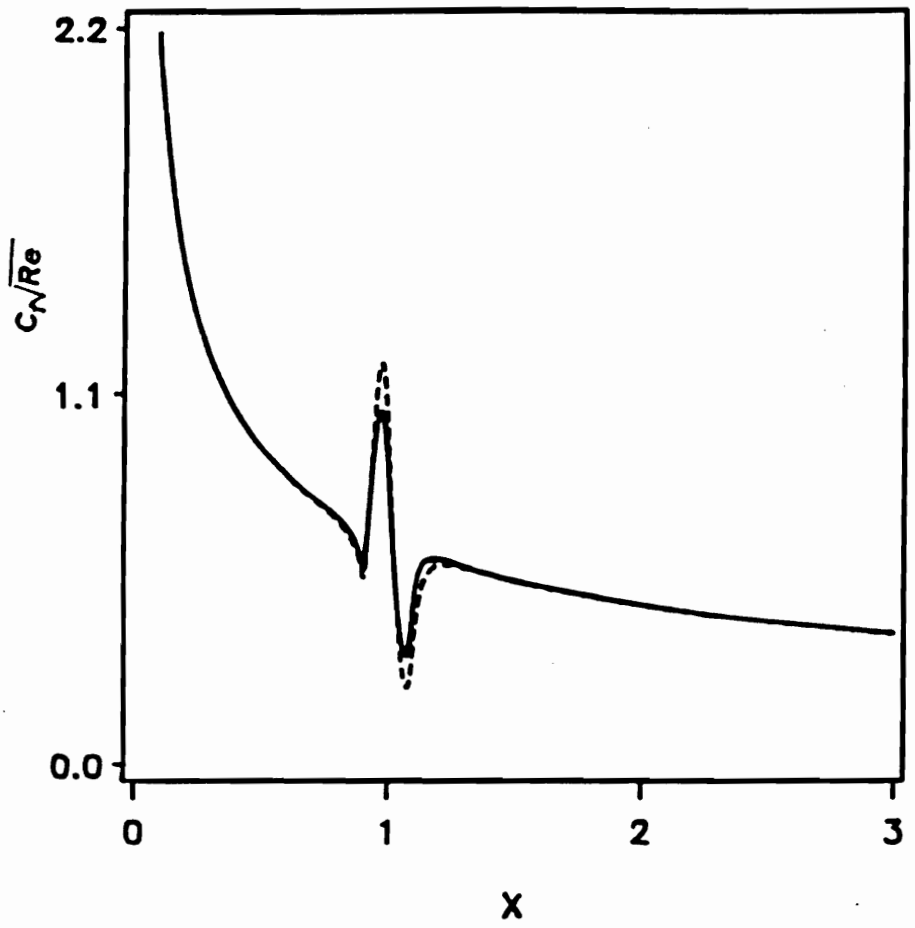

Figure 7.4. Distribution of the scaled skin-friction coefficient $C_f\sqrt{Re}$ for $\tilde{h} = 1.0$ and $Re = 10^6$; case of no separation: (___) $M_\infty = 0.0$ and (...) $M_\infty = 0.8$.

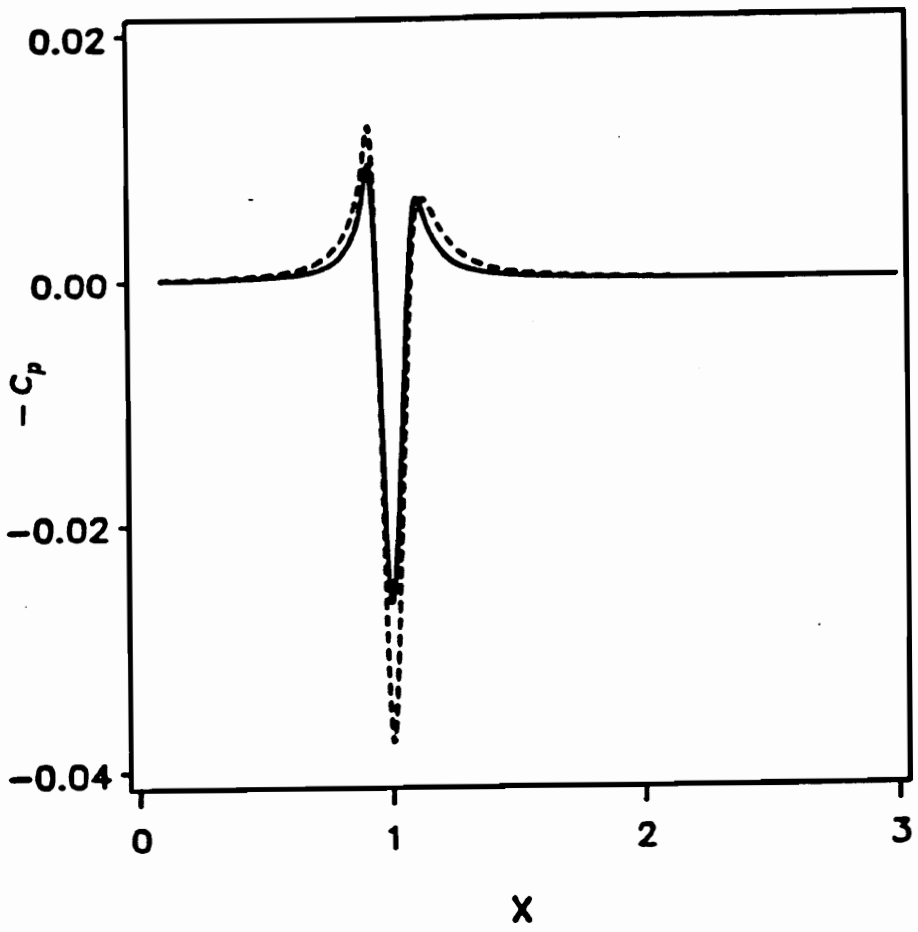

Figure 7.5. Distribution of the pressure coefficient C_p for $\tilde{h} = 1.0$ and $Re = 10^6$; case of no separation: (___) $M_\infty = 0.0$ and (...) $M_\infty = 0.8$.

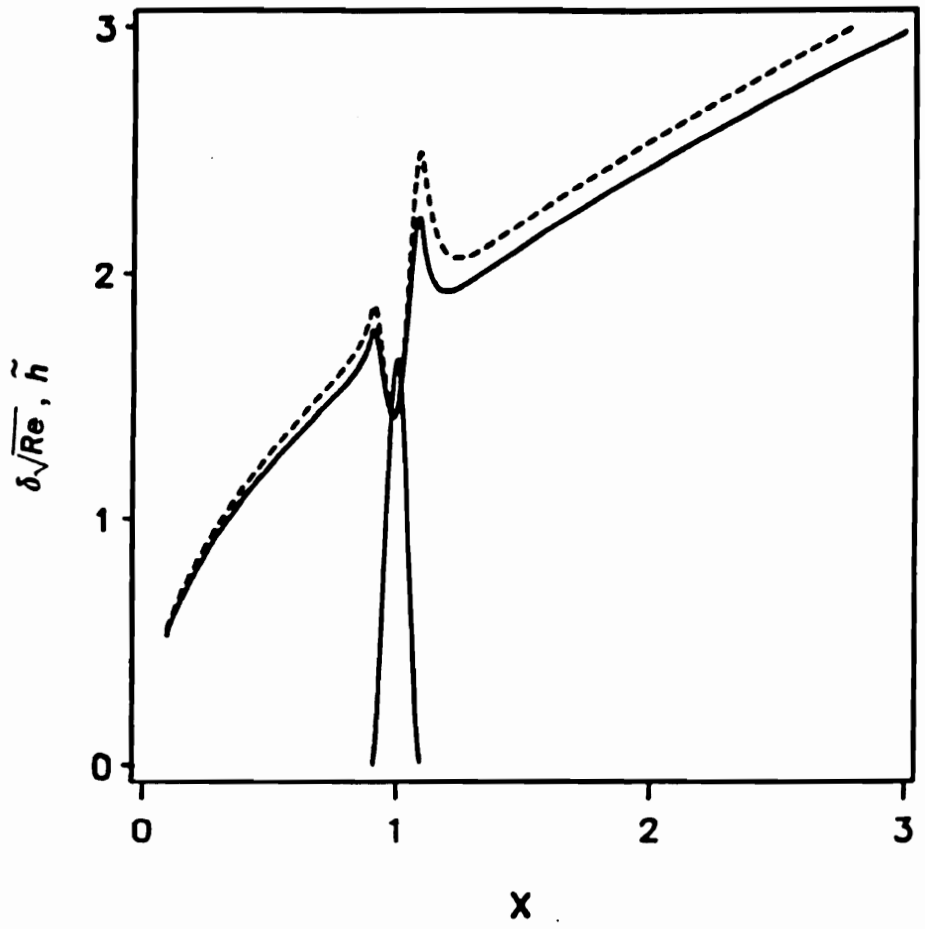

Figure 7.6. Hump shape and corresponding scaled displacement surface $\delta\sqrt{Re}$ for $\tilde{h} = 1.65$ and $Re = 10^6$: (___) $M_\infty = 0.0$ and (...) $M_\infty = 0.8$.

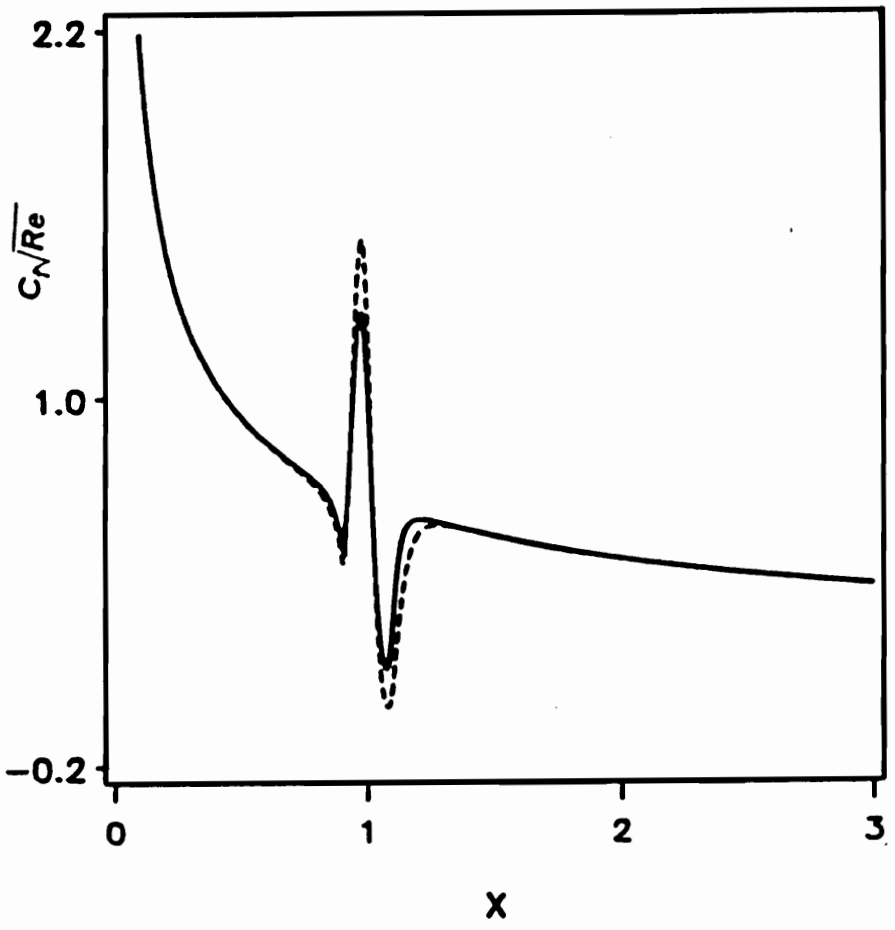

Figure 7.7. Distribution of the scaled skin-friction coefficient $C_f\sqrt{Re}$ for $\tilde{h} = 1.65$ and $Re = 10^6$; case of incipient separation at $M_\infty = 0.8$: (___) $M_\infty = 0.0$ and (...) $M_\infty = 0.8$.

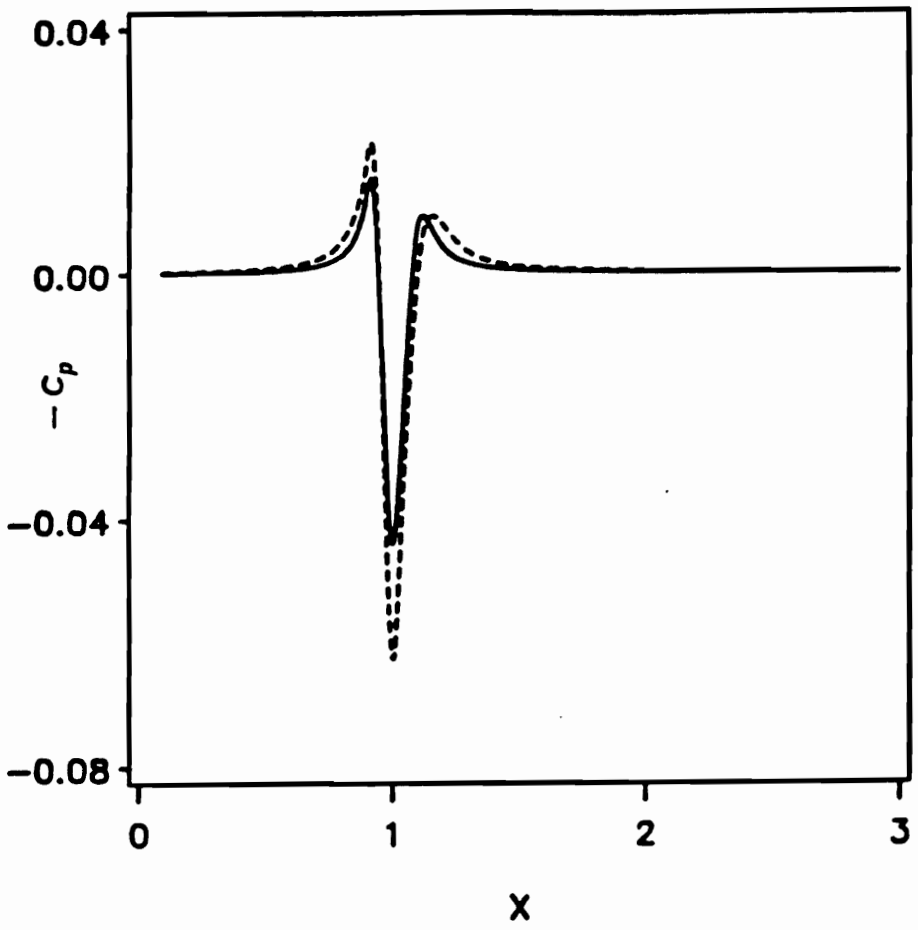

Figure 7.8. Distribution of the pressure coefficient C_p for $\tilde{h} = 1.65$ and $Re = 10^6$; case of incipient separation at $M_\infty = 0.8$: (___) $M_\infty = 0.0$ and (...) $M_\infty = 0.8$.

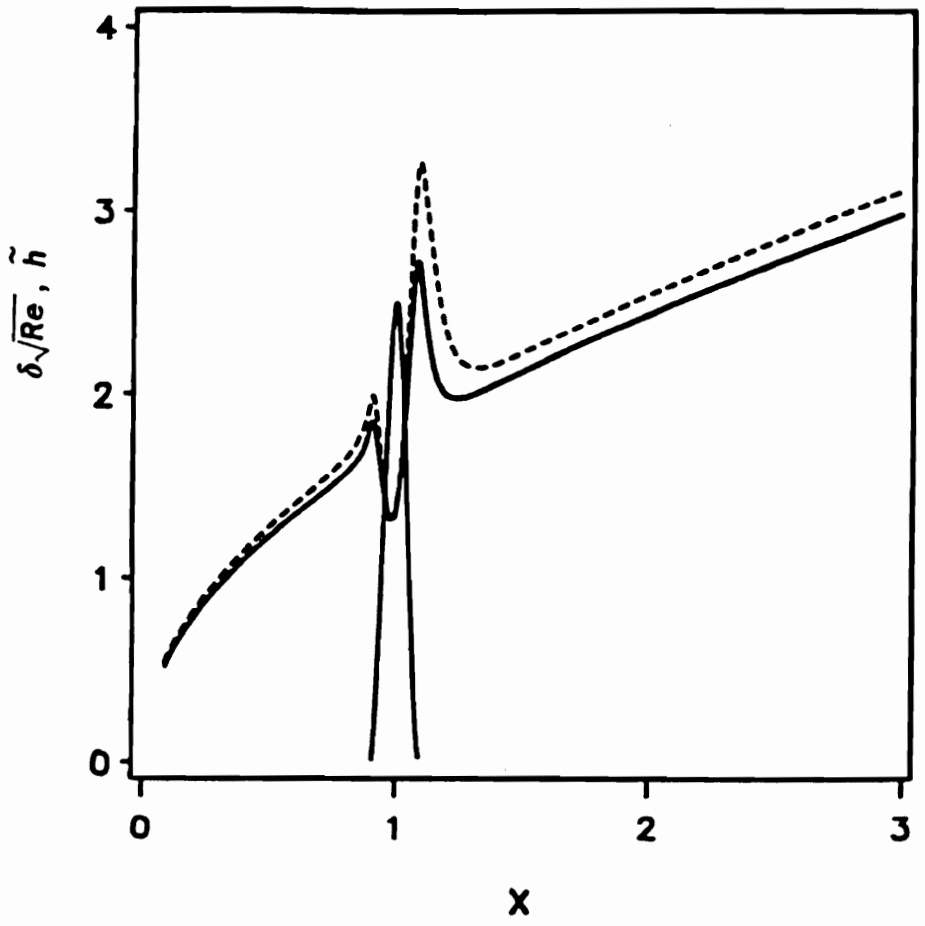

Figure 7.9. Hump shape and corresponding scaled displacement surface $\delta\sqrt{Re}$ for $\tilde{h} = 2.5$ and $Re = 10^6$: (___) $M_\infty = 0.0$ and (...) $M_\infty = 0.8$.

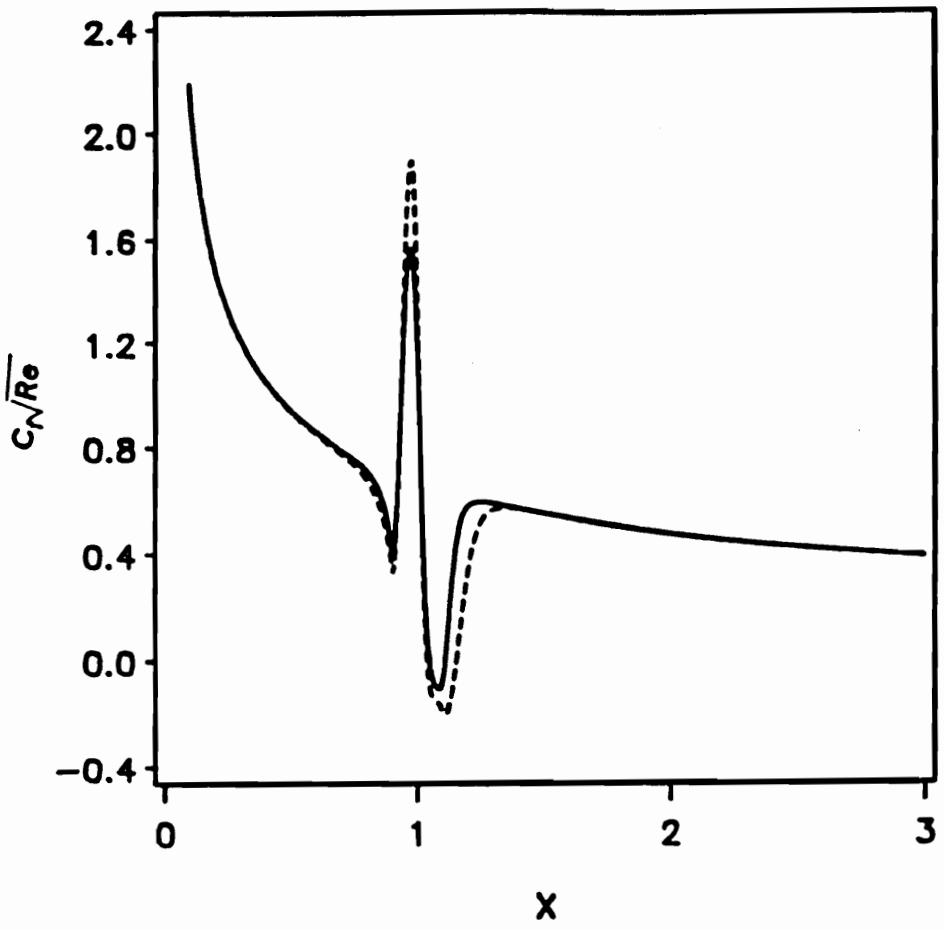

Figure 7.10. Distribution of the scaled skin-friction coefficient $C_f\sqrt{Re}$ for $\tilde{h} = 2.5$ and $Re = 10^6$: (___) $M_\infty = 0.0$ and (...) $M_\infty = 0.8$.

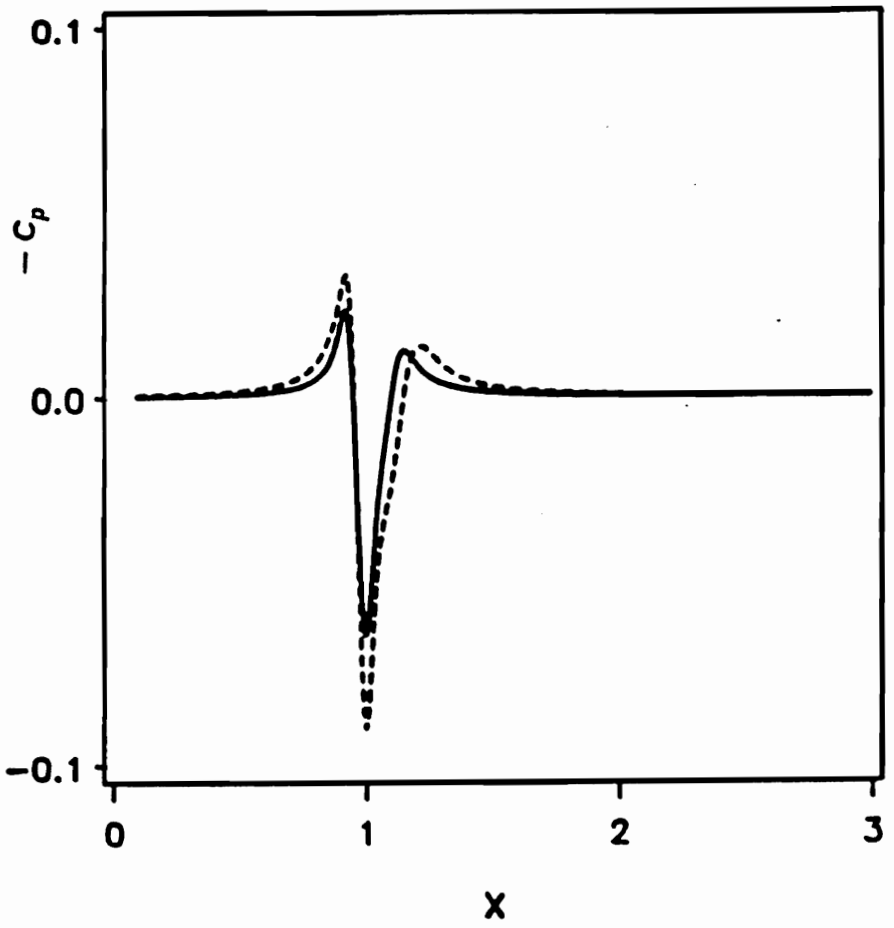

Figure 7.11. Distribution of the pressure coefficient C_p for $\tilde{h} = 2.5$ and $Re = 10^6$: (___) $M_\infty = 0.0$ and (...) $M_\infty = 0.8$.

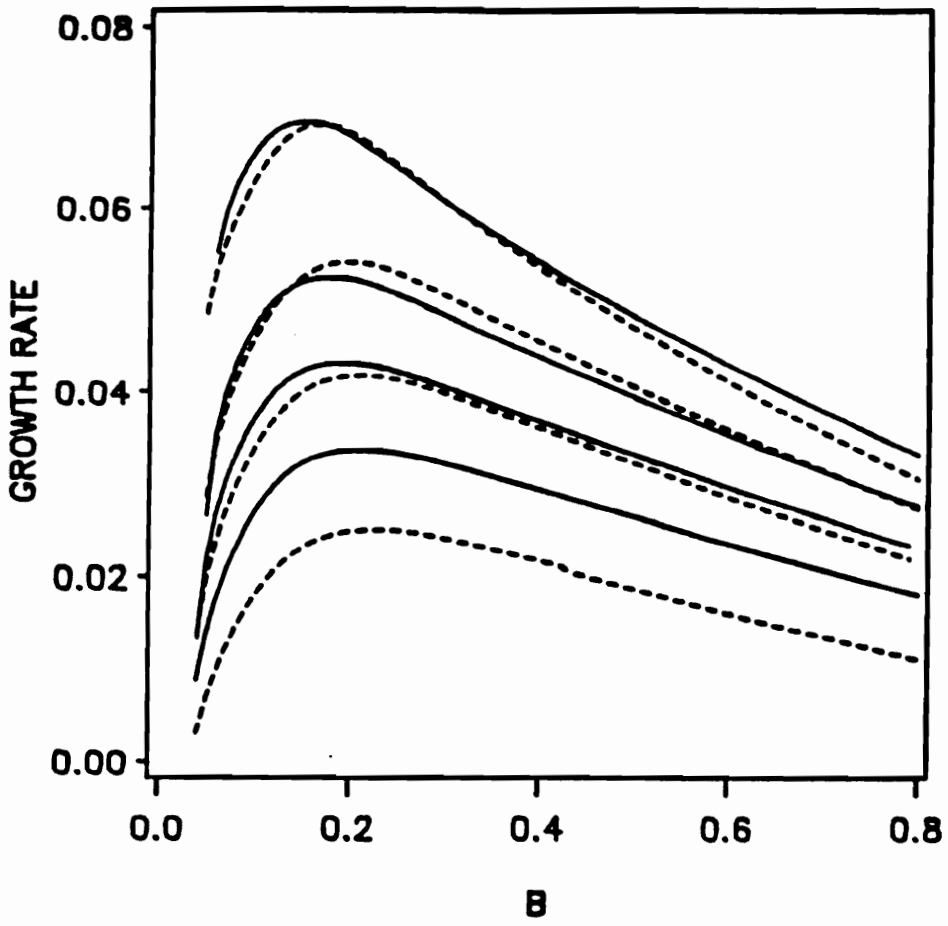

Figure 7.12. Variation of the subharmonic growth rate σ_r with spanwise wavenumber at $R = 1049$, $F_{2D} = 83x10^{-6}$, $x = 1.1$, and $A_{rms} = 0.01$: (___) $M_\infty = 0.0$ and (...) $M_\infty = 0.8$. The hump height $\tilde{h}$ proceeding downward is 2.5, 1.65, 1.0, and 0.0, respectively.

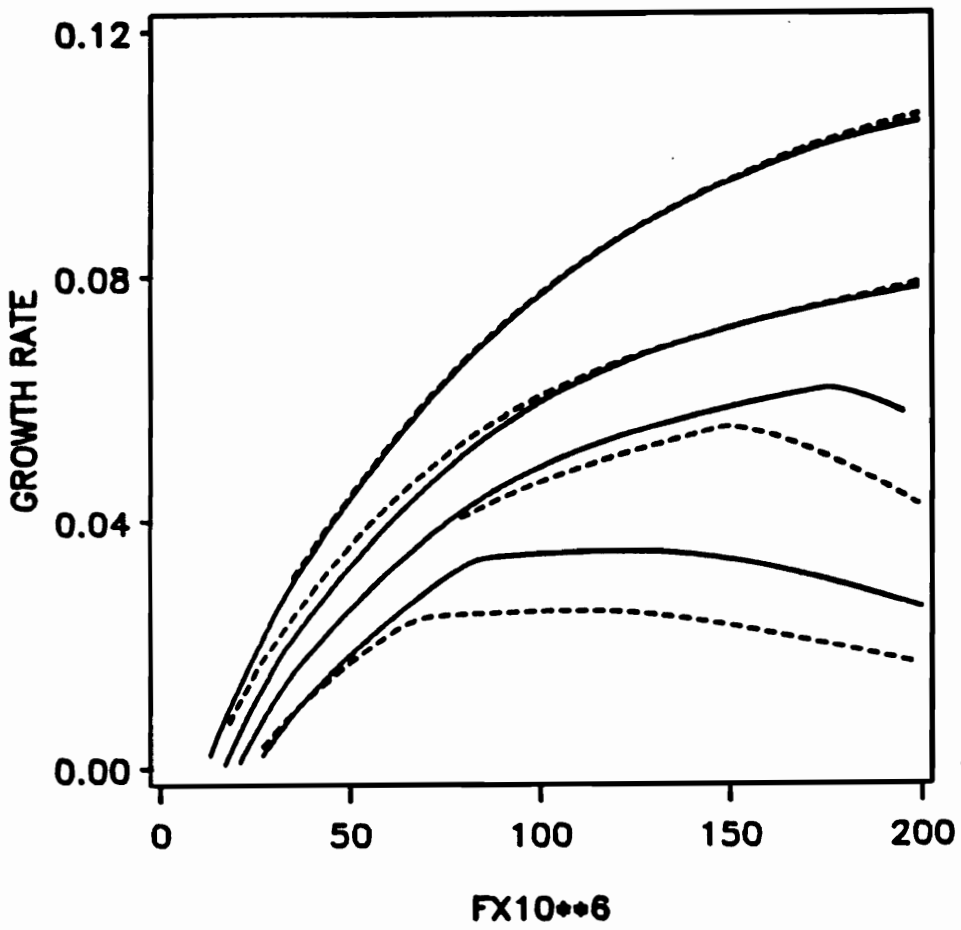

Figure 7.13. Variation of the subharmonic growth rate σ_r with the frequency of the 2-D wave at $R = 1049$, $B = 0.2$, $x = 1.1$, and $A_{rms} = 0.01$: (___) $M_\infty = 0.0$ and (...) $M_\infty = 0.8$. The hump height $\tilde{h}$ proceeding downward is 2.5, 1.65, 1.0, and 0.0, respectively.

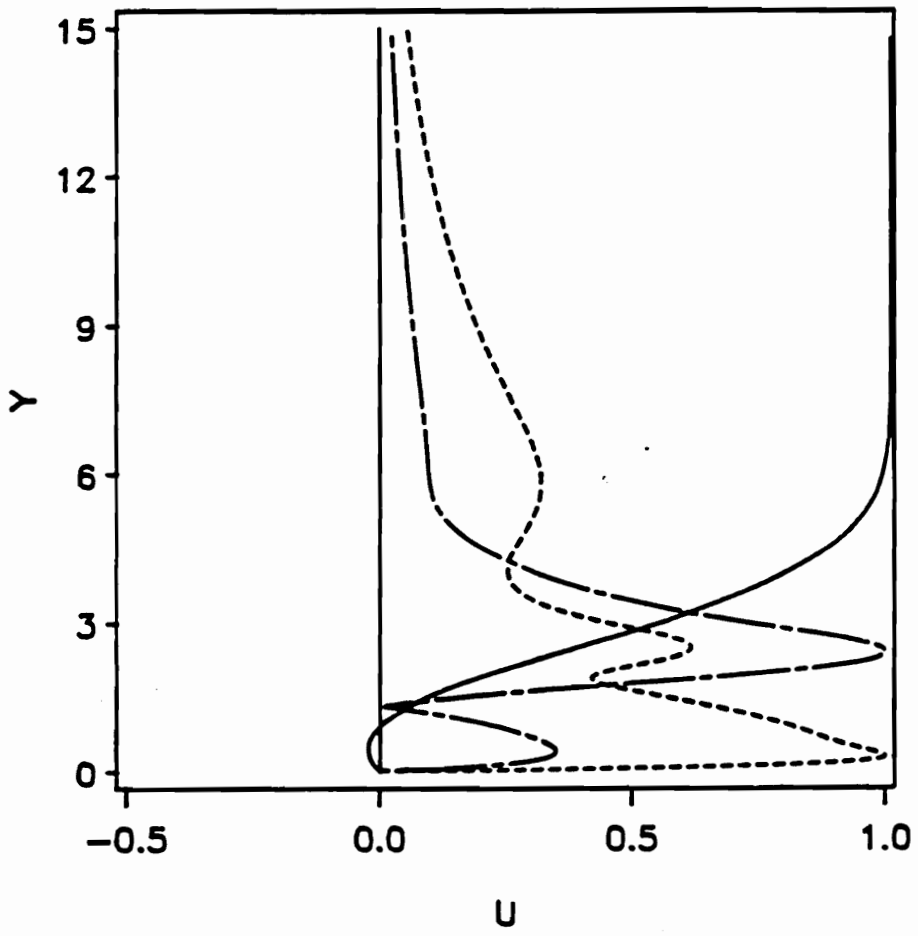

Figure 7.14. (___) mean flow profile U(y), (...) $|u'(y)|$ for the primary wave and (__ . __ .) $|u'(y)|$ for the subharmonic wave: $\tilde{h} = 2.5$, $F = 83x10^{-6}$, $M_\infty = 0.8$, R = 1049, x = 1.1, $A_{rms} = 0.01$, and B = 0.124.

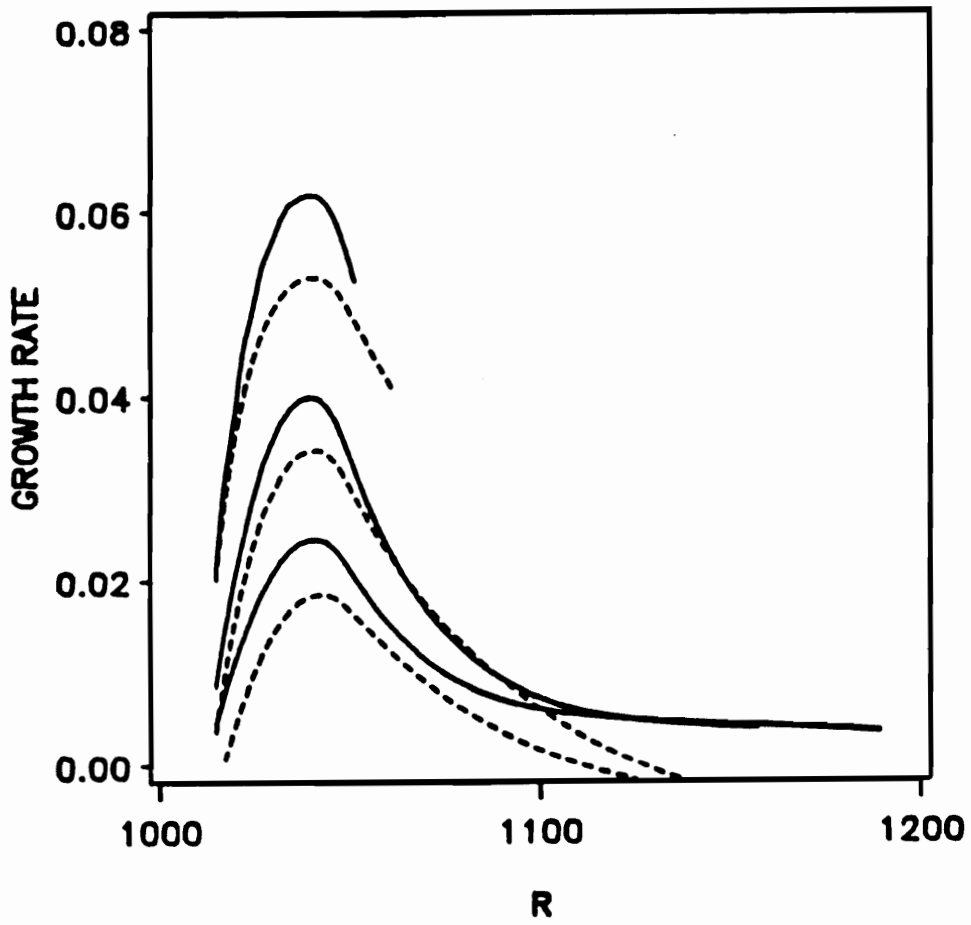

Figure 7.15. Streamwise variation of the growth rate $-\alpha_i$ of the primary wave at $F_{20} = 45 \times 10^{-6}$: (___) $M_\infty = 0.0$ and (...) $M_\infty = 0.8$. The hump height $\tilde{h}$ proceeding downward is 2.5, 1.65, and 1.0, respectively.

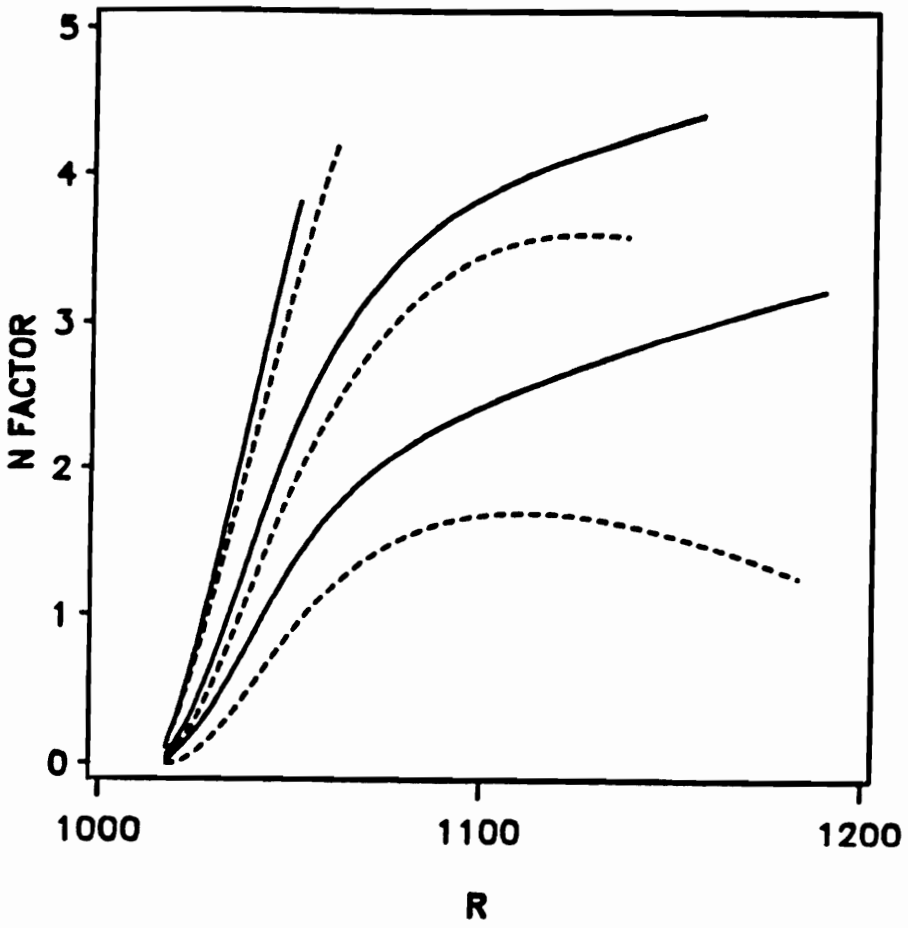

Figure 7.16. Streamwise variation of the amplification factor of the primary wave at $F_{2D} = 45x10^{-6}$: (___) $M_\infty = 0.0$ and (...) $M_\infty = 0.8$. The hump height $\tilde{h}$ proceeding downward is 2.5, 1.65, and 1.0, respectively.

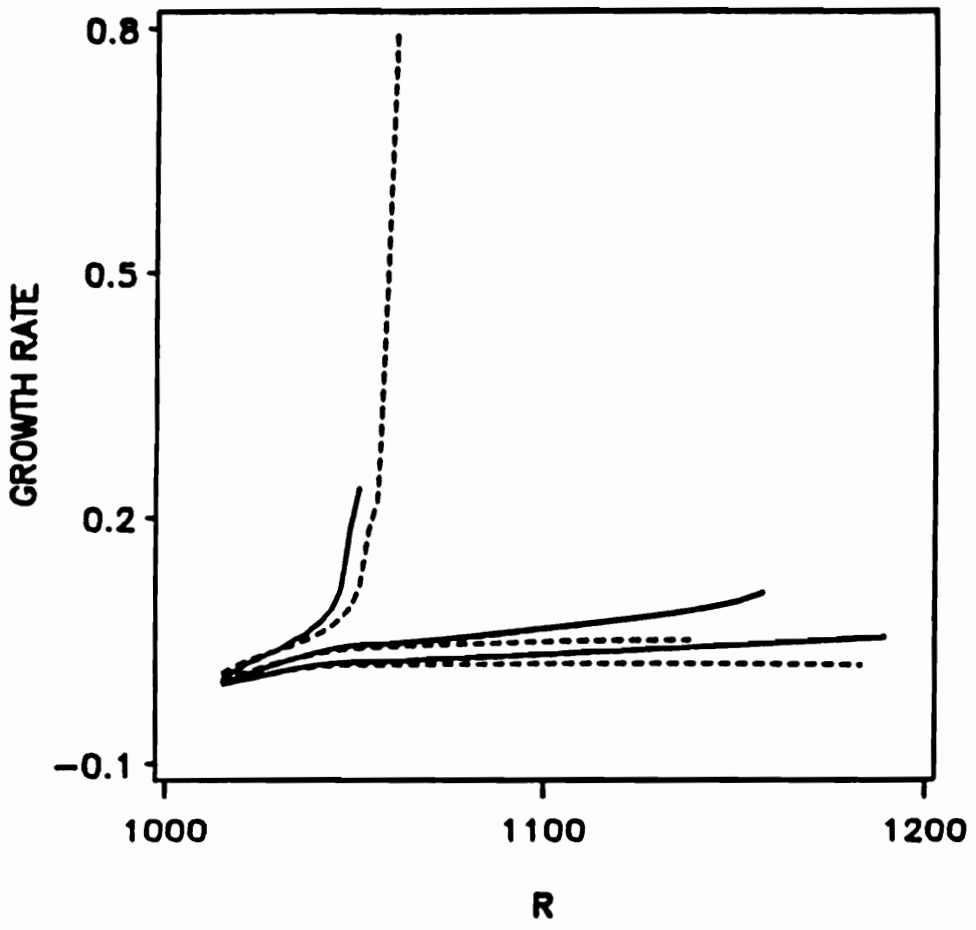

Figure 7.17. Streamwise variation of the growth rate of the subharmonic wave for B = 0.2, $F_{2D} = 45x10^{-6}$, and $A_{rms} = 0.003$ at the initial station x = 1.03: (___) $M_\infty = 0.0$ and (...) $M_\infty = 0.8$. The hump height $\tilde{h}$ proceeding downward is 2.5, 1.65, and 1.0, respectively.

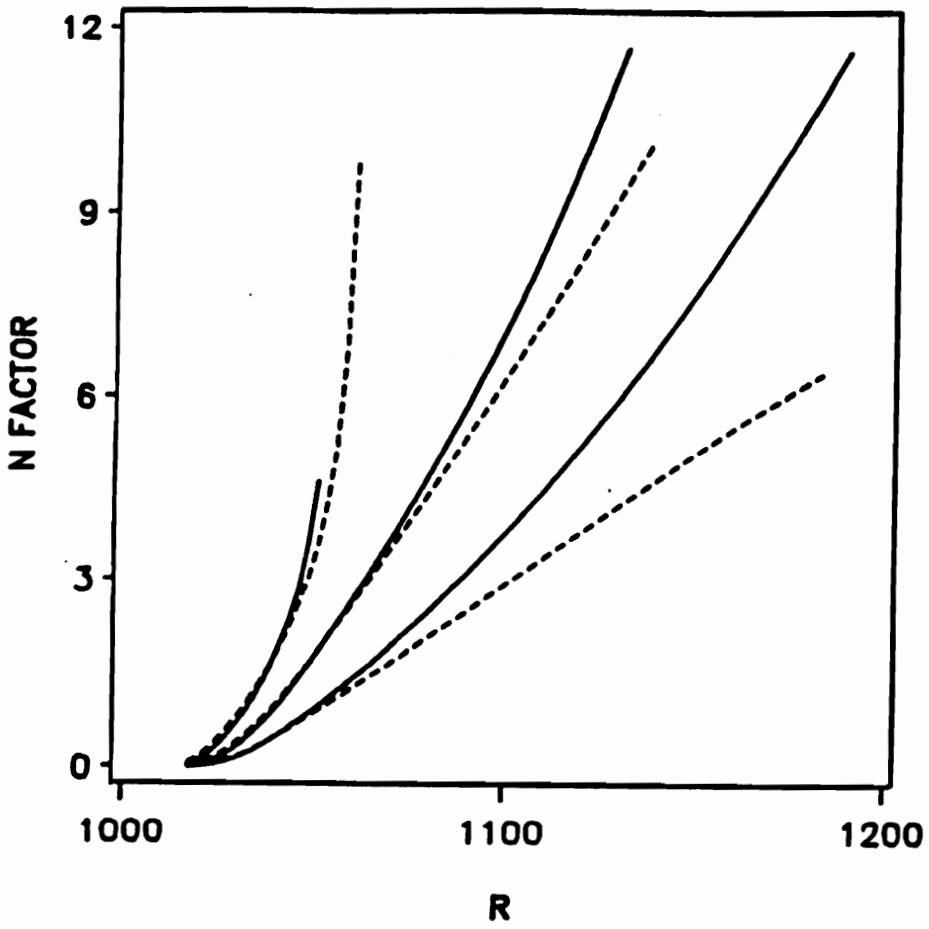

Figure 7.18. Streamwise variation of the amplification factor of the subharmonic wave: (___) $M_\infty = 0.0$ and (...) $M_\infty = 0.8$. The hump height $\tilde{h}$ proceeding downward is 2.5, 1.65, and 1.0, respectively.

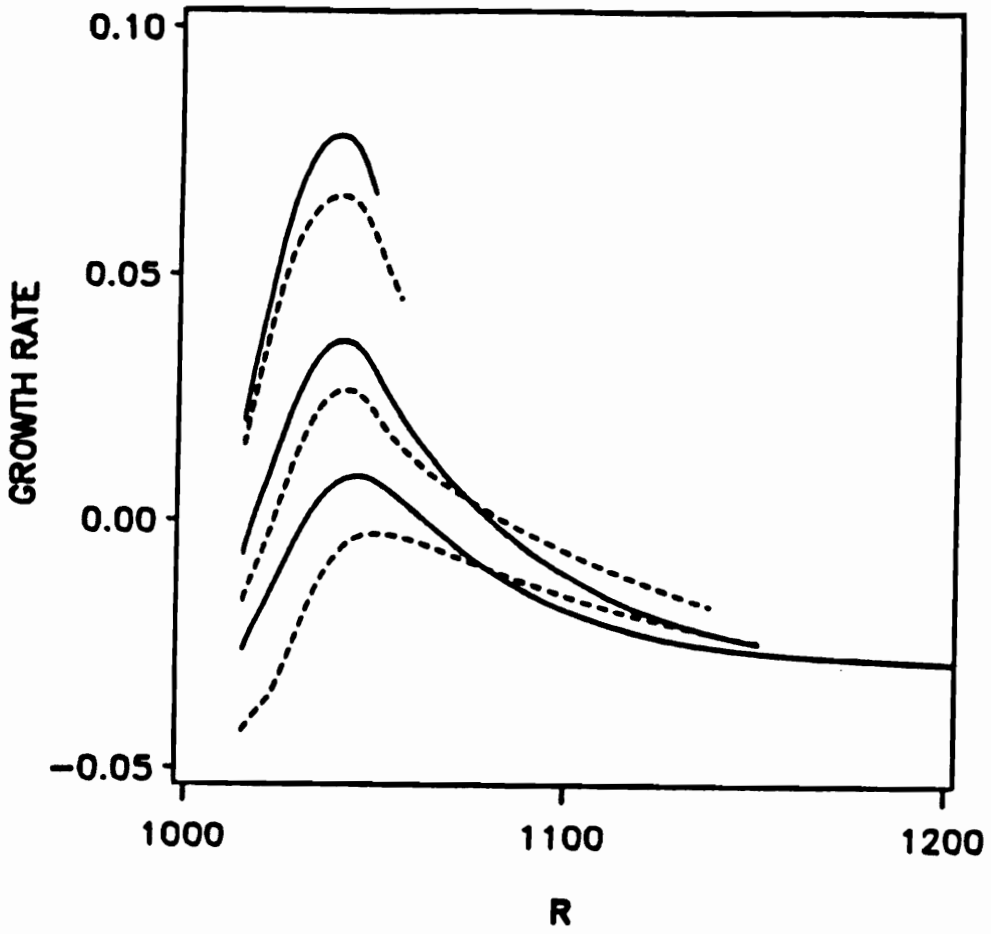

Figure 7.19. Streamwise variation of the growth rate $-\alpha$, of the primary wave at $F_{2D} = 90x10^{-6}$: (___) $M_\infty = 0.0$ and (...) $M_\infty = 0.8$. The hump height $\tilde{h}$ proceeding downward is 2.5, 1.65, and 1.0, respectively.

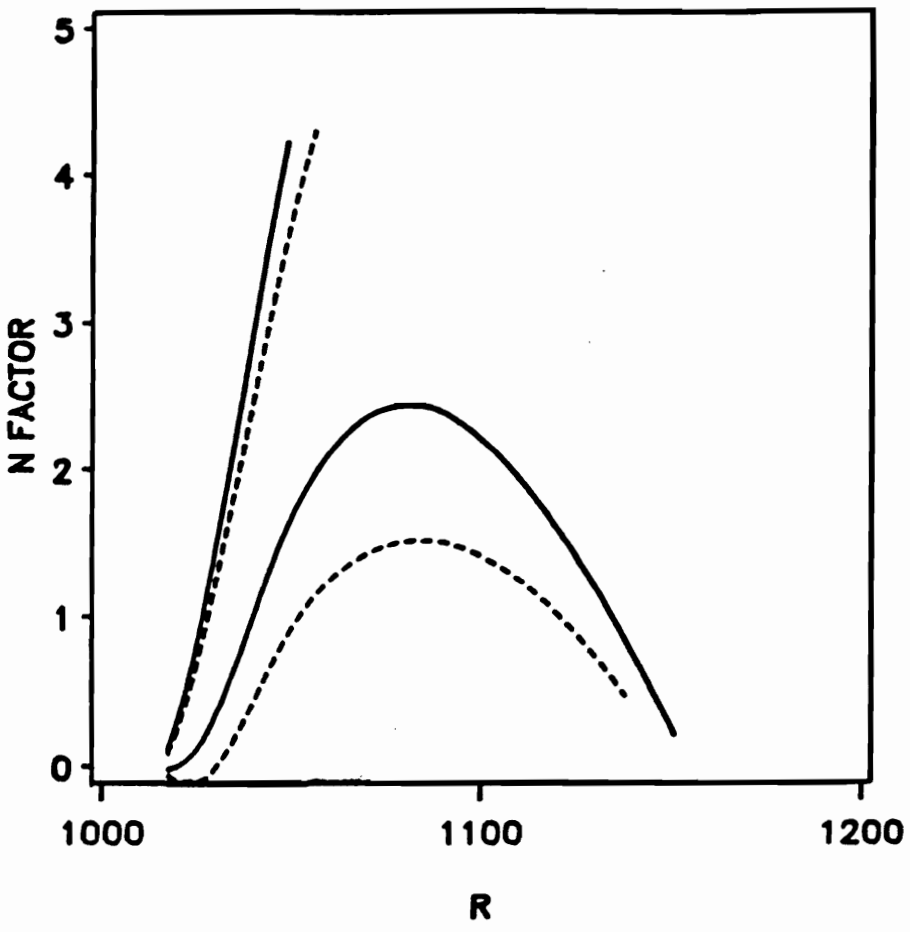

Figure 7.20. Streamwise variation of the amplification factor of the primary wave at $F_{2D} = 90x10^{-6}$: (___) $M_\infty = 0.0$ and (...) $M_\infty = 0.8$. The hump height $\tilde{h}$ proceeding downward is 2.5, 1.65, and 1.0, respectively.

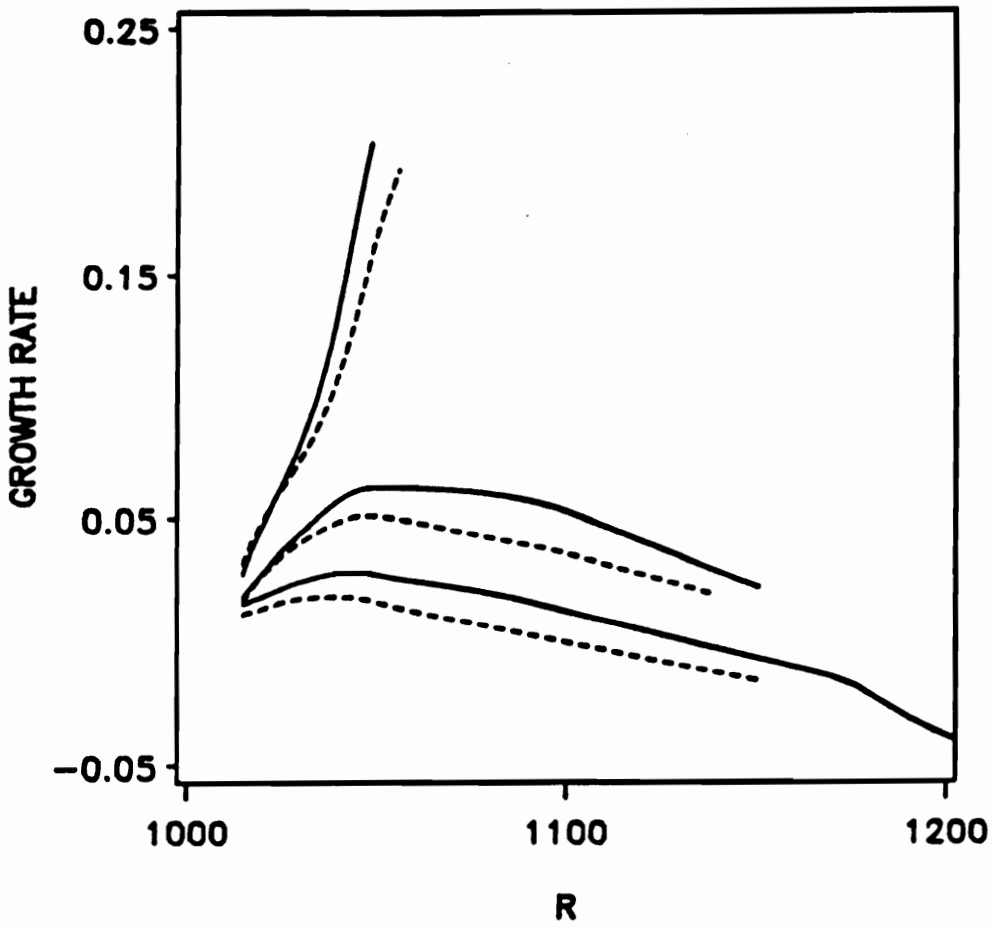

Figure 7.21. Streamwise variation of the growth rate of the subharmonic wave for B = 0.2 , $F_{2D} = 90x10^{-6}$, and $A_{rms} = 0.003$ at the initial station x = 1.03: (___) $M_\infty = 0.0$ and (...) $M_\infty = 0.8$. The hump height $\tilde{h}$ proceeding downward is 2.5, 1.65, and 1.0, respectively.

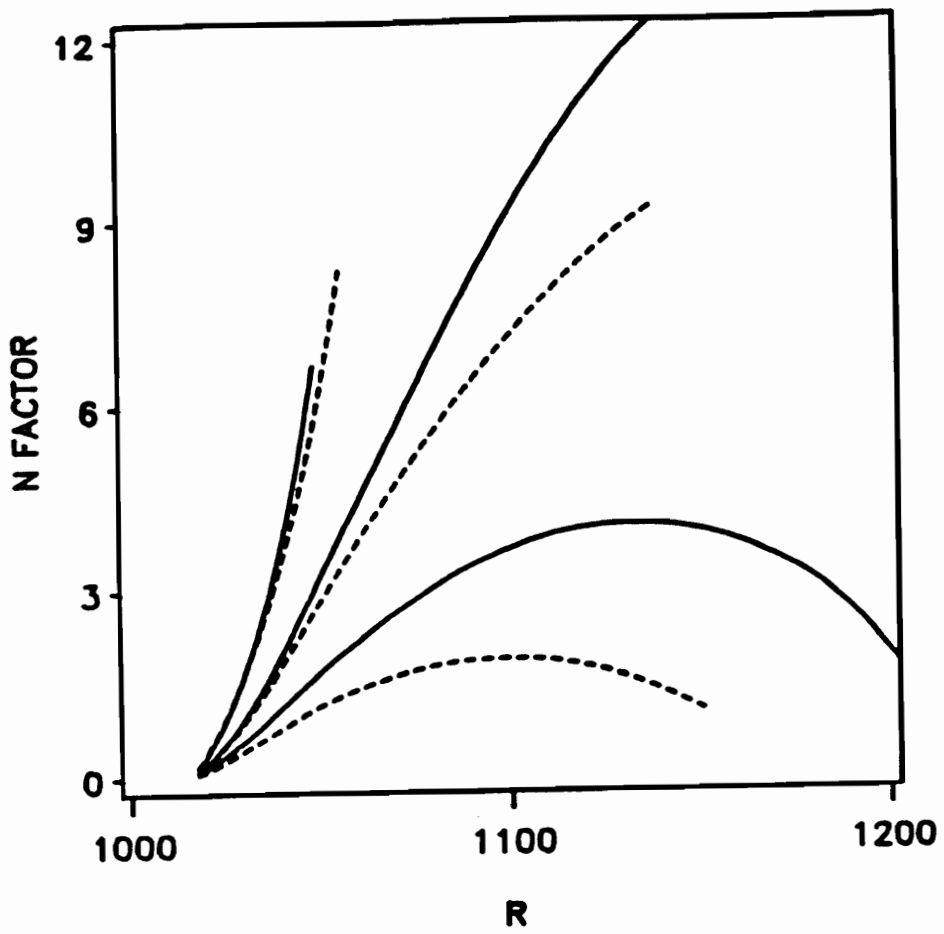

Figure 7.22. Streamwise variation of the amplification factor of the subharmonic wave: (___) $M_\infty = 0.0$ and (...) $M_\infty = 0.8$. The hump height $\tilde{h}$ proceeding downward is 2.5, 1.65, and 1.0, respectively.

8. CONCLUSIONS

In this thesis several aspects of the subharmonic instability of flow over a flat plate have been studied. In this chapter we introduce the major conclusions of the corresponding studies.

8.1. Subharmonic Instability in Incompressible Boundary Layers Over a Flat Plate

In Chapter 2, the subharmonic instability in a 2-D boundary layer on a flat plate has been analyzed using the Floquet and resonant triad models. The problems arising from both models have been solved numerically using finite-differences. Numerical results obtained using both models are compared with each other as well as with the experimental data of Kachanov and Levchenko (1984) and Corke and Mangano (1989). Results of the Floquet model are compared with the numerical simulations of Spalart and Yang (1987).

Results from the Floquet model show that at the same amplitude of the primary wave, increasing the frequency of the primary wave increases the growth rate of the subharmonic wave and shifts the most amplified subharmonic wave towards a higher spanwise wavenumber. The subharmonic mode is found to be amplified over a large band of frequencies. The variation of the growth rate of the subharmonic wave with the frequency of the primary wave for different Reynolds number shows that increasing the Reynolds number results in shifting the most amplified subharmonic wave towards a lower frequency. As the frequency of the primary wave increases, it takes a smaller amplitude of the primary wave to initiate the subharmonic instability.

Results from the resonant triad model show that the interaction affects the 3-D wave much more than it affects the 2-D wave. The variation of the interaction coefficient with the spanwise wavenumber when the 3-D wave is an Orr-Sommerfeld or a Squire mode indicates that the growth rate as predicted by the resonant triad does not decrease at large values of the spanwise wavenumber. This is a major qualitative disagreement between the resonant triad model and the Floquet model.

Whereas the results of the Floquet model agree fairly well with the experimental data of Kachanov and Levchenko, they do not agree as well with the experimental data of Corke and Mangano. The results obtained using the resonant triad model agree only qualitatively with the experimental data of Kachanov and Levchenko. Results of the Floquet model agree well with the numerical simulations of Spalart and Yang.

8.2. Subharmonic Instability in Incompressible Boundary Layers Over a Bulge

The subharmonic instability of incompressible flows over a 2-D hump is studied using the Floquet model. The mean flow over the hump is calculated by using interacting boundary layers, thereby accounting for viscid/inviscid interactions. The results show that increasing the hump height results in an increase in the amplification factors of the primary and subharmonic waves. When the hump causes separation, the growth rates of both the primary and subharmonic waves are considerably larger than those obtained in the case of no separation.

8.3. Subharmonic Instability in Compressible Boundary Layers Over an Adiabatic Flat Plate

The subharmonic instability of compressible boundary layers over a flat plate is studied using the Floquet model. Results are presented for adiabatic wall boundary conditions and subsonic, transonic, and supersonic flows. For supersonic flows results are presented for first- and second-mode primary waves. The effect of Mach number, spanwise wavenumber, primary-wave amplitude, Reynolds number, and frequency are studied. It is found that when the primary wave is a first mode, the variations of the growth rate of the subharmonic wave with the spanwise wavenumber and the amplitude of the primary wave share a lot of features with those

of the incompressible case: the broadband character of the unstable spanwise wavenumbers, the sharp cutoff at low spanwise wavenumbers, and the shift in the most amplified spanwise wavenumber towards a higher value as the amplitude of the primary wave increases. When the primary wave is a second-mode wave there is a shift in the most amplified spanwise wavenumber towards a lower value as the amplitude of the primary wave increases. At the same initial amplitude of the primary wave, the onset of the subharmonic instability was found to move towards a lower Reynolds number as the Mach number increases. The subharmonic mode was found to be unstable over a wide band of frequencies. Except at low frequencies and low Reynolds numbers, the growth rate decreases by increasing the Mach number. The bandwidth of unstable spanwise wavenumbers decreases with increasing Mach number.

8.4. Effect of Heat Transfer on the Subharmonic Instability of Boundary Layers Over a Flat Plate

Results for the effect of heat transfer on the subharmonic instability of a two-dimensional compressible boundary layer over a flat plate are presented for different Mach numbers. For supersonic flows results are presented for first- and second-mode waves. The effect of different levels of heat transfer on changing the features of the subharmonic compressible instability is evaluated. It is found that the subharmonic wave is stabilized by cooling when the primary wave is a second-mode wave. When the primary wave is a first-mode wave, the effect of cooling might be stabilizing or destabilizing depending on the frequency and spanwise wavenumber.

When the primary wave is a first mode, cooling stabilizes the subharmonic wave at low spanwise wavenumbers and destabilizes it at higher spanwise wavenumbers. When the primary wave is either a first- or second-mode wave the most amplified subharmonic mode shifts towards a higher spanwise wavenumbers as the cooling level increases.

8.5. Effect of Suction on the Subharmonic Instability of Boundary Layers Over an Adiabatic Flat Plate

Results for the effect of suction on the subharmonic instability of a two-dimensional compressible boundary layer over an adiabatic flat plate are presented. It is found that when the primary wave is a first mode, suction stabilizes the subharmonic wave at low and moderate Mach numbers. However, at high Mach numbers suction loses its effectiveness, and its effect becomes negligible. At moderate Mach numbers, when the primary wave is a first mode the variation of the growth rate of the subharmonic wave with the spanwise wavenumber indicates that suction decreases the bandwidth of unstable spanwise wavenumbers and produces a sharp cutoff in the growth rate at low spanwise wavenumbers. When the primary wave is a second mode, suction is found to stabilize the subharmonic mode; it decreases the maximum growth rate and the bandwidth of unstable spanwise wavenumbers. Increasing the suction level results in a shift of the most amplified subharmonic mode towards a higher spanwise wavenumber. When the primary wave is a first mode merging with a second mode, the subharmonic wave is strongly destabilized by suction.

8.6. Subharmonic Instability in Compressible Boundary Layers Over a Bulge

The subharmonic instability of compressible flows over a 2-D adiabatic hump is studied. The mean flow over the hump is calculated by using interacting boundary layers. Increasing the hump height results in a shift of the most amplified spanwise wavenumber towards a lower value. The variation of the growth rate of the subharmonic wave with the frequency of the 2-D wave shows a broadband of unstable frequencies and a shift in the most amplified frequency towards a higher value as the height of the hump increases. The results show that, although the effect of the compressibility on reducing the amplification factor is strong in the case of no hump, this effect decreases as the hump height increases.

References

1. A. A. Al-Maaitah, A. H. Nayfeh, and S. A. Ragab, 'Effect of wall cooling on the stability of compressible subsonic flows over smooth humps and backward-facing steps,' Physics of Fluids A2, 381-389 (1990a).

2. A. A. Al-Maaitah, A. H. Nayfeh, and S. A. Ragab, 'Effect of wall suction on the stability of compressible subsonic flows over smooth two-dimensional backward-facing steps,' AIAA Journal, in press, (1990b).

3. A. A. Al-Maaitah, A. H. Nayfeh, and J. A. Masad, 'Effect of heat transfer on the stability of supersonic and hypersonic boundary layers,' Computers and Fluids, submitted for publication (1990c).

4. A. A. Al-Maaitah, A. H. Nayfeh, and J. A. Masad, 'Effect of suction on the stability of supersonic and hypersonic boundary layers, I: the first mode,' Journal of Fluids Engineering, submitted for publication (1990d).

5. A. A. Al-Maaitah, A. H. Nayfeh, and J. A. Masad, 'Effect of suction on the stability of supersonic and hypersonic boundary layers, II. the second mode,' Journal of Fluids Engineering, submitted for publicaiton (1990e).

6. F. P. Bertolotti, 'Temporal and spatial growth of subharmonic disturbances in Falkner-Skan flows,' M.S. Thesis, VPI&SU (1985).

7. H. Bestek, K. Gruber, and H. Fasel, 'Numerical investigation of unsteady laminar boundary layer flows over backward-facing steps,' The Fourth Asian Congress of Fluid Mechanics, Hong Kong, August 19-23, 1989.

8. B. H. Carmichael, 'Surface waviness criteria for swept and unswept laminar suction wings,' Norair Report No. NOR-59-438 (BLC-123) (1959).

9. B. H. Carmichael, and W. Pfenninger, 'Surface imperfection experiments on a swept laminar suction wing,' Norair Report No. NOR-59-454 (BLC-124) (1959).

10. B. H. Carmichael, R. C. Whites, and W. Pfenninger, 'Low drag boundary layer suction experiment in flight on the wing glove of a F-94A airplane,' Northrup Aircraft Report No. NAI-57-1163 (BLC-101) (1957).

11. T. Cebeci and D. A. Egan, 'Effect of wave-like roughness on transition,' AIAA Journal 27, 870-875 (1989).

12. T. C. Corke and R. A. Mangano, 'Resonant growth of three-dimensional modes in transitioning Blasius boundary layers,' Journal of Fluid Mechanics 209, 93-150 (1989).

13. A. D. D. Craik, 'Nonlinear resonant instability in boundary layers,' Journal of Fluid Mechanics, 50, 393-413 (1971).

14. A. D. D. Craik, 'Second order resonance and subcritical instability,' Proceedings of the Royal Society, London, A343, 351-362 (1975).

15. A. D. D. Craik, 'Evolution in space and time of resonant wave triads. II. A class of exact solutions,' Proceedings of the Royal Society, London, A363, 257-269 (1978).

16. A. D. D. Craik, Wave Interactions and Fluid Flows, Cambridge, New York (1985).

17. A. D. D. Craik and J. A. Adam, 'Evolution in space and time of resonant wave triads, I. The pump wave approximation,' Proceedings of the Royal Society, London, A363, 243-255 (1978).

18. J. D. Crouch, 'The nonlinear evolution of secondary instabilities in boundary layers,' Ph.D. Thesis, VPI&SU (1988).

19. R. T. Davis and M. J. Werle, 'Progress on interacting boundary-layer computations at high Reynolds number,' in Numerical and Physical Aspects of Aerodynamic Flows, edited by T. Cebeci, Springer-Verlag, Berlin, pp. 187-198 (1982).

20. A. V. Dovgal and V. V. Kozlov, 'Hydrodynamic instability and receptivity of small scale separation regions,' presented at the Third IUTAM Symposium on Laminar-Turbulent Transition, Toulouse, France, September 13-17, 1989.

21. N. M. El-Hady, 'Secondary instability of compressible boundary layer to subharmonic three-dimensional disturbances,' NASA Contractor Report 4144 (1988).

22. N. M. El-Hady, 'Secondary instability of compressible boundary layer to subharmonic three-dimensional disturbances,' AIAA Paper No. 89-0035 (1989).

23. G. Erlebacher and M. Y. Hussaini, Stability and transition in supersonic boundary layers, AIAA Paper No. 87-1416 (1987).

24. A. Fage, 'The smallest size of spanwise surface corrugation which affect boundary layer transition on an airfoil,' British Aeronautical Research Council, Report and Memoranda No. 2120 (1943).

25. H. Fasel, 'Numerical simulation of instability and transition in boundary layer flows,' Proceedings of the IUTAM Symposium on Laminar-Turbulent Transition, Toulouse, France (1990).

26. M. E. Goldstein, 'Scattering of acoustic waves into Tollmien-Schlichting waves by small streamwise variation in surface geometry,' Journal of Fluid Mechanics 154, 509-528 (1985).

27. Th. Herbert, 'Analysis of the subharmonic route to transition in boundary layers,' AIAA Paper No. 84-0009 (1984).

28. Th. Herbert, 'Three-dimensional phenomena in the transitional flat-plate boundary layer,' AIAA Paper No. 85-0489 (1985).

29. Th. Herbert, 'Secondary instability of boundary layers,' Annual Review of Fluid Mechanics, 20, 487-526 (1988).

30. J. Hilsenrath, C. W. Beckett, W. S. Benedict, L. Fano, H. J. Hoge, J. F. Masi, R. L. Nuttall, Y. S. Touloukian, and H. W. Woolley, 'Tables of thermal properties of gases,' National Bureau of Standards (1955).

31. G. S. Hislop, British Aeronautical Research Council 6443 (1943).

32. B. J. Holmes, C. J. Obara, G. L. Martin, and C. S. Domack, 'Manufacturing tolerances for natural laminar flow airframe surfaces,' NASA CP 2413 (1986).

33. B. J. Holmes, C. J. Obara, and L. P. Yip, 'Natural laminar flow flight experiments on modern airplane surfaces,' NASA TP 2256 (1984).

34. Yu. S. Kachanov, 'On the resonant nature of the breakdown of a laminar boundary layer,' Journal of Fluid Mechanics, 184, 43-74 (1987).

35. Yu. S. Kachanov, V. V. Kozlov, and V. Ya. Levchenko, 'Nonlinear development of a wave in a boundary layer,' Fluid Dynamics, 3, 383-390 (1977).

36. Yu. S. Kachanov and V. Ya. Levcheno, 'The resonant interaction of disturbances of laminar-turbulent transition in boundary layers,' Journal of Fluid Mechanics 138, 209-247 (1984).

37. P. S. Klebanoff, K. D. Tidstrom, and L. M. Sargent, 'The three-dimensional nature of boundary-layer instability,' Journal of Fluid Mechanics, 12, 1-34 (1962).

38. M. Kloker and H. Fasel, 'Numerical simulation of two- and three-dimensional instability waves in two-dimensional boundary layers with streamwise pressure gradient,' Proceedings of the IUTAM Symposium on Laminar-Turbulent Transition, Toulouse, France (1990).

39. S. G. Lekoudis, 'On the triad resonance in the boundary layer,' Lockheed-Georgia Company Report No. LG77ER0152 (1977).

40. V. I. Lysenko and A. A. Maslov, 'The effect of cooling on supersonic boundary-layer stability,' Journal of Fluid Mechanics, 147, 39-52 (1984).

41. L. M. Mack, 'Boundary-layer linear stability theory, in Special Course on Stability and Transition of Laminar Flow,' AGARD Report No. 709 (1984).

42. L. M. Mack, 'Boundary-layer stability theory,' Jet Propulsion Laboratory, Pasadena, CA, Document No. 900-277, Rev. A (1969).

43. L. M. Mack, 'Linear stability theory and the problem of supersonic boundary-layer transition,' AIAA Journal 13, 278-289 (1975).

44. M. R. Malik, 'Prediction and control of transition in hypersonic boundary layers,' AIAA Journal 27, 1487-1493 (1989).

45. L. M. Maseev, 'Occurrence of three-dimensional perturbations in a boundary layer,' Fluid Dynamics, 3, 23-24 (1968).

46. A. H. Nayfeh, 'Stability of compressible boundary layers,' in Transonic Symposium: Theory, Application, and Experiment (NASA-Langley Research Center, Hampton, VA), NASA Conf. Pub. 3020, 1, 629 (1988).

47. A. H. Nayfeh, 'Nonlinear stability of boundary layers,' AIAA Paper No. 87-0044 (1987).

48. A. H. Nayfeh and D. T. Mook, Nonlinear Oscillations, Wiley-Interscience, New York (1979).

49. A. H. Nayfeh and A. N. Bozatli, 'Secondary instability in boundary-layer flows,' Physics of Fluids, 22, 805-813 (1979).

50. A. H. Nayfeh, S. A. Ragab, and A. A. Al-Maaitah, 'Effect of bulges on the stability of boundary-layers,' Physics of Fluids 31, 796-806 (1988).

51. C. J. Obara and B. J. Holmes, 'Flight measured laminar boundary-layer transition phenomena including stability theory analysis,' NASA TP 2417 (1985).

52. V. Pereyra, 'PASVA3: An adaptive finite difference Fortran program for first order nonlinear, ordinary boundary problems,' in Lecture Notes in Computer Science, 76, 67-88 (1976).

53. S. A. Ragab and A. H. Nayfeh, 'A comparison of the second-order triple-deck theory with interacting boundary layers,' in Numerical and Physical Aspects of Aerodynamic Flows, edited by T. Cebeci, Springer-Verlag, Berlin, pp. 237-254 (1982).

54. S. A. Ragab, A. H. Nayfeh, and R. C. Krishna, 'Stability of compressible boundary layers over smooth backward- and forward-facing steps,' AIAA Paper No. 90-1450 (1990).

55. S. A. Ragab and J. L. Wu, 'Instabilities of supersonic shear flows,' AIAA Paper No. 90-0712 (1990).

56. G. S. Raetz, 'Current status of resonance theory of transition,' Norair Report NOR-64-111, Hawthorne, CA (1964); available NTIS AD-605185.

57. R. C. Reid, J. M. Prausnitz, and B. E. Poling, The Properties of Gases and Liquids, McGraw-Hill, New York (1987).

58. G. R. Santos, 'Studies on secondary instabilities,' Ph.D. Thesis, VPI&SU (1987).

59. W. S. Saric and A. S. W. Thomas, 'Experiments on the subharmonic route to turbulence in boundary layers,' Turbulence and Chaotic Phenomena in Fluids, Proceedings of the IUTAM Symposium, Kyoto (ed. T. Tatsumi). North Holland (1984).

60. M. R. Scott and H. A. Watts, 'Computational solution of linear two-point boundary value problem via orthonormalization,' SIAM Journal of Numerical Analysis 14, 40-70 (1977).

61. F. T. Smith and P. A. Stewart, 'The resonant-triad nonlinear interaction in boundary-layer transition,' Journal of Fluid Mechanics, 179, 227-252 (1987).

62. P. R. Spalart and K. Yang, 'Numerical study of ribbon-induced transition in Blasius flow,' Journal of Fluid Mechanics 178, 345-365 (1987).

63. O. A. Spence and D. G. Randall, 'The influence of surface waves on the stability of a laminar boundary layer with uniform suction,' British Aeronautical Research Council Technical Note No. 2241 (1953).

64. J. T. Stuart, 'On three-dimensional non-linear effects in the stability of parallel flows,' Advances in Aerospace Sciences, 3, 121-142 (1961).

65. A. Thumm, W. Wolz, and H. Fasel, 'Numerical simulation of spatially growing three-dimensional disturbance waves in compressible boundary layers,' Proceedings of the IUTAM Symposium on Laminar-Turbulent Transition, Toulouse, France (1990).

66. J. R. Usher and A. D. D. Craik, 'Nonlinear wave interactions in shear flows. Part 2. Third-order theory,' Journal of Fluid Mechanics, 70, 437-461 (1975).

67. A. E. P. Veldman, 'New quasi-simultaneous method to calculate interacting boundary layers," AIAA Journal 19, 79-85 (1981).

68. A. G. Volodin and M. B. Zel'man, 'Three-wave resonance interaction of disturbances in a boundary layer,' Fluid Mechanics, 13, 698-703 (1979). [trs. of Mekh. Zhid. i Gaza 5, 78-84].

69. W. S. Walker and R. J. Cox, British Aeronautical Research Council 6126 (1942).

70. W. S. Walker and J. R. Greening, British Aeronautical Research Council 5950 (1942).

Appendix A. The adjoint problem of the 3-D linear quasi-parallel stability problem

$$i\alpha_1\xi_1^* - D\xi_3^* - \beta\xi_5^* = 0,$$

$$-\frac{1}{R}D^2\xi_1^* + \frac{\Lambda}{R}\xi_1^* + i\alpha_1\xi_4^* = 0,$$

$$-\frac{1}{R}D^2\xi_3^* + \Lambda_R\xi_3^* + DU\xi_1^* - D\xi_4^* = 0,$$

$$-\frac{1}{R}D^2\xi_5^* + \frac{\Lambda}{R}\xi_5^* + \beta\xi_4^* = 0,$$

$$\xi_1^* = \xi_3^* = \xi_5^* = 0 \quad \text{at} \quad y = 0,$$

$$\xi_n^* \to 0 \quad \text{as} \quad y \to \infty.$$

The adjoint problem of the 2-D linear quasi-parallel stability problem

$$i\alpha\zeta_1^* - D\zeta_3^* = 0,$$

$$-\frac{1}{R}D^2\zeta_1^* + \frac{\Gamma}{R}\zeta_1^* + i\alpha\zeta_4^* = 0,$$

$$-\frac{1}{R}D^2\zeta_3^* + \frac{\Gamma}{R}\zeta_3^* + u_0'\zeta_1^* - D\zeta_4^* = 0,$$

$$\zeta_1^* = \zeta_3^* = 0 \quad \text{at} \quad y = 0,$$

$$\zeta_n^* \to 0 \quad \text{at} \quad y \to \infty$$

Appendix B. Coefficients of the resonant triad model

$$H_1 = \int_0^\infty (\dot{\xi_1}\xi_1 + \dot{\xi_3}\xi_3 + \dot{\xi_5}\xi_5)dy,$$

$$H_2 = \int_0^\infty \left[\dot{\xi_4}\xi_1 + \dot{\xi_1}(U\xi_1 + \xi_4) + \dot{\xi_3}U\xi_3 + \dot{\xi_5}U\xi_5\right]dy,$$

$$H_4 = \int_0^\infty \left[\dot{\xi_4}\frac{\partial \xi_1}{\partial x} + \dot{\xi_1}\left(U\frac{\partial \xi_1}{\partial x} + \frac{\partial \xi_4}{\partial x} + \frac{\partial U}{\partial x}\xi_1 + VD\xi_1\right)\right.$$
$$\left. + \dot{\xi_3}\left(U\frac{\partial \xi_3}{\partial x} + VD\xi_3 + \xi_3 DV\right) + \dot{\xi_5}\left(U\frac{\partial \xi_5}{\partial x} + VD\xi_5\right)\right]dy,$$

$$\Lambda_2 = \int_0^\infty \left[\dot{\xi_1}\{i(\alpha - \bar{\alpha}_1)\zeta_1\bar{\xi}_1 + \zeta_3 D\bar{\xi}_1 + \bar{\xi}_3 D\zeta_1\}\right.$$
$$+ \dot{\xi_3}\{i\alpha\zeta_3\bar{\xi}_1 - i\bar{\alpha}_1\zeta_1\bar{\xi}_3 + \zeta_3 D\bar{\xi}_3 + \bar{\xi}_3 D\zeta_3\}$$
$$\left. + \dot{\xi_5}\{\zeta_3 D\,\bar{\xi}_5 - i\bar{\alpha}_1\zeta_1\bar{\xi}_5\}\right]dy,$$

$$h_1 = \int_0^\infty \left[\zeta_1^{\cdot}\zeta_1 + \zeta_3^{\cdot}\zeta_3\right] dy,$$

$$h_2 = \int_0^\infty \left[\zeta_4^{\cdot}\zeta_1 + \zeta_1^{\cdot}(U\zeta_1 + \zeta_4) + \zeta_3^{\cdot}U\zeta_3\right] dy,$$

$$h_4 = \int_0^\infty \left[\zeta_4^{\cdot}\frac{\partial\zeta_1}{\partial x} + \zeta_1^{\cdot}\left(U\frac{\partial\zeta_1}{\partial x} + \frac{\partial\zeta_4}{\partial x} + \frac{\partial U}{\partial x}\zeta_1 + VD\zeta_1\right) + \zeta_3^{\cdot}\left(U\frac{\partial\zeta_3}{\partial x} + VD\zeta_3 + \zeta_3 DV\right)\right] dy,$$

$$\Lambda_1 = 2\int_0^\infty \left(\zeta_1^{\cdot}\left(i\alpha_1\xi_1^2 + \xi_3 D\xi_1 - \beta\xi_1\,\xi_5\right) + \zeta_3^{\cdot}\left(i\alpha_1\xi_1\xi_3 + \xi_3 D\xi_3 - \beta\xi_3\xi_5\right)\right] dy,$$

Appendix C. Elements of the matrix F for the linear quasiparallel problem

$f_{12} = f_{15} = 1, \quad f_{21} = f_{65} = \Lambda,$

$f_{23} = RDU, \quad f_{24} = i\alpha_1 R, \quad f_{31} = -i\alpha_1, \quad f_{35} = -\beta,$

$f_{42} = -\frac{i\alpha_1}{R}, \quad f_{43} = -\frac{\Lambda}{R}, \quad f_{46} = -\frac{\beta}{R}, \quad f_{64} = -\beta R.$

The rest of the elements are zero.

Appendix D. Nonzero elements of the matrix A

$$a_{12} = a_{56} = 1$$

$$a_{21} = \alpha^2 - i\hat{\omega}R/\mu_m T_m$$

$$a_{22} = -D\mu_m/\mu_m$$

$$a_{23} = -i\alpha(m+1)DT_m/T_m - i\alpha D\mu_m/\mu_m + RDU_m/\mu_m T_m$$

$$a_{24} = i\alpha R/\mu_m + (m+1)\gamma M_\infty^2 \alpha\hat{\omega}$$

$$a_{25} = -\alpha(m+1)\hat{\omega}/T_m - D(\mu_m' DU_m)/\mu_m$$

$$a_{26} = -\mu_m' DU_m/\mu_m$$

$$a_{31} = -i\alpha$$

$$a_{33} = DT_m/T_m$$

$$a_{34} = i\gamma M_\infty^2 \hat{\omega}$$

$$a_{35} = -i\hat{\omega}/T_m$$

$$a_{41} = -i\chi\alpha(rDT_m/T_m + 2D\mu_m/\mu_m)$$

$$a_{42} = -i\chi\alpha$$

$$a_{43} = \chi\left[-\alpha^2 + i\hat{\omega}R/\mu_m T_m + rD^2T_m/T_m + rD\mu_m DT_m/\mu_m T_m\right]$$

$$a_{44} = -i\chi r\gamma M_\infty^2\left[\alpha DU_m - \hat{\omega}DT_m/T_m - \hat{\omega}D\mu_m/\mu_m\right]$$

$$a_{45} = i\chi\left[r\alpha DU_m/T_m + \mu_m'\alpha DU_m/\mu_m - r\hat{\omega}D\mu_m/\mu_m T_m\right]$$

$$a_{46} = -i\chi r\hat{\omega}/T_m$$

$$a_{62} = -2(\gamma - 1)M_\infty^2 PrDU_m$$

$$a_{63} = -2i(\gamma - 1)M_\infty^2 Pr\alpha DU_m + RPrDT_m/\mu_m T_m$$

$$a_{64} = i(\gamma - 1)M_\infty^2 PrR\hat{\omega}/\mu_m$$

$$a_{65} = \alpha^2 - iRPr\hat{\omega}/\mu_m T_m - (\gamma - 1)M_\infty^2 Pr\mu_m'(DU_m)^2/\mu_m - D^2\mu_m/\mu_m$$

$$a_{66} = -2D\mu_m/\mu_m$$

where

$$\mu_m' = \frac{d\mu_m}{dT_m} \quad , DS = \partial S/\partial y \ ,$$

$$\hat{\omega} = \omega - \alpha U_m \ , \chi = \left[R/\mu_m - ir\gamma M_\infty^2\hat{\omega}\right]^{-1}$$

VITA

The author was born on July 15, 1960 in the village of Zeita, the West Bank of Jordan. After graduation from high school he entered the University of Jordan at Amman, Jordan. He graduated with a Bachelor of Mechanical Engineering in June 1983. In September 1983 the author started his graduate studies in the Department of Mechanical Engineering at Yarmouk University in Irbid, Jordan. He transferred to Virginia Tech in the winter of 1985 and enrolled in the Graduate program at the Department of Engineering Science and Mechanics. He obtained his MSc. in the winter of 1988.